IMPACTS OF CONFINED SPACE ON PRODUCTION FROM TIGHT RESERVOIRS

A Thesis

by

BRIAN C. STIMPSON

Submitted to the Office of Graduate and Professional Studies of
Texas A&M University
in partial fulfillment of the requirements for the degree of

MASTER OF SCIENCE

Chair of Committee,	Maria A. Barrufet
Committee Members,	Thomas A. Blasingame
	Marcelo Sanchez
Head of Department,	A. Daniel Hill

May 2017

Major Subject: Petroleum Engineering

ABSTRACT

This work develops a rigorous method for including confinement effects in fluid modeling. This method was implemented into phase modeling and compositional reservoir simulation to show the impacts of tight media on hydrocarbon phase behavior and production. The rigorous aspect of this method improves upon current methods of incorporating confinement effects in both fluid modeling and reservoir simulation. It is particularly useful for porous media with small pores, where the ratio of medium surface area to fluid volume and fluid-to-rock interaction are significant.

The proposed model utilizes the Peng-Robinson equation of state coupled with the Young-Laplace equation for capillary pressure. The interfacial tension is determined using the parachor model, which is dependent on phase compositions and molar volumes. Capillary pressure is therefore implemented within the vapor-liquid equilibrium (VLE) calculations. Contact angle is an input and can be updated as a temperature-dependent function. When implemented inside the VLE loop, calculation time is minimally impacted, making this a very efficient method.

Vapor-liquid equilibrium using this method for small pores is validated by modeling cases presented in published literature. These published data are obtained either experimentally or by using molecular simulation. In all cases, the model presented in this work is able to closely match phase behavior, showing a decrease in bubble point pressure, and an increase in dew point pressure. Changes in saturation pressure approach zero as the mixture critical point is approached.

Implementation of this method into compositional reservoir simulation shows that confinement generally increases oil and gas production from tight oil reservoirs and generally decreases oil and gas production from tight gas condensate reservoirs, compared with the traditional bulk compositional simulators.

Simple cases of a reservoir cell can be modeled with capillary pressure using a constant-composition expansion or constant-volume depletion method. This results in a capillary pressure curve as a function of liquid saturation. With these curves, relative permeability can be predicted by integration of the reciprocal of the square of capillary pressure.

Reservoir simulation of an Eagle Ford reservoir fluid at various initial pressures shows the impact of capillary pressure and relative permeability on production. At high initial reservoir pressure, oil/gas relative permeability is insignificant, but capillary pressure still significantly impacts oil production. At lower initial pressure, capillary pressure and oil/gas relative permeability both significantly impact production.

ACKNOWLEDGEMENTS

I would first like to express my gratitude to my advisor Dr. Maria Barrufet for the time and attention she gave me throughout this project. She truly was a mentor and great source of knowledge and perspective throughout my experiences working on this project and in my studies. I am grateful for the time and encouragement she gave me; I would not have been able to accomplish what I did without her.

I would also like to thank my committee members. I am grateful to Dr. Tom Blasingame for the incredible courses he taught and the standard of excellence he helped me learn. I would also like to thank Dr. Marcelo Sanchez for the course he taught and the perspectives I gained from it that helped me understand fundamentals related to this project.

All my experiences at Texas A&M were excellent and I would like to thank the Department of Petroleum Engineering and the professors who invest time and effort into teaching and helping students like me succeed.

I would also like to thank my family for their constant support, encouragement, and prayers throughout my studies whenever I needed it.

I am grateful for the Crisman Institute for Petroleum Research for funding my project, which allowed me to develop, present, and publish our research.

CONTRIBUTORS AND SOURCES OF FUNDING

Contributors

This work was supervised by a thesis committee consisting of Professor Maria A. Barrufet of the Department of Petroleum Engineering, Professor Thomas A. Blasingame of the Department of Petroleum Engineering, and Professor Marcelo Sanchez of the Department of Civil Engineering.

All work for the thesis was completed independently by the student.

Funding Sources

Graduate study was supported by an assistantship from The Crisman Institute for Petroleum Research.

NOMENCLATURE

Symbol	Definition
A^j	Polynomial EOS constant of phase j
a_i	EOS attraction parameter of component i, ft^6 psi/lbmol^2
$a\alpha^j$	EOS attraction parameter of phase j, ft^6 psi/lbmol^2
B^j	Polynomial EOS constant of phase j
b_i	EOS co-volume parameter of component i, ft^3/lbmol
b^j	EOS co-volume parameter of phase j, ft^3/lbmol
C	Cumulative density function
D_{BA}	Bentsen-Anli relative permeability denominator
d	Pore diameter, nm
dP_c	Change in capillary pressure, psia
E	Interfacial tension exponent
E_i	Exponential integral function
f_d^j	Phase distribution of depleted volume
f_i^j	Fugacity of component i in phase j, psia
G	Thomeer coefficient
ip	Pore number
K_i	Vapor-liquid equilibrium constant (K-value)
k_{rj}	Relative permeability of phase j
L_p	Pore length, nm
M_i	Molar mass of component i, lbm/lbmol
M^j	Molar mass of phase j, lbm/lbmol
m	Slope of contact angle versus temperature, degrees/°F
N	Probability density function
N_c	Number of components
$N_{BA,j}$	Bentsen-Anli relative permeability numerator of phase j

N_p	Number of pores
N_s	Number of steps
n_d^j	Number of moles depleted of phase j, lbmol
$n_{d,i}$	Number of depleted moles of component i, lbmol
n_i	Number of moles of component i, lbmol
n_t	Total number of moles, lbmol
P_c	Capillary pressure, psia
P_{cs}	Bentsen-Anli shape parameter, psia
P_{ct}	Threshold capillary pressure, psia
P_i	Parachor of component i, dyne$^{1/E}$ cm$^{3-1/E}$/gmol
p^j	Pressure of phase j, psia
p^s	Saturation pressure, psia
$p_{c,i}$	Critical pressure of component i, psia
R	Gas constant, 10.731 ft^3 psi/lbmol R
R_c	Principal radius of curvature, nm
r	Pore radius, nm
S_j	Volume saturation of phase j
S_o^*	Normalized oil saturation
S_∞	Thomeer coefficient
s_i	Volume shift parameter of component i
T	Temperature, °F
$T_{c,i}$	Critical temperature of component i, °F
$T_{cp,i}$	Pore critical temperature of component i
$T_{r,i}$	Reduced temperature of component i
T_{ref}	Reference temperature, °F
V_d	Depleted volume, ft^3
$\tilde{V}_m$	Corrected total molar volume, ft^3/lbmol
V_m^j	Molar volume of phase j, ft^3/lbmol

$\tilde{V}_m^j$	Corrected molar volume of phase j, ft^3/lbmol
V_{ip}^o	Volume of oil in pore number ip
V_p	Volume of pores, nm^3
$\tilde{V}_t$	Corrected total volume, ft^3/lbmol
x	Density function variable
x_i	Liquid mole fraction of component i
x_i^j	Mole fraction of component i in phase j
y_i	Vapor mole fraction of component i
Z^j	Compressibility factor of phase j
$\tilde{Z}^j$	Corrected compressibility factor of phase j
$Z_{c,i}$	Critical compressibility factor of component i
z_i	Overall mole fraction of component i

Greek Symbols

α_i	EOS scaling factor
β	Fraction of total moles in vapor phase
δ_{ik}	Binary interaction parameter between components i and j
ε_K	Convergence criterion for K-values
ε_{P_c}	Convergence criterion for capillary pressure, psia
θ	Contact angle, degrees
θ_{ref}	Reference contact angle, degrees
κ_i	EOS characteristic constant of component i
λ	Brooks-Corey exponent
λ^j	Mobility of phase j, md/cP
μ	Distribution mean
μ^j	Viscosity of phase j, cP
$\tilde{\rho}^j$	Corrected mass density of phase j, lbm/ft^3
σ	Interfacial tension, dyne/cm

σ_d	Distribution standard deviation
ϕ_i^j	Fugacity coefficient of component i in phase j
ϕ^j	Single component fugacity coefficient of phase j
ψ_i^j	EOS mixture parameter of component i in phase j, ft^6 $psi/lbmol^2$
ω_i	Acentric factor of component i

Subscripts

g	Gas phase (for saturation, flow rates, cumulative oil)
i	Component i
k	Component k
o	Oil phase (for saturation, flow rates, cumulative oil)

Superscripts

j	Phase j
l	Liquid phase
v	Vapor phase

Abbreviations

BHP	Bottomhole pressure, psia
EOS	Equation of state
GOR	Gas-oil ratio, SCF/STB
PR	Peng-Robinson
PVT	Pressure-volume-temperature
SCF	Standard cubic feet
STB	Stock tank barrel
VLE	Vapor-liquid equilibrium

TABLE OF CONTENTS

Page

LIST OF FIGURES

Page

LIST OF TABLES

Page

CHAPTER I
INTRODUCTION

Oil production in the United States has recently shifted to the exploitation of shales. There has been a steep learning curve with this shift in focus. Some of the major technological changes consist of advanced drilling techniques for horizontal and directional wells and multiple larger fractures in these horizontal wells. Some of the challenges faced in engineering in the oil and gas industry include describing the mechanics of the shale rock and describing the interaction of the shale rock with the fluid inside the pores. The pore sizes in shales are of the order of magnitude of molecular diameters, whereas conventional sandstones contain pores that are tens to hundreds of times larger. This work focuses on the behavior of fluids inside the shale rock, which have been shown to behave differently than if these fluids were contained in conventional reservoir rock because of the small pores.

Various methods exist for describing the behavior of fluids confined in small pores. These methods include performing molecular simulation, applying a shift in critical properties, and incorporating capillary pressure from a model or correlation. The most fundamental and mechanistic capillary pressure model is the Young-Laplace equation, which can be derived from either force balance or thermodynamics. Implementation of the Young-Laplace equation is the best option for modeling two hydrocarbon phases in equilibrium because it adds very little computational effort and can be applied at a very wide range of pore sizes, reaching as low as 1-2 nanometers for weakly wetting systems and 7-10 nanometers for more strongly wetting systems.

Capillary pressure can be incorporated in phase equilibrium calculations, which are used in phase behavior prediction and reservoir simulation. Current reservoir simulators do not rigorously incorporate capillary pressure into simulation. The rigorous approach allows for updating capillary pressure based on changes in interfacial tension. Interfacial tension can significantly change inside the reservoir throughout production due to compositional and pressure changes in the reservoir.

1.1 Objectives

The main objective of this research was to study the impact of confinement on phase behavior and hydrocarbon production in tight media. To do this, we incorporated the effects of capillarity in fluid behavior modeling and compositional reservoir simulation. To accomplish this we fulfill the following objectives:

1. Develop an algorithm for rigorously incorporating capillary pressure in vapor-liquid equilibrium calculations with an equations of state (EOS)
2. Validate the model against published phase equilibrium data for single and multiple component systems
3. Implement the algorithm into a compositional reservoir simulator

1.2 Description of chapters

Chapter I discusses the problem and identifies the objectives.

Chapter II gives an overview of published literature pertaining to the topic of unconventional reservoirs and reservoir characterization. It also discusses work done on describing hydrocarbon systems using an equation of state. It discusses the modeling of reservoir fluids, compositional reservoir simulation, and thermodynamics in confined spaces.

Chapter III discusses the theory of implementing capillary pressure in vapor-liquid equilibrium. It gives an overview of vapor-liquid equilibrium using the Peng-Robinson (PR) equation of state, then discusses how we implement interfacial surface effects using capillary pressure. This chapter also shows the expected effects of capillary pressure on hydrocarbon phase behavior.

Chapter IV validates the developed model by modeling various systems for which published data exist. These systems vary in number of component and component type to show the versatility and accuracy of the model.

Chapter V discusses implementation of the model into compositional reservoir simulation. It compares the production forecasts of reservoirs with and without the effects of capillary pressure.

Chapter VI develops a method of predicting oil/gas relative permeability curves from capillary pressure curves generated using fluid modeling. It shows the results of these relative permeabilities as inputs into compositional reservoir simulations.

Chapter VII lists the fluids used in this research and their components, compositions, and properties as inputs for the model.

Chapter VIII discusses the conclusions of this work and recommendations for implementation and future work.

CHAPTER II

LITERATURE REVIEW

2.1 Unconventional Reservoirs

Petroleum reservoirs are accumulations of hydrocarbon mixtures in a subsurface porous medium and come in a variety of different forms. Conventional reservoirs contain fluids that have migrated from a source rock and have accumulated into a trap. These reservoirs have been studied extensively and well-known methods exist of understanding their behavior. However, these reservoirs are fairly few compared with other types of reservoirs, such as tight oil and gas, heavy oil, coalbed methane, oil and gas shales, and gas hydrates. Many of these reservoir types are termed *unconventional* reservoirs. Masters (1979) and Holditch (2006) represent the types of petroleum reservoirs using a resource triangle, shown in Figure 2-1. The conventional reservoirs are much higher quality, but are fewer in quantity. Unconventional reservoirs are much more plentiful, but are lower in quality. The lower quality reservoirs cost more to exploit and require better technology.

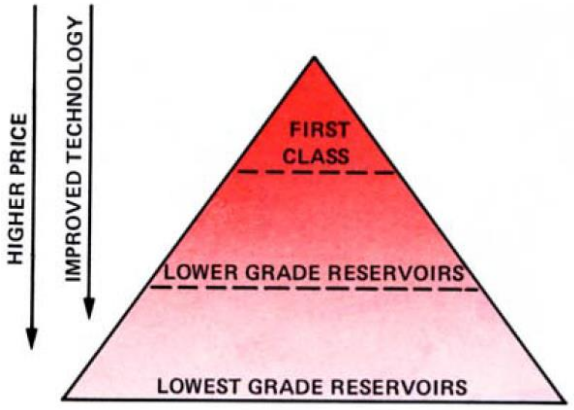

Figure 2-1. Hydrocarbon resource triangle from Masters (1979).

In the United States, shale gas production is primarily located in the Marcellus and Utica shales in Pennsylvania and West Virginia, the Haynesville shale in Louisiana and Texas, the Eagle Ford shale in Texas, with other production spread across the United States. Much of the oil production activity is concentrated the Bakken in North Dakota, the Permian Basin in west Texas and New Mexico, the Eagle Ford formation in south Texas, with some production from others scattered across the United States. A map of the current shale plays in the United States is shown in Figure 2-2. Most of the activity in recent years has been in the Bakken, Eagle Ford, and Permian formations. However, due to recent economic conditions, the industry has focused mainly on the more economically favorable plays in the Permian formations in west Texas. The Permian Basin is the only area in the United States to increase in production since the decrease in oil price in late 2014. The production history is shown in Figure 2-3, which shows the highest historical producing formation to be the Eagle Ford. (EIA 2016)

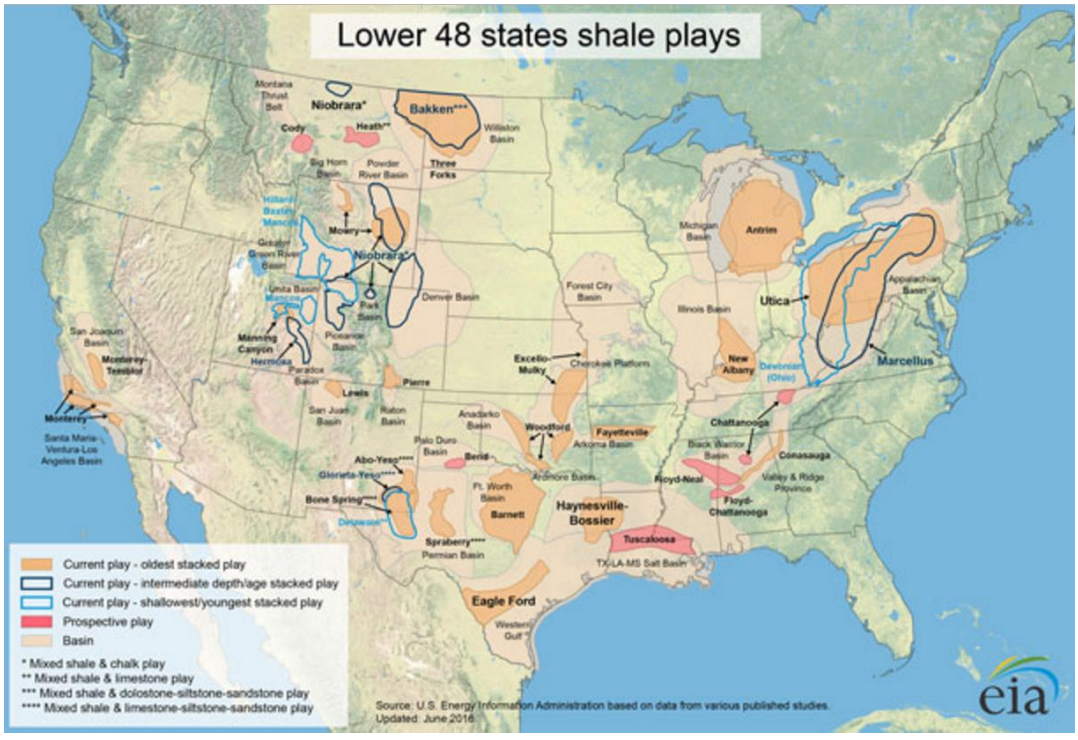

Figure 2-2. Current shale plays in the United States (EIA 2016).

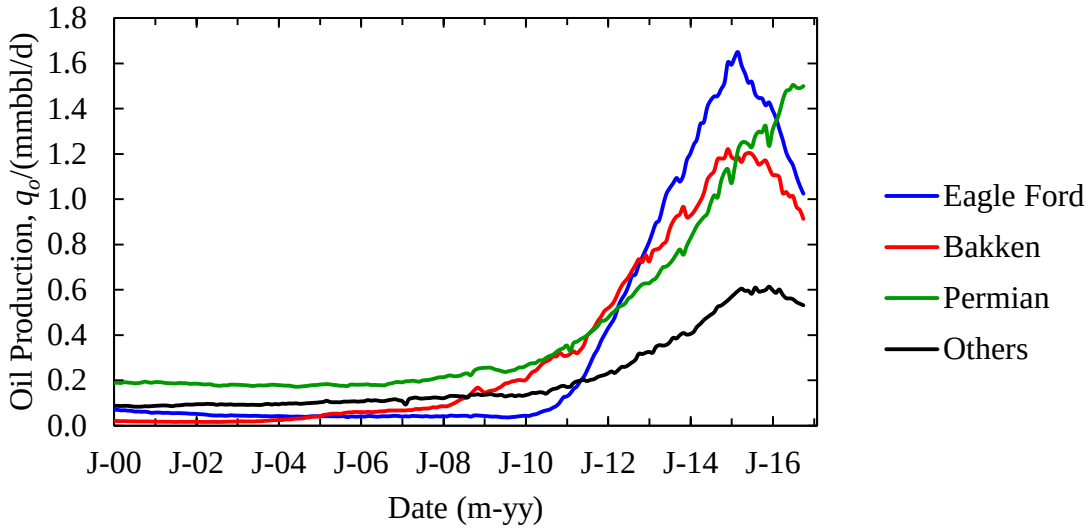

Figure 2-3. Production history of major shale oil formation in the United States; data from EIA (2016)

Shale reservoirs exhibit unique characteristics. One major characteristic is the pore size. Nelson (2009) describes the pore size of different types of sedimentary rocks. Figure 2-4 shows this variation and includes the molecular sizes of various compounds found in reservoir fluids. It also shows the methods used to determine pore diameter. Many of the shales listed contain pore diameters in the range of a few nanometers to hundreds of nanometers. The smaller pore diameters are on the order of molecular size. In addition to various pore sizes, reservoir composition and pore structure are important factors. Passey et al. (2010) describes the mineralogy of several shale reservoirs, including some description on pore structure. Riewchotisakul and Akkutlu (2016) state that hydrocarbons are stored in the inorganic-rock matrix, pores within the organic matter, and natural fractures, all of which interact differently with the hydrocarbon fluids. In addition, each shale formation contains different fluids, and fluid compositions can even vary significantly across a formation, such as the Eagle Ford formation (Gong et al. 2013).

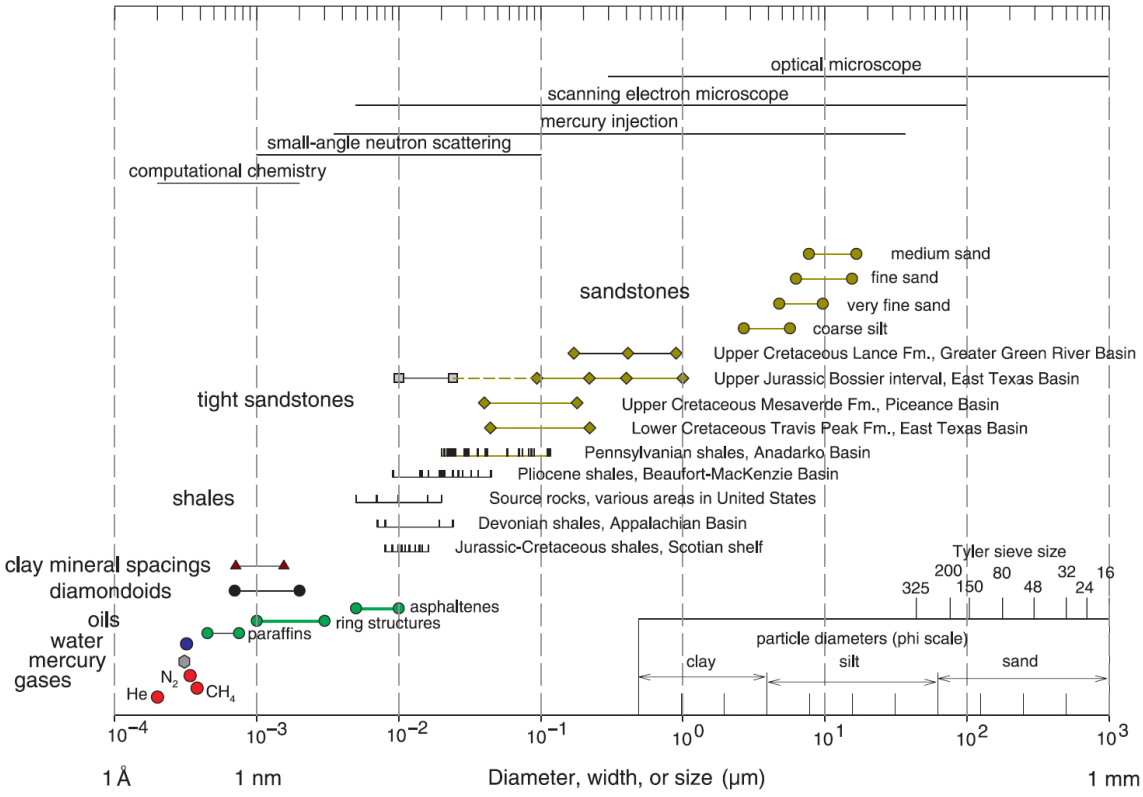

Figure 2-4. Pore sizes of various formation types (Nelson 2009).

2.2 Reservoir Characterization

Production optimization from reservoirs requires understanding of both reservoir and fluid properties. Conventional reservoir properties are obtained by running drawdown or shut-in tests in the field (Matthews and Russell 1967), analyzing core samples collected from the reservoir (Pyle and Sherborne 1939), evaluating well logs (Johnson 1961), and by matching a reservoir simulator to production history to obtain or improve estimates of saturation, pressure, permeability, or porosity (Rwechungura et al. 2011). For all reservoir types, fluid properties can be obtained by analyzing fluid samples in a laboratory and by simulating these properties using a model.

Field samples can be collected downhole (Schilthuis 1935) or by recombining separator fluids using the produced gas-oil-ratio (GOR) to create a representative sample of the reservoir fluid (Standing 1977). Downhole samples of shale reservoirs are difficult to collect. The collected fluids are sent to a laboratory, where various tests are run, which describe how the reservoir fluid behaves under various conditions. This can also be referred to as pressure-temperature-volume (PVT) analysis.

In the PVT laboratory, flash liberation (or constant composition expansion), differential liberation, and constant volume depletion (CVD) tests describe fluid saturation points and how phases separate at pressures below the saturation pressure (bubble point for oil systems or dew points for gas condensates) (McCain 1990). Constant composition expansion (CCE) is used to determine the saturation pressure of the fluid, which is the pressure at which two phases begin to form out of one phase. Oil and gas formation volume factors and solution gas oil ratios are obtained from the differential liberation (DL) tests. These values are critical to be able to use the material balance equation in reservoir engineering. Another important test is compositional analysis, which determines the mass, volume, or mole fraction for each component in the sample. This is normally done using gas chromatography and dictates what type of products can be obtained from the reservoir fluid. Compositional data is needed for equation of state (EOS) modeling. (Freyss et al. 1989)

2.3 Modeling Reservoir Fluids

Modeling of reservoir fluids using an equation of state began in 1979 by Yarborough (1979), who implemented advanced cubic equations of state, specifically those by Redlich and Kwong (1949) and Peng and Robinson (1976). EOS models can produce phase diagrams, which describe the distribution of phases at any temperature and pressure for a given fluid. These diagrams are useful in describing two-phase fluid flow through the reservoir, wellbore, and throughout surface equipment and pipelines. The temperature and pressure path of a given fluid through the production process can be plotted on this phase diagram. An example of a phase diagram is shown in Figure 2-5 for the synthetic fluid

described in Table 2-1 (same as synthetic fluid 5 on p. 126). Major advantages of EOS modeling include its low cost compared to laboratory testing and its range of application. The biggest disadvantage is the error associated with EOS modeling. Ashour et al. (2011) give a good overview of the uses of EOS in the oil and gas industry.

Table 2-1. Synthetic fluid composition and properties for synthetic fluid (same as synthetic fluid 5 on p. 126).

Species	x_i	M_i	$p_{c,i}$ (psia)	$T_{c,i}$ (°F)	ω_i	s_i	$Z_{c,i}$	P_i
C_1	0.65	16.043	667.4	-116.9	0.008	-0.154	0.288	77
C_2	0.1	30	708.5	89.7	0.098	-0.1002	0.284	108
nC_4	0.05	58.1	551.3	305.4	0.193	-0.0641	0.2743	189.9
nC_{10}	0.2	134	367	659.8	0.444	0.0803	0.249	505.88

$\delta_{ik} = 0$ for all components

When determining PVT properties, such as formation volume factor and GOR using classical thermodynamics, whether done experimentally or with a model, the results are assumed to represent the fluid in place. This assumption is valid for most conventional reservoirs. However, when fluids are confined in small spaces, phase behavior is altered due to the effects of the container. This is similar to the surface area concept in catalysis, which describes the surface area as a ratio of area to volume.

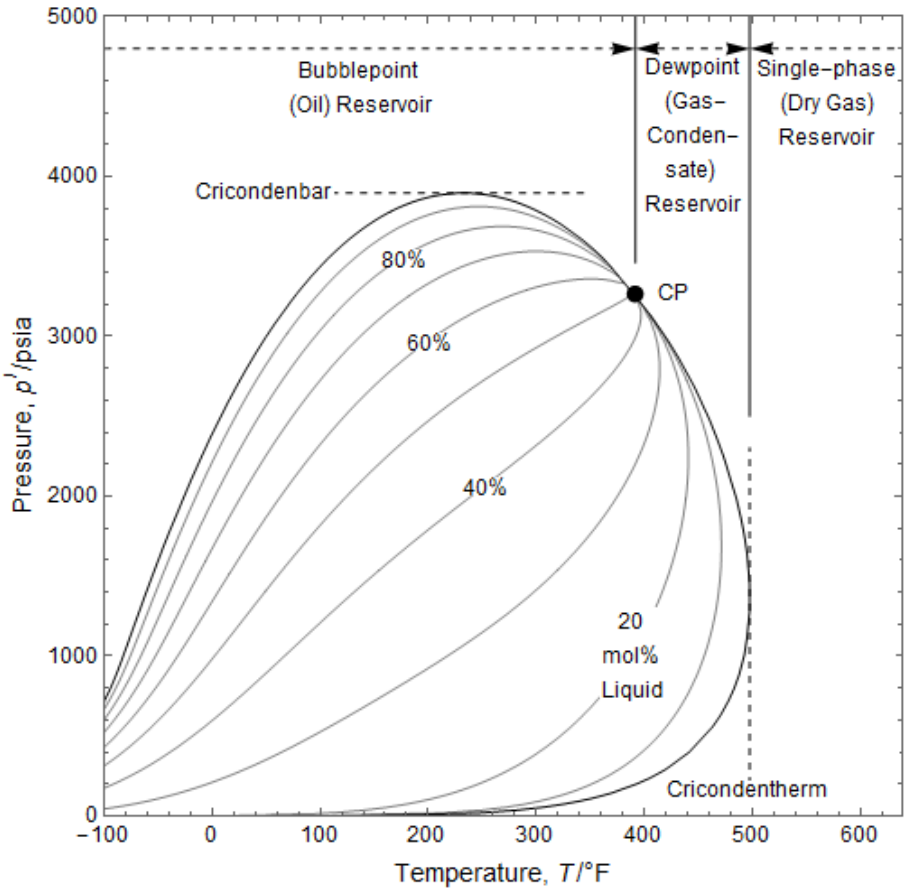

Figure 2-5. Computed phase diagram for a synthetic fluid mixture of 65% methane, 10% ethane 5% n-butane, and 15% n-decane, as described in Table 2-1.

2.4 Compositional Reservoir Simulation Using Equation of State

Compositional reservoir simulation began in 1969 as a way to simulate fluid flow through a porous medium where mass transfer between phases is significant (Roebuck et al. 1969). However, phase equilibrium in the first simulators was determined using correlations for vapor-liquid distribution ratios (K-values). Implementation of an EOS in a compositional simulator did not begin until 1980, where phase compositions were allowed to vary by using K-values calculated with the Redlich-Kwong EOS (Coats 1980). The Peng-Robinson EOS was also implemented shortly thereafter (Nghiem et al. 1981).

Compositional simulation with an EOS has been a useful way to model various enhanced oil recovery (EOR) techniques, such as carbon dioxide injection and thermal EOR, where miscibility and PVT changes are introduced into the reservoir.

2.5 Thermodynamics in Confined Spaces

Various methods for incorporating the effects of confinement have been implemented in thermodynamic modeling. One method is incorporating a shift in critical temperature and pressure based on the Lennard-Jones potential and pore radius (Zarragoicoechea and Kuz 2004). However, the relationship for the shift in critical pressure has not been experimentally confirmed (Teklu et al. 2014) and this methodology makes it difficult to incorporate fluid to rock interaction. Another method is to use molecular simulation, which provides interesting insights into fluid behavior in small pores, such as the study done by Feng and Akkutlu (2015). However, use of this method is limited because of the expensive computing requirements for results (Islam et al. 2015), which is impractical for reservoir simulation. Implementation of adsorption using a method, such as that developed by Ambrose et al. (2011), is useful for single phase reservoirs that have significant rock surface area in contact with the reservoir fluid. A final method is incorporating capillary pressure in phase modeling, which has received recent focus due to its simple application and physics-based approach.

The study of capillary phenomena began as early as 1687 by Newton and some studies continued throughout the 18^{th} century (Sing and Williams 2012). The well-known works by Young (1805) and Laplace (1805) qualitatively describe capillary pressure and its relation to the shape of the curved interface. The next major work on capillary pressure was studied by Lord Kelvin (Thomson 1871), who developed the Kelvin equation. This equation describes the height of a fluid in a capillary based on difference in density, interfacial tension, and radius of curvature. Work performed by Shereshefsky (1928) and others (Wilsdon et al. 1935) studied the effects of capillary pressure on the vapor pressure of water and showed that the actual change in vapor pressure due to capillarity is much larger than is predicted by the Kelvin equation.

The first work to couple capillarity with an EOS was performed by Udell (1982), who coupled the van der Waals EOS with the Young-Laplace equation to describe the change in saturation pressure and temperature of fluids confined in pores. He showed that in small pores, saturation pressure decreases and saturation temperature increases. Brusilovsky (1992) was the first to couple the Peng-Robinson EOS with the Young-Laplace equation for real reservoir fluids. Due to the recent development of shale resources, which contain very small pores, Nojabaei et al. (2013), Pang et al. (2012), Sandoval et al. (2015), Islam et al. (2015), and Zhang et al. (2016) incorporate capillarity into thermodynamic modeling to describe phase behavior in confined spaces. They all observe a suppression of the phase envelope, which is consistent among all methods of incorporating confinement effects. Other works by Abu Al-Rub and Datta (1998) and Firincioglu et al. (2012) include other effects with capillary pressure to describe the effects of confinement on phase behavior.

2.6 Other Applications of Modelling in Confined Space

Capillarity is seen in many environments other than hydrocarbons in shales. Clarke et al. (1999) and Pesaran and Shariati (2013) study the impact of capillary pressure on gas hydrate formation. Tsakiroglou (2011) analyzed capillary pressure and relative permeability of the oil-water system in simulated pores and soil. The removal of water from porous media using drying methods has been studied by Scherer (1990), Metzger et al. (2007), and Vorhauer et al. (2015). Peng et al. (2011) studied the application of drying in the paper making-process using capillary pressure. Shi and Yuan (2012) used capillarity in modeling wicking properties of textiles. Morrow (1970) explained capillarity in dewatering porous solids, centrifuging, and other applications.

Other interesting applications of the capillary pressure equation include work by Si et al. (2015) in modeling mass transport in fuel cells. León et al. (2008) incorporates surface tension using the Young-Laplace equation for heterogeneous surface reactions. The effect of capillarity on wetting properties of nanotubes has been studied by Dujardin et al. (1994) and Jayaraman et al. (2005). Nanotube growth (Gupta 2010) and deformation due to phase behavior (Rossi et al. 2009) also sees the effects of capillarity.

CHAPTER III
THEORY

3.1 Phase Behavior Modeling

We model phase behavior using the Peng-Robinson EOS for mixtures, shown in Eq. (3.1)-(3.7) (Peng and Robinson 1976). We use the correction for heavier components shown in Eq. (3.8) from Robinson and Peng (1978). Eq. (3.2) and (3.3) incorporate quadratic mixing rules for the attraction parameter and linear mixing rules for the repulsion (or co-volume) parameter. Many authors have reported modifications to the alpha function in Eq. (3.6) to improve accuracy. These modifications are presented by Young et al. (2016). However, we use the original alpha functions.

$$p^j = \frac{RT}{V_m^j - b^j} - \frac{a\alpha^j}{V_m^j\left(V_m^j + b^j\right) + b^j\left(V_m^j - b^j\right)} \tag{3.1}$$

$$a\alpha^j = \sum_{i=1}^{N_c}\sum_{k=1}^{N_c} x_i^j x_k^j (a_i a_k \alpha_i \alpha_k)^{1/2}(1 - \delta_{ik}) \tag{3.2}$$

$$b^j = \sum_{i=1}^{N_c} x_i^j b_i \tag{3.3}$$

$$a_i = 0.45724\frac{R^2 {T_{c,i}}^2}{p_{c,i}} \tag{3.4}$$

$$b_i = 0.07780\frac{RT_{c,i}}{p_{c,i}} \tag{3.5}$$

$$\alpha_i = \left(1 + \kappa_i\left(1 - \sqrt{T_{r,i}}\right)\right)^2 \tag{3.6}$$

$$\kappa_i = 0.37464 + 1.54226\omega_i - 0.26992\omega_i^2, \qquad \omega_i \le 0.491 \tag{3.7}$$

$$\kappa_i = 0.379642 + 1.487503\omega_i - 0.164423\omega_i^2 + 0.016666\omega_i^3, \qquad \omega_i > 0.491 \tag{3.8}$$

$$T_{r,i} = \frac{T + 459.76}{T_{c,i} + 459.67} \tag{3.9}$$

Peng and Robinson (1976) derive a convenient cubic form of the Peng Robinson EOS that introduces the compressibility factor Z, shown by Eq. (3.10)-(3.13). A significant attribute of this is its ease of solving in any numerical or analytical cubic solver.

$$Z^{j^3} - \left(1 - B^j\right)Z^{j^2} + \left(A^j - 3B^{j^2} - 2B^j\right)Z^j - \left(A^j B^j - B^{j^2} - B^{j^3}\right) = 0 \tag{3.10}$$

$$A^j = \frac{a\alpha^j p^j}{R^2 T^2} \tag{3.11}$$

$$B^j = \frac{b^j p^j}{RT} \tag{3.12}$$

$$Z^j = \frac{p^j V_m^j}{RT} \tag{3.13}$$

Molar volumes calculated using the PR EOS are not as accurate, so Péneloux et al. (1982) proposed a volume translation. We apply this translation after VLE is solved, since the change in volume does not affect phase boundaries (temperature or pressure) and/or phase compositions obtained from VLE computations for specified pressure and temperature. Constant shift parameters are reported in literature (Jhaveri and Youngren 1988) or calculated using an EOS-based method, such as that proposed by Soreide (1989), or other correlation. The shift parameter is shown to change and sharply increase as it nears the critical point (Soave 1984). Methods such as those proposed by Mathias et al. (1989), Watson et al. (1986), Monnery et al. (1998), or Miqueu et al. (2003) consider the temperature-dependence of the shift parameter. Eq. (3.15) shows the simple estimation of s_i as a function of temperature from Miqueu et al. (2003). Figure 3-1 shows the impact of temperature on volume shifts using the correlation by Miqueu at various acentric factors. Corrected densities can then be calculated from the molar volumes, as in Eq. (3.16), with phase mixture molar mass defined by Eq. (3.17). A constant value for the volume shift may be approximated using a fixed reduced temperature (usually $T_{r,i} = 0.7$). This is useful because high reservoir temperatures may be above the critical temperature of some components, making the temperature-dependent volume shift method unreasonable.

$$\tilde{V}_m^j = V_m^j - \sum_{i=1}^{N_c} s_i b_i x_i^j \tag{3.14}$$

$$s_i = \left|T_{r,i} - 0.628\right|^{2.28} - 0.155 + 0.421\omega_i + 0.590\exp\left[28.40\left(T_{r,i} - 1\right)\right] \tag{3.15}$$

$$\tilde{\rho}^j = \frac{M^j}{\tilde{V}_m^j} \tag{3.16}$$

$$M^j = \sum_{i=1}^{N_c} x_i^j M_i \tag{3.17}$$

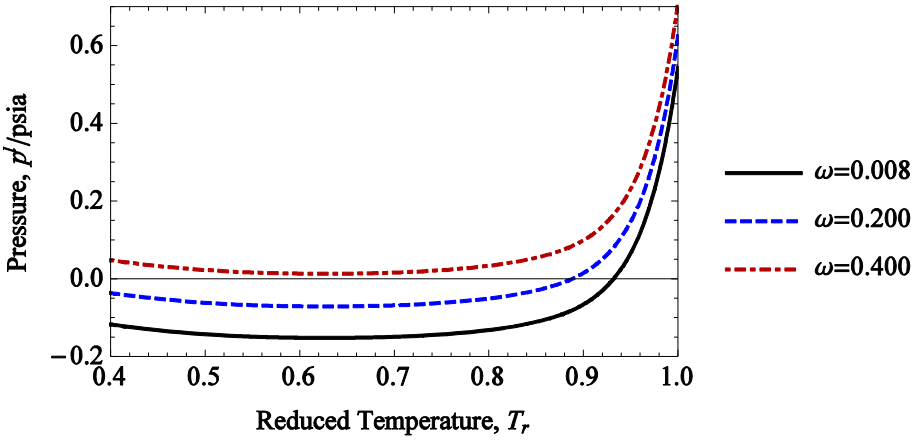

Figure 3-1. Temperature dependence of volume shift parameter calculated using correlation by Miqueu et al. (2003).

To obtain phase distributions and molar volumes when two phases exist, vapor-liquid equilibrium (VLE) calculations are required. This is accomplished using the flash equation from Rachford and Rice (1952), which employs the equilibrium constants (K-values) of the components in the mixture to determine the fraction of the total mixture in the vapor phase, β. The K-values are defined by Eq. (3.19) and the compositions of each phase by Eq. (3.20) - (3.21). Various methods exist for solving the Rachford-Rice equation, proposed by Michelsen (1982), Li and Johns (2006), and Nichita and Leibovici (2013).

$$\sum_{i=1}^{N_c} \frac{(K_i - 1)z_i}{(K_i - 1)\beta + 1} = 0 \tag{3.18}$$

$$K_i = \frac{y_i}{x_i} \tag{3.19}$$

$$x_i = \frac{z_i}{(K_i - 1)\beta + 1} \tag{3.20}$$

$$y_i = x_i K_i \tag{3.21}$$

We must first estimate the K-values, which we accomplish using the equation from Wilson (1969) shown in Eq. (3.22). A more involved, but more accurate guess method is given by Varotsis (1989), which is not implemented or shown here.

$$K_i = \frac{p_{c,i}}{p} \exp\left[5.37(1 + \omega_i)\left(1 - \frac{1}{T_{r,i}}\right)\right] \tag{3.22}$$

To calculate the K-values for subsequent iterations, component phase fugacities are equated by Eq. (3.23). The fugacity of a particular component in a phase *j* is calculated using the phase pressure, fugacity coefficient, and component molar fraction, shown in Eq. (3.24).

$$f_i^l = f_i^v \tag{3.23}$$

$$f_i^j = p^j \phi_i^j x_i^j \tag{3.24}$$

By equating fugacities and solving for the K-value, we derive Eq. (3.25). For typical flash calculations, the vapor and liquid pressures are considered equal, so the K-value simplifies to a ratio of fugacity coefficients.

$$K_i = \frac{p^l \phi_i^l}{p^v \phi_i^v} \tag{3.25}$$

The fugacity coefficient can be derived from the chosen equation of state using the thermodynamic relationship in Eq. (3.26) (Smith et al. 2005). For the Peng Robinson EOS, the equation is shown in Eq. (3.27)-(3.28), derived by Peng and Robinson (1976). A derivation of the fugacity equation for the PR EOS and the corresponding mixing rules are given in the Appendix.

$$\ln \phi_i^j = \int_0^{p^j} \left(Z^j - \frac{1}{p} \right) dp \tag{3.26}$$

$$\phi_i^j = \exp\left[\frac{b_i}{b^j}\left(Z^j - 1\right) - \ln\left(Z^j - B^j\right) - \frac{A^j}{2\sqrt{2}B^j}\left(\frac{\psi_i^j}{a\alpha^j} - \frac{b_i}{b^j} \right) \ln\left(\frac{Z^j + \left(1+\sqrt{2}\right)B^j}{Z^j + \left(1-\sqrt{2}\right)B^j} \right) \right] \tag{3.27}$$

$$\psi_i^j = 2\sum_{k=1}^{N_c} x_k^j \left(a_i \alpha_i a_k \alpha_k\right)^{1/2} (1 - \delta_{ik}) \tag{3.28}$$

The process for performing a VLE calculation is shown in Figure 3-2. Once the flash calculation is complete, the molar volumes are corrected using the volume translation and density is calculated using Eq. (3.16). This volume translation is permissible because when calculating VLE, the translation terms cancel and yield the identical result as the case without translation (Péneloux et al. 1982). With the phase compositions, temperature, and pressure, phase viscosities can be calculated using the method from Lohrenz et al. (1964), which requires the critical compressibility factor Z_c for each component.

The VLE solution yields the molar fraction of vapor β. However, the liquid phase volume saturation can be calculated from the mole fraction of vapor, corrected liquid molar volume, and corrected total molar volume, using Eq. (3.29) for saturation and Eq. (3.30) for total molar volume.

$$S_l = \frac{(1-\beta)\tilde{V}_m^l}{\tilde{V}_m} \tag{3.29}$$

$$\tilde{V}_m = \beta \tilde{V}_m^l + (1-\beta)\tilde{V}_m^v \tag{3.30}$$

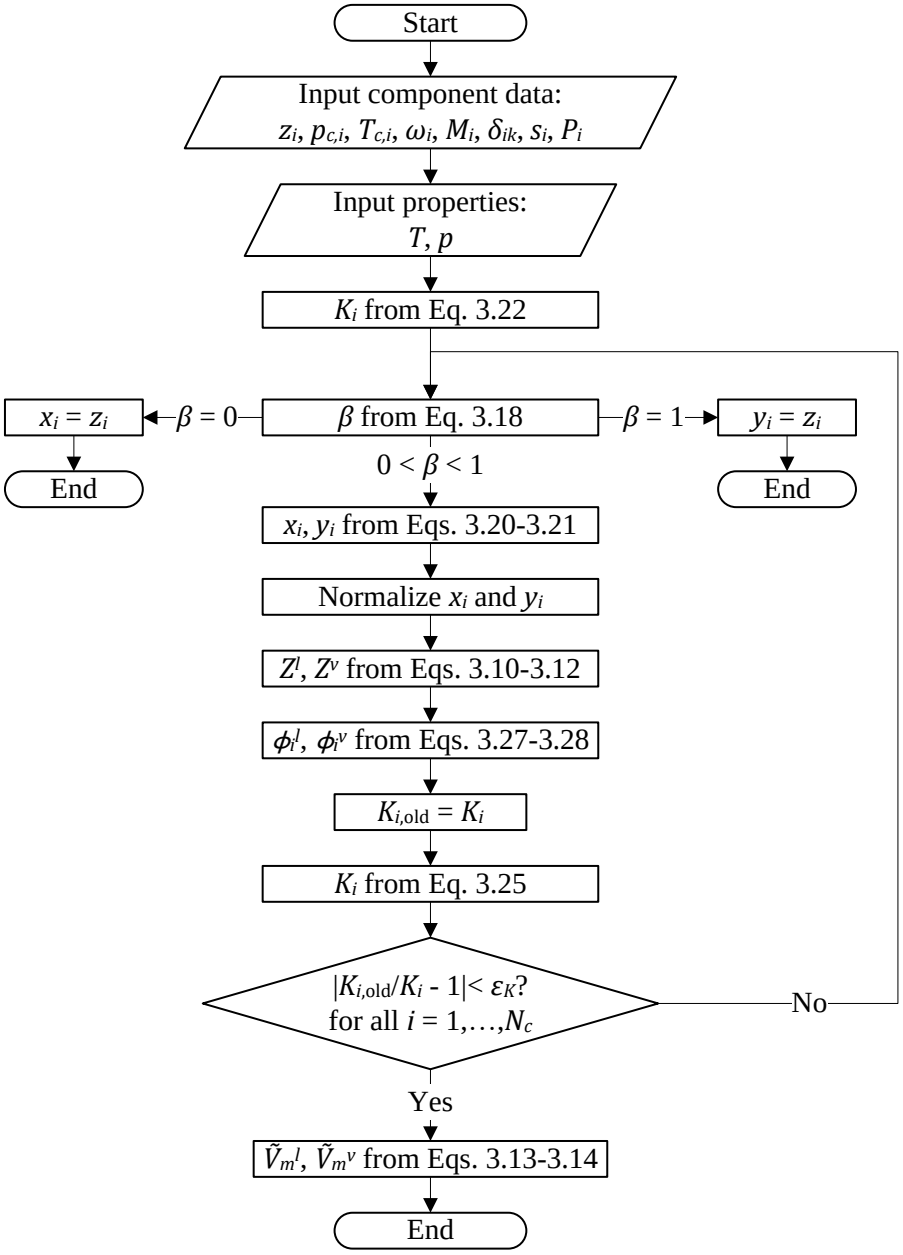

Figure 3-2. Flow diagram of typical VLE calculation.

3.1.1 Pure Component Vapor-Liquid Equilibrium

For a pure species, the same process applies for VLE calculations. However, the fugacity equation is simplified to Eq. (3.31) and the component subscript is dropped. A full development of the PR EOS for single components is presented by Stimpson and Barrufet (2016b).

$$\phi^j = \exp\left[Z^j - 1 - \ln\left(Z^j - B^j\right) - \frac{A^j}{2\sqrt{2}B^j}\ln\left(\frac{Z^j + \left(1+\sqrt{2}\right)B^j}{Z^j + \left(1-\sqrt{2}\right)B^j}\right)\right] \tag{3.31}$$

3.2 Incorporating Surface Effects

When two fluid phases are in contact with each other, a phase interface exists. Due to the density discontinuity at the phase interface, a surface or interfacial tension (IFT) exists. This tension is dependent on the distance between molecules, which is related by a fourth power (Lewis 1923). The dependency of IFT on the difference of phase density was first established by Macleod (1923) and reiterated by Sugden (1924). The constant in the equation was termed the *parachor* by Sugden (1930). Weinaug and Katz (1943) show that this equation is additive and can be used for mixtures. Since then, modifications have been made to more accurately predict IFT of mixtures. One useful correction is a density dependent exponent proposed by Danesh et al. (1991). The original equation is shown by Eq. (3.32) where $E = 4$. The modified exponent is shown in Eq. (3.33). The original equation carries an estimated error of ±24%, whereas the exponent modification has an error of only ±10% (Danesh et al. 1991). These error values vary based on the data type, so we assumed a rounded value between the reported values of different data types. Figure 3-3 shows the difference in IFT calculation and error bands for the two methods over a range of pressures at a constant temperature of 200 °F for the synthetic fluid shown in Table 3-1 (same as synthetic fluid 4 on p. 126). Figure 3-4 shows the two methods for a constant pressure of 1,000 psia for the same fluid over a range of temperatures.

$$\sigma^{1/E} = \sum_{i=1}^{N_c} P_i \left(\frac{x_i}{\tilde{V}_m^l} - \frac{y_i}{\tilde{V}_m^v} \right) = \sum_{i=1}^{N_c} P_i \left(\frac{x_i \tilde{\rho}^l}{M^l} - \frac{y_i \tilde{\rho}^v}{M^v} \right) \tag{3.32}$$

$$E = 3.583 + 0.16 \left(\frac{\tilde{\rho}^l}{M^l} - \frac{\tilde{\rho}^v}{M^v} \right) = 3.583 + 0.16 \left(\frac{1}{\tilde{V}_m^l} - \frac{1}{\tilde{V}_m^v} \right) \tag{3.33}$$

Table 3-1. Synthetic fluid composition and properties for synthetic volatile oil (same as synthetic fluid 4 on p. 126).

Species	x_i	M_i	$p_{c,i}$ (psia)	$T_{c,i}$ (°F)	ω_i	s_i	$Z_{c,i}$	P_i
C_1	0.60	16.043	667.4	-116.9	0.008	-0.154	0.288	77
C_2	0.1	30	708.5	89.7	0.098	-0.1002	0.284	108
nC_4	0.05	58.1	551.3	305.4	0.193	-0.0641	0.2743	189.9
nC_{10}	0.25	134	367	659.8	0.444	0.0803	0.249	505.88

$\delta_{ik} = 0$ for all components

The parachor value is a constant of proportionality that is unique to a particular species. Parachors are reported by Amyx et al. (1960), Fanchi (1985), and Schechter and Guo (1998). For species that do not have reported parachor values, Fanchi (1985), Alkan and Luan (1993), and Broseta and Ragil (1995) present correlations based on critical properties and acentric factors. One simple correlation from Alkan and Luan (1993) is shown in Eq. (3.34), where $T_{c,i}$ has units of K.

$$P_i = 33.2309 \exp\left(0.004085 T_{c,i}\right) \tag{3.34}$$

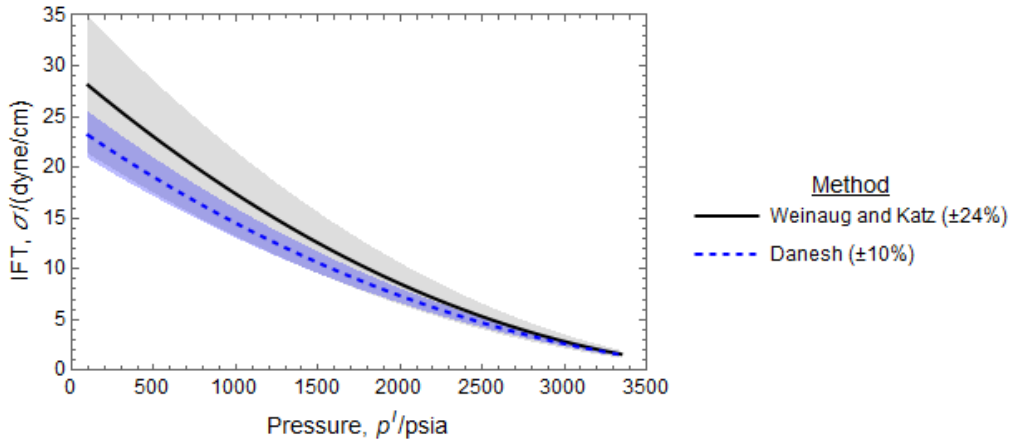

Figure 3-3. Comparison of IFT by methods with error bands for a range of pressures at constant temperature of 200 °F for the synthetic oil in Table 3-1 (60% methane, 10% ethane, 5% n-butane, and 25% n-decane).

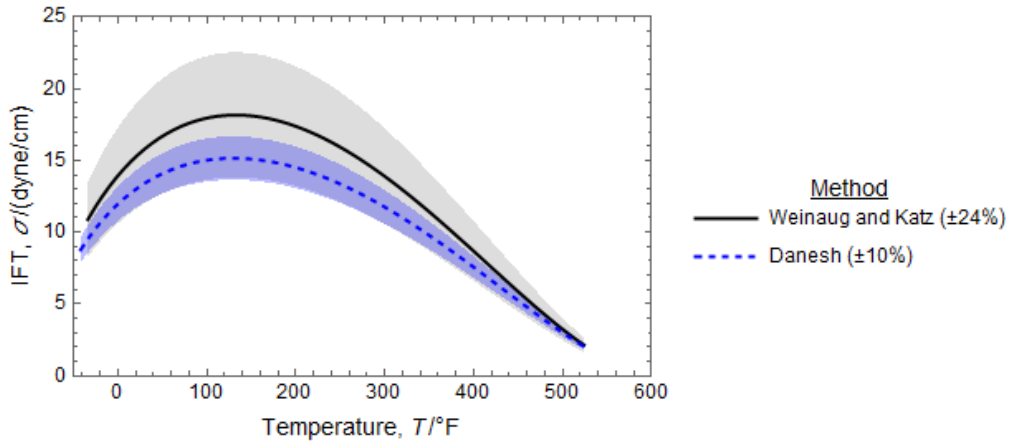

Figure 3-4. Comparison of IFT by methods with error bands for a range of temperatures at constant pressure of 1000 psia for the synthetic oil in Table 3-1 (60% methane, 10% ethane, 5% n-butane, and 25% n-decane).

Performing VLE calculations and calculating interfacial tension for the synthetic oil in Table 3-1 yields the results shown in Table 3-2. The molar volume reported is computed using the compressibility factor with shift.

Table 3-2. Flash results, densities, viscosities, compositions, and IFT of the synthetic fluid in Table 3-1 at T = 200 °F and p = 2,000 psia.

Phase	Mole Fraction	S^j	$\tilde{\rho}^j$ (lbm/ft^3)	$\tilde{V}_m$ (ft^3/lbmol)	μ^j cP	Z^j (no shift)	$\tilde{Z}^j$ (shift)
Liquid	0.532	0.414	38.84	1.92	0.158	0.559	0.543
Vapor	0.468	0.586	6.41	3.09	0.016	0.856	0.874

Species	z_i	x_i	y_i
C_1	0.60	0.371	0.861
C_2	0.10	0.097	0.103
nC_4	0.05	0.072	0.025
nC_{10}	0.25	0.460	0.011

σ dyne/cm
13.71

When two fluids are confined in a small spaces, surface effects become significant. Because of the IFT, there exists a discontinuity in pressure at the phase interface. This pressure difference is related to the IFT and the container in which the fluids are confined, qualitatively shown by Young (1805) and Laplace (1805). The explicit Young-Laplace equation was derived later (Sing and Williams 2012) and is given by Eq. (3.35). This equation allows for two radii of curvature R_c for cases where an elliptical interface exists. However, when a spherical interface exists, the two radii of curvature are equal, and the Young-Laplace equation simplifies to Eq. (3.36). This is the typical case for a cylindrical container or tube. Another useful form relates the radius of curvature to the diameter of the tube and introduces a contact angle, shown in Eq. (3.37). A derivation of Eq. (3.37) from thermodynamics using the Helmholtz Energy is given in the Appendix.

$$P_c = \sigma\left(\frac{1}{R_{c,1}} + \frac{1}{R_{c,2}}\right) \tag{3.35}$$

$$P_c = \frac{2\sigma}{R_c} \tag{3.36}$$

$$P_c = \frac{2\sigma \cos\theta}{r} \tag{3.37}$$

The contact angle is a measure of the angle from the tube wall to the edge of the interface through the denser phase. Several difficulties exist when measuring contact angles, such as disturbances in the apparatus, nonuniform material properties, and uncertainty in perimeter measurements (Yuan and Lee 2013). Some simulation methods exist for predicting contact angle in polygonal tubes (Son et al. 2016). The pore size is also a limitation on contact angle measurements. However, Liu and Cao (2016) showed that at nanoscale, the Young-Laplace still holds. Melrose (1965) and Zettlemoyer (1968) show that contact angle is also dependent on temperature. Experimental studies by Petke and Ray (1969) show that this temperature dependence is mostly linear. They also give slopes for both advancing and receding contact angles for various fluids and materials. The linear equation used for calculating contact angle at various temperatures is given in Eq. (3.38). This equation is the point-slope form of a linear trend, which requires a known reference point and slope.

$$\theta = m(T - T_{\text{ref}}) + \theta_{\text{ref}} \tag{3.38}$$

3.3 Shifts in Critical Properties

Zarragoicoechea and Kuz (2004) propose equations to shift the critical temperature and pressure of each component to account for confinement. The form of these equations is derived from Zarragoicoechea and Kuz (2002). The scaling factor for temperature and pressure are the same, based on van der Waals theory (Teklu et al. 2014). The temperature equation is easier to validate and Teklu et al. (2014) stated the equation for shift in critical pressure has not been experimentally confirmed. The units for these equations are $T_{c,i}$ in K, $p_{c,i}$ in atm, and r in nm (Teklu et al. 2014). Once shifted critical properties are calculated, they can be used in the classical VLE calculations.

$$T_{cp,i} = T_{c,i} - T_{c,i}\left[0.9409\frac{0.244}{r}\sqrt[3]{\frac{T_{c,i}}{p_{c,i}}} - 0.2415\left(\frac{0.244}{r}\sqrt[3]{\frac{T_{c,i}}{p_{c,i}}}\right)^2\right] \tag{3.39}$$

$$p_{cp,i} = p_{c,i} - p_{c,i}\left[0.9409\frac{0.244}{r}\sqrt[3]{\frac{T_{c,i}}{p_{c,i}}} - 0.2415\left(\frac{0.244}{r}\sqrt[3]{\frac{T_{c,i}}{p_{c,i}}}\right)^2\right] \tag{3.40}$$

3.4 Capillary Pressure in Vapor-Liquid Equilibrium

We couple the Young-Laplace equation with the VLE calculation to determine phase behavior and fluid properties in confined space. The flowchart in Figure 3-2 is altered to include capillary pressure. The phase molar volumes must be calculated and volume translation applied before the final solution is achieved since IFT is a function of volume. Figure 3-5 shows coupling of the Young-Laplace as an external loop after all K-values reach convergence for a particular capillary pressure. One advantage of this method is that it prevents excessively large capillary pressure values during iteration before convergence is achieved. However, it requires very good guess values for capillary pressure for some regions of the phase envelope, particularly near the dew point saturation line. It is also very slow because full VLE convergence must be achieved before iterating on capillary pressure. To improve this, we calculate capillary pressure in the same loop, parallel to the fugacity calculation, as shown in Figure 3-6. This method requires a significantly lower number of iterations, making it a much faster method. One other method for incorporating capillary pressure is through the use of a lookup function based on saturation, shown in Figure 3-7. This method is not fully rigorous, but can be convenient. Using the rigorous method in Figure 3-6 for the synthetic oil in Table 3-1 (same as synthetic fluid 4 on p. 126), we present the flash results in Table 3-3. Comparing the results of Table 3-2 and Table 3-3 we see that when confined, the fluid exhibits higher oil saturation, lower oil and higher gas density, lower oil and higher gas viscosity, and lower IFT. When confined, the methane mole fraction in both oil and gas phases is higher. Due to changes in vapor and liquid phase distribution when confined, this does not violate mass balance.

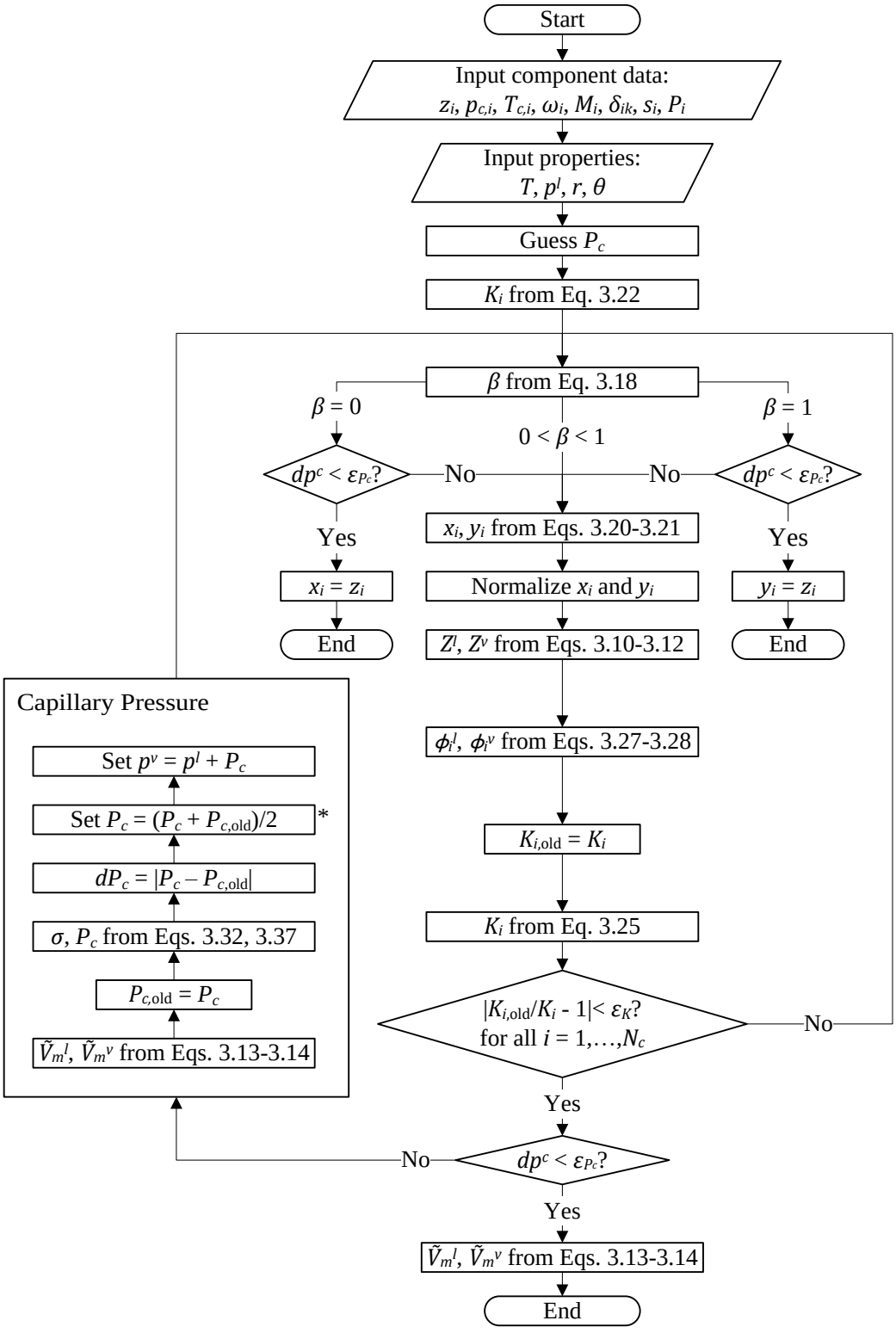

Figure 3-5. Flowchart of capillary pressure in VLE with external capillary pressure loop.

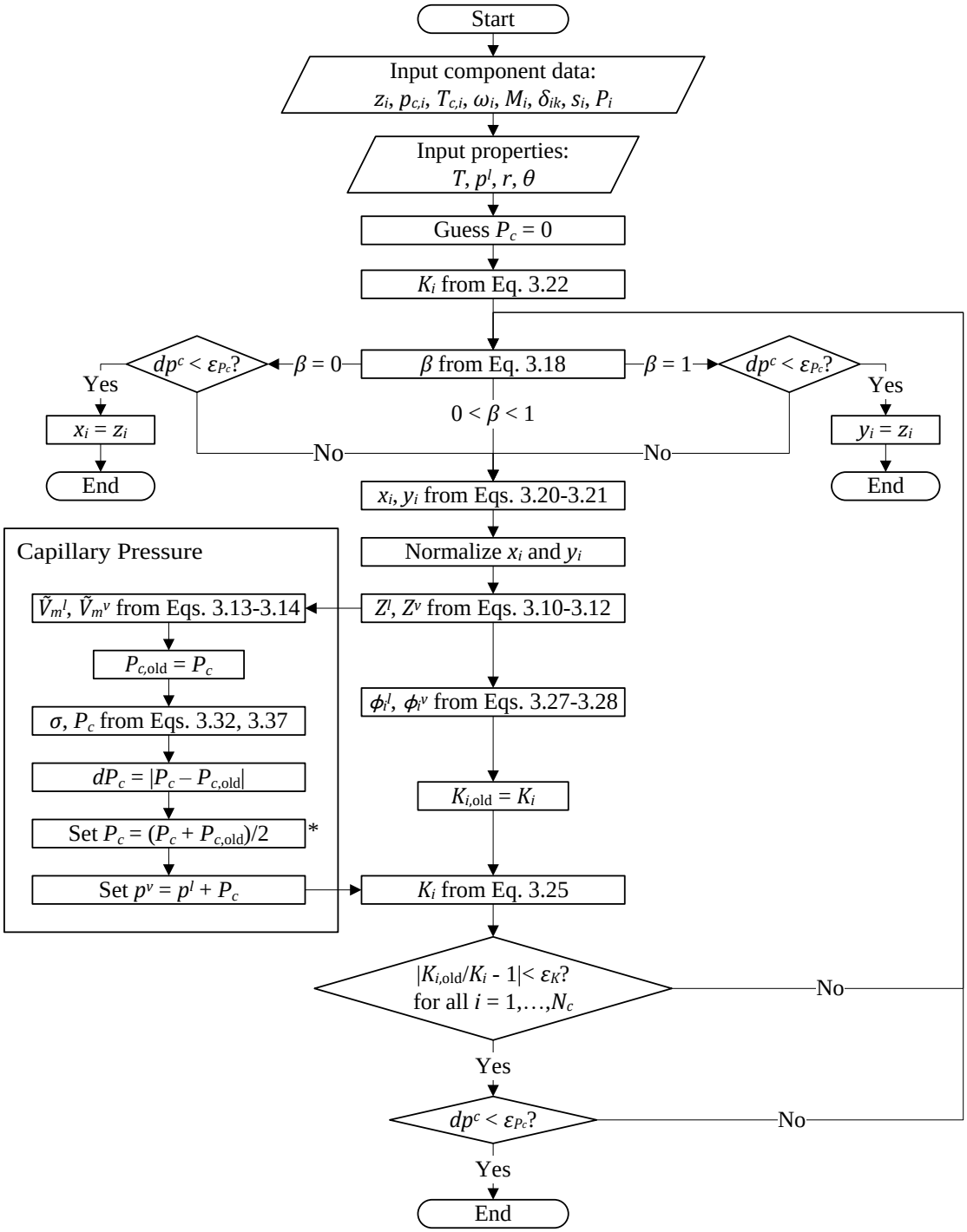

Figure 3-6. Flowchart of capillary pressure in VLE with parallel capillary pressure calculation.

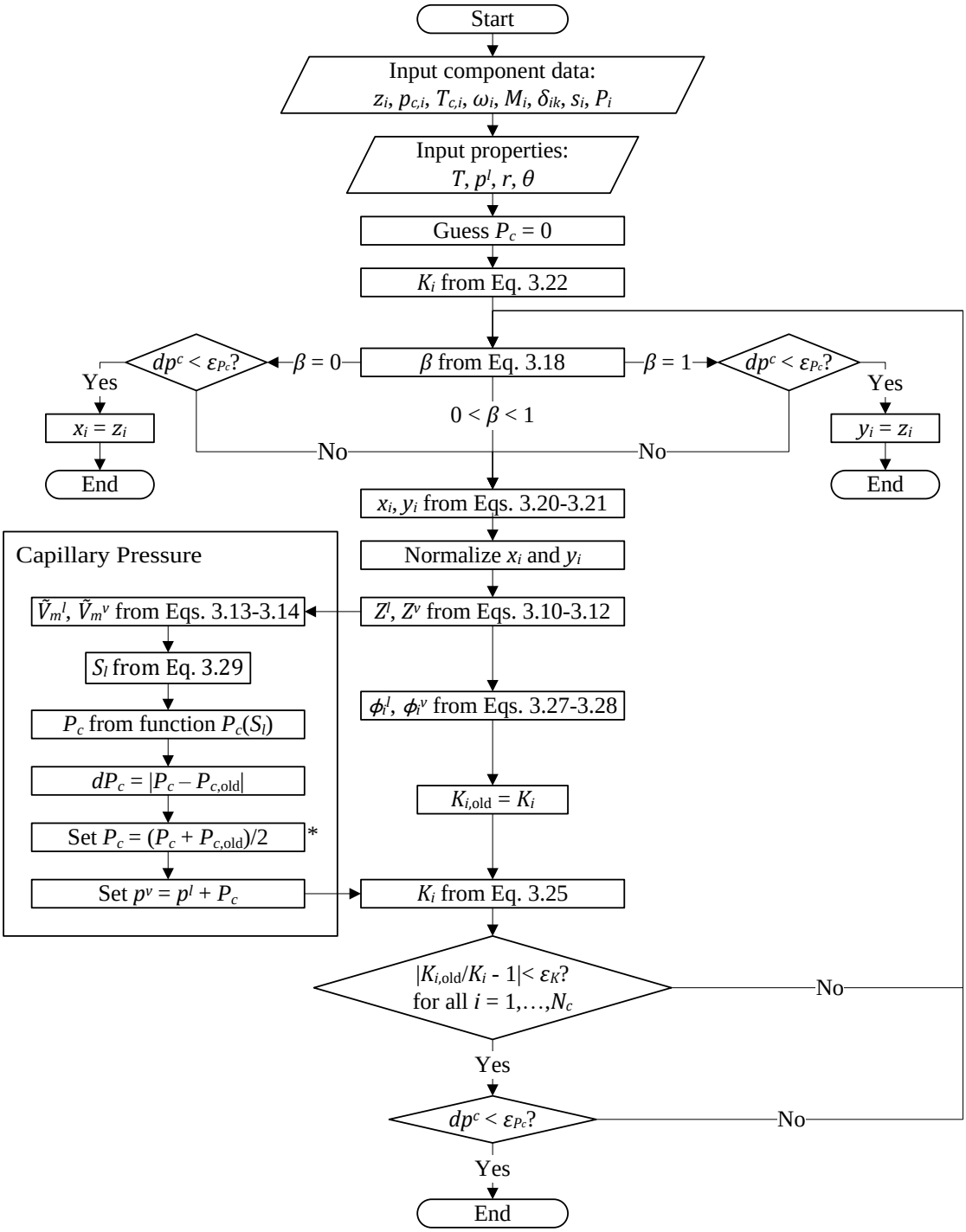

Figure 3-7. Flowchart of capillary pressure in VLE using a lookup function.

Table 3-3. Flash results, densities, viscosities, compositions, and IFT of the synthetic fluid in Table 3-1 at T = 200 °F and p^l = 2,000 psia, confined in a pore of d = 15 nm and θ = 30°.

Phase	Mole Fraction	S^j	$\tilde{\rho}^j$ (lbm/ft^3)	$\tilde{V}_m$ (ft^3/lbmol)	μ^j cP	Z^j (no shift)	Z^j (shift)
Liquid	0.655	0.557	35.52	1.82	0.113	0.514	0.514
Vapor	0.345	0.443	7.12	2.74	0.017	0.879	0.879

Species	z_i	x_i	y_i
C_1	0.60	0.457	0.872
C_2	0.10	0.102	0.096
nC_4	0.05	0.065	0.022
nC_{10}	0.25	0.376	0.010

σ dyne/cm	P_c psia
8.05	269.8

3.5 Effect of Capillary Pressure on Pure Component Phase Behavior

To examine the effect of confinement on phase behavior, we use the method shown in Figure 3-6 simplified for a single component. We show phase diagrams in Figure 3-8 and Figure 3-9 for n-butane with the properties shown in Table 3-4. As a result of confinement, the phase envelope is suppressed and densities at saturation are altered. Point A in Figure 3-9 is a point where the system in bulk will be vapor, but in confined space will be liquid. Phase densities at the saturation pressure are slightly altered, as shown in Figure 3-10. These changes becomes larger as deviation from critical point increases, and become zero as the critical point is approached. Figure 3-11 shows that at a given temperature, liquid volume saturation is higher in confined space, which is consistent with the predictions by Firoozabadi (1999). Saturation in the pore for a single component is defined by a given number of moles and volume, as shown in Eq. (3.41).

$$S^l = \frac{\frac{n_t}{\tilde{V}_t} - \frac{1}{\tilde{V}_m^v}}{\frac{1}{\tilde{V}_m^l} - \frac{1}{\tilde{V}_m^v}} \tag{3.41}$$

Table 3-4. Properties of n-butane

Property/Units	Value
Component	n-Butane
M	58.1
p_c/psia	551.3
T_c/°F	305.4
ω	0.193
s	-0.06413
P_i/(dyne$^{0.25}$ cm$^{2.75}$/gmol)	189.9
r/nm	5
θ/°	60

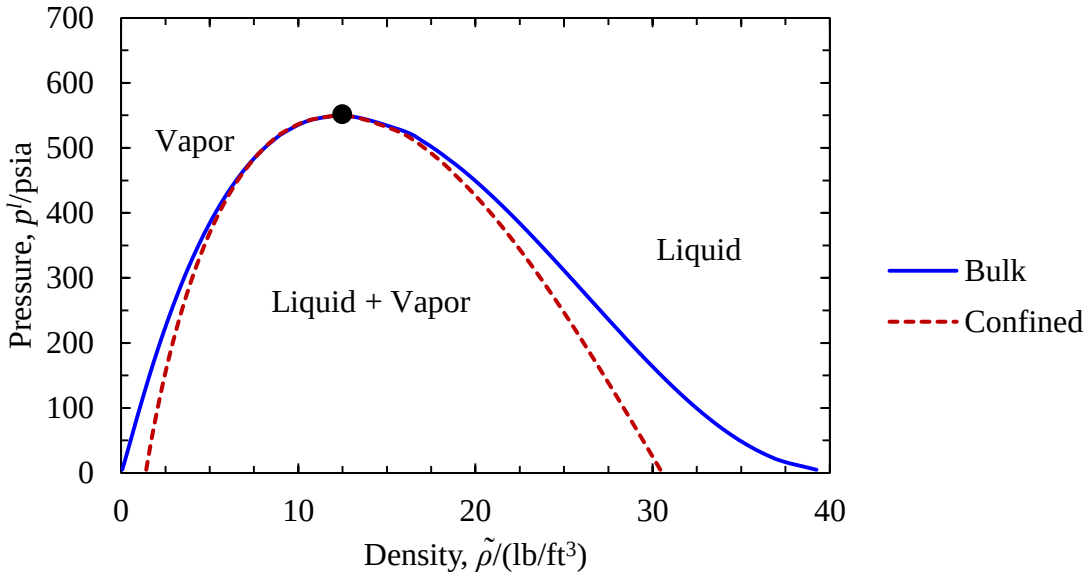

Figure 3-8. Pressure-density phase diagram for n-butane in bulk and confined spaces.

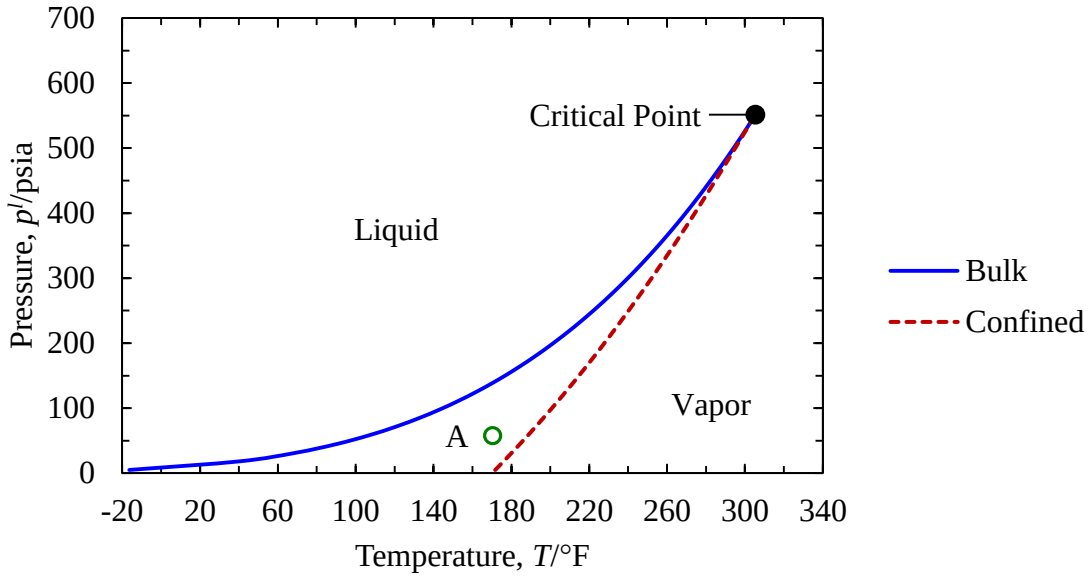

Figure 3-9. Pressure-temperature phase diagram for n-butane in bulk and confined spaces.

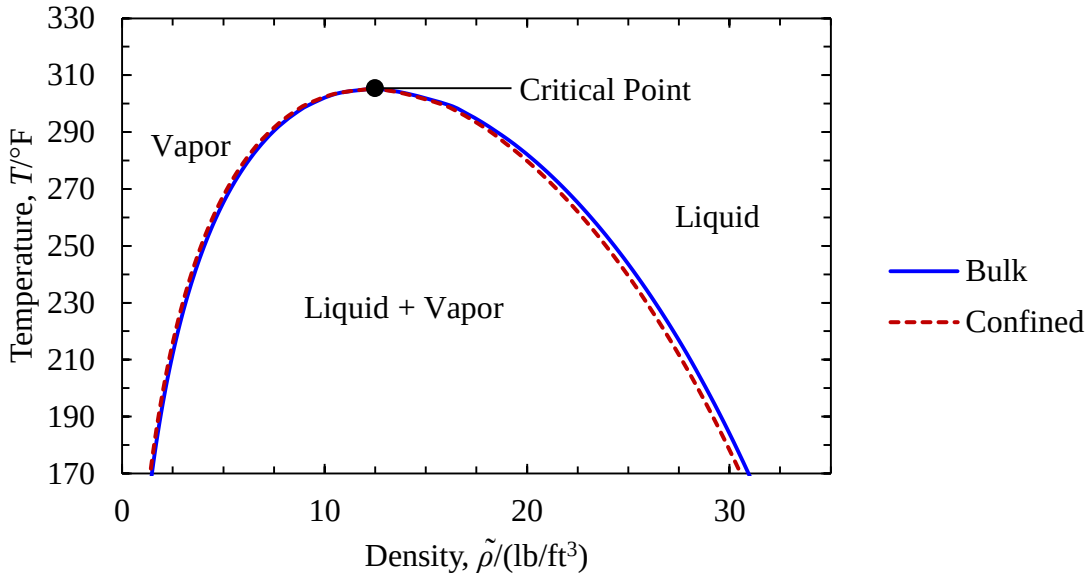

Figure 3-10. Temperature-density plot for n-butane in bulk and confined spaces.

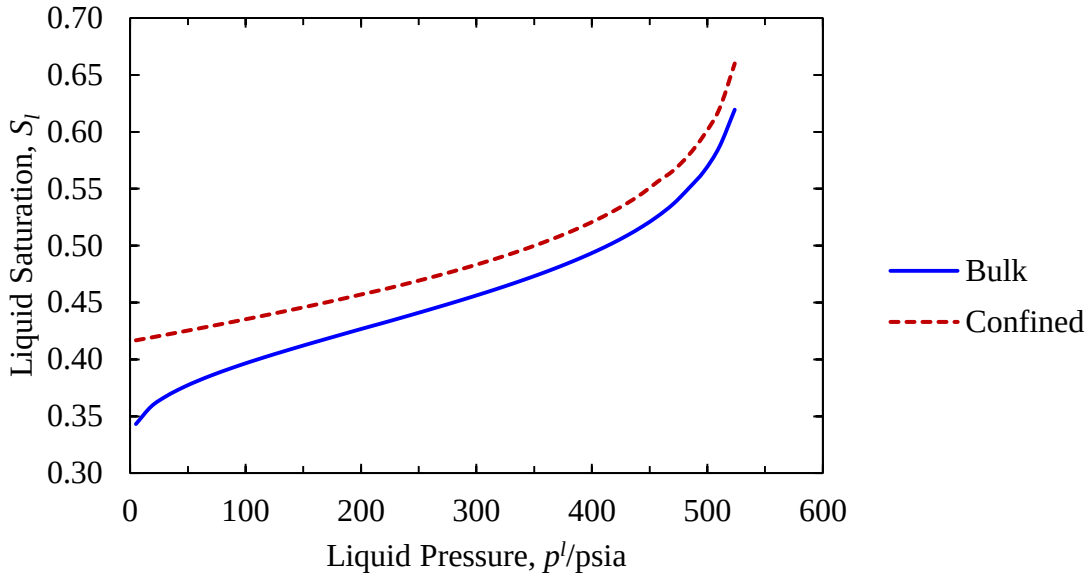

Figure 3-11. Liquid volume saturation of n-butane in bulk and confined spaces.

3.6 Effect of Capillary Pressure on Mixture Phase Behavior

3.6.1 Saturation Pressure, Saturation Temperature, and Liquid Saturation

The behavior of mixtures is very valuable since most reservoir fluids are a mixture of many species. Figure 2-5 in the previous chapter showed a phase diagram of a mixture with a few quality lines indicated. A similar diagram is also shown in Figure 3-16 below. Phase diagrams are useful for showing the path of a reservoir in relation to the two-phase region and critical point. Capillary pressure can be incorporated to show how the phase diagram changes when we consider confinement. For the synthetic oil in Table 3-1, the bubble pressure of confined fluids decreases in smaller pores, as shown in Figure 3-12. Figure 3-13 shows that at constant temperature, the bubble point pressure decreases as pore size decreases. The effect is magnified for smaller contact angles, which implies greater wetting. Figure 3-14 shows that the bubble temperature increases as pore size decreases. Figure 3-15 shows a phase diagram of a simplified fluid from Whitson and

Sunjerga (2012), shown in Table 3-5 (same as described on p. 133). Capillary pressure is also shown as contours inside the confined two-phase region.

Table 3-5. Simplified Eagle Ford oil from full characterization, same as on p. 133.

Species	z_i	M_i	$p_{c,i}$ (psia)	$T_{c,i}$ (°F)	ω_i	s_i	P_i
CO_2	0.0232	44.01	1069.5	87.73	0.225	0.2175	82.00
C_1	0.5816	16.04	667.0	-116.67	0.011	-0.0025	74.05
C_2	0.0744	30.07	706.6	89.93	0.099	0.0589	112.91
C_3	0.0417	44.1	616.1	206.03	0.152	0.0908	154.03
C_4	0.0259	58.12	542.19	294.00	0.1948	0.1100	189.30
$C_{5\text{-}6}$	0.0269	76.502	489.75	414.41	0.2398	0.1197	247.57
C_{7+}	0.1321	122.96	392.81	632.37	0.3548	0.1723	402.33
C_{13+}	0.0942	255.28	226.23	941.29	0.7408	0.2877	834.82

Figure 3-16 shows how the liquid saturation of this fluid is changed inside the two-phase region when considering confinement. Figure 3-17 and Figure 3-18 compares oil saturation in bulk and confined spaces at constant temperature and constant pressure, respectively for the synthetic fluid in Table 3-1. For both cases, the oil saturation in small pores is higher.

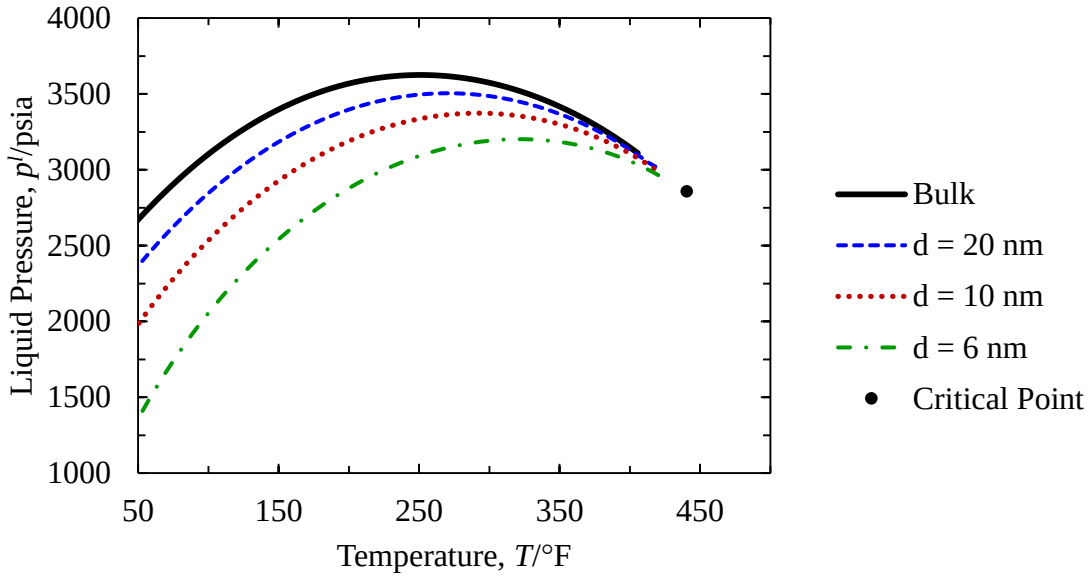

Figure 3-12. Suppression of bubble point due to confinement in various pore sizes for a mixture of 60% methane, 10% ethane, 5% n-butane, and 25% n-decane.

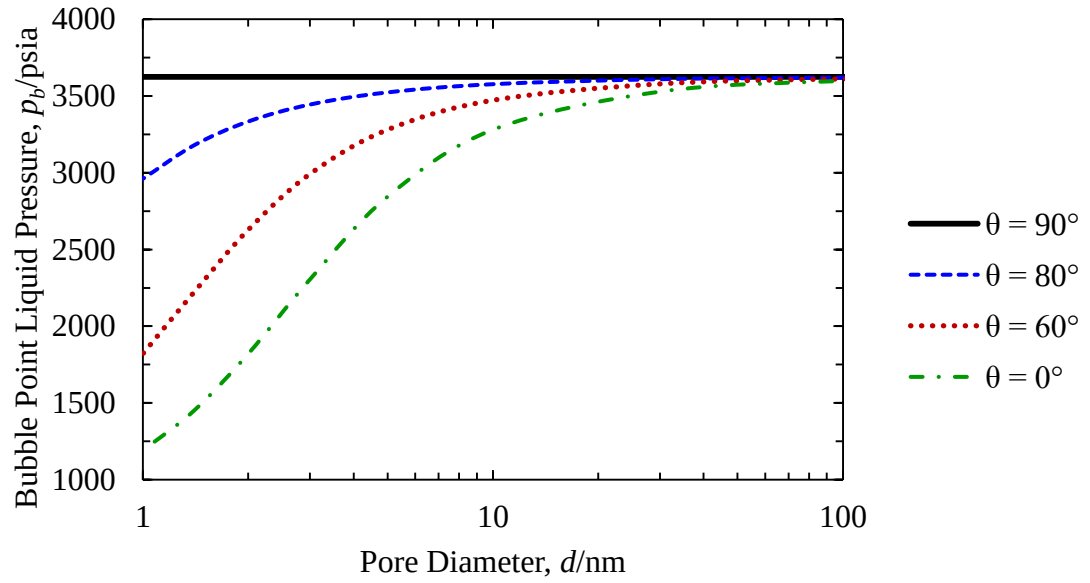

Figure 3-13. Impact of pore diameter on bubble point pressure for various contact angles for a mixture of 60% methane, 10% ethane, 5% n-butane, and 25% n-decane at 250 °F.

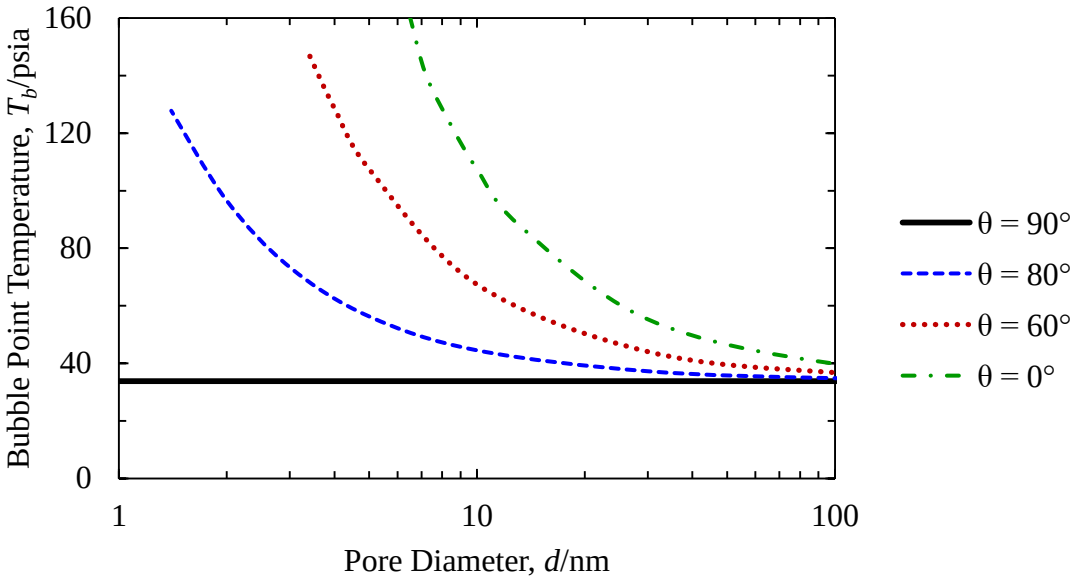

Figure 3-14. Impact of pore diameter on bubble point temperature for various contact angles for a mixture of 60% methane, 10% ethane, 5% n-butane, and 25% n-decane at 2500 psia.

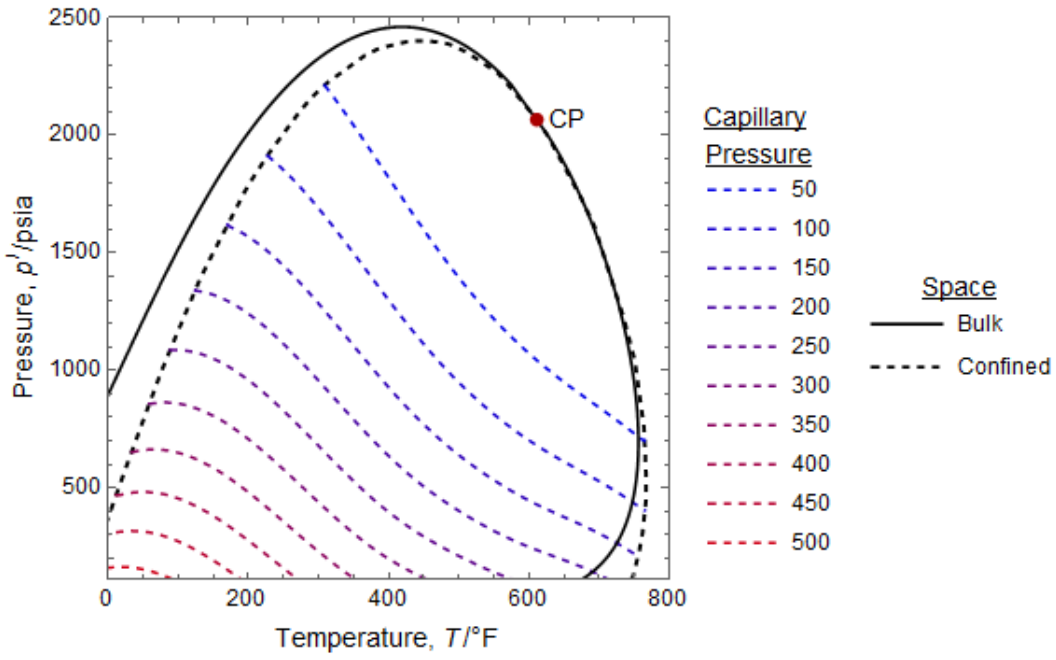

Figure 3-15. Phase diagram in bulk and confined spaces of an Eagle Ford oil described in Table 3-5.

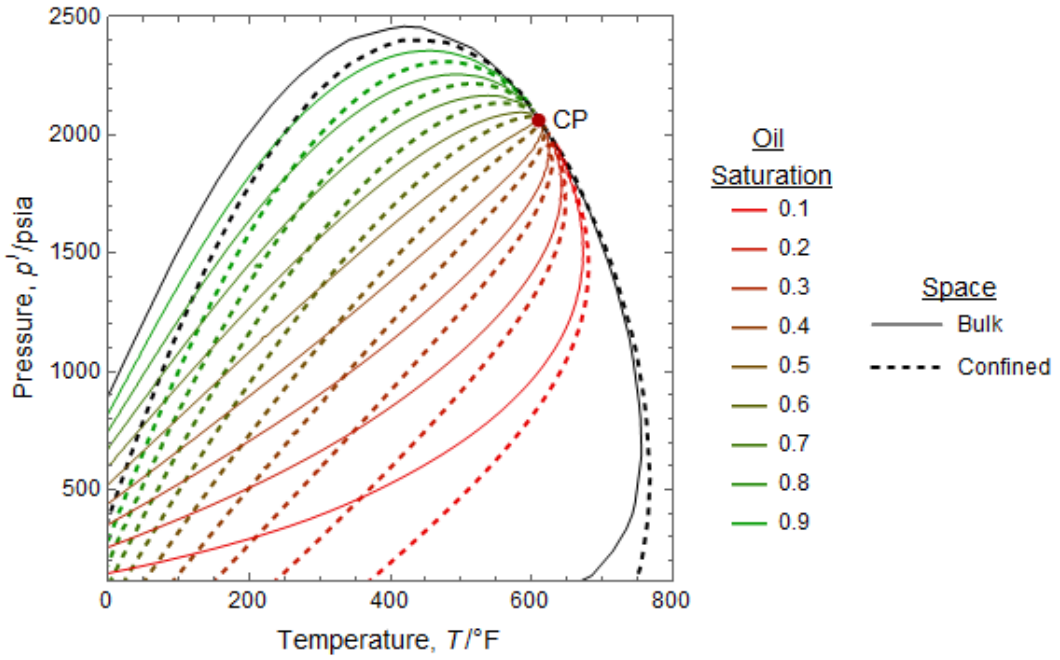

Figure 3-16. Liquid saturation quality lines for bulk and confined spaces of the Eagle Ford oil described in Table 3-5.

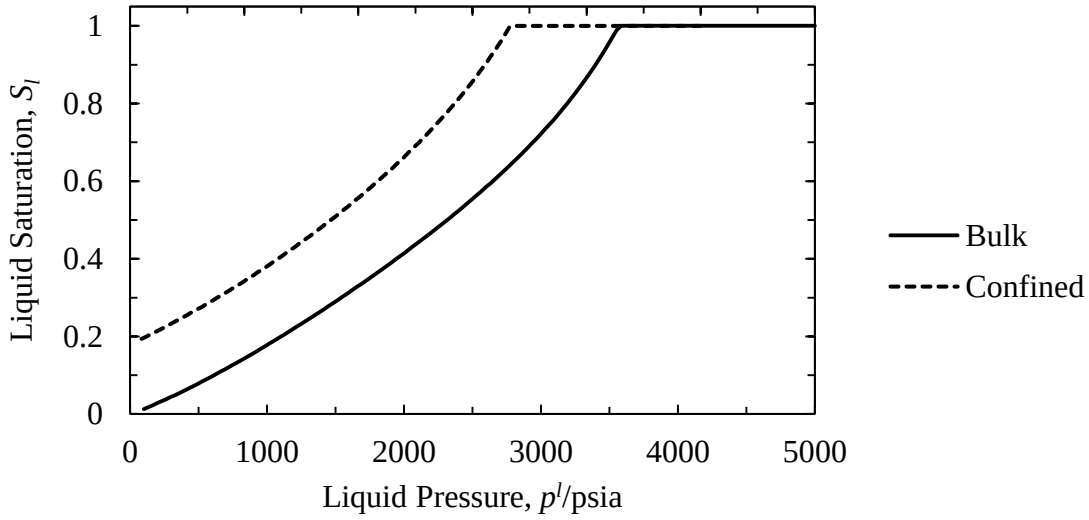

Figure 3-17. Bulk and confined liquid saturation as a function of pressure at constant temperature of 200 °F for a mixture of 60% methane, 10% ethane, 5% n-butane, and 25% n-decane.

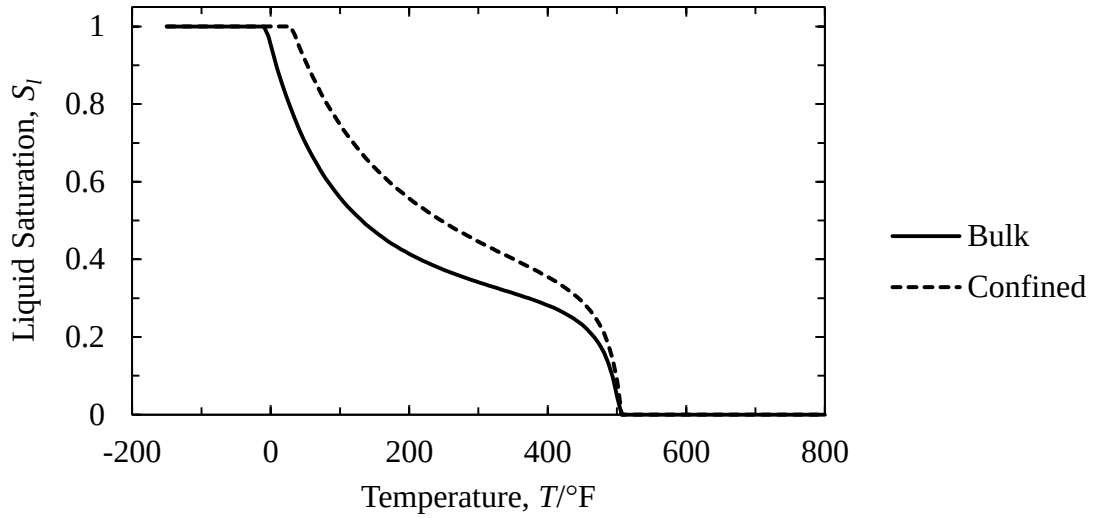

Figure 3-18. Bulk and confined liquid saturation as a function of temperature at constant pressure of 2,000 psia for a mixture of 60% methane, 10% ethane, 5% n-butane, and 25% n-decane.

3.6.2 Fluid Density and Viscosity

Capillary pressure also affects the phase densities and viscosities. This is mainly due compositional changes at equilibrium. In addition, the change in vapor pressure due to capillary pressure impacts phase property calculations. Figure 3-19 shows that for the two-phase system at constant temperature of 200 °F, oil density is lower and gas density is higher when confined, for the synthetic fluid in Table 3-1. Figure 3-20 shows this same effect at constant pressure of 2,000 psia. Oil viscosity is lower and gas viscosity is higher when confined in pores, as shown in Figure 3-21 for constant temperature and Figure 3-22 for constant temperature. Figure 3-23 and Figure 3-24 show how the liquid and vapor phase compositions change as a function of pore diameter.

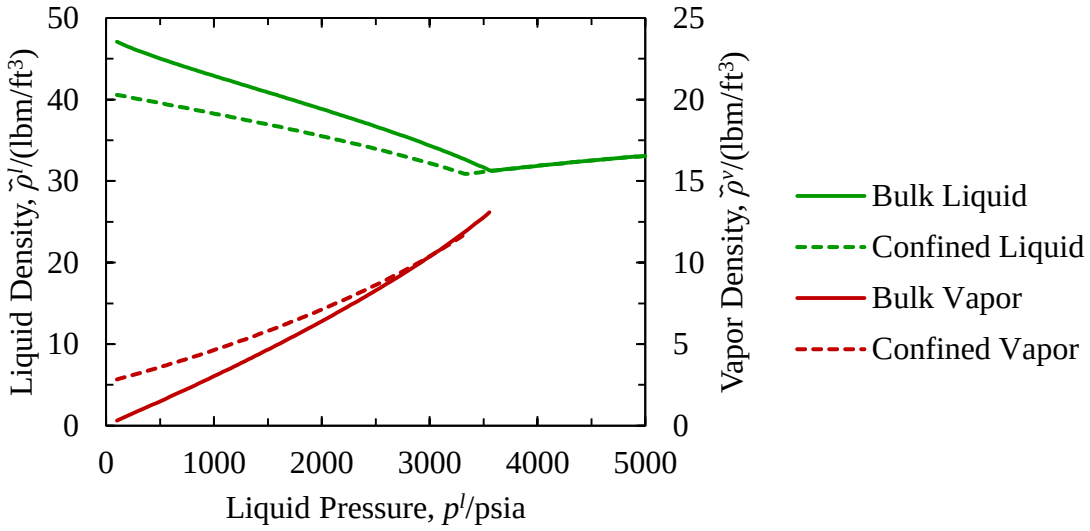

Figure 3-19. Phase density as a function of pressure in bulk and confined spaces at constant temperature of 200 °F for a mixture of 60% methane, 10% ethane, 5% n-butane, and 25% n-decane.

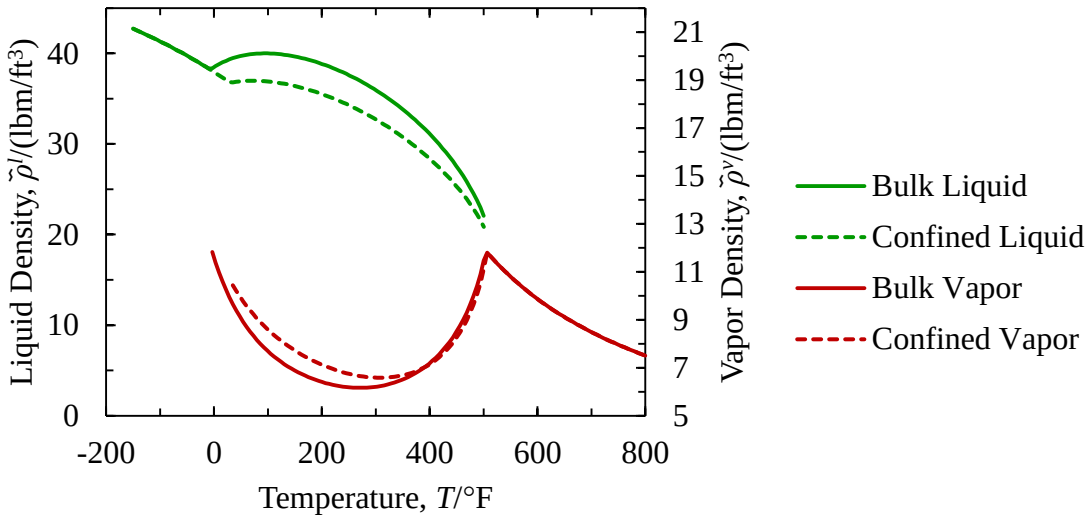

Figure 3-20. Phase density as a function of temperature in bulk and confined spaces at constant pressure of 2,000 psia for a mixture of 60% methane, 10% ethane, 5% n-butane, and 25% n-decane.

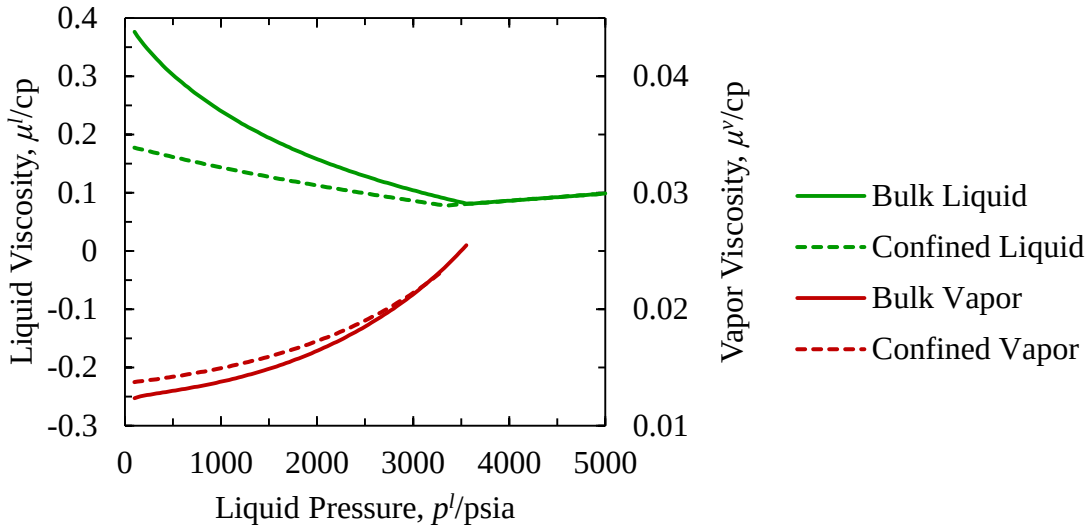

Figure 3-21. Phase viscosities as a function of pressure in bulk and confined spaces at constant temperature of 200 °F for a mixture of 60% methane, 10% ethane, 5% n-butane, and 25% n-decane.

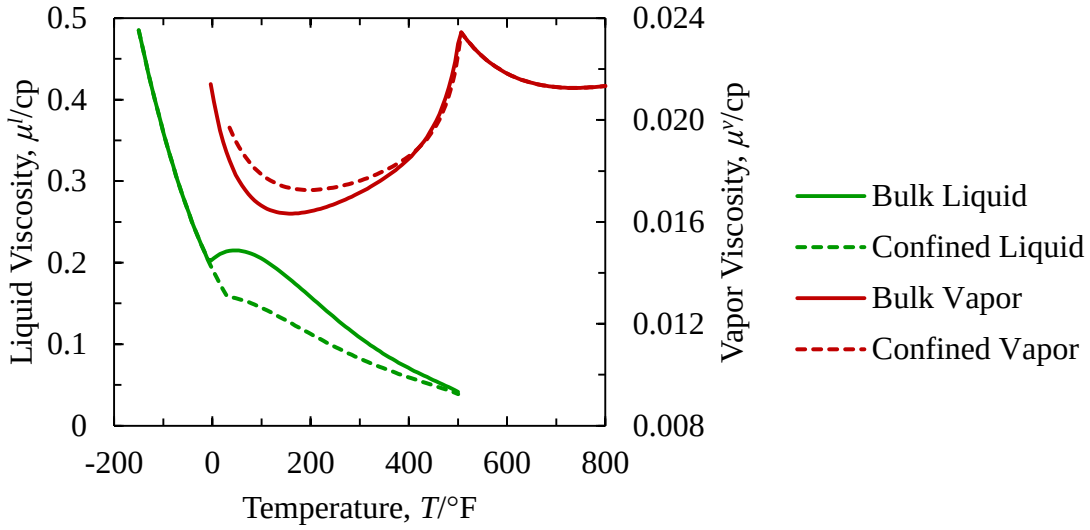

Figure 3-22. Phase viscosity as a function of temperature in bulk and confined spaces at constant pressure of 2,000 psia for a mixture of 60% methane, 10% ethane, 5% n-butane, and 25% n-decane.

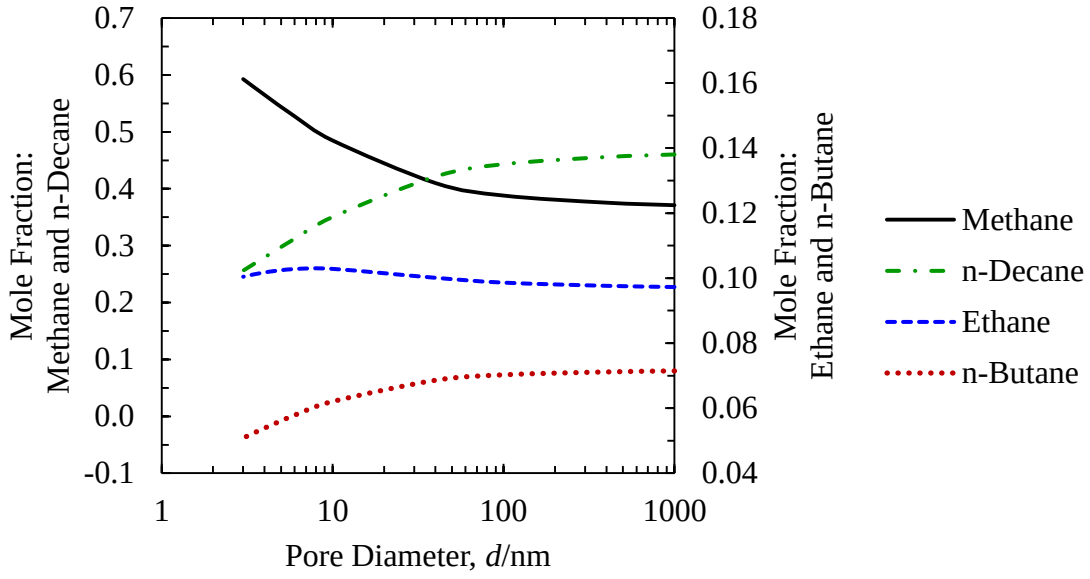

Figure 3-23. Impact of pore size on liquid phase composition at T = 200 °F and p^l = 2,000 psia with contact angle θ = 30° for a mixture of 60% methane, 10% ethane, 5% n-butane, and 25% n-decane.

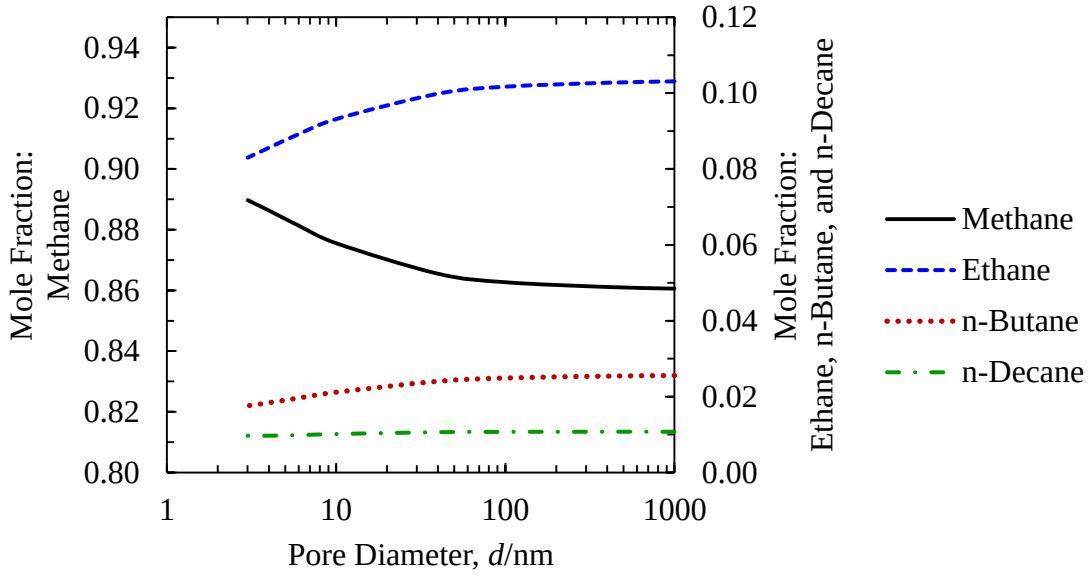

Figure 3-24. Impact of pore size on vapor phase composition at T = 200 °F and p^l = 2,000 psia with contact angle θ = 30° for a mixture of 60% methane, 10% ethane, 5% n-butane, and 25% n-decane.

3.6.3 Fluid Properties as a Function of Pore Size

For a given fluid at constant temperature, pressure, and composition, estimated fluid properties are impacted by confinement. When calculating fluid properties in a reservoir, it is important to incorporate capillarity because these properties can be significantly altered due to capillary pressure and largely impact fluid flow. Figure 3-25 shows that oil saturation increases in smaller pores, for the same oil pressure, temperature, and composition. Figure 3-26 shows the oil density decreases and gas density increases as pore diameter decreases. This is due to the phases becoming more mixed, so the oil phase becomes lighter while the gas phase becomes heavier. The same effect can be seen when calculating phase viscosities, shown in Figure 3-27.

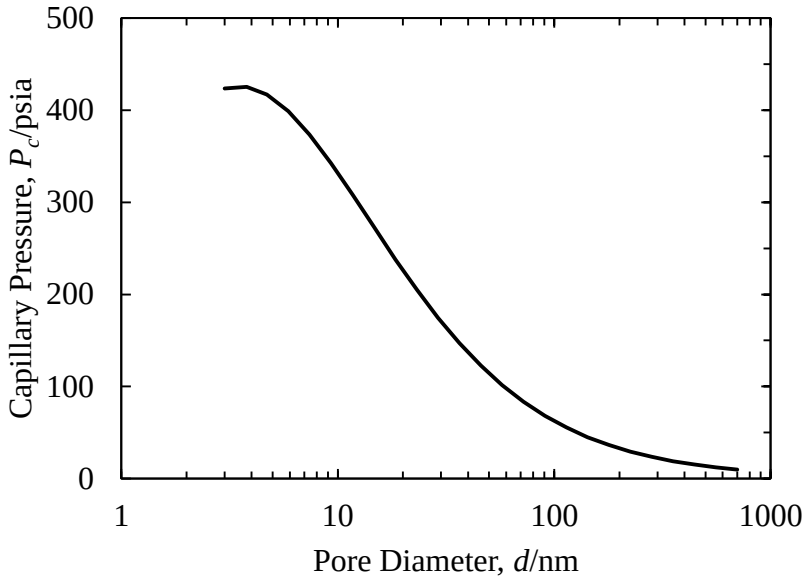

Figure 3-25. Impact of pore size on capillary pressure and oil saturation in various pore diameters at 200 °F and 2,000 psia for the fluid in Table 3-1 (60% methane, 10% ethane, 5% n-butane, and 25% n-decane).

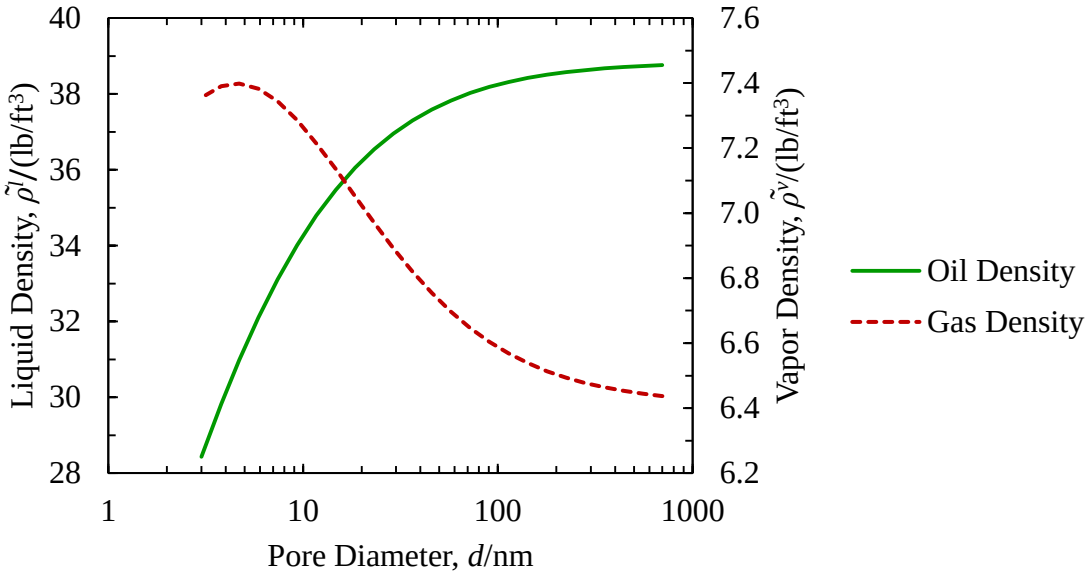

Figure 3-26. Impact of pore size on oil and gas density in various pore diameters at 200 °F and 2,000 psia for the fluid in Table 3-1 (60% methane, 10% ethane, 5% n-butane, and 25% n-decane).

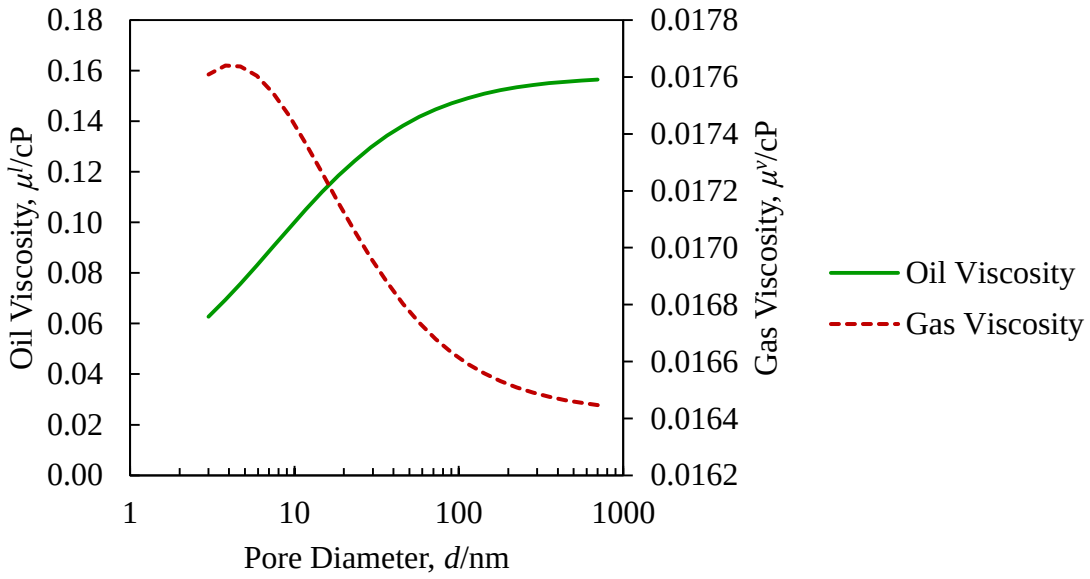

Figure 3-27. Impact of pore size on oil and gas viscosity in various pore diameters at 200 °F and 2,000 psia for the fluid in Table 3-1 (60% methane, 10% ethane, 5% n-butane, and 25% n-decane).

CHAPTER IV
VALIDATION OF MODEL

4.1 Experimental Data for a Single Component

A reasonable collection of data exists of the effect of confinement on phase behavior and fluid properties. Wilkinson et al. (1992) showed experimentally that the vapor-liquid phase boundary is shifted toward a higher temperature (for constant pressure), or lower pressure (for constant temperature) using Nitrogen in Vycor glass with pore diameter of 2 nm. We model this system using capillary pressure with a fixed contact angle, shifts in critical properties, and capillary pressure with a temperature-dependent contact angle. The results are shown in Figure 4-1. The contact angle for the capillary pressure method is 72 degrees and pore diameter was 2 nm. The critical shift method was only able to fit the data using a pore diameter of 0.191 nm. Using the temperature dependent contact angle method, the reference contact angle was 72° and temperature-dependent contact angle slope of -0.6 degrees/°F, with a reference temperature of -270 °F and pore diameter of 2 nm, using Eq. (3.38). The slope value is approximately six times larger than the values reported by Petke and Ray (1969); however the values reported are not for similar systems, so this value may still be valid for this system. Figure 4-1 shows good agreement between the model and experimental data for the range indicated for both bulk and confined data. The critical shift method achieved good results, but requires the pore diameter to be 0.191 nanometers, which approximately the same size at the nitrogen molecule itself (0.155 nm).

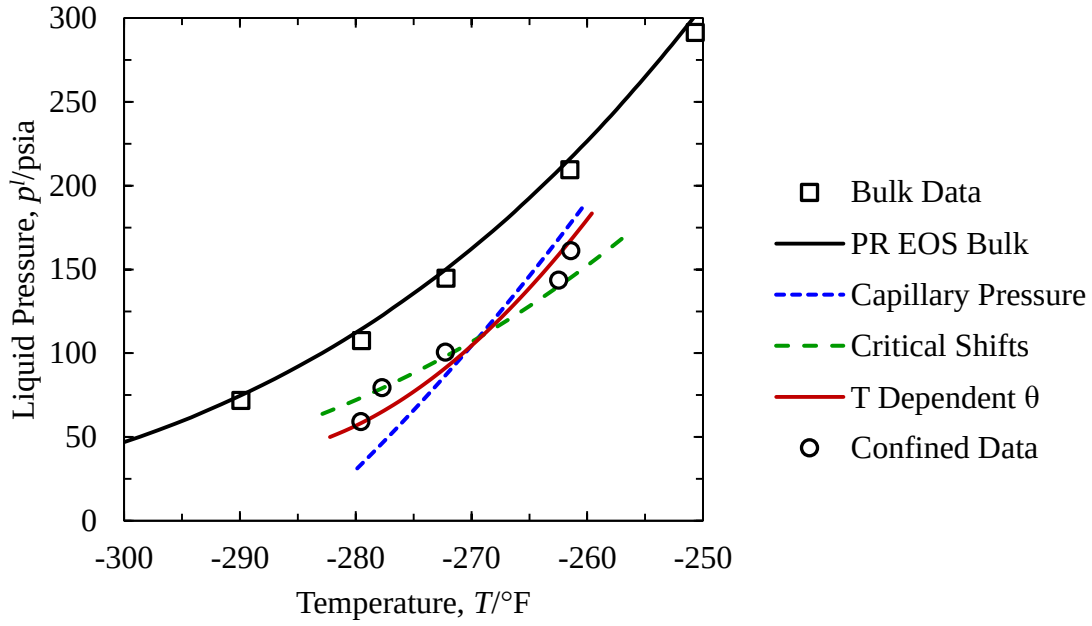

Figure 4-1. Comparison of experimental data of nitrogen in 2 nm capillaries with EOS modeling (Capillary Pressure: θ = 72°; Critical Shifts: d = 0.191 nm; Temperature-dependent: θ_{ref} = 72°, m = -0.6 degrees/°F, T_{ref} = -270 °F). Experimental bulk and confined data from Wilkinson et al. (1992).

Another experimental work by Duffy et al. (1995) measured a similar shift in phase transitions of carbon dioxide in Vycor glass with pore diameter of 4 nm. Performing the same modeling on this systems yields reasonable results, as shown in Figure 4-2. The contact angle that fits the data is 89.6 degrees, which is close to 90 degrees, which means carbon dioxide is very weakly wetting in the Vycor glass. This is consistent with the observation by Gubbins et al. (2014), who stated that carbon dioxide weakly wets Vycor glass.

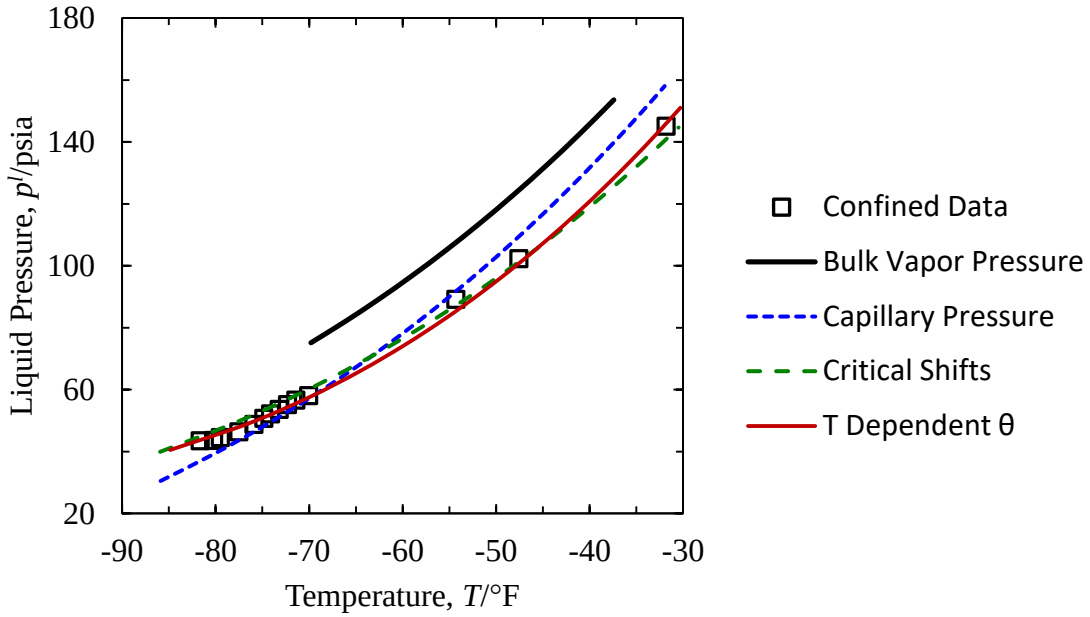

Figure 4-2. Comparison of experimental data of carbon dioxide in 4 nm capillaries with EOS modeling (Capillary Pressure: θ = 89.6°; Critical Shifts: d = 0.2001 nm; Temperature-dependent θ_{ref} = 89.6°, m = -0.0103 degrees/°F, T_{ref} = -67.27 °F). Experimental confined data from Duffy et al. (1995).

Kruk and Jaroniec (2000) studied the change in saturation pressure of argon due to confinement in small pores at -303.07 °F. We calculate the saturation pressure including capillary pressure for their data. Our results are compared with the data in Figure 4-3. Our results match the data very closely when using a contact angle of 89.884 degrees.

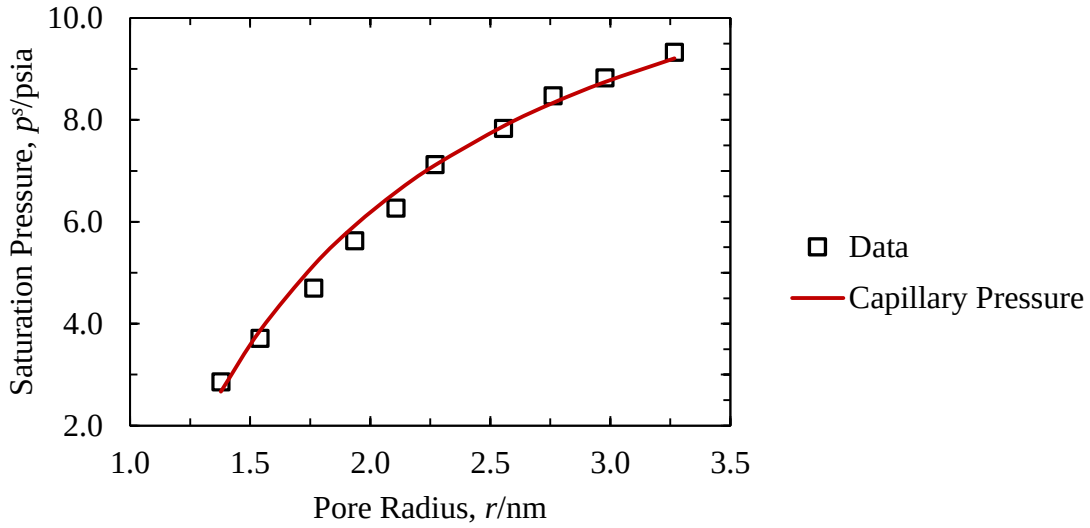

Figure 4-3. Comparison of experimental and modeled saturation pressure of argon at various pore radii (T = -303.07 °F, θ = 89.884 degrees) from Kruk and Jaroniec (2000).

Qiao et al. (2004) performed experiments using hexane in silica to show how adsorbed n-hexane alters saturation pressure at various temperatures. We model the same system using the capillary pressure method with the PR EOS. The results are shown in Figure 4-4. Our results show similar behavior at all temperatures. At smaller pores for the lower temperatures, the model failed at the smaller pores, as indicated in Figure 4-4.

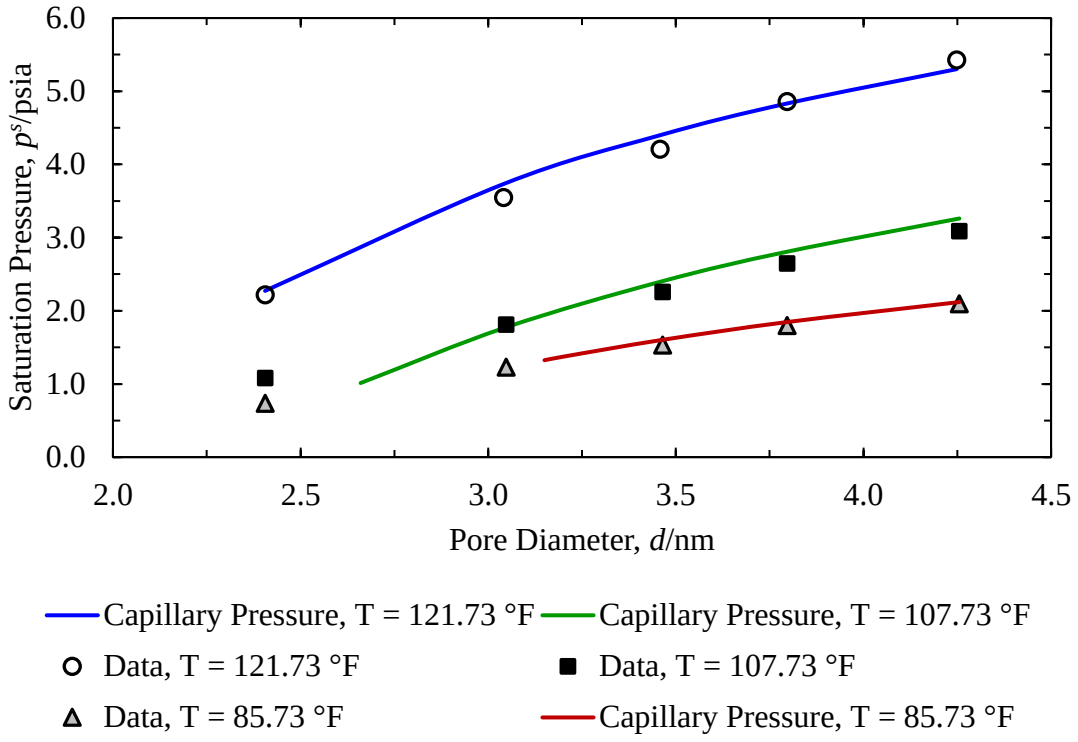

Figure 4-4. Comparison of experimental and modeled saturation pressure suppression for n-hexane (T = 121.73 °F, θ = 89.957°; T = 107.73 °F, θ = 89.961°; T = 85.73 °F, θ = 89.978°) from Qiao et al. (2004).

Other data exist, such as that presented by Luo et al. (2015), who performed laboratory experiments in micro-channels to study the contact angle and saturation temperature of pure components. They show a dual bubble point at small pores. Our model is able to match the data given for both bubble points, given two contact angles. Tan and Piri (2015) use the Perturbed-Chain Statistical Associated Fluid Theory (PC-SAFT) EOS and incorporate confinement to model confined fluids. They compare other datasets of pure components and binary mixtures in small pores with their EOS.

4.2 Experimental Data for a Multiple Component Mixture

Liu et al. (2016) performed experiments on a binary mixture of 24% methane and 76% n-decane inside a shale core to study the bubble point suppression of the fluid. We matched the reported data with a radius of curvature R_c of 50 nm, shown in Figure 4-5. Liu et al. (2016) also use the PR EOS to model the bulk data. Their model results for the bulk data are also shown. The data deviate slightly from the expected model trend for the bulk data. Due to the extensive validation of the PR EOS for binary mixtures, the deviation is most likely experimental error. The confined data also deviate from the expected trend at the highest temperature, which is also most likely experimental error.

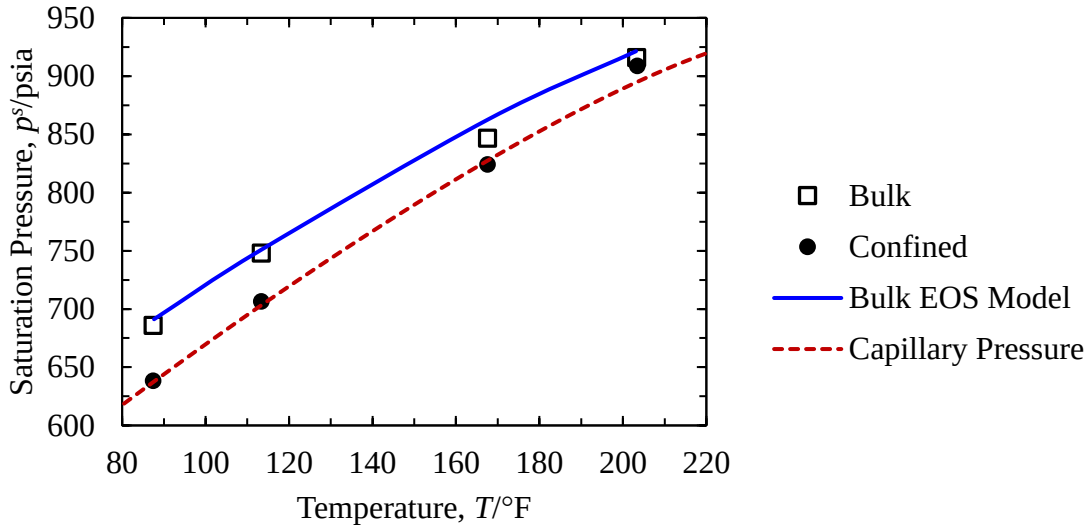

Figure 4-5. Comparison of experimental and modeled bubble point suppression for a binary mixture of 24% methane and 76% n-decane (R_c = 50 nm). Data from Liu et al. (2016).

Wang et al. (2014) present compositional data of a ternary mixture confined in small pores. They use a similar model to confirm their experiments and the model.

4.3 Data from Molecular Simulation

Molecular simulation is a powerful tool that can be used to predict phase behavior at conditions or in spaces that are not feasible for laboratory conditions. Simulations by Watanabe et al. (2008) examined the decrease in saturation pressure of methane due to confinement inside a jungle gym structure of carbon rods and in a slit pore. We calculated the equivalent pore diameters and calculated saturation pressures of methane with a contact angle of 88.85 degrees. We show very similar behavior in very small pores, as shown in Figure 4-6.

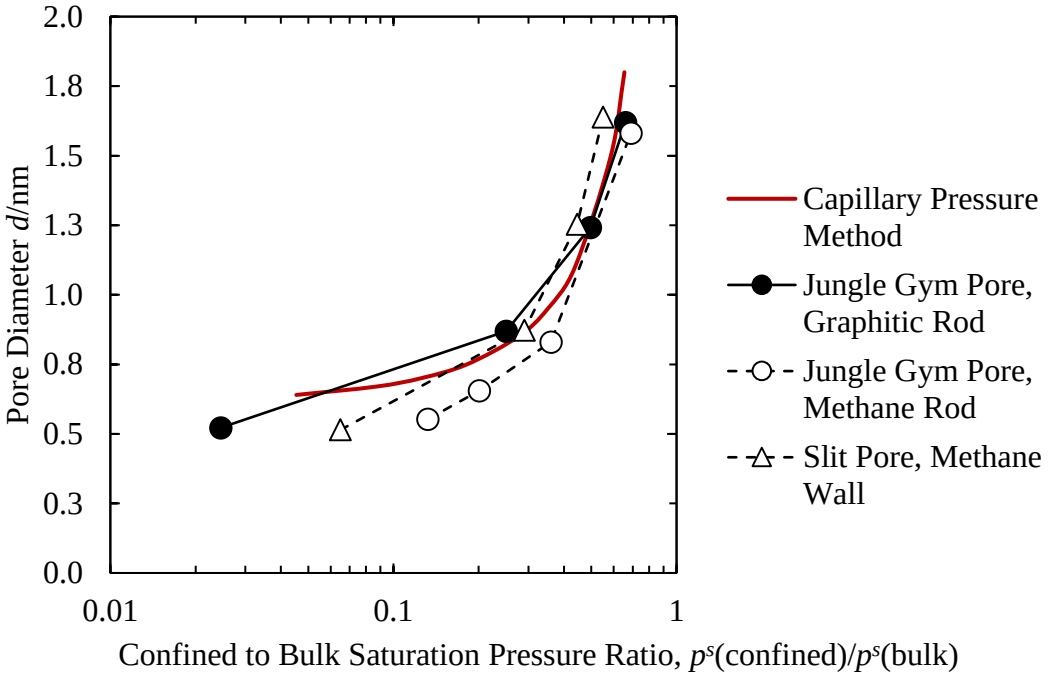

Figure 4-6. Saturation pressure comparison of capillary pressure method to molecular simulation. Simulated data from Watanabe et al. (2008).

At nanoscale, it is difficult to determine contact angle, since it is usually seen macroscopically. However, Liu and Cao (2016) performed molecular dynamic simulations to study whether the Young-Laplace equation still holds in very small pores

(1.3-2.7 nm). Their simulations show that the contact angle still exists as a defined property and is independent of pore size. This is a significant finding for our work, given that pore sizes in shales can be as on the same order as those studied by Liu and Cao (2016).

CHAPTER V
CAPILLARY PRESSURE IN RESERVOIR SIMULATION

To examine the effects of capillary pressure on production from shale reservoirs, we take a compositional simulation approach. Our simulator was built in-house by Gonzalez Abad (2013) with the EOS from Valbuena Olivares (2015) and modified to include capillary pressure in the VLE calculation. The additional inputs required for simulation with our method are pore diameter and contact angle. This simulator was validated by Gonzalez Abad (2016), who performed a three-phase simulation on a square reservoir for a 5-component mixture.

5.1 Simulations

The reservoir shape for this study is shown in Figure 5-1 and contains one producer well in the center grid cell. The simulator makes the following assumptions stated by Gonzalez Abad (2016):

1. Isothermal system
2. Steady-state during a time step calculation
3. Multi-phase (oil, gas) and multi-component flow represented by Darcy's law
4. Instantaneous thermodynamic equilibrium between oil and gas phase
5. Slightly compressible rock
6. No chemical reactions or adsorption

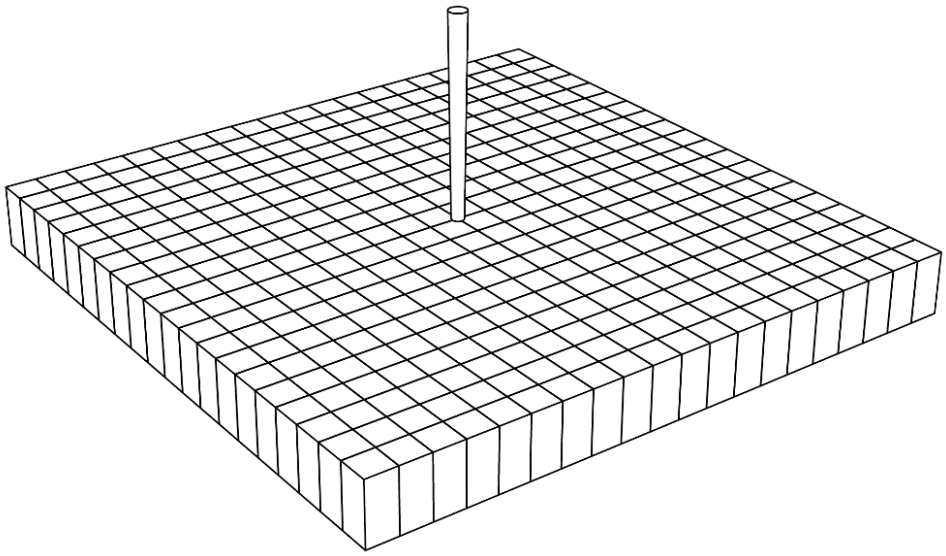

Figure 5-1. Simulated reservoir grid

5.2 Comparison of Methods

To study the effect of capillary pressure on production, we first compare simulation results with and without capillary pressure and with capillary pressure using a lookup function using the methods shown in Figure 3-2 and Figure 3-6, Figure 3-7, respectively. The fluid is given in Table 5-1, which is the same as the fluid in Table 3-1 (same as the synthetic fluid 4 on p. 126). The reservoir properties are described in Table 5-2. The cumulative oil production is shown in Figure 5-2 and cumulative oil production is shown in Figure 5-3. Gas-oil ratio (GOR) is compared in Figure 5-4. Capillary pressure shows higher oil production, slightly higher gas production, and an overall lower GOR when considering confinement. While the lookup method provides a similar result as the rigorous method, the results cannot be generalized, and other cases may show a more significant difference.

Table 5-1. Synthetic fluid composition and properties for synthetic volatile oil (same as synthetic fluid 4 on p. 126).

Species	x_i	M_i	$p_{c,i}$ (psia)	$T_{c,i}$ (°F)	ω_i	s_i	$Z_{c,i}$	P_i
C_1	0.60	16.043	667.4	-116.9	0.008	-0.154	0.288	77
C_2	0.1	30	708.5	89.7	0.098	-0.1002	0.284	108
nC_4	0.05	58.1	551.3	305.4	0.193	-0.0641	0.2743	189.9
nC_{10}	0.25	134	367	659.8	0.444	0.0803	0.249	505.88

$\delta_{ik} = 0$ for all components

Table 5-2. Reservoir properties of simulation comparing capillary pressure methods.

Grid Size	Cell Dimensions	p_i (psia)	k (md)	ϕ	d (nm)	θ (°)	T (°F)	BHP (psia)
11x11x1	50x50x100	4,000	0.1	0.2	15	30	216	1,000

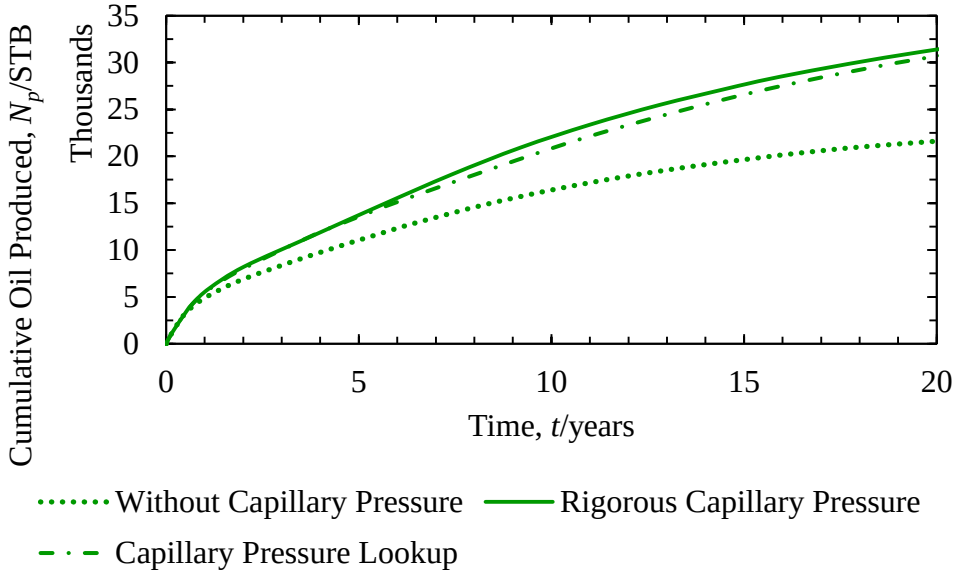

Figure 5-2. Comparison of cumulative oil production using various VLE methods in compositional reservoir simulation.

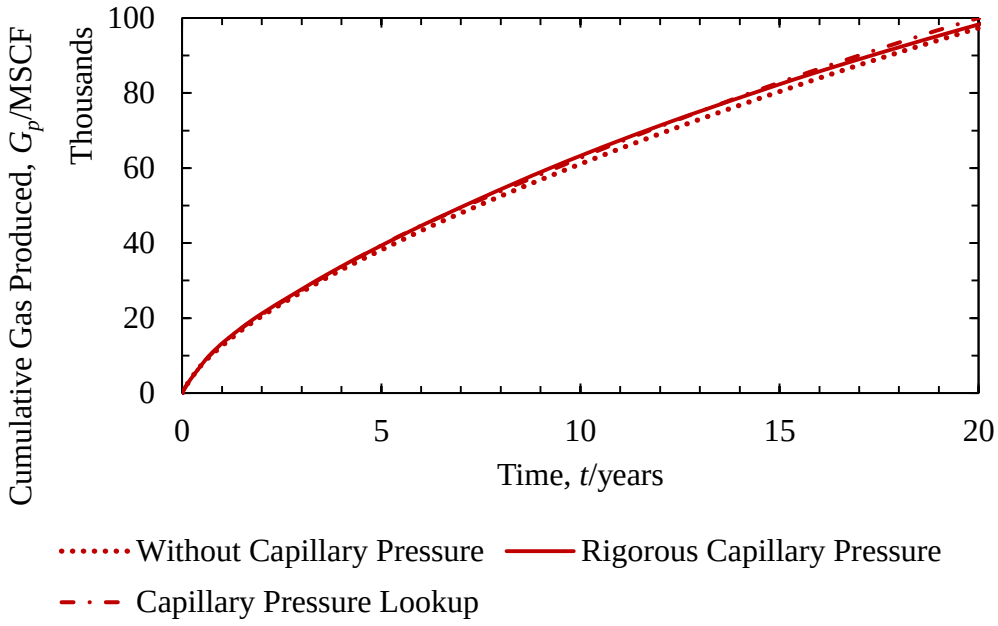

Figure 5-3. Comparison of cumulative gas production using various VLE methods in compositional reservoir simulation.

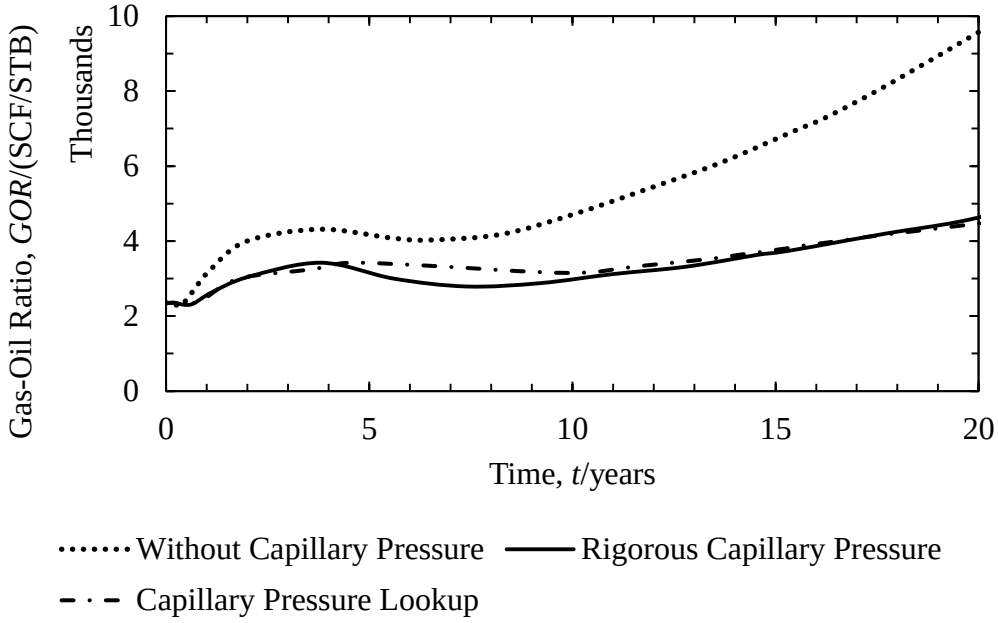

Figure 5-4. Comparison of cumulative GOR using various VLE methods in compositional reservoir simulation.

5.3 Synthetic Fluid Results

We perform simulations on the square reservoir shown in Figure 5-1 for the synthetic oil in Table 5-1 for a homogeneous reservoir with and without capillary pressure. The reservoir properties are listed in Table 5-3 The cumulative production and GOR are shown in Figure 5-5 and Figure 5-6, respectively. The oil production from this reservoir is higher when considering confinement. The main reason for this is the higher liquid saturation in the reservoir, which results in a higher relative permeability to oil. The gas production also increases when considering confinement. This is most likely due to the fact that when capillary pressure is present, lighter components are forced into the liquid phase. So, the higher quantity of oil releases more gas when brought to the surface.

Table 5-3. Reservoir properties of the synthetic oil simulation.

p_i (psia)	k (md)	ϕ	d (nm)	θ (°)	T (°F)	BHP (psia)
6,000	0.005	0.1	15	30	200	1,500

The liquid saturation through production and average pressures are shown in Figure 5-7 and Figure 5-8, respectively. Once two-phase flow is reached, the liquid saturation in the reservoir is higher when considering capillary pressure. In addition, the reservoir pressure is lower than without capillary pressure. These results are also shown by Stimpson and Barrufet (2016a). Figure 5-9 and Figure 5-10 show how the pressure and saturation distribution throughout the reservoir vary when considering capillary pressure.

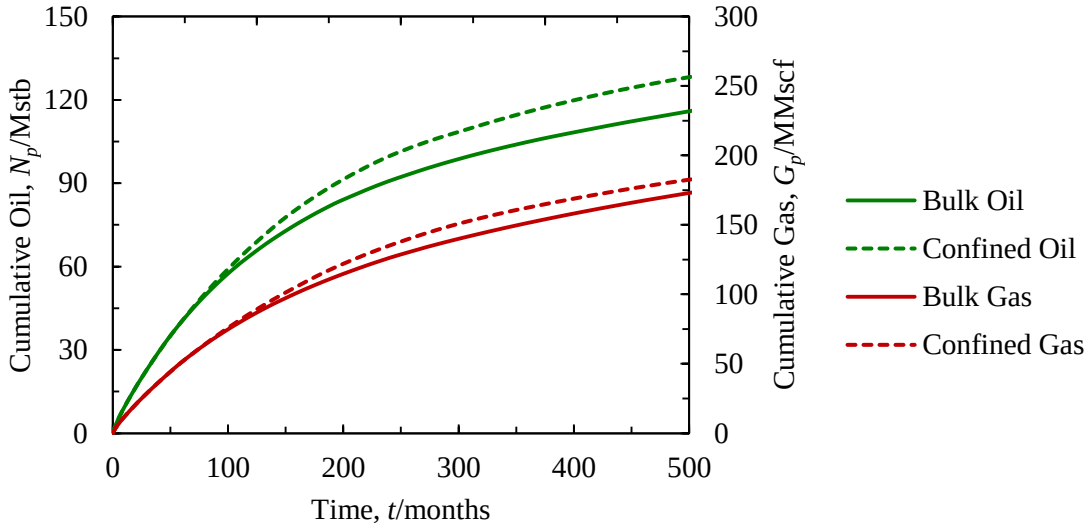

Figure 5-5. Oil and gas production of a synthetic oil with and without considering capillary pressure.

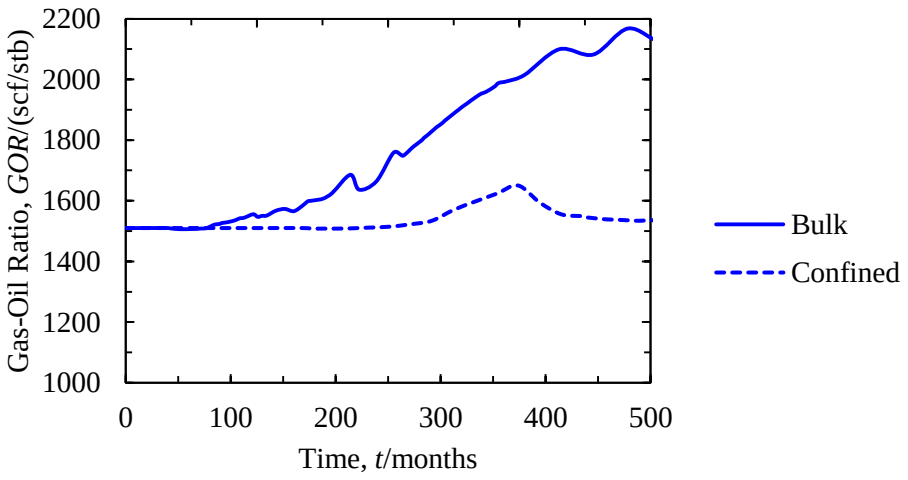

Figure 5-6. Gas-oil ratio of the synthetic fluid with and without considering capillary pressure.

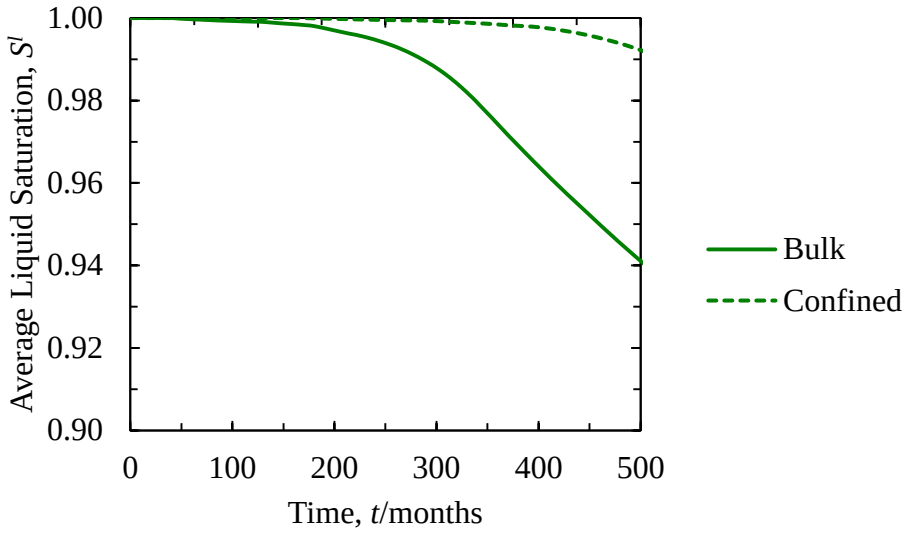

Figure 5-7. Average liquid saturation during production with and without considering capillary pressure.

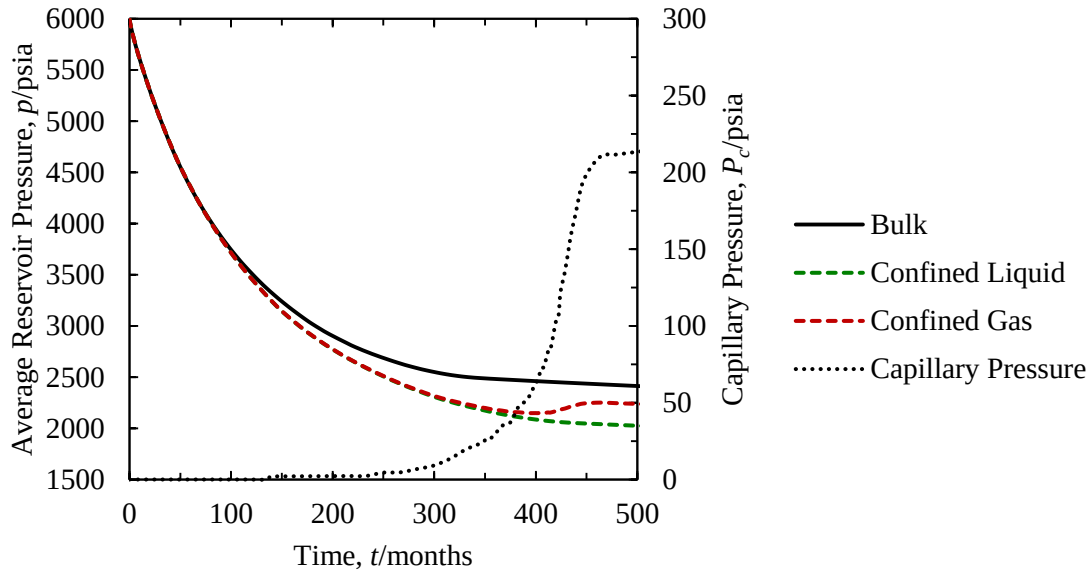

Figure 5-8. Average pressures in the reservoir through production.

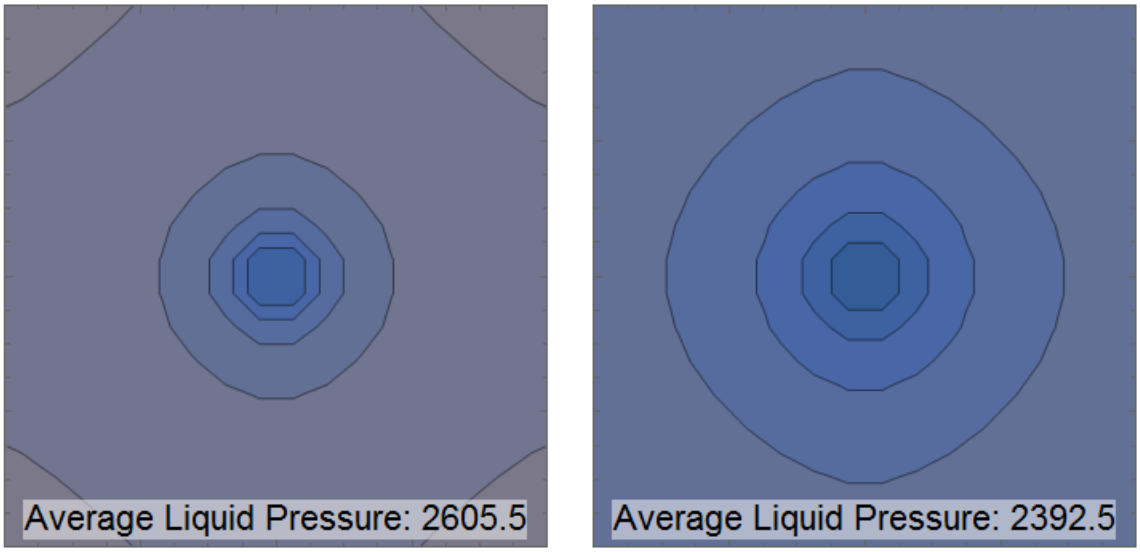

a. **b.**

Figure 5-9. Reservoir pressure distribution in the synthetic oil simulation (a) without capillary pressure and (b) with capillary pressure at 280 months.

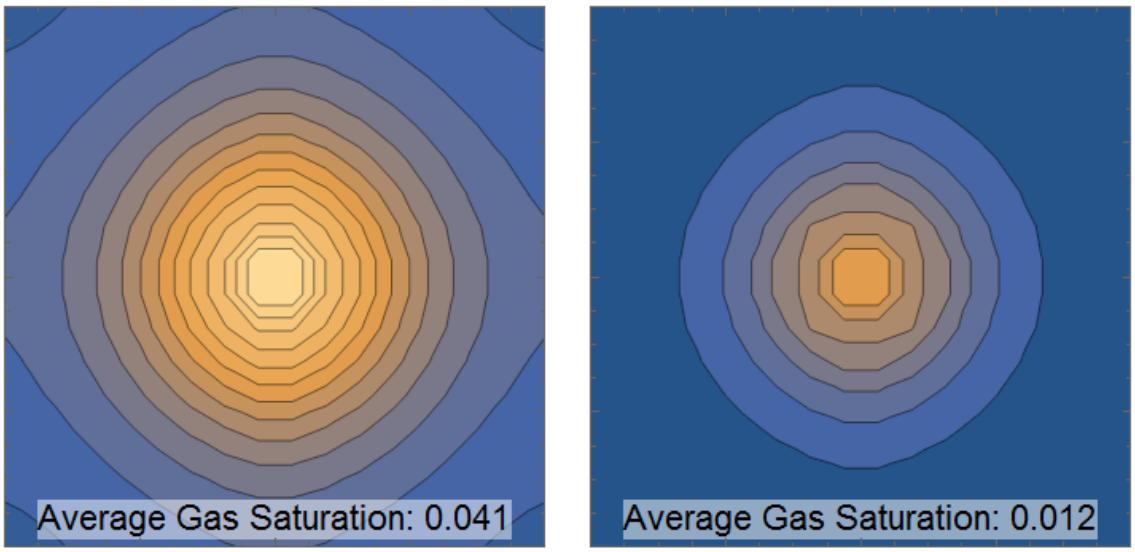

a. **b.**

Figure 5-10. Average gas saturation in synthetic oil reservoir (a) without capillary pressure and (b) with capillary pressure at 440 months.

Due to capillary pressure shifting equilibrium in the reservoir, densities will also be shifted. The surface densities of the simulations performed for section 5.2 also show how the densities change throughout production. Figure 5-11 shows that for early time, the surface density when including capillary pressure in the reservoir is lower, which is expected. However, during later time, that density rises and becomes larger than the surface density without capillary pressure. However, the variation is very small. The oil and gas density in the reservoir are expected to behave similar to Figure 3-19. Figure 5-12 shows that oil density in the reservoir at the wellbore when considering capillary pressure is lower, due to lighter components being forced into the liquid phase. Gas density begins against the expected trend, but is becomes higher after some time.

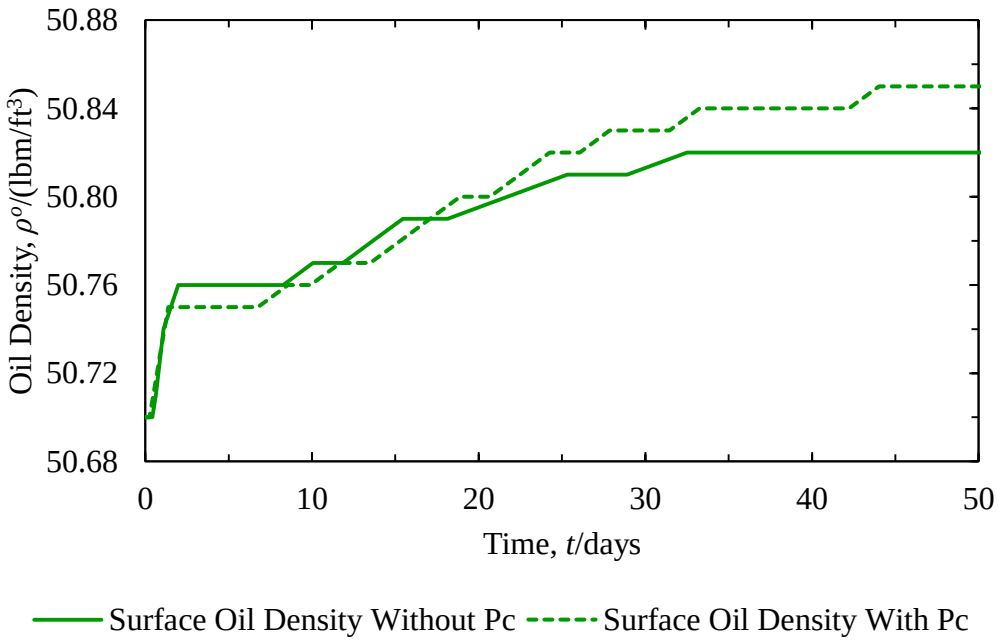

Figure 5-11. Surface oil density throughout production of the synthetic oil case.

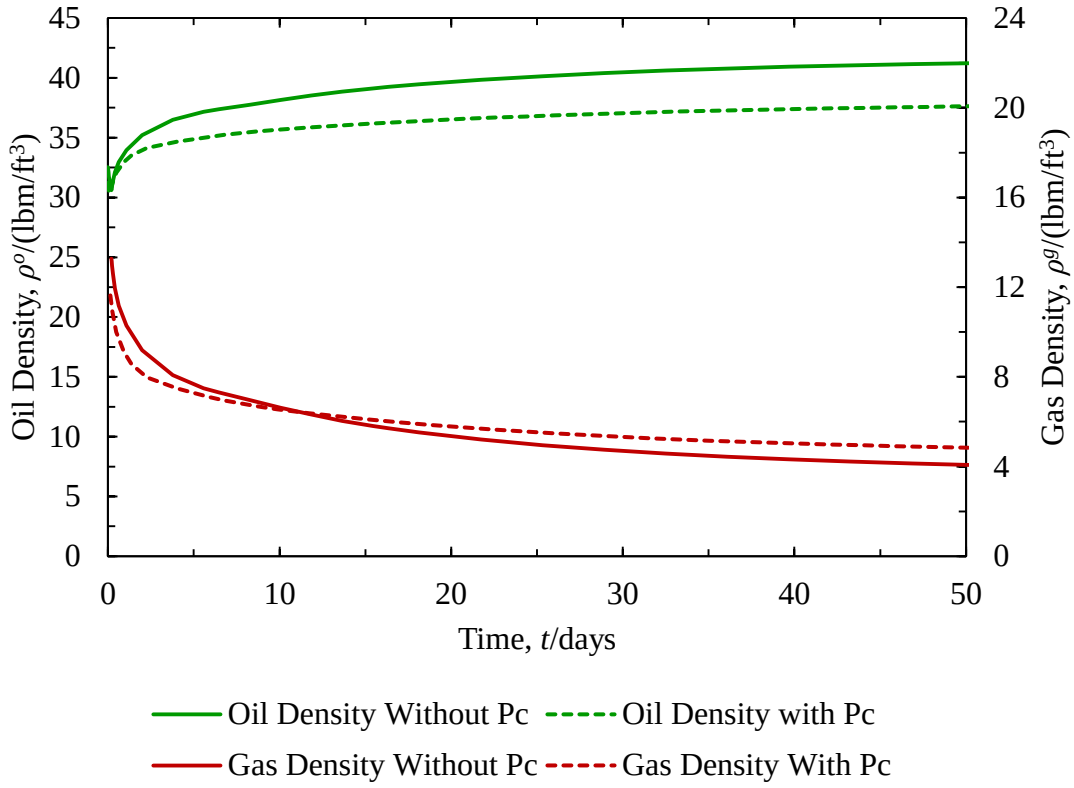

Figure 5-12. Oil and gas phase densities in the reservoir at the wellbore of the synthetic oil case with and without capillary pressure.

5.4 Real Fluid Results

5.4.1 Bakken Reservoir

We performed simulations for the Bakken fluid presented by Yu et al. (2015), shown in

Table 5-5 and

Table 5-6 with the reservoir properties in Table 5-4. The behavior of the Bakken fluid was very similarly to the synthetic oil case, seen by the cumulative production shown in Figure 5-13. Again, oil and gas production both increase due to capillary pressure. The produced GOR is shown in Figure 5-14. The GOR is lower and constant for a longer period of time

when considering capillary pressure compared to no capillary pressure. This is consistent with the observations of Nojabaei et al. (2013), who showed that the GOR of typical Bakken wells remains somewhat constant and may decrease over time.

Table 5-4. Reservoir properties of the Bakken oil simulation from Yu et al. (2015) and Tran et al. (2011).

p_i (psia)	k (md)	ϕ	d (nm)	θ (°)	T (°F)	BHP (psia)
8,000	0.02	0.07	15	30	240	1,000

Table 5-5. Bakken fluid composition and component properties from Yu et al. (2015), also shown on p. 128.

Species	z_i	M_i	$p_{c,i}$ (psia)	$T_{c,i}$ (°F)	ω_i	s_i	P_i
C_1	0.2506	16.04	667.17	-116.59	0.008	-0.154	77
C_2-C_4	0.22	42.82	625.11	194.27	0.1432	-0.0921	145.2
C_5-C_7	0.2	83.74	496.17	461.138	0.2474	-0.0482	250
C_8-C_9	0.13	105.91	454.26	583.142	0.2861	-0.032	306
C_{10+}	0.1994	200	317.2	960.062	0.6869	0.1368	686.3

Table 5-6. Bakken fluid binary interaction coefficients δ_{ik} from Yu et al. (2015), also shown on p. 128.

	C_1	C_2-C_4	C_5-C_7	C_8-C_9	C_{10+}
C_1	0	0.0078	0.0242	0.0324	0.0779
C_2-C_4	0.0078	0	0.0046	0.0087	0.0384
C_5-C_7	0.0242	0.0046	0	0.0006	0.0169
C_8-C_9	0.0324	0.0087	0.0006	0	0.0111
C_{10+}	0.0779	0.0384	0.0169	0.0111	0

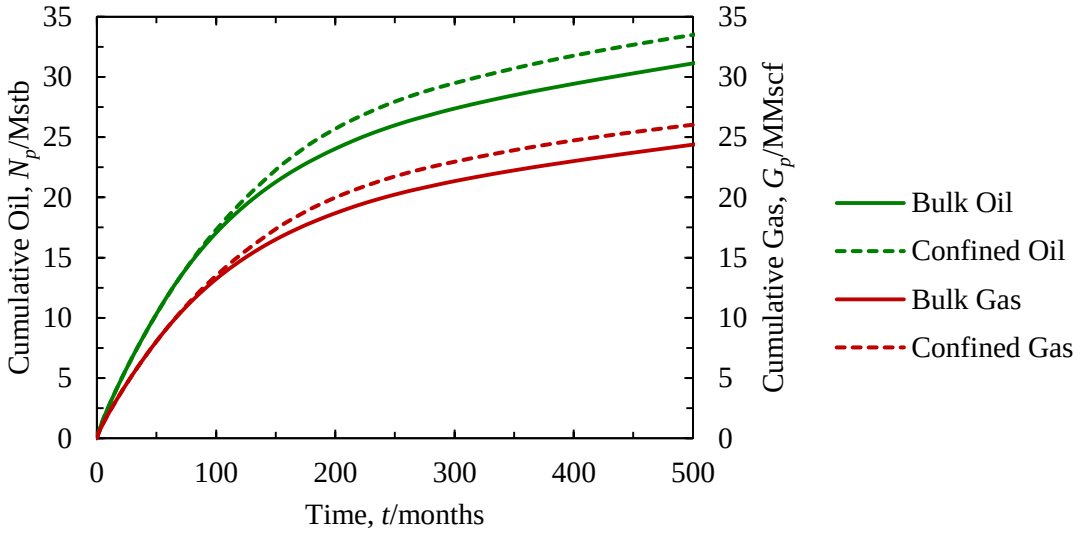

Figure 5-13. Cumulative oil and gas production from a Bakken reservoir.

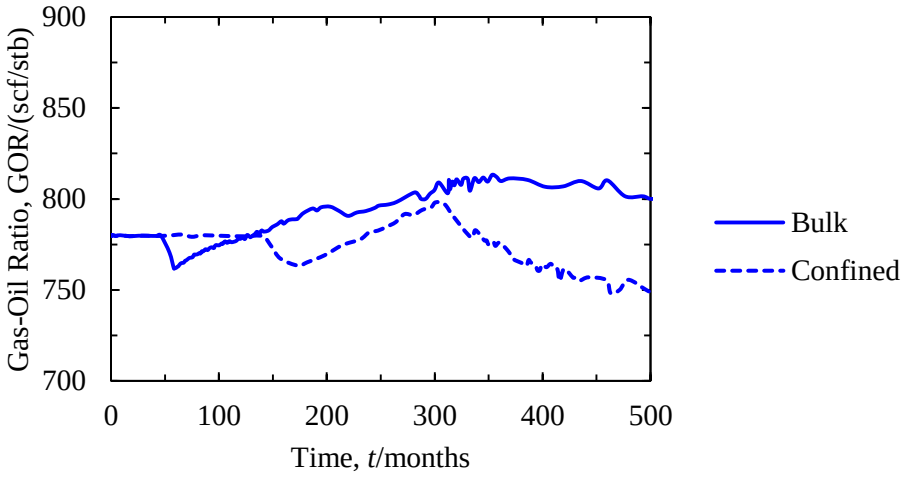

Figure 5-14. Gas-oil ratio of the produced Bakken oil.

5.4.2 Eagle Ford Volatile Oil Reservoir

We simulated a volatile oil from the Eagle Ford formation using the fluid in Table 5-8 with the reservoir properties in Table 5-7. From Figure 5-15 we see a higher oil production when considering capillary pressure, but the gas production remains very similar to the case without capillary pressure. Figure 5-16 shows that throughout production, the GOR slightly increases, but remains much lower than the case without capillary pressure.

Table 5-7. Reservoir properties of the Eagle Ford oil simulation from Gong et al. (2013).

p_i (psia)	k (md)	ϕ	d (nm)	θ (°)	T (°F)	BHP (psia)
4,259	0.001	0.0875	15	30	189	1,500

Table 5-8. Eagle Ford volatile oil fluid composition and component properties from Gong et al. (2013), also shown on p. 129.

Species	z_i	M_i	$p_{c,i}$ (psia)	$T_{c,i}$ (°F)	ω_i	s_i	P_i
N_2	0.0007	28	492.5	-232.8	0.04	-0.13556	41
CO_2	0.0081	44.01	1070.2	87.6	0.225	-0.05768	78
C_1	0.6554	16.043	667.4	-116.9	0.008	-0.154	77
C_2	0.1297	30	708.5	89.7	0.098	-0.1002	108
C_3	0.0617	44.1	615.9	205.6	0.152	-0.08501	150.3
nC_4	0.0242	58.1	551.3	305.4	0.193	-0.06413	189.9
iC_4	0.015	58.1	529.2	274.6	0.176	-0.07935	181.5
nC_5	0.0102	72.2	489.5	385.3	0.251	-0.04183	268.01
iC_5	0.0108	72.2	491	368.7	0.227	-0.0435	225
C_6	0.0138	86	477.2	453.5	0.275	-0.01478	314.21
C_{7+}	0.0704	177.11	274.3	782.9	0.536	0.12873	666.8

$\delta_{ik} = 0$ for all components

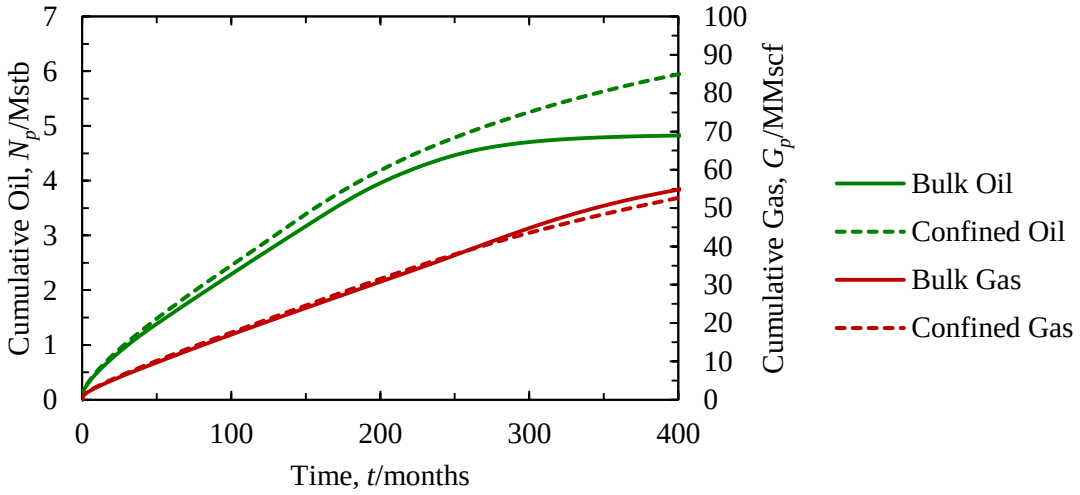

Figure 5-15. Cumulative production from an Eagle Ford volatile oil reservoir.

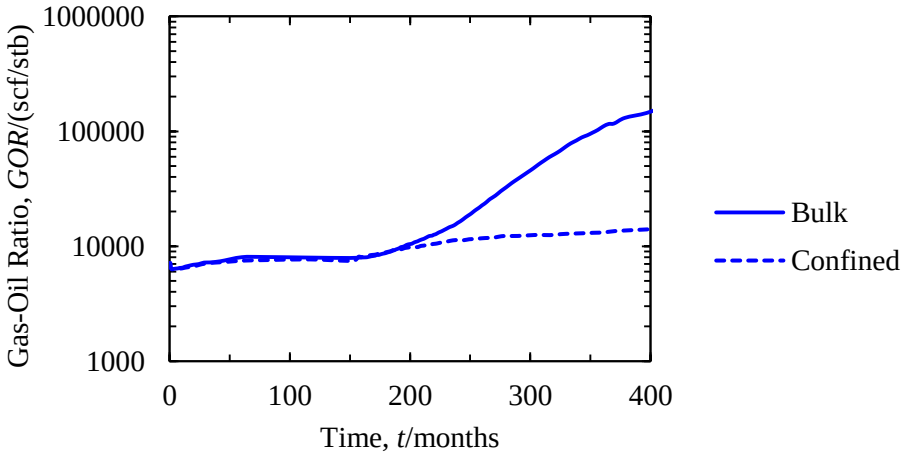

Figure 5-16. Gas-oil ratio throughout production of an Eagle Ford volatile oil.

5.4.3 Eagle Ford Gas Condensate

We expect the effects of capillary pressure on production to be reversed in a gas condensate reservoir. This is partially due to the higher dew point pressure, so two-phase flow is reached sooner. The higher dew point can be seen in Figure 5-17. Also, the liquid

saturation is higher, which impedes gas flow. This is sometimes referred to as condensate banking. At the low oil saturations, the oil phase is very immobile, so it blocks gas production. We simulate a reservoir using the condensate shown in Table 5-10 with the reservoir properties shown in Table 5-9. These effects are seen in Figure 5-18. The GOR is also expected to behave opposite in a gas condensate reservoir as an oil reservoir. Figure 5-19 shows that the GOR in the Eagle Ford gas condensate reservoir is higher than without capillary pressure.

Table 5-9. Reservoir properties of the Eagle Ford oil simulation from Gong et al. (2013).

p_i (psia)	k (md)	ϕ	d (nm)	θ (°)	T (°F)	BHP (psia)
6,500	0.007	0.12	15	30	329	1,500

Table 5-10. Eagle Ford gas condensate fluid composition and component properties from Gong et al. (2013), also shown on p. 129.

Species	z_i	M_i	$p_{c,i}$ (psia)	$T_{c,i}$ (°F)	ω_i	s_i	P_i
N_2	0.0011	28	492.5	-232.8	0.04	-0.13556	41
CO_2	0.0127	44.01	1070.2	87.6	0.225	-0.05768	78
C_1	0.6959	16.043	667.4	-116.9	0.008	-0.154	77
C_2	0.1137	30	708.5	89.7	0.098	-0.1002	108
C_3	0.0486	44.1	615.9	205.6	0.152	-0.08501	150.3
nC_4	0.0195	58.1	551.3	305.4	0.193	-0.06413	189.9
iC_4	0.0142	58.1	529.2	274.6	0.176	-0.07935	181.5
nC_5	0.0084	72.2	489.5	385.3	0.251	-0.04183	268.01
iC_5	0.0105	72.2	491	368.7	0.227	-0.0435	225
C_6	0.0117	86	477.2	453.5	0.275	-0.01478	314.21
C_{7+}	0.0637	156.69	295.1	735.6	0.483	0.10851	591.1

$\delta_{ik} = 0$ for all components

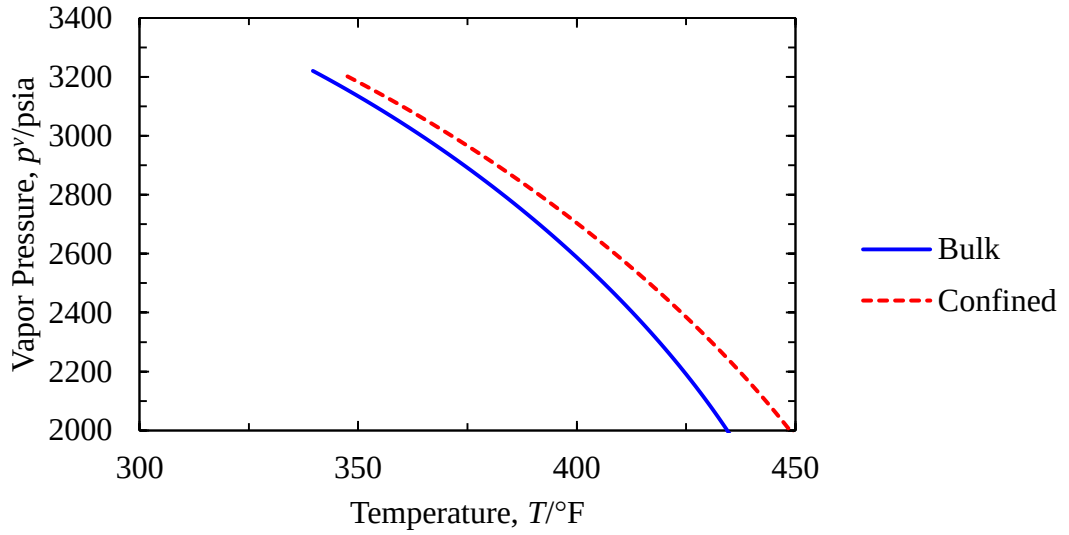

Figure 5-17. Phase envelope for the dew point region of the Eagle Ford gas condensate for bulk and confined spaces (d = 15 nm, θ = 30°).

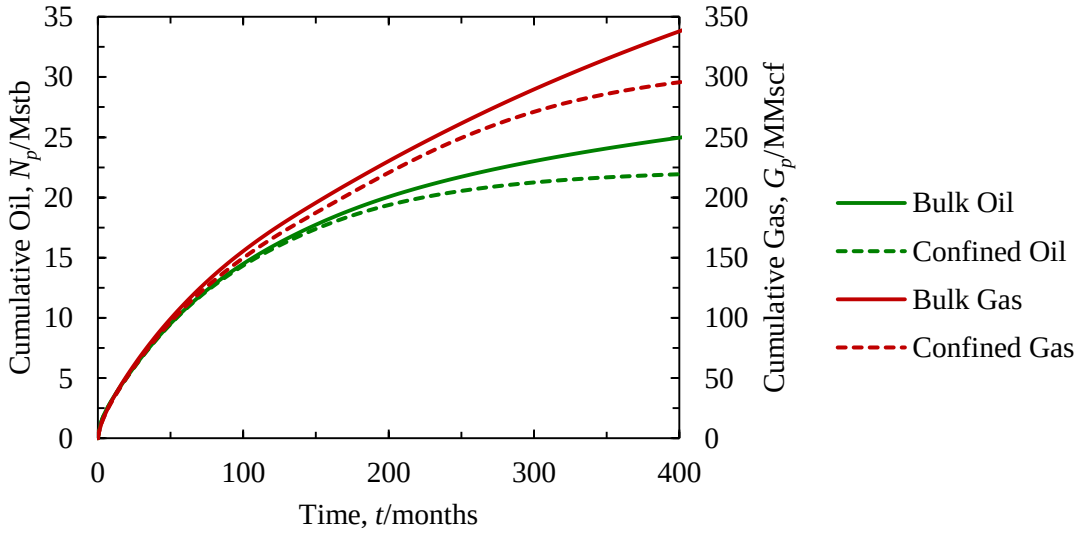

Figure 5-18. Oil and gas production from an Eagle Ford gas condensate reservoir.

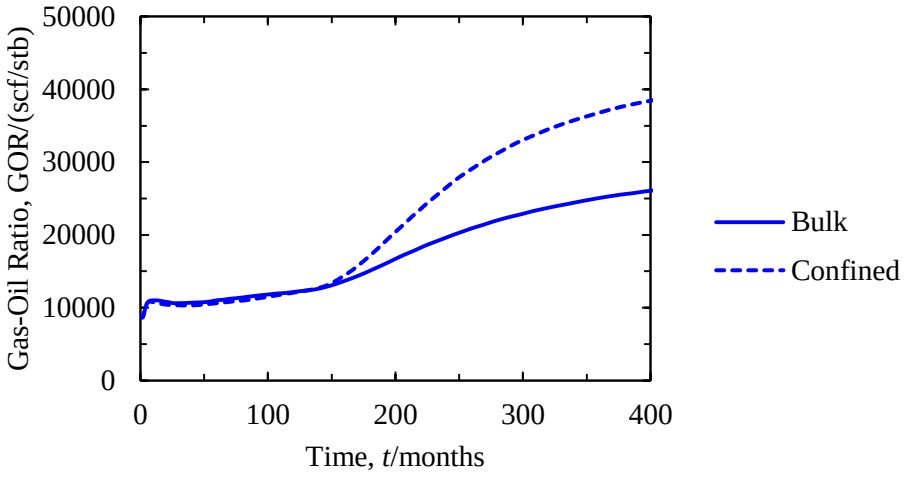

Figure 5-19. Gas-oil ratio of an Eagle Ford gas condensate reservoir.

CHAPTER VI

RELATIVE PERMEABILITY FROM CAPILLARY PRESSURE

6.1 Capillary Pressure in a Single Pore Size

With capillary pressure in VLE, we can simulate laboratory experiments in tight porous media at reservoir conditions. Two useful tests are the constant composition expansion (CCE) and constant volume depletion (CVD) tests. The constant composition expansion test uses an expanding cell filled with a reservoir fluid at reservoir conditions. The cell is then expanded, lowering the pressure in the cell. Fluid properties and oil saturation are determined at each pressure step. The CCE method as described in this work is representative of a constant volume cell, in which **both** liquid and vapor are produced to keep the overall composition constant. The constant volume depletion test also expands the cell volume to lower pressure, but returns to the original volume by depleting gas while maintaining pressure constant for that step. When we incorporate capillary pressure, we also obtain information on the capillary pressure in the reservoir at a given pressure. These two tests yield datasets consisting of oil pressure, oil saturation, capillary pressure, and compositions for a constant temperature.

For the CVD method, we first calculate the overall pore volume V_p using Eq. (6.1). The number of pores N_p and pore length L_p are arbitrary, since saturation is relative to total volume. We then determine the saturation pressure of the given fluid at the given temperature. We then determine the overall molar volume at the saturation pressure and calculate the total number of moles n_t and moles of each component n_i from Eq. (6.2) and Eq. (6.3). We then decrease the pressure and calculate the total volume $\tilde{V}_t$. The difference between the pore volume and the volume at the lower pressure is the excess volume V_d, shown in Eq. (6.5). If the excess volume is less than the volume of vapor, the depleted phase is then all vapor. If the excess volume is greater than the vapor volume, then the entire vapor volume and part of the liquid phase are depleted to return the system back to the pore volume. The fraction of total volume depleted of each phase is identified as f_d^j,

where $f_d^l + f_d^v = 1$. For the CVD method, $f_d^l = 1$ and for the CCE method, $f_d^j = S_j$, implying perfect mixing. Once we determine the phase distribution, we calculate the total number of moles depleted from each phase n_d^j using Eq. (6.6). The combined moles of each component depleted $n_{d,i}$ are then calculated using Eq. (6.7). The pressure is then decreased by steps until a designated pressure, with these calculations at each step. The process for the CVD method is described in detail in Figure 6-1. The difference in pressure for each step Δp is calculated by the difference between the saturation pressure p^s, minimum pressure $p_{\min}$, and number of steps n_s as showin in Eq. (6.8).

$$V_p = \frac{\pi}{4} N_p d^2 L_p \tag{6.1}$$

$$n_t = \frac{V_p}{\tilde{V}_m} \tag{6.2}$$

$$n_i = n_t z_i \tag{6.3}$$

$$\tilde{V}_t = n_t \tilde{V}_m \tag{6.4}$$

$$V_d = \tilde{V}_t - V_p \tag{6.5}$$

$$n_d^j = \frac{V_d f_d^j}{\tilde{V}_m^j} \tag{6.6}$$

$$n_{d,i} = n_d^l x_i + n_d^v y_i \tag{6.7}$$

$$\Delta p = \frac{p^s - p_{\min}}{N_s - 1} \tag{6.8}$$

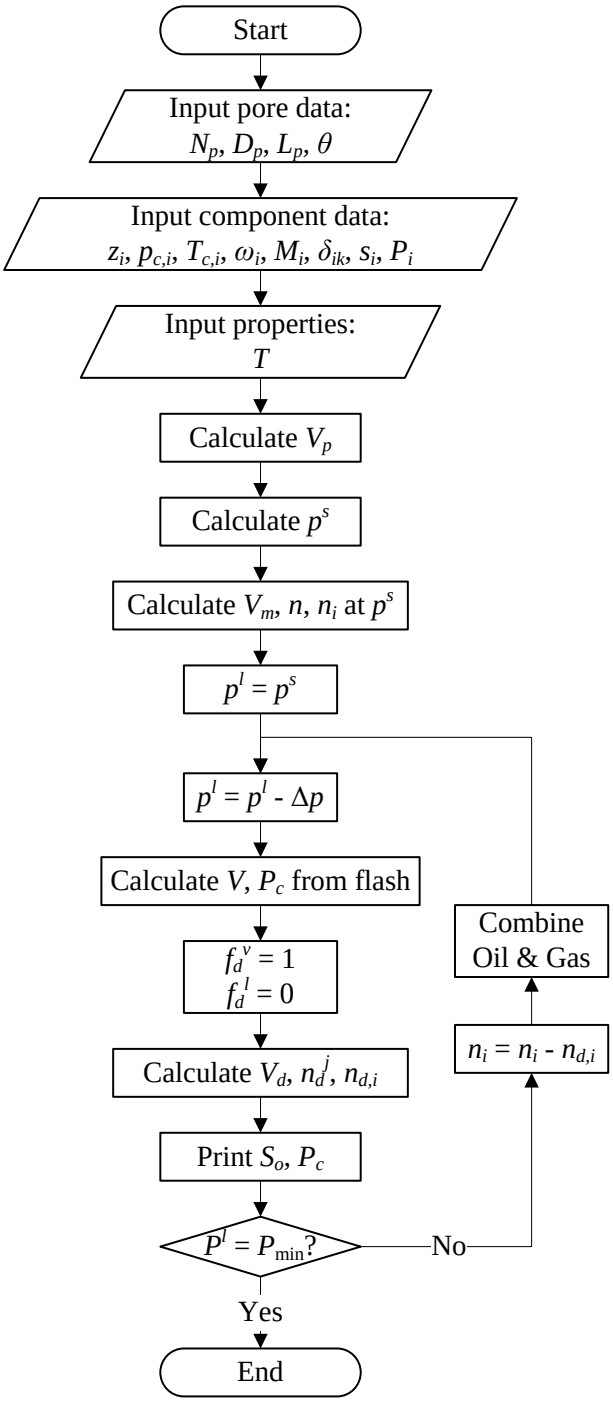

Figure 6-1. Capillary pressure curve from CVD method.

The CCE method is similar to the CVD method, except the CCE method assumes that the depleted moles of fluids are distributed according to the molar fraction of each phase. In other words, if 70% of the overall moles are in the liquid phase, 70% of the depleted moles will be liquid. On a volume basis, the volume fraction f_d^j of each phase being depleted will equal the volume saturation of that phase. This can be verified by mass balance. Similar to a relative permeability plot, the depleted phase distributions can be plotted against the liquid mole fraction, as shown in Figure 6-2. Using this method, the overall composition remains constant during each step. The CCE method is described in Figure 6-3.

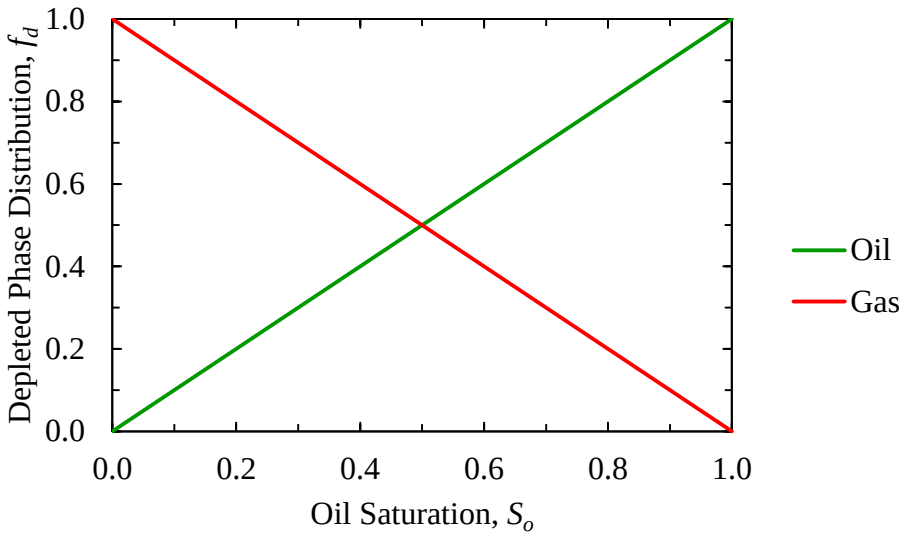

Figure 6-2. Depleted phase distribution for CCE method

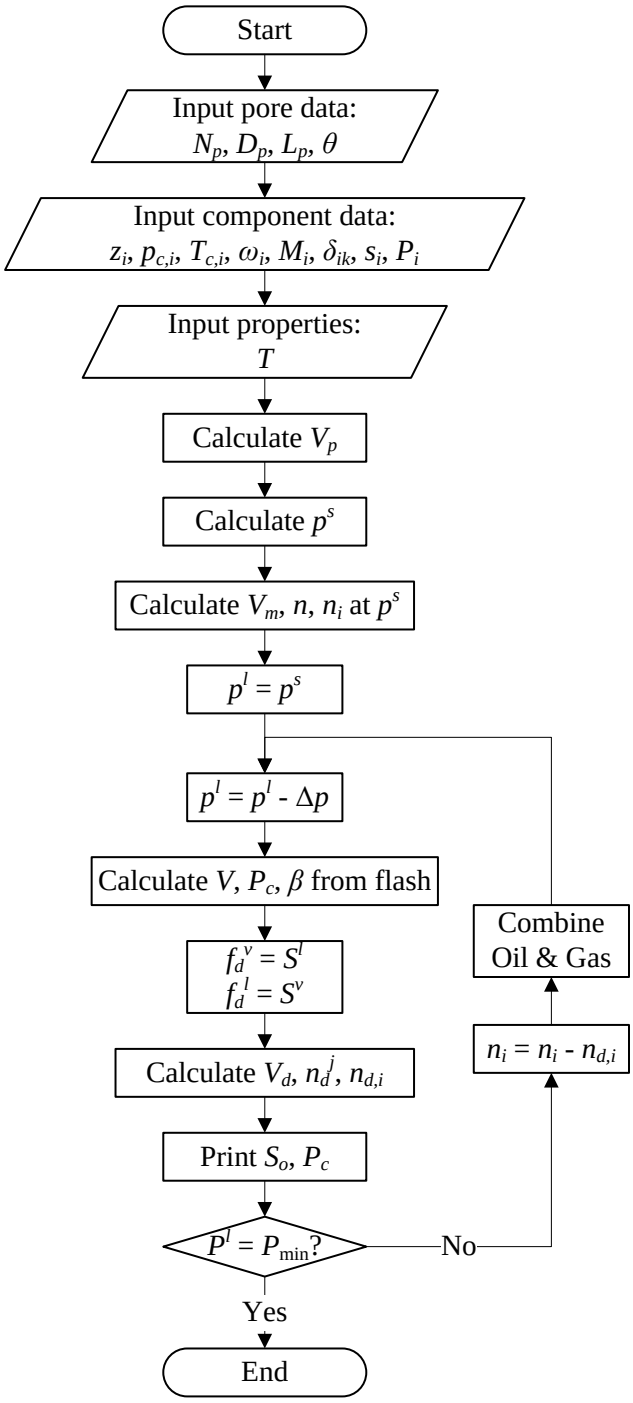

Figure 6-3. Capillary pressure curve from CCE method.

The CCE and CVD methods represent the two extremes in production, when considering mobility. Mobility is defined as the ratio of relative permeability to viscosity, as shown in Eq. (6.9). Due to the much lower gas viscosity, the gas phase is generally more mobile than the oil phase. The mobility ratio quantifies this by taking the ratio of gas mobility to oil mobility. The CVD method assumes the mobility ratio is so high that only gas is produced. However, the CCE method assumes the mobility ratio that will keep the system at a constant composition. The depleted phase distribution can be written in terms of mobility, shown in Eq. (6.10). Oil and gas relative permeability with this set of equations in not unique. However, if we define one relative permeability curve, the other can be calculated to show the difference of each method in terms of flow distribution. For the CVD method, the gas relative permeability curve is defined and the oil relative permeability is zero. For the CCE method, the oil relative permeability is defined and the gas relative permeability is calculated from Eq. (6.11). The equivalent relative permeabilities are shown in Figure 6-4 and Figure 6-5 for the synthetic oil 1 in Table 6-1 and Table 6-2 (same as synthetic fluid 1 on p. 126). From this, we see that the CVD and CCE methods are essentially the two extremes of gas and oil depletion, respectively.

$$\lambda^i = \frac{k_{rj}}{\mu^i} \tag{6.9}$$

$$f_d^j = \frac{\lambda^l}{\lambda^l + \lambda^v} \tag{6.10}$$

$$k_{rg} = \frac{1 - f_d^o}{f_d^o} \frac{\mu_g}{\mu_o} k_{ro} \tag{6.11}$$

Table 6-1. Synthetic fluid component properties

Species	M_i	$p_{c,i}$ (psia)	$T_{c,i}$ (°F)	ω_i	s_i	$Z_{c,i}$	P_i
C_1	16.043	667.4	-116.9	0.008	-0.154	0.288	77
C_2	30	708.5	89.7	0.098	-0.1002	0.284	108
nC_4	58.1	551.3	305.4	0.193	-0.0641	0.2743	189.9
nC_{10}	134	367	659.8	0.444	0.0803	0.249	505.88

$\delta_{ik} = 0$ for all components

Table 6-2. Synthetic fluid compositions.

	1	2	3	4	5	6	7
C_1	0.45	0.5	0.55	0.6	0.65	0.7	0.75
C_2	0.12	0.11	0.11	0.1	0.1	0.1	0.1
nC_4	0.1	0.08	0.06	0.05	0.05	0.05	0.09
C_{10}	0.33	0.31	0.28	0.25	0.2	0.15	0.06
$\overline{MW}$	60.85	57.51	53.13	49.03	43.13	37.24	28.30
Type	Black Oil	Volatile Oil	Volatile Oil	Volatile Oil	Volatile Oil	Volatile Oil	Gas Condensate

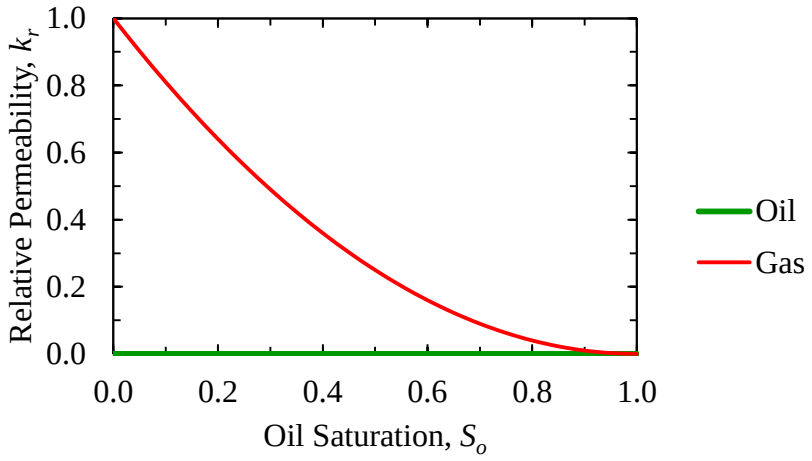

Figure 6-4. Equivalent relative permeability describing CVD depletion method.

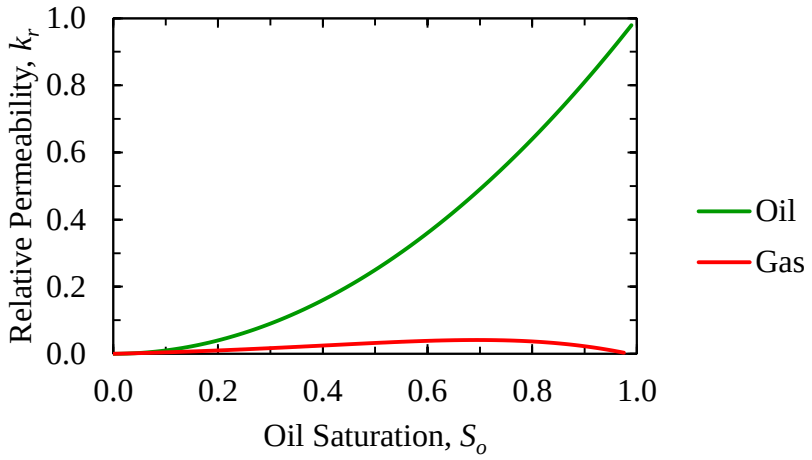

Figure 6-5. Equivalent relative permeability describing CCE depletion method for the synthetic oil 1 in Table 6-2 (45% methane, 12% ethane, 10% n-butnae, and 33% n-decane).

Using the CCE and CVD methods including capillary pressure, we examine capillary pressure as a function of pressure. Figure 6-6 shows the pressure dependence of capillary pressure for the synthetic fluids 1, 4, and 7 in Table 6-2 at $T = 225$ °F. At this temperature, the synthetic fluid 7 is a gas condensate fluid and is therefore plotted versus the gas pressure, since gas is the reference or initial reservoir phase. The other two fluids are plotted against liquid pressure. Figure 6-6 shows that for a given fluid type, the two methods match fairly closely for most pressures. At lower pressures, the capillary pressures from the two methods begin to deviate slightly from each other. This deviation is due to compositional variations between the two depletion methods and shows that capillary pressure is highly dependent on pressure.

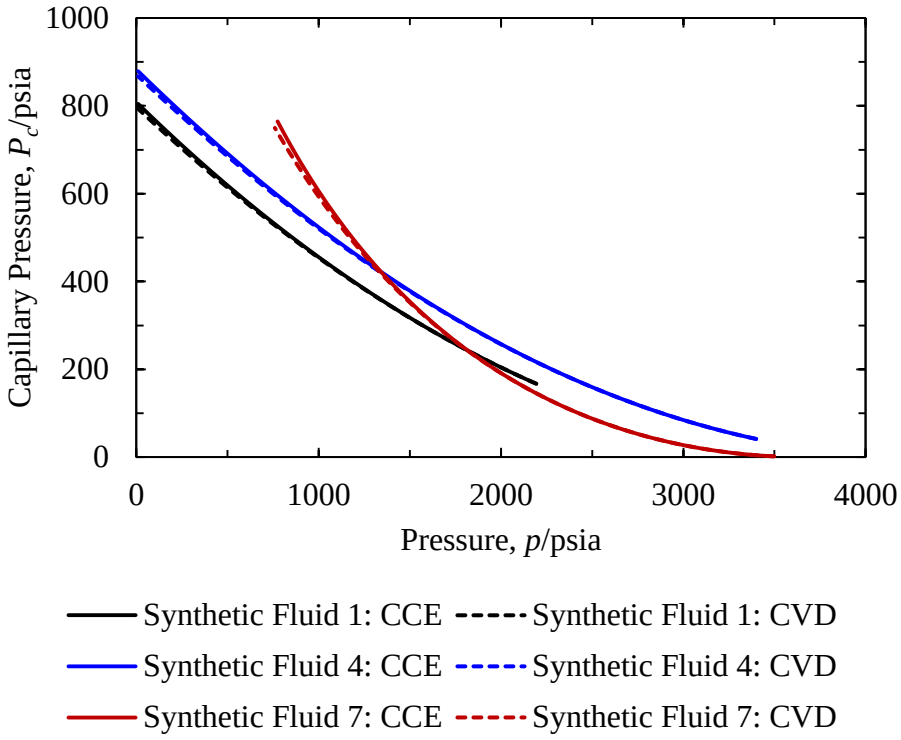

Figure 6-6. Capillary pressure as a function of pressure for various fluids by CCE and CVD methods with T = 225 °F, d = 15 nm, and θ = 30°.

Results of the two methods are shown in Figure 6-7 for the synthetic fluid 4 in Table 6-2 at 225 °F with a pore diameter of 15 nm and contact angle of 30°. For this case, the bubble point pressure is 3399.8 psia and the minimum pressure is 1,000 psia, with 50 pressure steps, giving a pressure step of 48.97 psia. The minimum pressure is selected to represent the bottom-hole pressure. The major difference is the residual oil saturation. When capillary pressure is plotted against normalized oil saturation S_o^* defined by Eq. (6.12) with $S_{o,r}$ being residual oil saturation, the capillary pressure curves match very closely, as shown in Figure 6-8.

$$S_o^* = \frac{S_o - S_{o,r}}{1 - S_{o,r}} \tag{6.12}$$

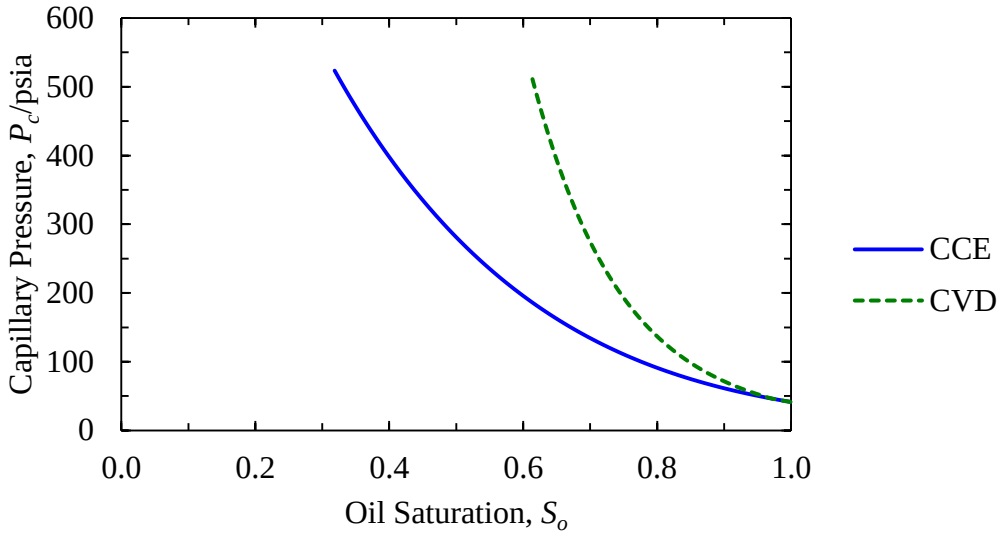

Figure 6-7. Capillary pressure curve from CCE and CVD methods for a mixture of 60% methane, 10% ethane, 5% n-butane, and 25% n-decane for T = 225 °F, d = 15 nm, and θ = 30° with minimum pressure of 1,000 psia and 50 pressure steps.

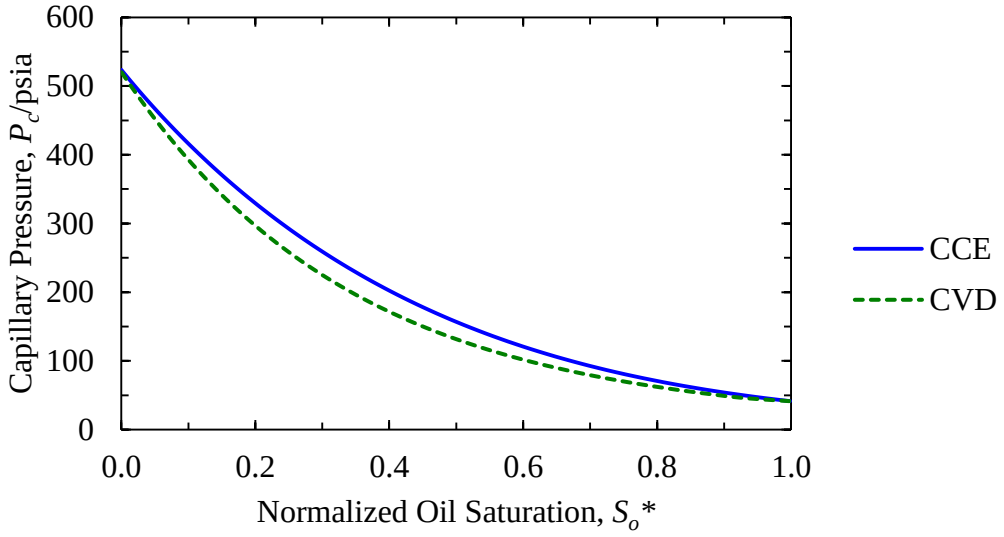

Figure 6-8. Capillary pressure plotted against normalized oil saturation for a mixture of 60% methane, 10% ethane, 5% n-butane, and 25% n-decane for T = 225 °F, d = 15 nm, and θ = 30° with minimum pressure of 1,000 psia and 50 pressure steps.

For the CCE method, the number of pressure depletion steps is irrelevant because the depleted moles of each phase are calculated to keep the overall composition constant. This simplifies the problem into a constant composition flash at varying pressures. However, for the CVD method, the number of steps becomes important. Figure 6-9 shows the impact of number of steps on the generated capillary pressure curve of synthetic fluid 4 from Table 6-2 at 225 °F with pore diameter of 15 nm and contact angle of 30°.

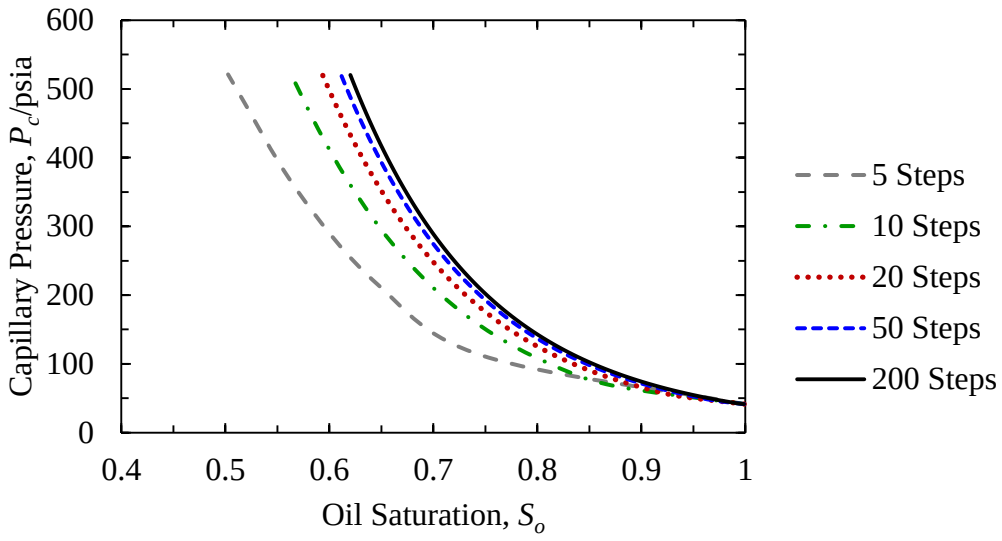

Figure 6-9. Number of steps for CVD method for a mixture of 60% methane, 10% ethane, 5% n-butane, and 25% n-decane for T = 225 °F, d = 15 nm, and θ = 30° with minimum pressure of 1,000.

6.2 Capillary Pressure in a Distribution of Pore Sizes

While a single pore size shows how the fluid behaves when confined, the pore systems in nature occur as distributions. A very common simplification of porous media is to assume the media is a bundle of capillary tubes of various sizes, as shown in Figure 6-10, first shown by Gates and Lietz (1950). Many distributions are being characterized for unconventional reservoirs. Pommer (2014) evaluates pore size distributions for samples collected from the Eagle Ford formation. Figure 6-11 shows three wells from the Eagle Ford formation with a lognormal distribution fit. The data follow the lognormal

distribution very closely and the mean and standard deviation for each well are given in Table 6-3. The lognormal distribution is defined by Eq. (6.13) and Eq. (6.14), where N is the probability density function, C is the cumulative density function, μ is the mean, and σ_d is the standard deviation.

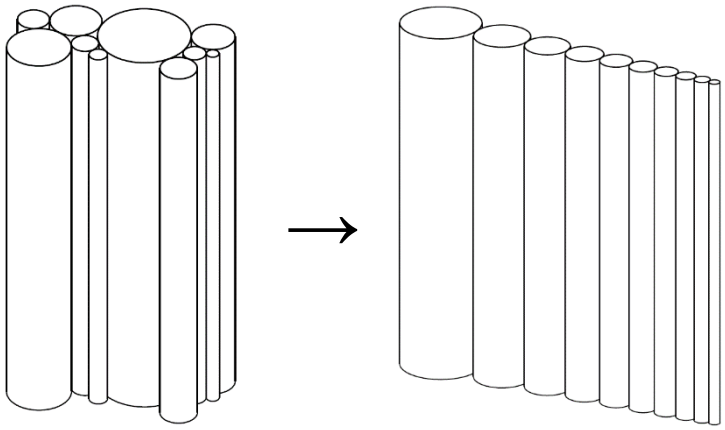

Figure 6-10. Distribution of pores arranged randomly and in size order.

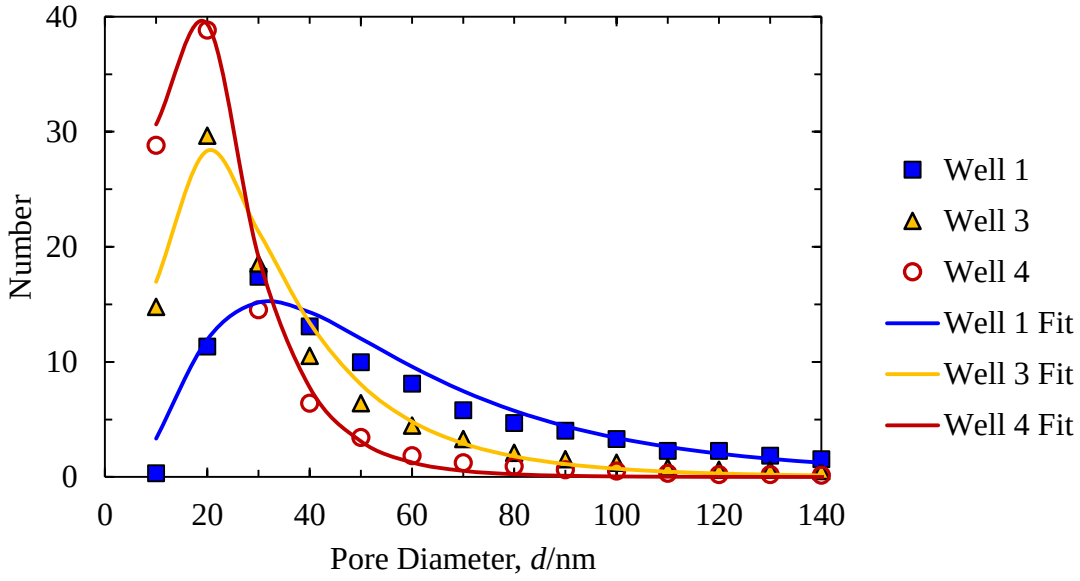

Figure 6-11. Pore size distribution of three Eagle Ford wells with lognormal distribution fits.

Table 6-3. Pore size distribution parameters for three Eagle Ford wells from Pommer (2014).

	Well 1	Well 3	Well 4
μ	3.897	3.312	2.999
$\exp\mu$ (nm)	49.24	27.43	20.06
σ_d	0.663	0.617	0.507

$$N = \frac{1}{\sigma_d\sqrt{2\pi}}\exp\left[-\frac{(\ln x-\mu)^2}{2\sigma_d^2}\right] \tag{6.13}$$

$$C = \frac{1}{2}\mathrm{erfc}\left(-\frac{\ln x-\mu}{\sigma_d\sqrt{2}}\right) \tag{6.14}$$

To model the system, a representative sample of pores must be selected. We first identify the number of pores in the system. With the cumulative lognormal distribution defined by mean μ and standard deviation σ_d, we split the distribution into the same number of bins as pores, identifying the range of probabilities for each bin. The midpoint probability of the range for each bin is selected and the inverse cumulative distribution is solved for the corresponding pore size. This is graphically represented by Figure 6-12, for a distribution with an average pore diameter of 20.086 nm $(\ln\mu = 3)$ and a standard deviation of 0.63. The selected pore diameters are shown in Table 6-4.

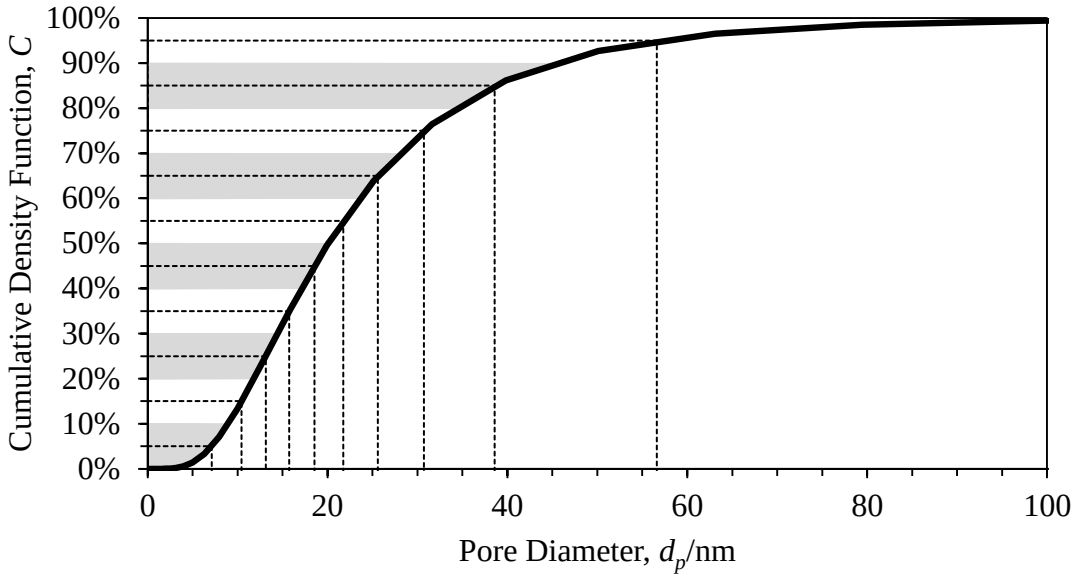

Figure 6-12. Graphical representation of pore selection by evenly distributed probability bins with μ = 20.086 nm ($\ln\mu$ = 3) and σ = 0.63.

Table 6-4. Representative pore diameters and volumes for a lognormal distribution with μ = 20.086 nm ($\ln\mu$ = 3) and σ = 0.63.

Probability Bin Range	Representative Percentile	Pore Diam. (nm)	Pore Volume (nm^3) or Area (nm^2)
0%-10%	5%	7.13	39.9
10%-20%	15%	10.45	85.8
20%-30%	25%	13.13	135.4
30%-40%	35%	15.76	195.1
40%-50%	45%	18.56	270.5
50%-60%	55%	21.74	371.2
60%-70%	65%	25.60	514.7
70%-80%	75%	30.72	741.2
80%-90%	85%	38.59	1169.6
90%-100%	95%	56.61	2517.0
		Total	6040.4

We generate capillary pressure curves for each pore in Table 6-4 with the synthetic fluid 4 at a temperature of 189 °F and contact angle of 30° in the distribution using the method shown in Figure 6-1 or Figure 6-3. Figure 6-13 shows capillary pressure curves for all pores in the distribution using both methods.

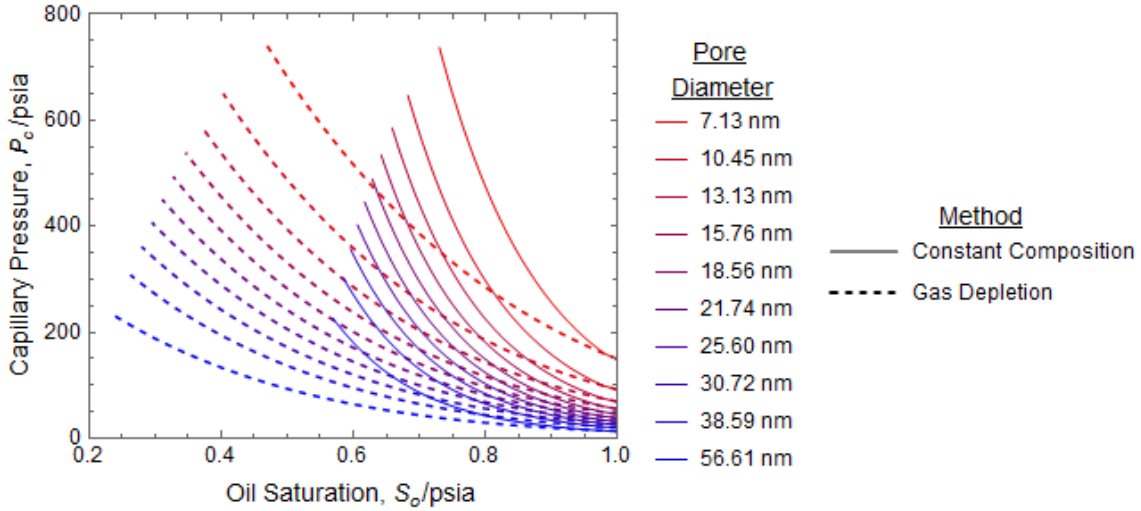

Figure 6-13. Capillary pressure curves for each pore in the distribution with 10 pores, μ = 20.086 nm (lnμ = 3) and σ = 0.63, using the CCE and CVD methods with 40 pressure steps for a mixture of 60% methane, 10% ethane, 5% n-butane, and 25% n-decane at T = 189 °F.

Once the pores are all depleted, the saturations and capillary pressures are interpolated and combined to generate a capillary pressure for the entire system. To do this, we select a capillary pressure and interpolate for saturation in each pore. The liquid volume in each pore is then added for that capillary pressure and divided by the total pore volume to obtain the overall saturation, as shown in Eq. (6.15). The method follows Figure 6-14.

$$S_o = \left(\sum_{ip=1}^{N_c} V_{ip}^o \right) \Big/ V_t \tag{6.15}$$

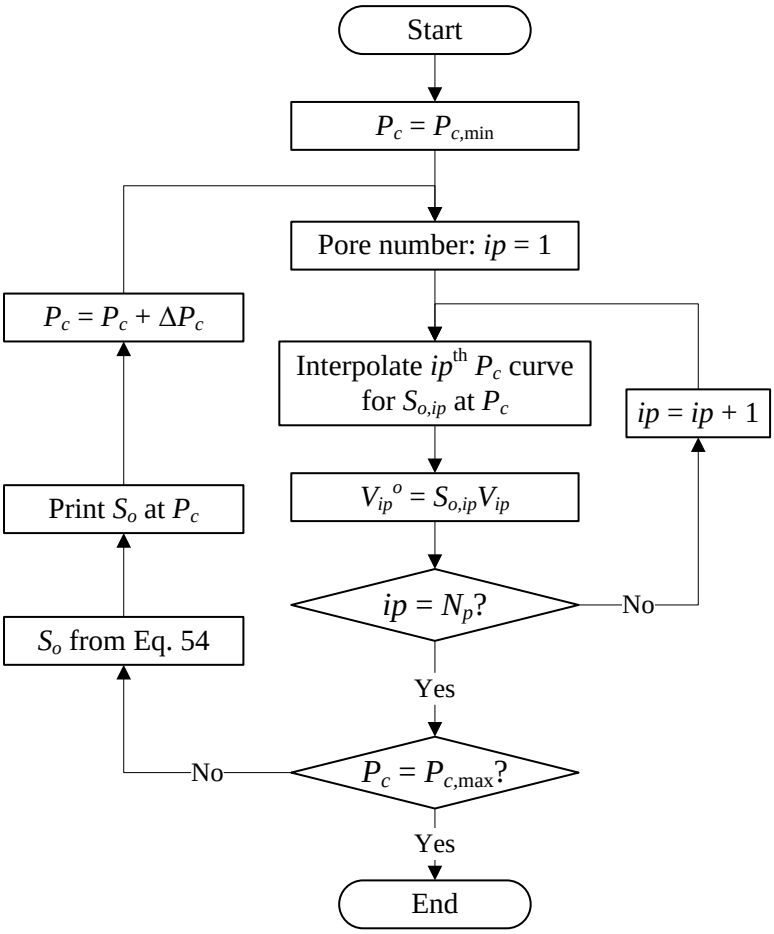

Figure 6-14. Capillary pressure interpolation for a distribution of pores.

When all pores are interpolated, a system capillary pressure is obtained. Figure 6-15 shows the capillary pressure curves interpolated from the curves in Figure 6-13 for the two methods. To compare the behavior of these curves, we plot them against normalized oil saturation, shown in Figure 6-16. This shows, again, that the curves match fairly closely, so the behavior then depends more on the residual oil saturation.

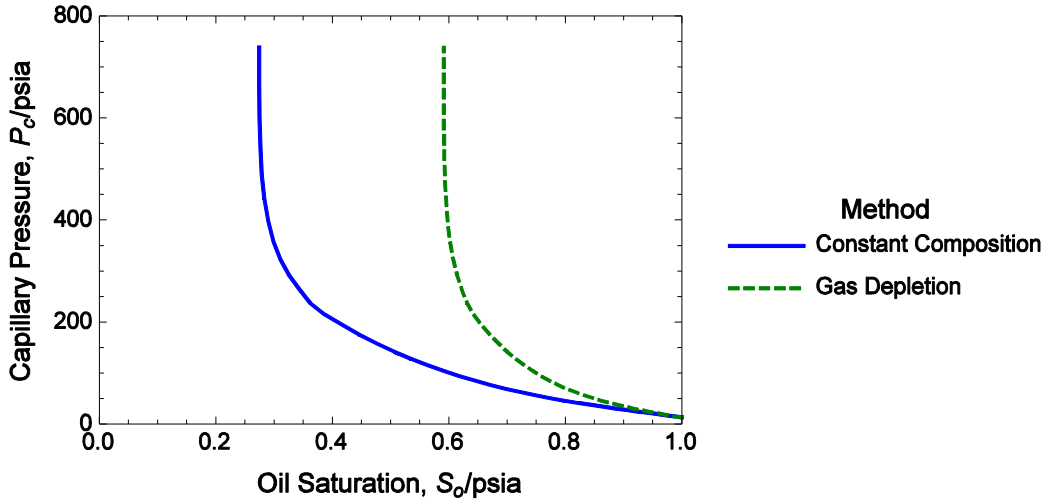

Figure 6-15. Interpolated capillary pressure curves using both CCE and CVD methods with 40 steps for a mixture of 60% methane, 10% ethane, 5% n-butane, and 25% n-decane at T = 189 °F for a distribution with 10 pores, μ = 20.086 nm (lnμ = 3) and σ = 0.63.

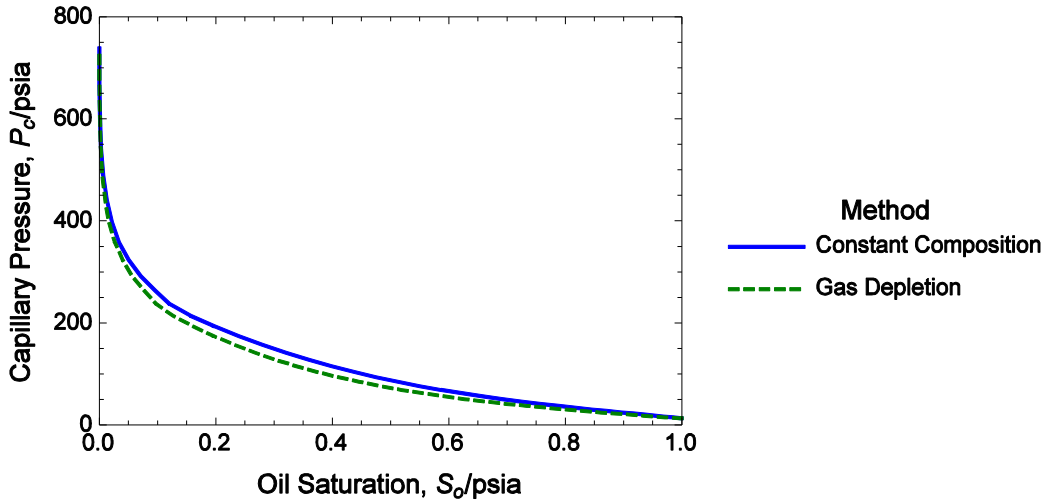

Figure 6-16. Capillary pressure of a distribution of pores using CCE and CVD methods with 40 pressure steps plotted against normalized oil saturation for a mixture of 60% methane, 10% ethane, 5% n-butane, and 25% n-decane at T = 189 °F for a distribution with 10 pores, μ = 20.086 nm (lnμ = 3) and σ = 0.63.

6.2.1 Pressure Stepping

Capillary pressure only exists in the two-phase region when the pressure is below the saturation pressure. However, pore diameter impacts the saturation pressure and the difference between the saturation point and the minimum pressure will vary for each pore size. This is seen in Table 6-5, which shows that for smaller diameter pores, the bubble point pressure is lower and therefore the difference between the bubble point pressure and the minimum pressure is smaller than that in larger pores. The pressure step Δp is calculated from the smallest pore using Eq. (6.8). This pressure difference is held constant, so the number of steps in each pore changes, as shown in Table 6-5. For the final pressure step, the pressure is allowed to go below the minimum pressure to keep the pressure step constant. The capillary pressure and saturation are then interpolated for their values at the minimum pressure.

Setting an external list of pressures would be useful, but the capillary pressure value at saturation near to one is critical to fitting the data to models and for determining relative permeability, which will be shown later. Therefore, for each pore depletion, the pressure stepping begins at the saturation point at each pore.

Table 6-5. Saturation pressure and difference between bubble point and minimum pressure for a distribution of pores with μ = 20.086 nm (lnμ = 3) and σ = 0.63 for a mixture of 60% methane, 10% ethane, 5% n-butane, and 25% n-decane at T = 189 °F, with θ = 30°.

Pore Diam. (nm)	Bubble Point Pressure (psia)	P_b - $P_{\min}$ (psia)	Number of Steps
7.13	2945.9	1945.9	20
10.45	3159.9	2159.9	23
13.13	3247.8	2247.8	23
15.76	3302.5	2302.5	24
18.56	3342.3	2342.3	24
21.74	3374.0	2374.0	25
25.60	3401.1	2401.1	25
30.72	3425.9	2425.9	25
38.59	3450.4	2450.4	25
56.61	3479.9	2479.9	26

6.2.2 Number of Representative Pores

The total number of pores chosen to represent the distribution is also a major factor in providing an accurate system capillary pressure. Figure 6-17 shows the capillary pressure curves for a varying number of pores using 50 pressure steps. When using a larger number of pores, the total run time is longer, but still fairly short (under a minute when using VBA).

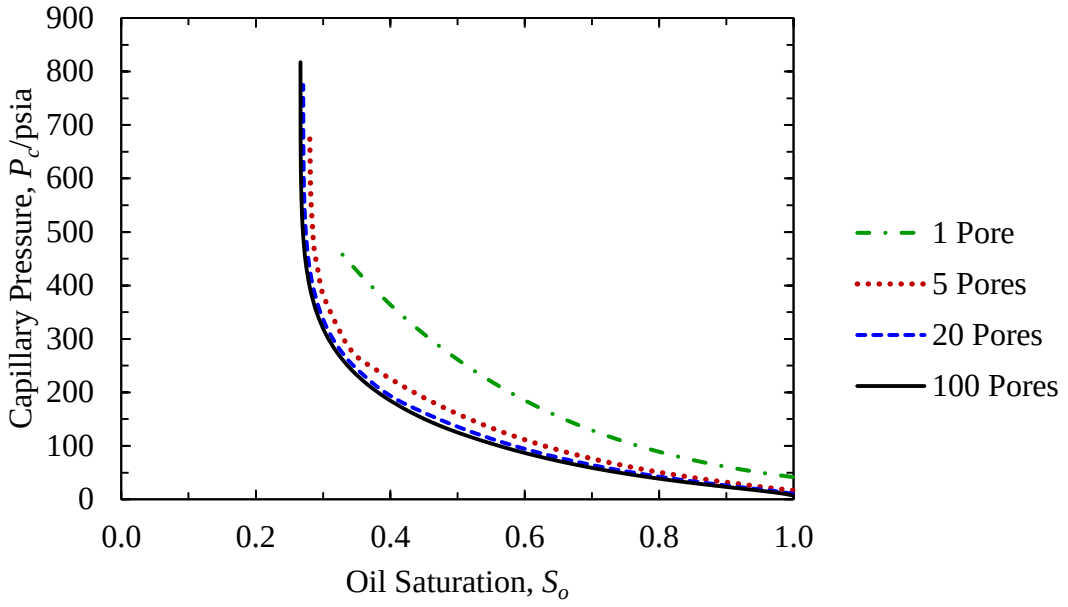

Figure 6-17. Capillary pressure curves for the CCE method varying number of pores distribution of pores with μ = 20.086 nm (lnμ = 3) and σ = 0.63 for a mixture of 60% methane, 10% ethane, 5% n-butane, and 25% n-decane at T = 189 °F, with θ = 30°.

6.2.3 Capillary Pressure with Various Fluid Types

Capillary pressure is also dependent on fluid type. As the oil type becomes lighter, the residual oil saturation and capillary pressure decrease. Figure 6-18 shows the generated capillary pressure curves for a single pore size of 15 nm and contact angle of 30° with the synthetic fluids 1-7 from Table 6-2 at a temperature of 225 °F and $p_{\min}$ of 1,000 psia. This plot shows the behavior of gas condensate capillary pressure as gas is depleted from a single pore size at pressures below the dew point. Since the retrograde condensate first increases then decreases in oil saturation as pressure decreases at constant temperature, there is unfortunately no functionality to this behavior. Figure 6-19 shows the capillary pressure curves for fluids 1-6 in Table 6-2 plotted against normalized oil saturation.

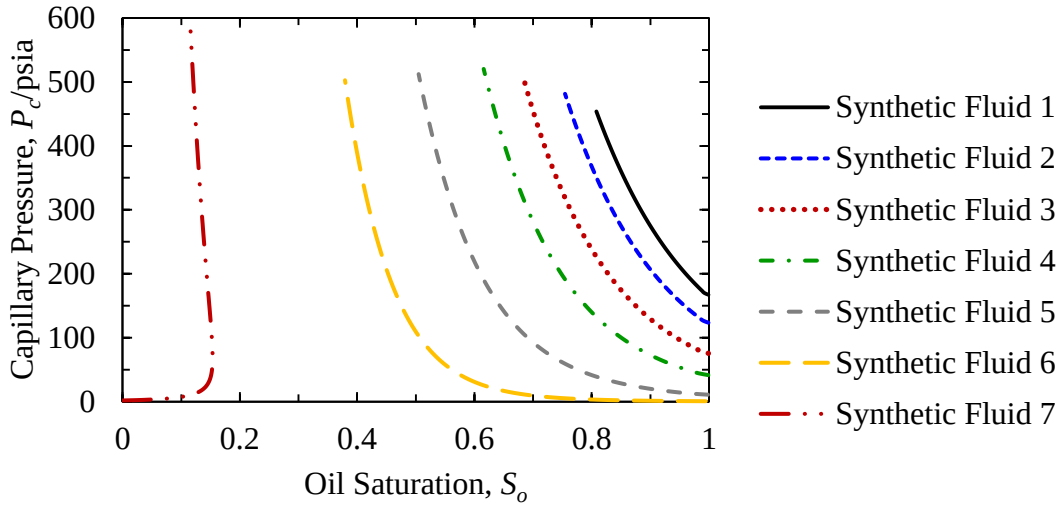

Figure 6-18. Capillary pressure curves using the CVD method for various fluid types decreasing in average molecular weight from black oil (1) to highly volatile oil (6) and a condensate (7) in a single pore size of d = 15 nm, with θ = 30°, at T = 225 °F with p_{min} = 1,000 psia.

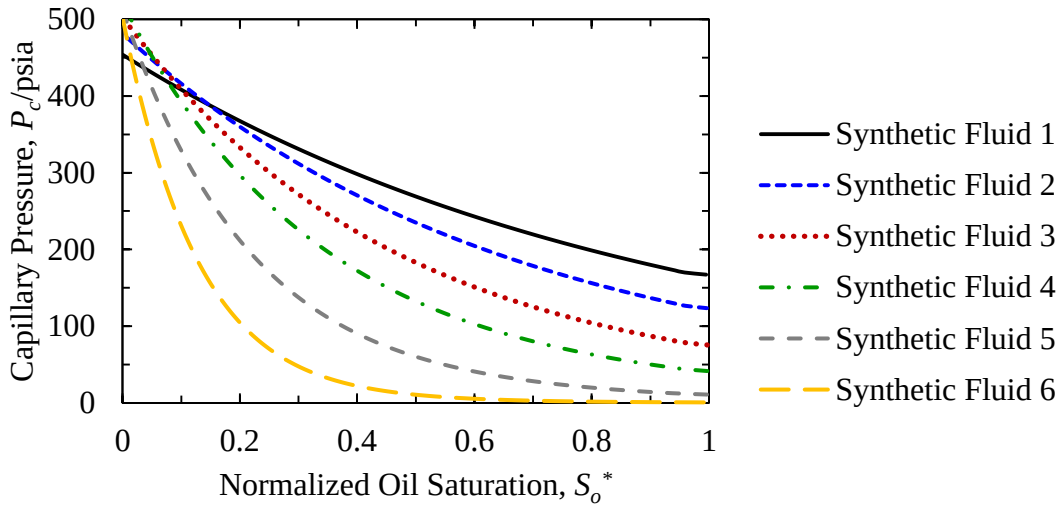

Figure 6-19. Capillary pressure curves using the CVD method plotted against normalized oil saturation for various fluid types decreasing in average molecular weight from black oil (1) to highly volatile oil (6) in a single pore size of d = 15 nm, with θ = 30°, at T = 225 °F with p_{min} = 1,000 psia.

6.3 Capillary Pressure Models

Several capillary pressure models have been developed to fit to data. These models include the models from Brooks and Corey (1964), Thomeer (1960), Bentsen and Anli (1976), and Helland and Skjæveland (2004). In addition, any function can be fit to the simulated data. These models and a rational polynomial are shown in Table 6-6.

Table 6-6. Capillary pressure models.

Model	P_c
Brooks and Corey (BC)	$P_{ct}(S_o^*)^{-1/\lambda}$
Thomeer (Th)	$P_{ct}\exp\left[\frac{-G}{\ln(S_o^*/S_\infty)}\right]$
Bentsen and Anli (BA)	$P_{ct} - P_{cs}\ln S_o^*$
Helland-Skjaeveland (HS)	$c_o(1-S_o^*)^{-a_o} + c_g(S_o^*)^{-a_g}$
Rational Polynomial (RP)	$\frac{a_1 + a_2S_o^* + a_3(S_o^*)^2 + a_4(S_o^*)^3}{1 + b_2S_o^* + b_3(S_o^*)^2}$

The capillary pressure models can be fit to the simulated data using a least-squares method. However, most capillary pressure curves tend toward infinity at the residual oil saturation. Therefore, a simple least squares regression on all data points may not provide the best fit. To show this for the models listen in Table 6-6, we performed a least squares regression including all points without fixing any constants, shown in Figure 6-20. The data are from the synthetic oil 4 in Table 6-2 at 189 °F and contact angle of 30° using the CCE method with 10 pores in a distribution with mean of 20.086 nm ($\ln\mu = 3$) and standard deviation of 0.63. The Thomeer model provides the best fit for this case and the Bentsen-Anli model is a good fit. However, the Brooks-Corey and Helland-Skjaevelland models do not result in good fits.

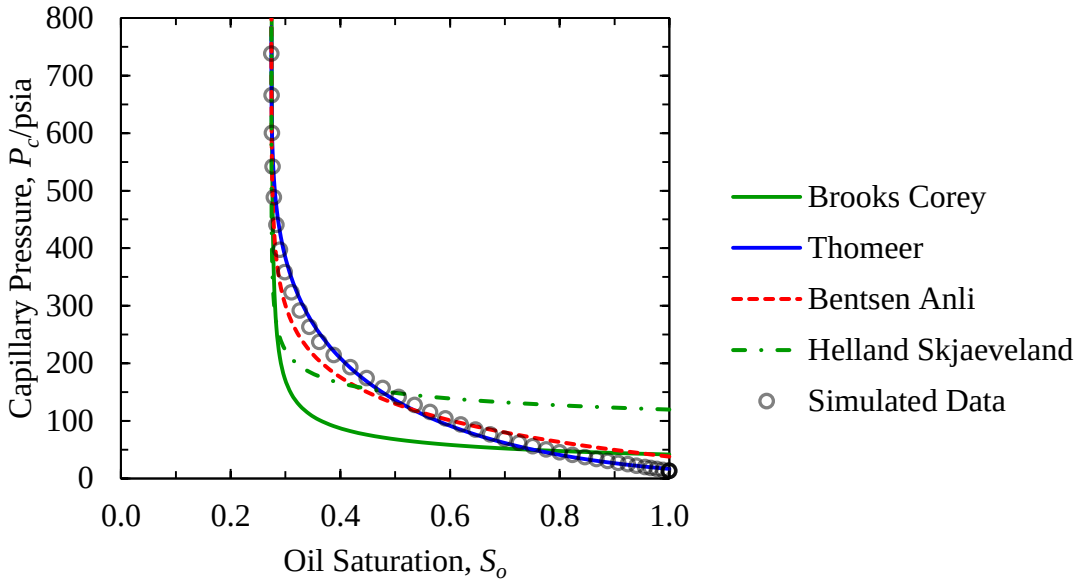

Figure 6-20. Least squares regression for capillary pressure models including all points for a CCE depletion of a mixture of 60% methane, 10% ethane, 5% n-butane, and 25% n-decane at T = 189 °F with θ = 30° in 10 pores in a distribution with μ = 20.086 nm (lnμ = 3) and σ_d = 0.63.

One way to improve the fit is to fix the P_{ct} value as the capillary pressure value at oil saturation of 1. This reduces the number of fit parameters for most models. For the Hellans-Skjaeveland model, the value of c_g is equal to the capillary pressure at oil saturation of 1. With a fixed P_{ct} value, the Thomeer model can be linearized and easily solved using a linear regression. This derivation is given in the appendix. We focus on obtaining a good fit for the lower capillary pressure values since the data and models tend toward infinity at the residual oil saturation. Figure 6-21 shows the models fit to the data with fixing the endpoint and excluding the larger capillary pressure values in the regression. To focus on the lower capillary pressure values, a log plot is useful to study the goodness of fit. Figure 6-22 shows that for lower capillary pressures, most models achieve a very good fit.

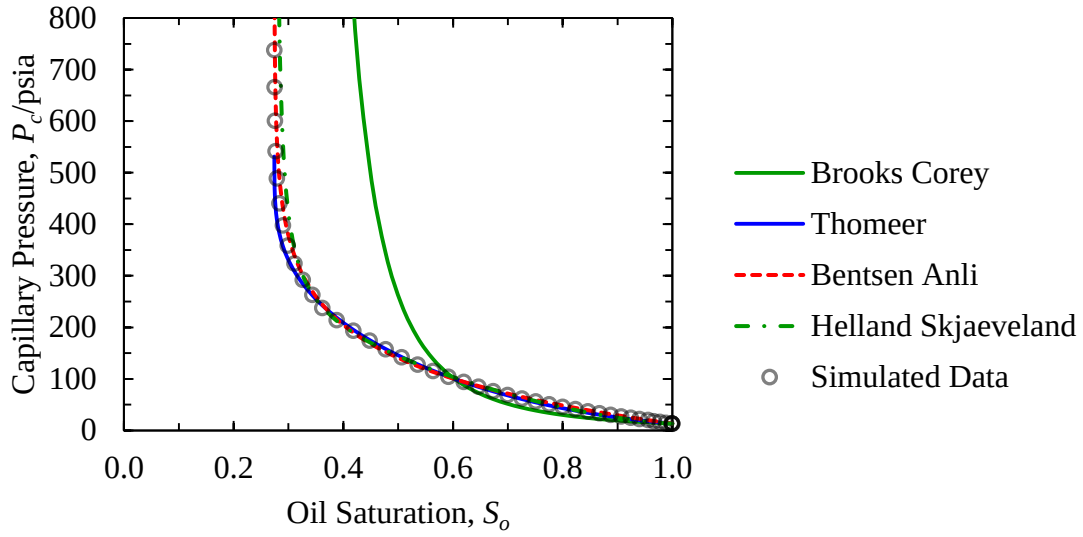

Figure 6-21. Capillary pressure curve fits of models, fixing the endpoint and excluding large capillary pressures for a CCE depletion of a mixture of 60% methane, 10% ethane, 5% n-butane, and 25% n-decane at T = 189 °F with θ = 30° in 10 pores in a distribution with μ = 20.086 nm (lnμ = 3) and σ_d = 0.63.

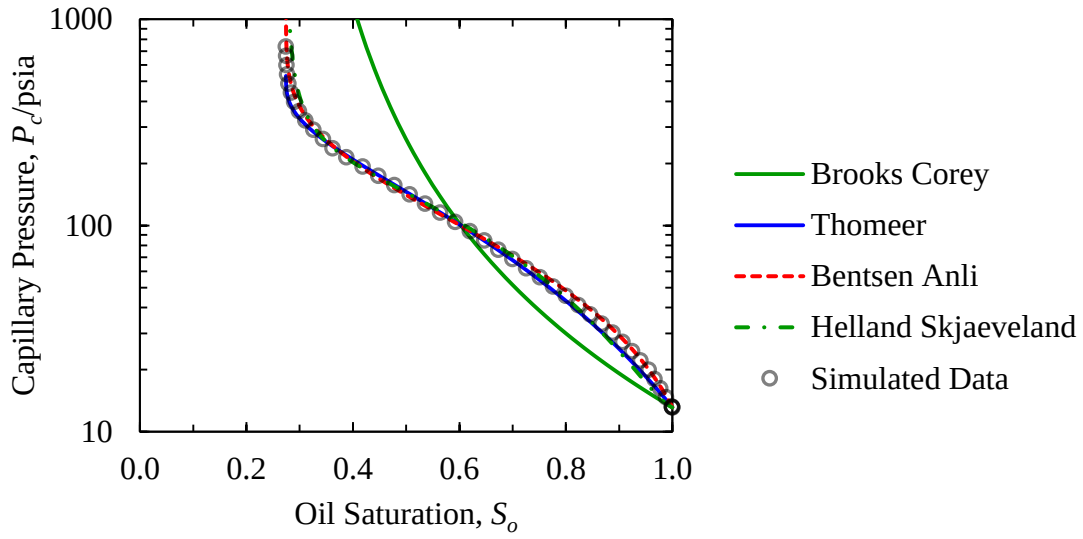

Figure 6-22. Log plot of capillary pressure data and the models fit for a CCE depletion of a mixture of 60% methane, 10% ethane, 5% n-butane, and 25% n-decane at T = 189 °F with θ = 30° in 10 pores in a distribution with μ = 20.086 nm (lnμ = 3) and σ_d = 0.63.

The constants obtained from the least squares regression for these models are shown in Table 6-7. The R^2 value is also shown for each model, which again exclude the high capillary pressure values. The Brooks-Corey model has the worst fit to this dataset, but the other models have very high R^2 values.

Table 6-7. Model constants and R^2 values obtained from least squares regression.

BC		Th		BA		HS		RP	
P_{ct}	13.11	P_{ct}	680.54	P_{ct}	13.11	c_o	189.13	a_1	625.20
λ	0.390	G	-2.954	P_{cs}	109.24	a_o	-1.504	a_2	23949.8
		S_∞	2.113			c_g	13.11	a_3	-23490.5
						a_g	0.874	a_4	2034
								b_2	81.02
								b_3	151.96
R^2	0.4124		0.9978		0.9980		0.9896		0.9999

6.4 Relative Permeability from Capillary Pressure

The relationship between capillary pressure and relative permeability was developed by Wyllie and Gardner (1958) and derived by Nakornthap and Evans (1986). The derivation is based on the connection of capillary ends to other capillaries, integrating for the entire distribution. Capillary pressure is incorporated using the Young-Laplace equation to relate pore size and capillary pressure. Relative permeabilities adapted for the oil/gas system from Nakornthap and Evans (1986) are shown in Eq. (6.16) and (6.17), where the normalized oil saturation is defined by Eq. (6.12). The assumptions made in the derivation from Nakornthap and Evans (1986), adapted to the oil/gas system are:

1. Porous media behaves as a bundle of capillary tubes with random connection of pore spaces

2. Two-phase (oil/gas) immiscible displacement
3. One-dimensional linear flow
4. Darcy's law
5. Oil-wet reservoir rock
6. Capillary tubes run parallel to the direction of flow

$$k_{ro} = (S_o^*)^2 \frac{\int_0^{S_o^*} \frac{1}{P_c^2} dS_o^*}{\int_0^1 \frac{1}{P_c^2} dS_o^*} \tag{6.16}$$

$$k_{rg} = (1 - S_o^*)^2 \frac{\int_{S_o^*}^1 \frac{1}{P_c^2} dS_o^*}{\int_0^1 \frac{1}{P_c^2} dS_o^*} \tag{6.17}$$

The oil/gas system is not completely immiscible, but for this derivation, it provides a good starting point. Interfacial tension could be included in the integral, but further development is needed to ensure IFT is properly incorporated.

The integrated relative permeabilities for the models in Table 6-6 are shown in Table 6-8. As discussed earlier, fixing the capillary pressure at S_o = 1 is very important for determining relative permeability because of the $1/P_c^2$ relationship. The larger capillary pressure values do not need as close a match because their effect is minimized. A rational polynomial is presented to provide a best fit to compare the other models. The Brooks-Corey and Bentsen-Anli models can be integrated analytically. However, the Thomeer and Helland-Skjaeveland models must be integrated numerically.

Table 6-8. Relative permeability integrated from capillary pressure models.

Model	k_{ro}	k_{rg}
BC	$(S_o^*)^{\left(2+\frac{2+\lambda}{\lambda}\right)}$	$(1-S_o^*)^2\left[1-(S_o^*)^{\frac{2+\lambda}{\lambda}}\right]$
Th	Numerical	Numerical
BA*	$(S_o^*)^2\frac{N_{BA,o}(S_o^*)}{D_{BA}}$	$(1-S_o^*)^2\frac{N_{BA,g}(S_o^*)}{D_{BA}}$
HS	Numerical	Numerical
RP	Numerical	Numerical

*

$$D_{BA}=\frac{P_{cs}}{P_{ct}}+\exp\left(\frac{P_{ct}}{P_{cs}}\right)E_i\left(-\frac{P_{ct}}{P_{cs}}\right)$$

$$N_{BA,o}(S_o^*)=\exp\left(\frac{P_{ct}}{P_{cs}}\right)E_i\left(-\frac{P_{ct}}{P_{cs}}+\ln S_o^*\right)+\frac{P_{cs}S_o^*}{P_{ct}-P_{cs}\ln S_o^*}$$

$$N_{BA,g}(S_o^*)=\exp\left(\frac{P_{ct}}{P_{cs}}\right)\left[E_i\left(-\frac{P_{ct}}{P_{cs}}\right)-E_i\left(\ln S_o^*-\frac{P_{ct}}{P_{cs}}\right)\right]+\frac{P_{cs}}{P_{ct}}-\frac{P_{cs}S_o^*}{P_{ct}-P_{cs}\ln S_o^*}$$

To determine relative permeability, either the data or a capillary pressure model can be integrated using Eq. (6.16) and Eq. (6.17). Figure 6-23 shows the relative permeability curves calculated using the models fit from the simulated data for the synthetic fluid 4 from Table 6-2. The oil relative permeability shows some minor deviations between most models, and a major deviation from the Brooks-Corey model. The gas relative permeability shows very minor deviations between the models. The rational polynomial is taken to be the most accurate calculation.

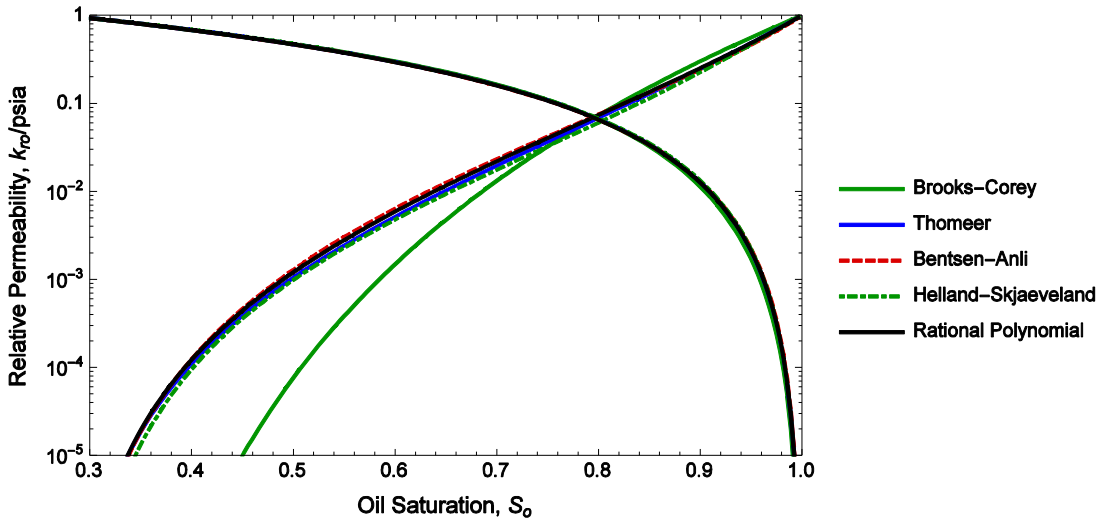

Figure 6-23. Relative permeability calculated from capillary pressure models for a CCE depletion of a mixture of 60% methane, 10% ethane, 5% n-butane, and 25% n-decane at T = 189 °F with θ = 30° in 10 pores in a distribution with μ = 20.086 nm (lnμ = 3) and σ_d = 0.63.

The CCE and CVD capillary pressure curves yield different relative permeability curves. The relative permeability curves from the capillary pressure curve in Figure 6-15 are shown in Figure 6-24. However, when calculated and plotted versus the normalized oil saturation, the relative permeability curves match very closely, as shown in Figure 6-25. This consistency reduces the uncertainty to the establishment of residual oil saturation.

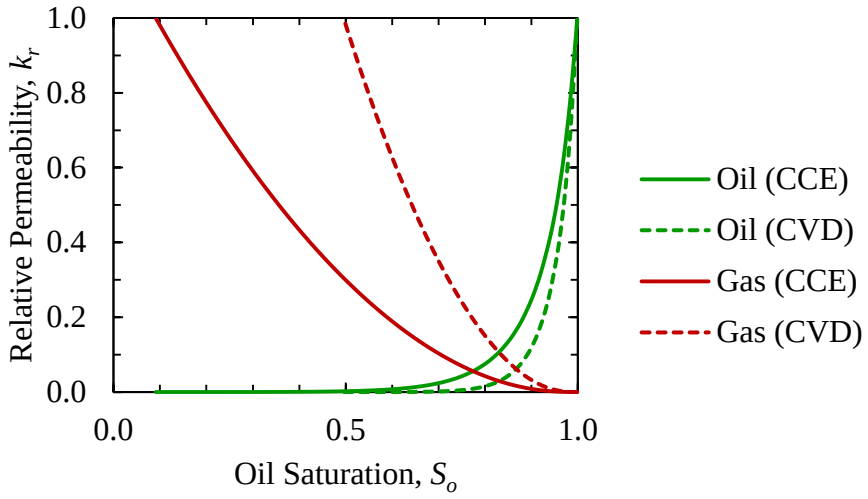

Figure 6-24. Comparison of CCE and CVD relative permeabilities for a mixture of 60% methane, 10% ethane, 5% n-butane, and 25% n-decane at T = 189 °F for a distribution with μ = 20.086 nm ($\ln\mu$ = 3) and σ = 0.63.

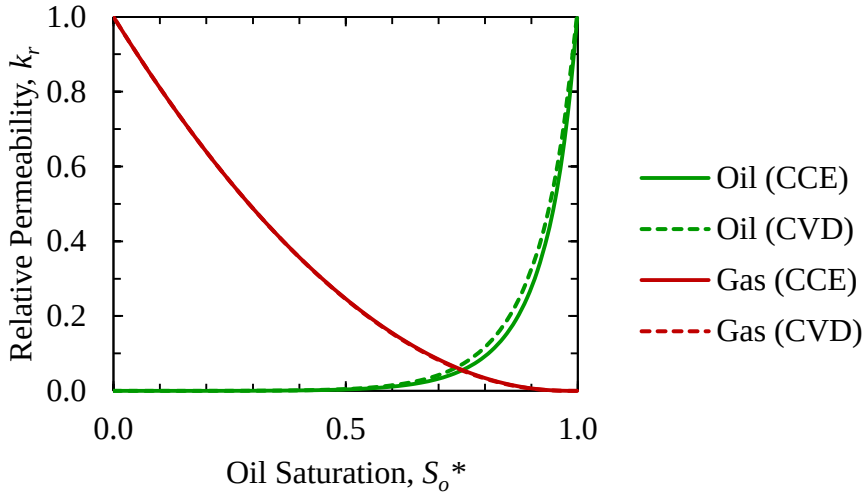

Figure 6-25. Oil and gas relative permeability curves plotted against normalized oil saturation for a mixture of 60% methane, 10% ethane, 5% n-butane, and 25% n-decane at T = 189 °F for a distribution with μ = 20.086 nm ($\ln\mu$ = 3) and σ = 0.63.

One other aspect is the effect of a pore size distribution on relative permeability. This was studied by Jin et al. (2015), who showed that including a pore size distribution generally lowered the relative permeability. Figure 6-26 shows that when including a pore size distribution, relative permeability changes and generally decreases.

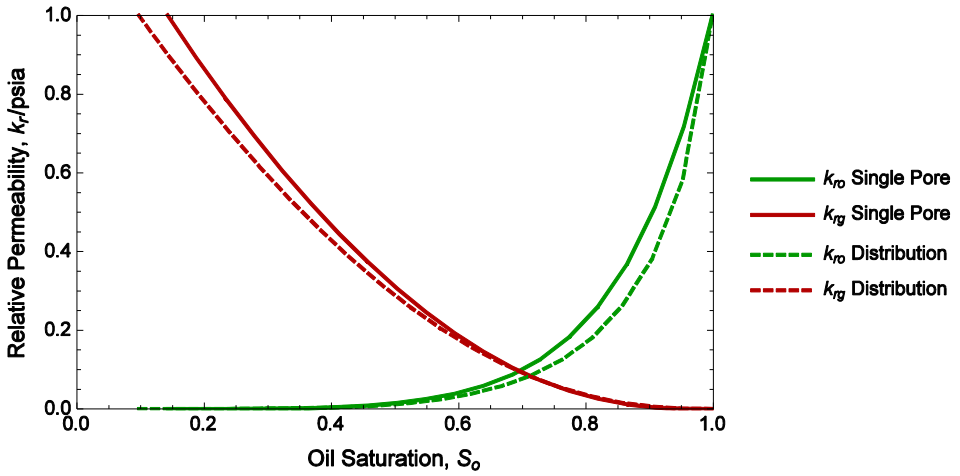

Figure 6-26. Relative permeability with and without pore size distribution.

We also examine how relative permeability changes with fluid type. For the synthetic oils, corresponding to the capillary pressure curves in Figure 6-18, we calculate the relative permeability using the CVD method. These relative permeabilities are shown in Figure 6-27. At high oil saturations, the oil relative permeabilities are very similar. At lower oil saturation, the lighter oils have higher oil relative permeability and lower gas relative permeability than the heavier oils. When plotted against normalized oil saturation, as shown in Figure 6-28, the effects are somewhat opposite.

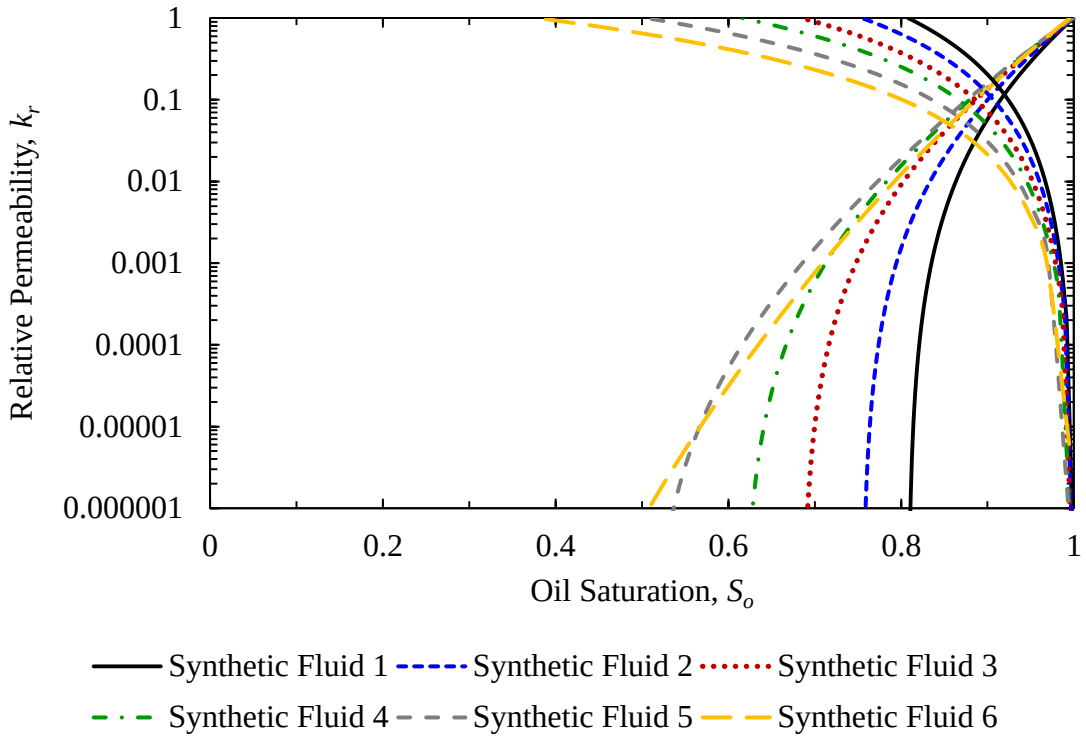

Figure 6-27. Oil and gas relative permeabilities using the CVD method for various fluids in a single pore size of d = 15 nm, with θ = 30°, at T = 225 °F with p_{min} = 1,000 psia.

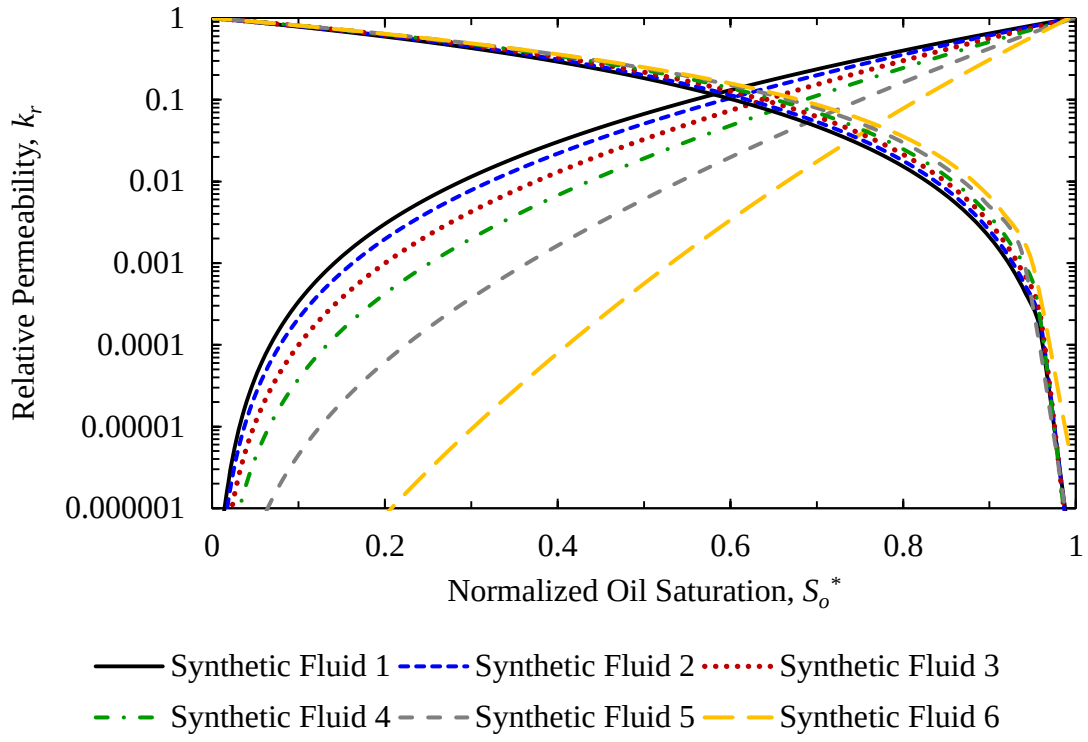

Figure 6-28. Oil and gas relative permeabilities using the CVD method plotted against normalized oil saturation for various fluids in a single pore size of d = 15 nm, with θ = 30°, at T = 225 °F with p_{min} = 1,000 psia.

6.5 Residual Oil Saturation

The major factor in the residual oil saturation using this method is the minimum pressure specified. Due to phase behavior, if the minimum pressure is high, then the residual oil saturation will also be high. However, if the minimum pressure is lower, the residual oil saturation will also be low. This can be seen in Figure 6-29 and Figure 6-30, which show capillary pressure curves for a distribution of pores using the CVD and CCE methods. Since relative permeability is dependent on integration of the entire curve, the relative permeabilities will change based on the minimum pressure selected. Figure 6-31 and Figure 6-33 show that for lower minimum pressure, the residual oil saturation decreases for the CVD and CCE methods, respectively. Figure 6-32 and Figure 6-34 show that when

plotted against normalized oil saturation, the gas relative permeabilities match and seem to be independent of minimum pressure. The oil relative permeabilities seem to be slightly lower with a lower minimum pressure.

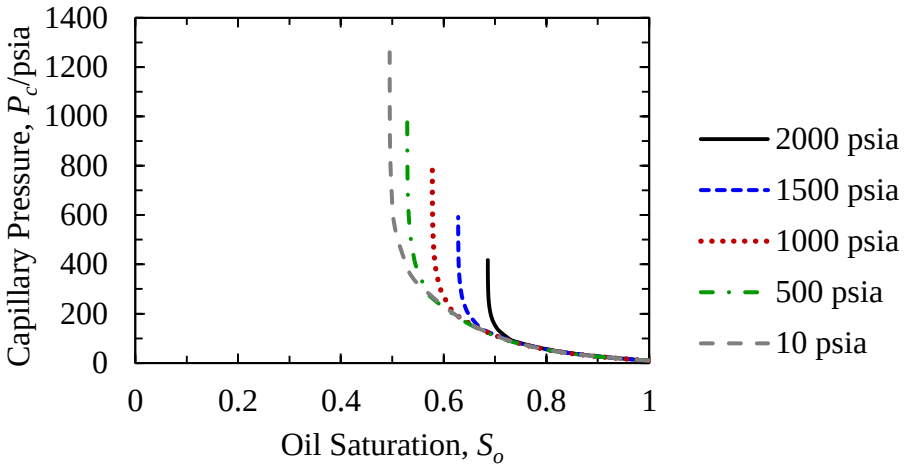

Figure 6-29. CVD capillary pressure curves with various minimum pressures for a mixture of 60% methane, 10% ethane, 5% n-butane, and 25% n-decane for T = 225 °F, d = 15 nm, and θ = 30°.

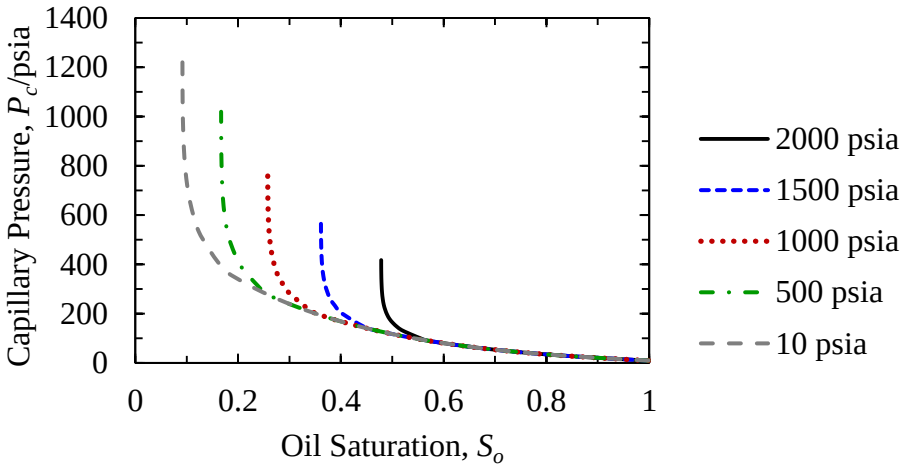

Figure 6-30. CCE capillary pressure curves with various minimum pressures for a mixture of 60% methane, 10% ethane, 5% n-butane, and 25% n-decane for T = 225 °F, d = 15 nm, and θ = 30°.

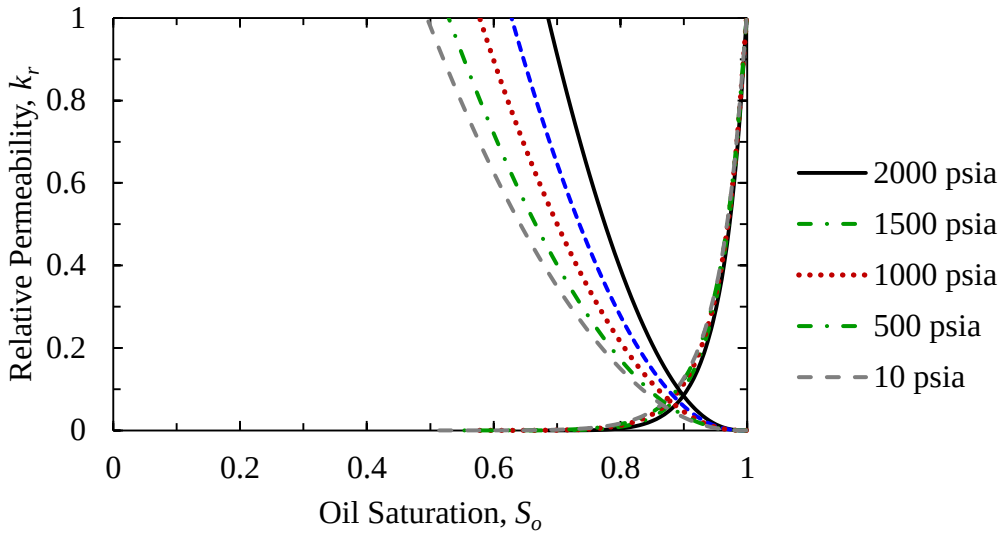

Figure 6-31. Relative permeabilities with various minimum pressure using the CVD method for a mixture of 60% methane, 10% ethane, 5% n-butane, and 25% n-decane for T = 225 °F, d = 15 nm, and θ = 30°.

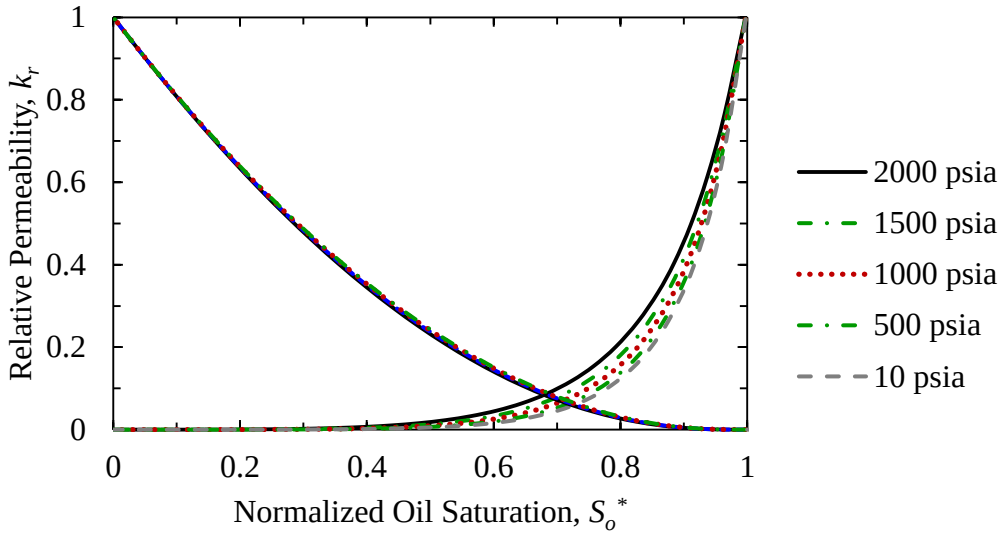

Figure 6-32. Relative permeabilities with various minimum pressures using the CVD method plotted against normalized oil saturation for a mixture of 60% methane, 10% ethane, 5% n-butane, and 25% n-decane for T = 225 °F, d = 15 nm, and θ = 30°.

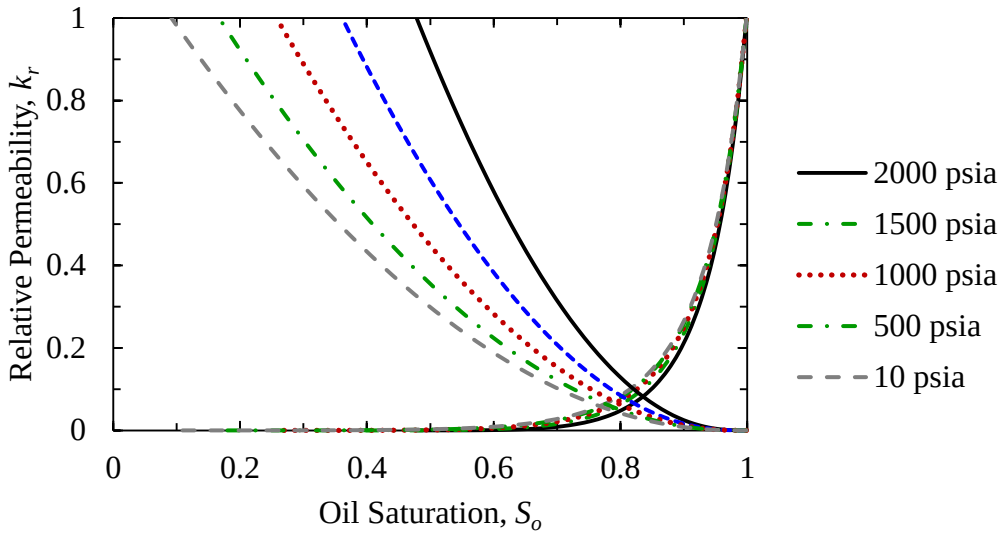

Figure 6-33. Relative permeabilities with various minimum pressure using the CCE method for a mixture of 60% methane, 10% ethane, 5% n-butane, and 25% n-decane for T = 225 °F, d = 15 nm, and θ = 30°.

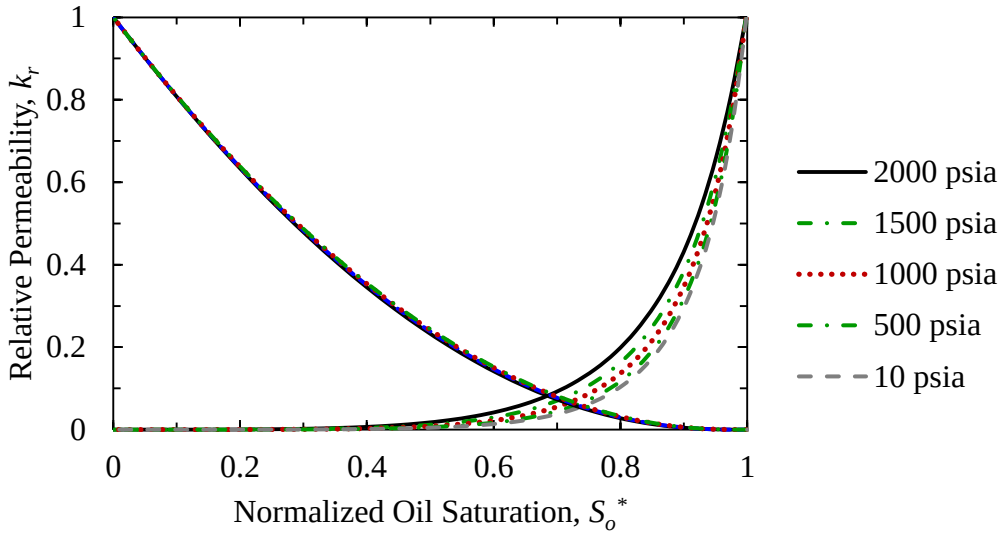

Figure 6-34. Relative permeabilities with various minimum pressures using the CCE method plotted against normalized oil saturation for a mixture of 60% methane, 10% ethane, 5% n-butane, and 25% n-decane for T = 225 °F, d = 15 nm, and θ = 30°.

6.6 Capillary Pressure Comparison with Simulation Results

Capillary pressure in the reservoir using the rigorous method is free to reach equilibrium independent of oil saturation. Therefore, a fixed capillary pressure curve as a function of oil saturation for all points in the reservoir is not consistent. This is due to compositional changes that occur throughout two-phase production. We performed simulations to study how closely capillary pressure at all points follows a capillary pressure curve in a homogeneous reservoir. The reservoir is the same shown in Figure 5-1 with the properties listed in Table 6-9 and the synthetic fluid 4 in Table 6-2. During the transient period, capillary pressures in the reservoir generally follow a consistent curve, as seen in Figure 6-35. A similar effect studied analytically by Zhang and Ayala (2016) shows that compositions follow a prescribed trend throughout the transient period. Once transient flow ends, the capillary pressures deviate from the constant composition line toward the gas depletion curve, as seen in Figure 6-36. As expected, the capillary pressure throughout the reservoir generally lies between the CCE and CVD capillary pressure curves for this case.

Table 6-9. Reservoir properties for simulation to compare with capillary pressure from CCE and CVD methods.

Grid Size	Cell Dimensions	p_i (psia)	k (md)	ϕ	d (nm)	θ (°)	T (°F)	BHP (psia)
25x25x1	50x50x100	4,000	0.01	0.1	15	30	189	1,000

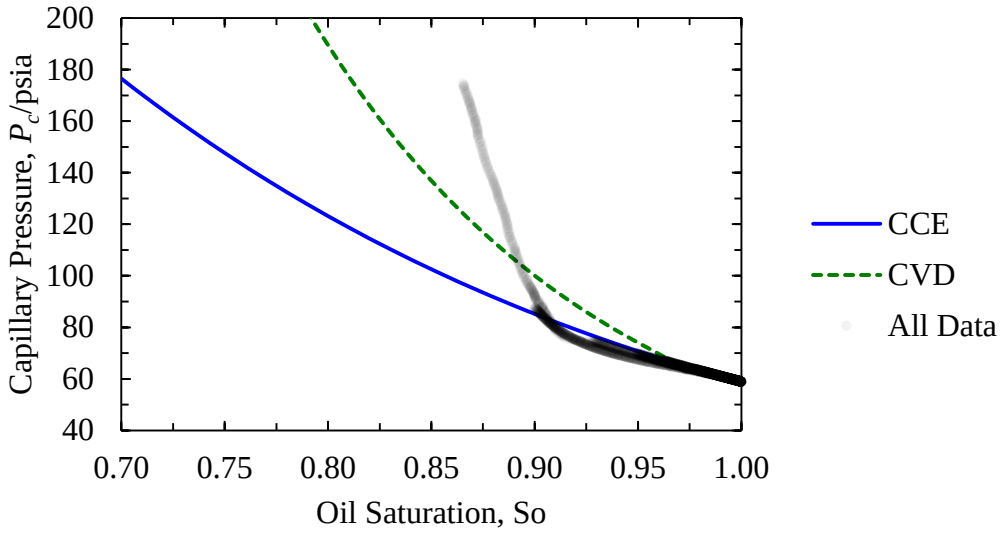

Figure 6-35. All capillary pressures as a function of oil saturation for the transient period of production, up to 13 years.

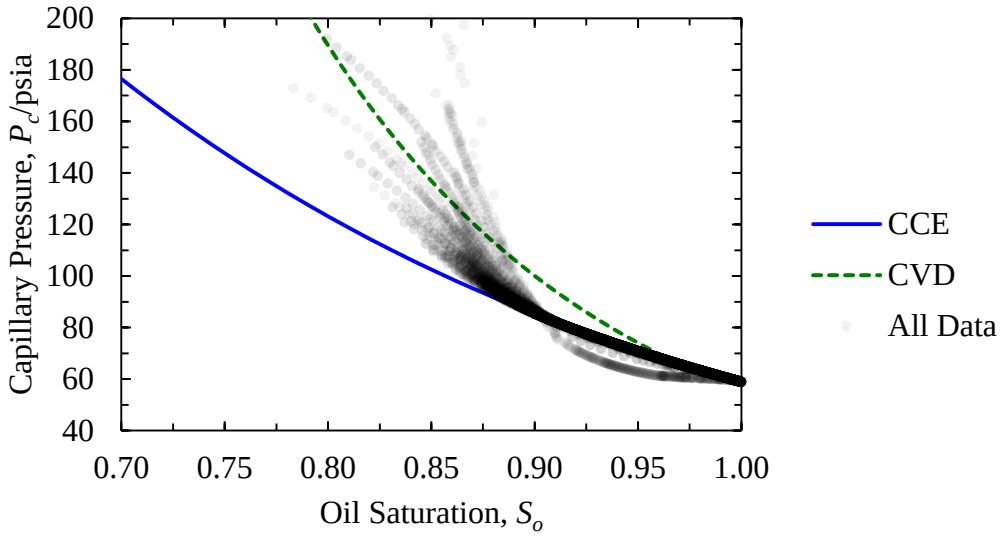

Figure 6-36All capillary pressures as a function of oil saturation for all time, up to 26 years of production.

6.7 Reservoir Simulations with Relative Permeability Inputs

We performed simulations for an Eagle Ford oil characterized by Whitson and Sunjerga (2012) and simplified in Table 6-13 and

Table 6-14 in the reservoir shown in Figure 5-1. We ran up to six variations for each case run. The variations include two main options: (1) with or without capillary pressure, and (2) relative permeability method from the constant composition (CC) method, the gas depletion (GD) method (same as CVD method), or a straight-line (SL) relationship.

Table 6-10. Consistent reservoir parameters.

k (md)	d (nm)	θ (°)	T (°F)	BHP (psia)
0.001	20	0	225	1,000

Table 6-11. Variations of each case.

Variation	Relative Permeability	Capillary Pressure
a	CC	No
b	CC	Yes
c	GD	No
d	GD	Yes
e	SL	No
f	SL	Yes

Table 6-12. Reservoir description of simulation runs.

Case	Grid Size	Cell Size (ft)	p_i (psia)	Variations
1	25x25	70x70x70	6,000	a-d
2	25x25	70x70x70	5,000	a-f
3	19x19	30x30x100	4,150	a-f

Table 6-13. Simplified Eagle Ford oil from the full characterization given on p. 131 from Whitson and Sunjerga (2012).

Species	z_i	M_i	$p_{c,i}$ (psia)	$T_{c,i}$ (°F)	ω_i	s_i	P_i
CO_2	0.0232	44.01	1069.5	87.73	0.225	0.2175	82.00
C_1	0.5816	16.04	667.0	-116.67	0.011	-0.0025	74.05
C_2	0.0744	30.07	706.6	89.93	0.099	0.0589	112.91
C_3	0.0417	44.1	616.1	206.03	0.152	0.0908	154.03
C_4	0.0259	58.12	542.19	294.00	0.1948	0.1100	189.30
C_{5-6}	0.0269	76.502	489.75	414.41	0.2398	0.1197	247.57
C_{7+}	0.1321	122.96	392.81	632.37	0.3548	0.1723	402.33
C_{13+}	0.0942	255.28	226.23	941.29	0.7408	0.2877	834.82

Table 6-14. Binary interaction parameters for the simplified Eagle Ford fluid in Table 6-13.

Species	CO_2	C_1	C_2	C_3	C_4	C_{5-6}	C_{7+}	C_{13+}
CO_2	0.00	0.12	0.12	0.12	0.12	0.12	0.10	0.10
C_1	0.12	0.00	0.00	0.00	0.00	0.00	0.00	0.00
C_2	0.12	0.00	0.00	0.00	0.00	0.00	0.00	0.00
C_3	0.12	0.00	0.00	0.00	0.00	0.00	0.00	0.00
C_4	0.12	0.00	0.00	0.00	0.00	0.00	0.00	0.00
C_{5-6}	0.12	0.00	0.00	0.00	0.00	0.00	0.00	0.00
C_{7+}	0.10	0.00	0.00	0.00	0.00	0.00	0.00	0.00
C_{13+}	0.10	0.00	0.00	0.00	0.00	0.00	0.00	0.00

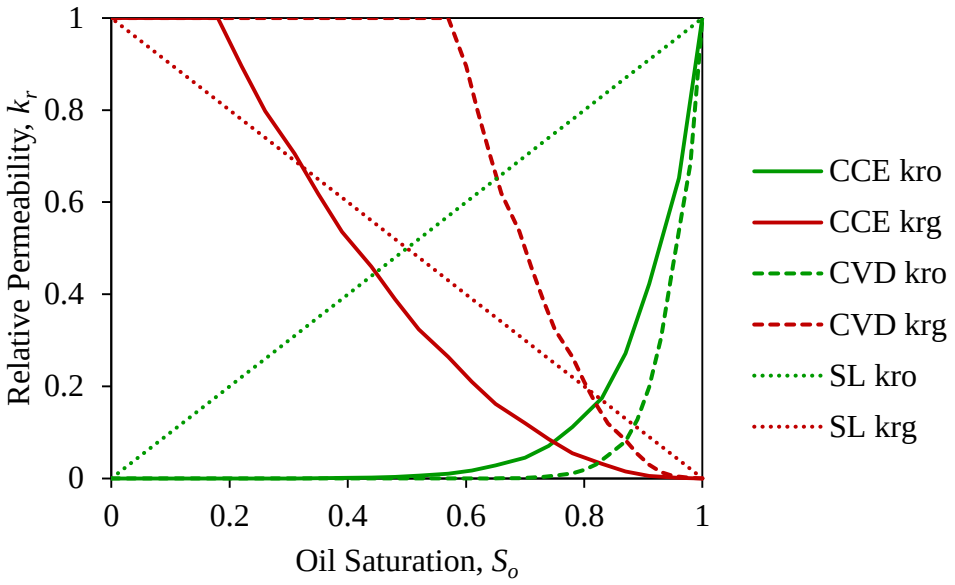

Figure 6-37. Relative permeabilities of cases a-f.

6.7.1 Case 1: Eagle Ford Oil with High Initial Pressure

The oil and gas production rates for variations a-d are shown in Figure 6-38 and Figure 6-39, respectively. Cumulative oil and gas production are shown in Figure 6-40 and Figure 6-41, respectively. These results show that even when the difference between initial reservoir pressure and saturation pressure is large, capillary pressure makes a significant impact on production. Much of this is due to a suppression of bubble pressure, which keeps reservoir production in single phase for a longer time. In addition, once two-phase flow is achieved near the wellbore, relative permeability effects may play a factor, though in these simulations, the difference is very small.

Due to longer single phase oil production from the reservoir, the reservoir pressure decreases faster than when not considering confinement. This is seen in Figure 6-42. Average gas saturation is very low for this case, but also varies between all cases. The cases with capillary pressure have a lower gas saturation (higher oil saturation), as seen in Figure 6-43. The case with constant composition relative permeabilities has higher gas

saturation. This is due to the higher oil relative permeability depleting oil quicker than the case with gas depletion relative permeabilities. Figure 6-44 shows the average capillary pressure in the reservoir for the two runs that considered capillary pressure. The difference between the two is very minimal, but the constant composition case has higher capillary pressure. Figure 6-45 shows the pressure distribution and average reservoir pressure for the four cases after 70 years of production.

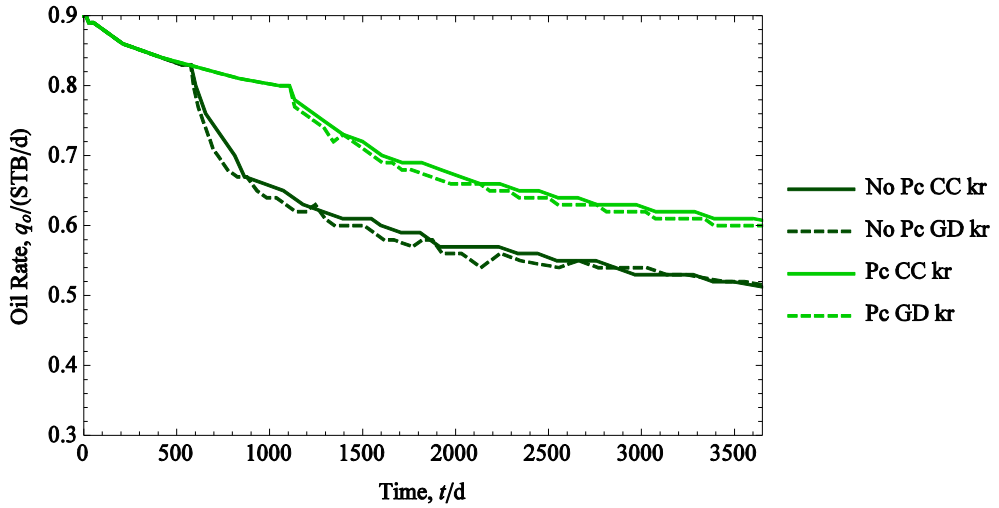

Figure 6-38. Oil production rate from an Eagle Ford oil reservoir with high initial pressure.

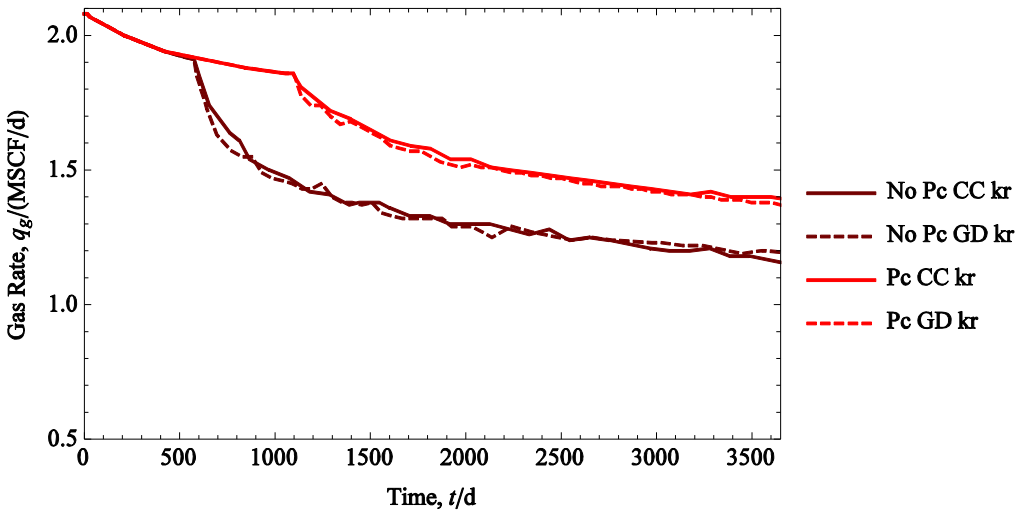

Figure 6-39. Gas production rate from an Eagle Ford oil reservoir with high initial pressure.

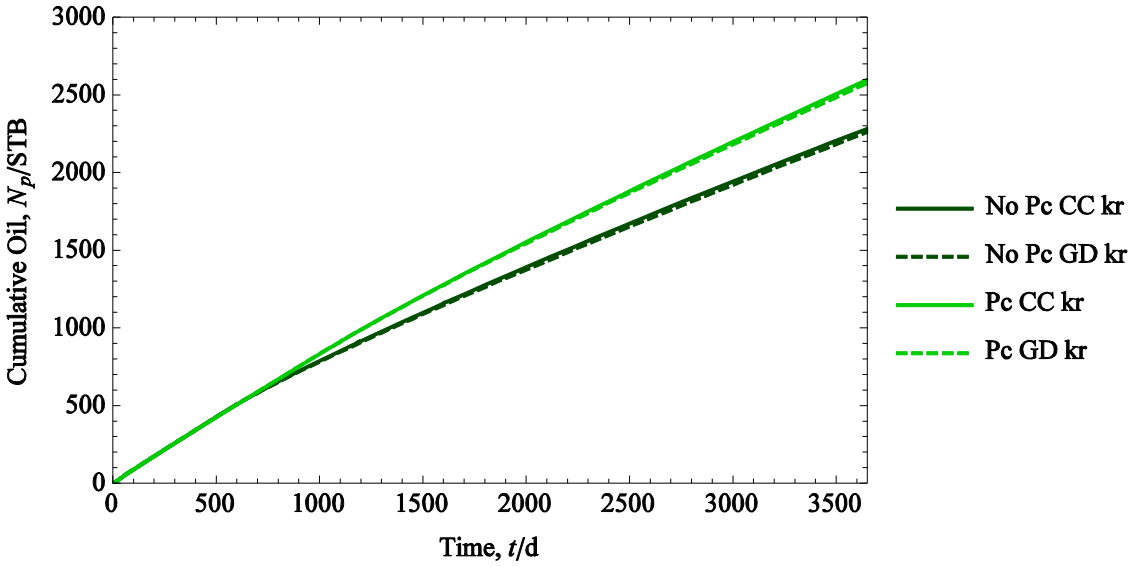

Figure 6-40. Cumulative oil production from an Eagle Ford oil reservoir with high initial pressure.

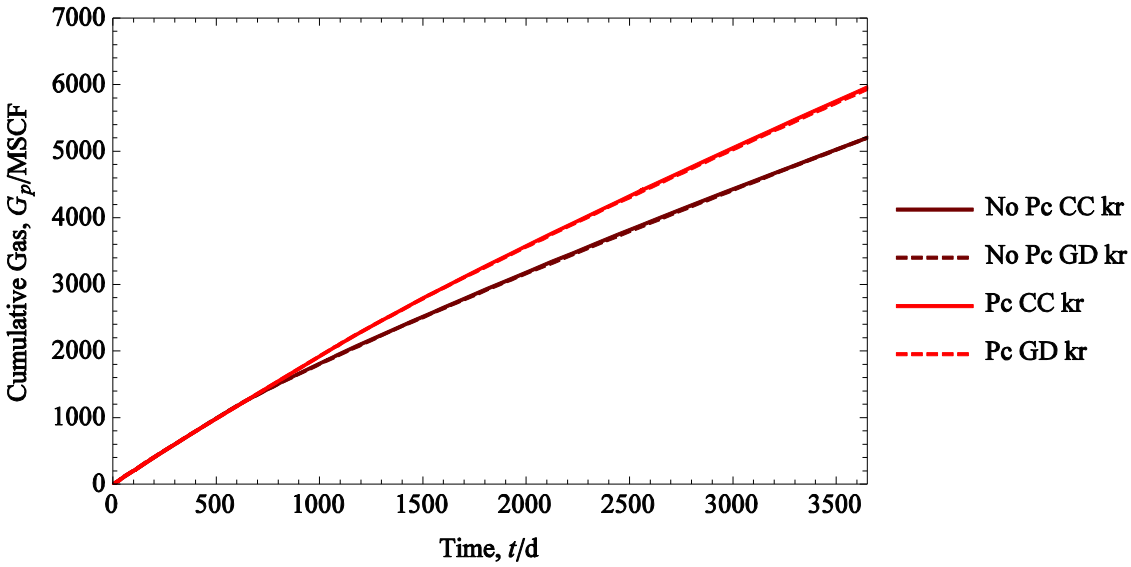

Figure 6-41. Cumulative gas production from an Eagle Ford oil reservoir with high initial pressure.

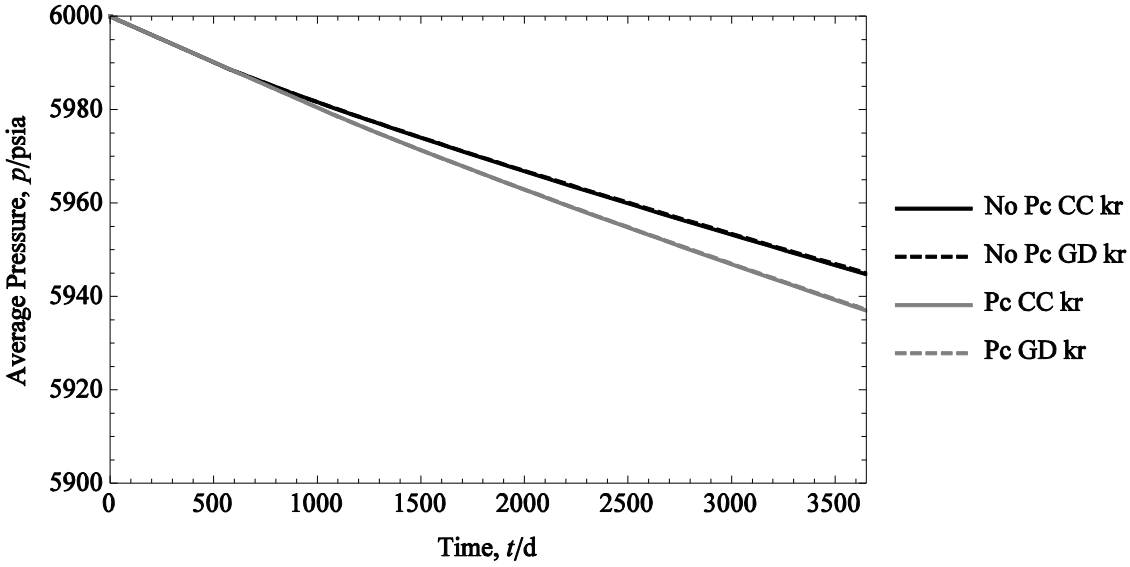

Figure 6-42. Average pressure of an Eagle Ford oil reservoir with high initial pressure.

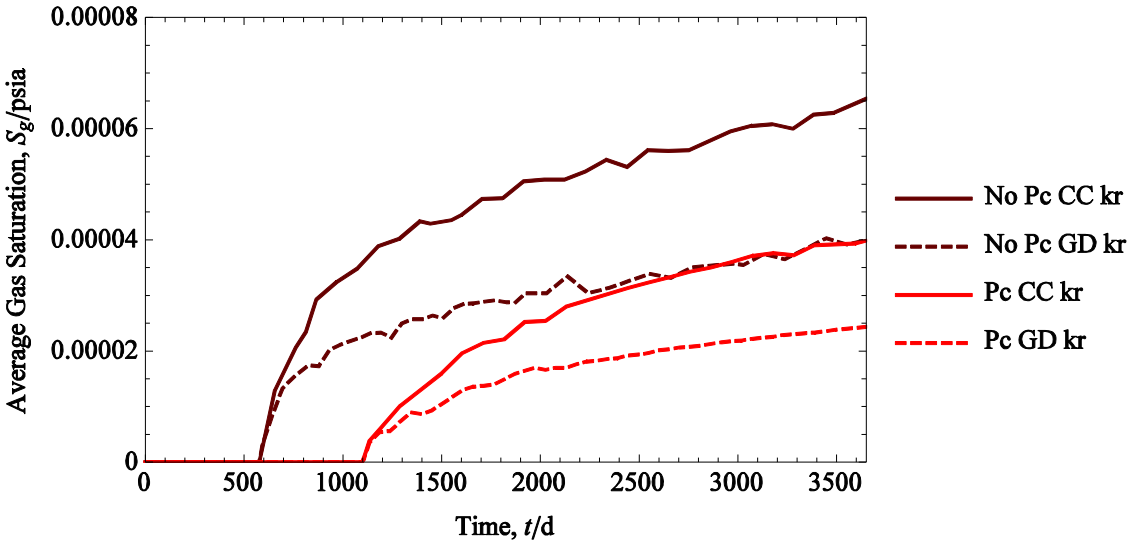

Figure 6-43. Average gas saturation of an Eagle Ford reservoir with high initial pressure.

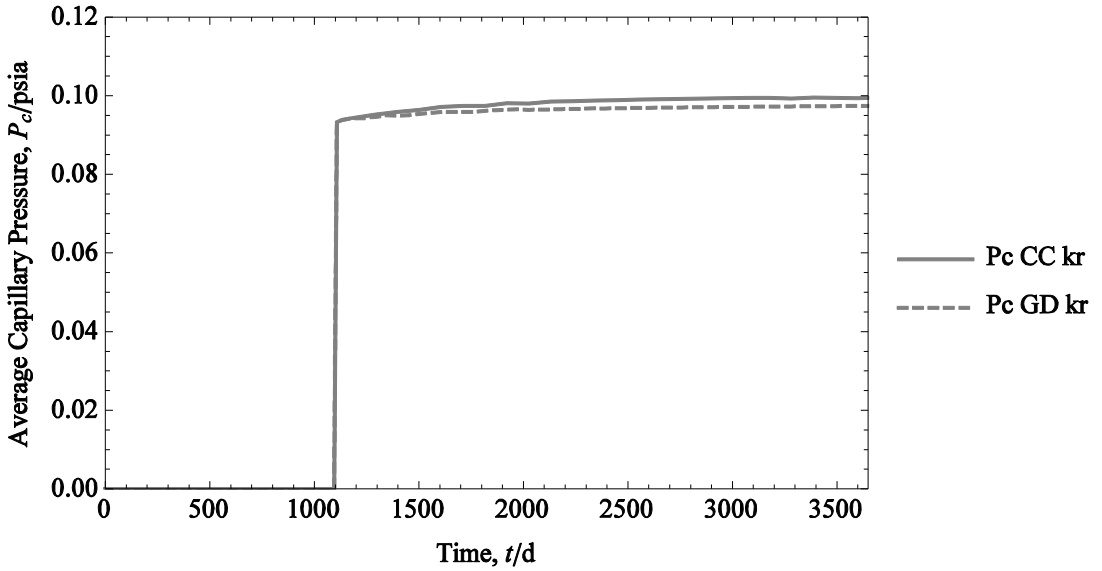

Figure 6-44. Average capillary pressure in an Eagle Ford oil reservoir with high initial pressure.

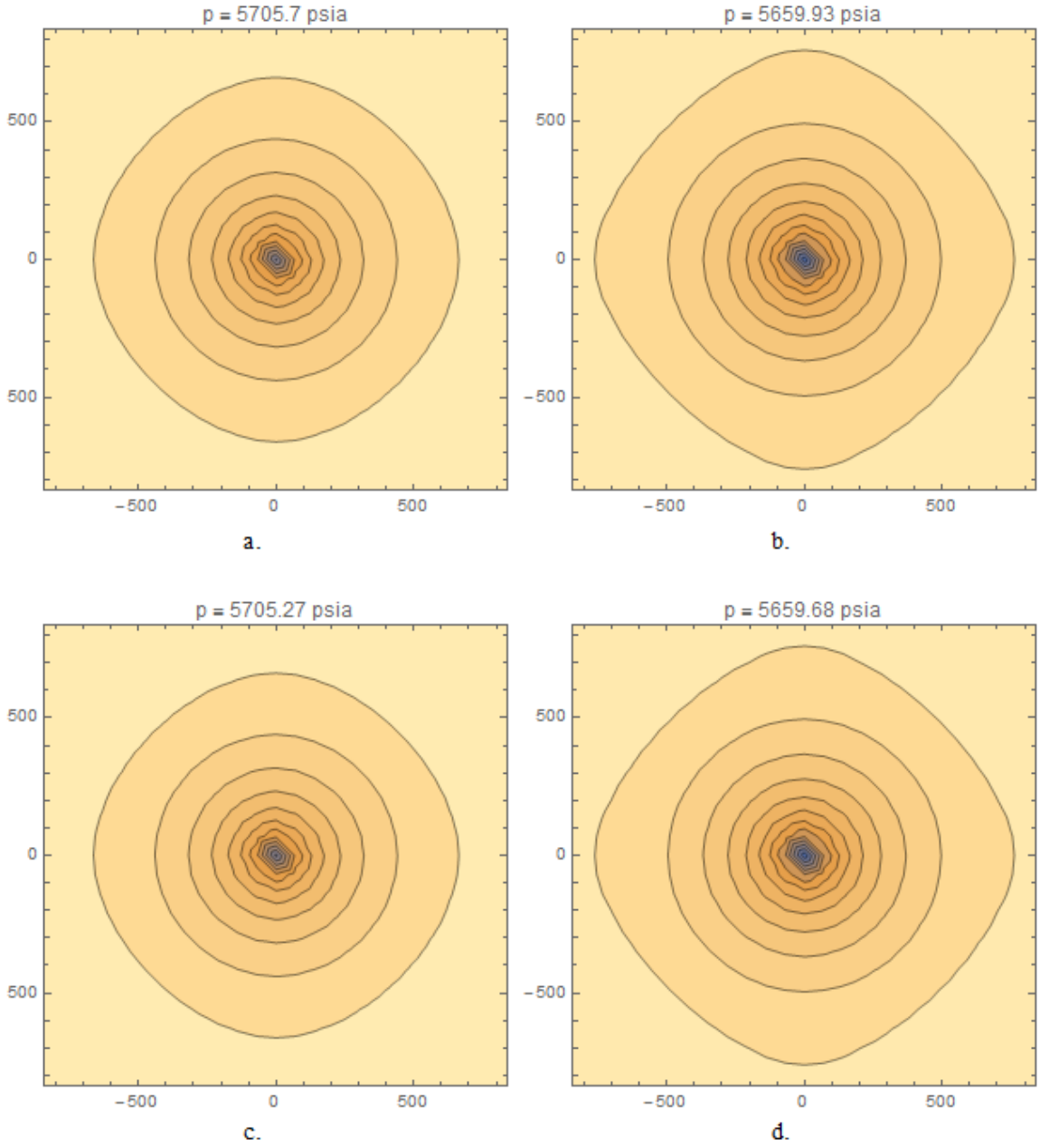

Figure 6-45. Pressure distribution in an Eagle Ford oil reservoir with high initial pressure for case 1 and all variations after 70 years of production.

6.7.2 Case 2: Eagle Ford Oil with Middle Initial Pressure

To see the effects of the relative permeability methods, a lower initial pressure was selected so that two-phase flow would be achieved sooner. In addition, we used the straight-line relative permeabilities as a case.

Figure 6-46 and Figure 6-47 show the oil and gas production rates. The constant composition relative permeabilities show higher oil and gas rates compared to the gas depletion relative permeability cases. This can be seen by higher oil cumulative production in Figure 6-48. The cumulative gas production in Figure 6-49 shows little difference between relative permeability methods since at high oil saturations, the gas relative permeability is nearly zero. The straight line relative permeability methods show higher oil production, but lower gas production when considering confinement.

The average reservoir pressure is shown in Figure 6-50, showing similar results as the first case. Average gas saturation is shown in Figure 6-51, which also shows lower gas saturation (higher oil saturation) for the cases when considering capillary pressure. Capillary pressure in Figure 6-52 is slightly higher for the constant composition relative permeability case. The straight-line method shows some variation in capillary pressure and gas saturation. Since the fluids are considered miscible, the overall compositions are changing much more rapidly than the other two methods, resulting in the abnormal behavior of saturation and capillary pressure. Figure 6-53 shows the pressure distribution of all cases. The gas saturation is so small that no apparent difference appears on similar plots.

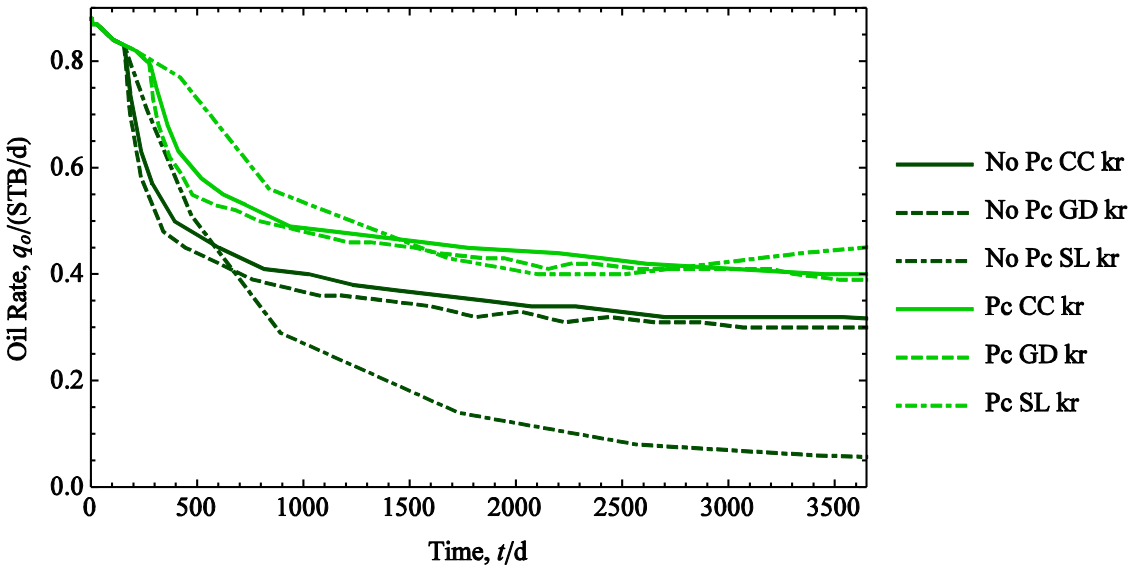

Figure 6-46. Oil production rate for an Eagle Ford oil reservoir with 5,000 psia initial reservoir pressure.

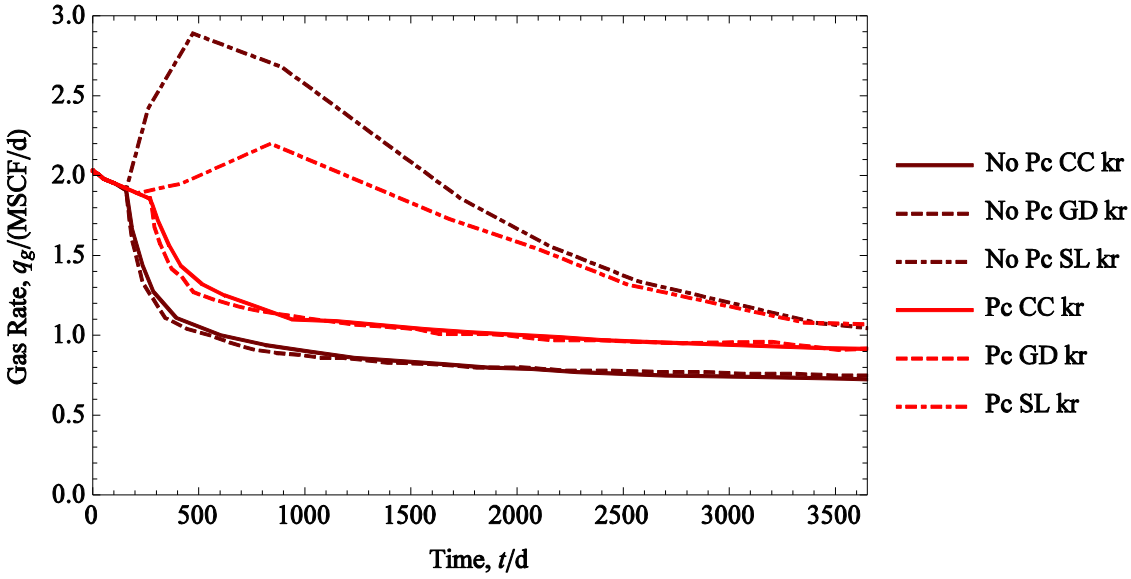

Figure 6-47. Gas production rate for an Eagle Ford oil reservoir with 5,000 psia initial reservoir pressure.

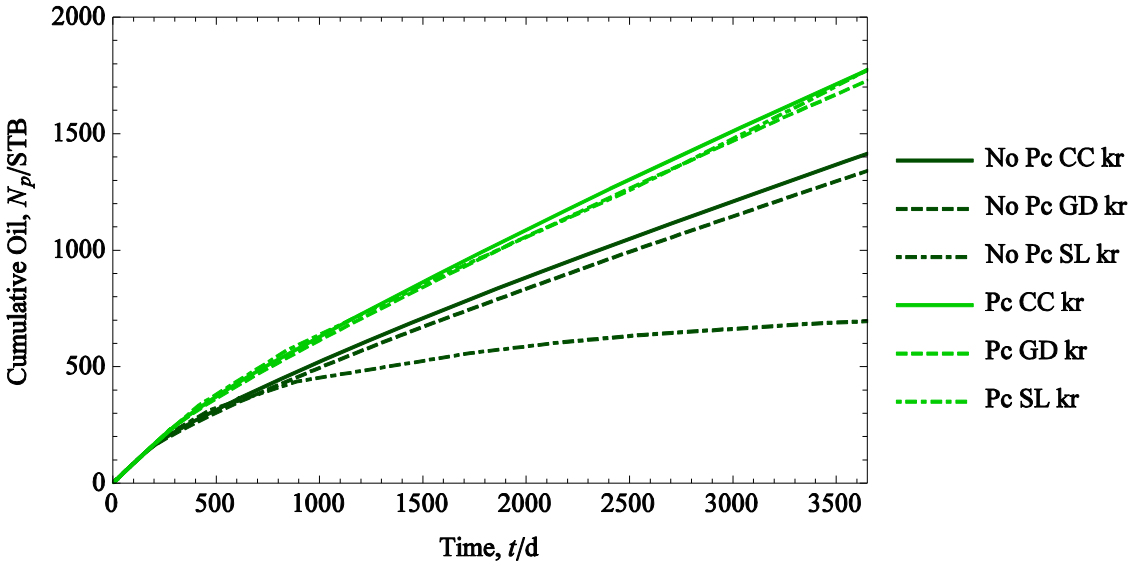

Figure 6-48. Cumulative oil production for an Eagle Ford oil reservoir with 5,000 psia initial reservoir pressure.

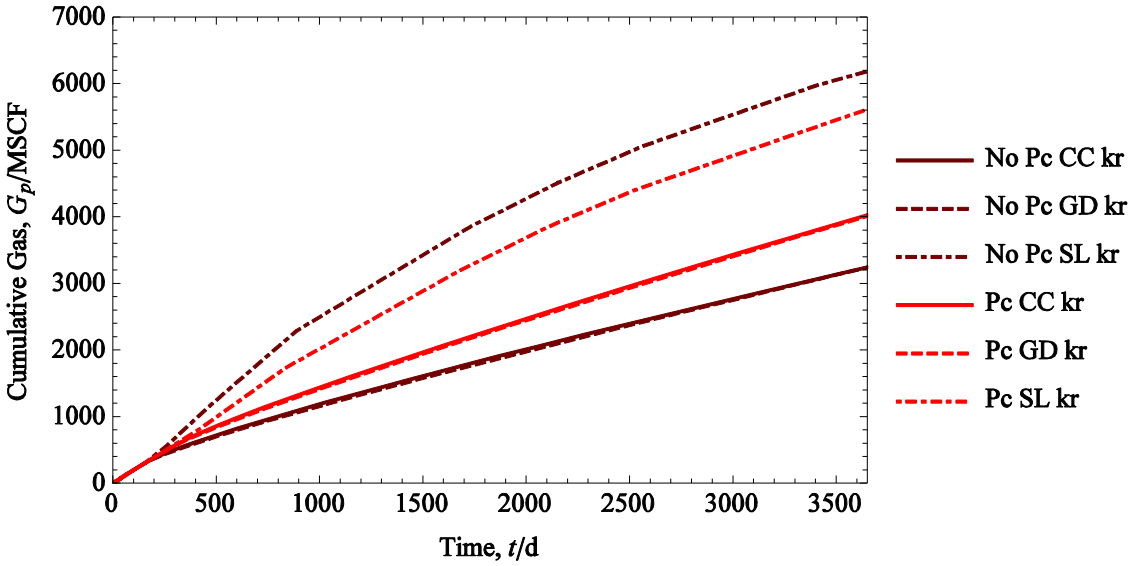

Figure 6-49. Cumulative gas production for an Eagle Ford oil reservoir with 5,000 psia initial reservoir pressure.

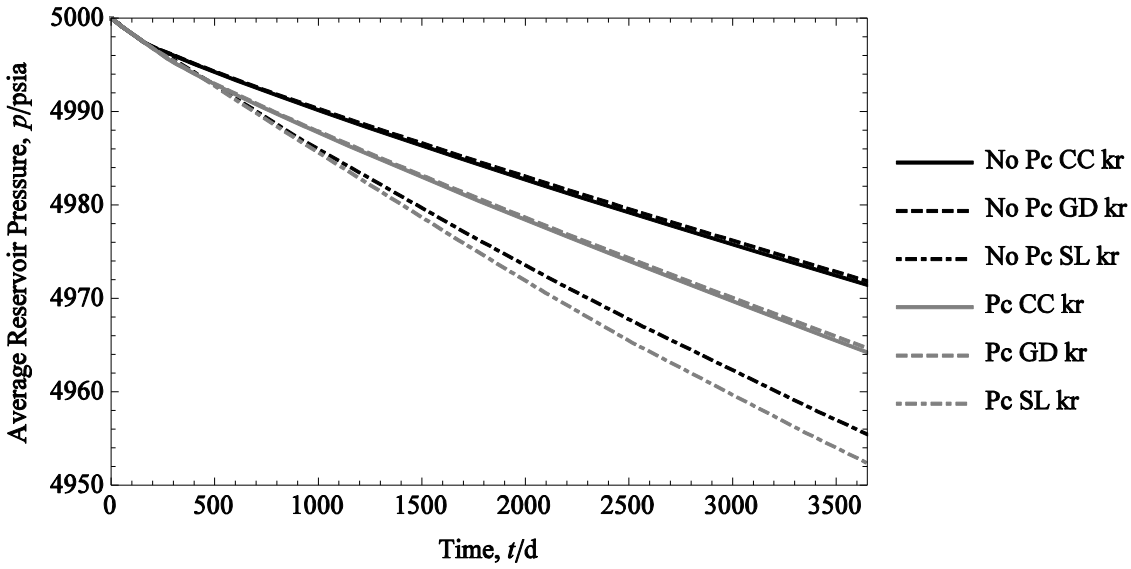

Figure 6-50. Average reservoir pressure for an Eagle Ford oil reservoir with 5,000 psia initial reservoir pressure.

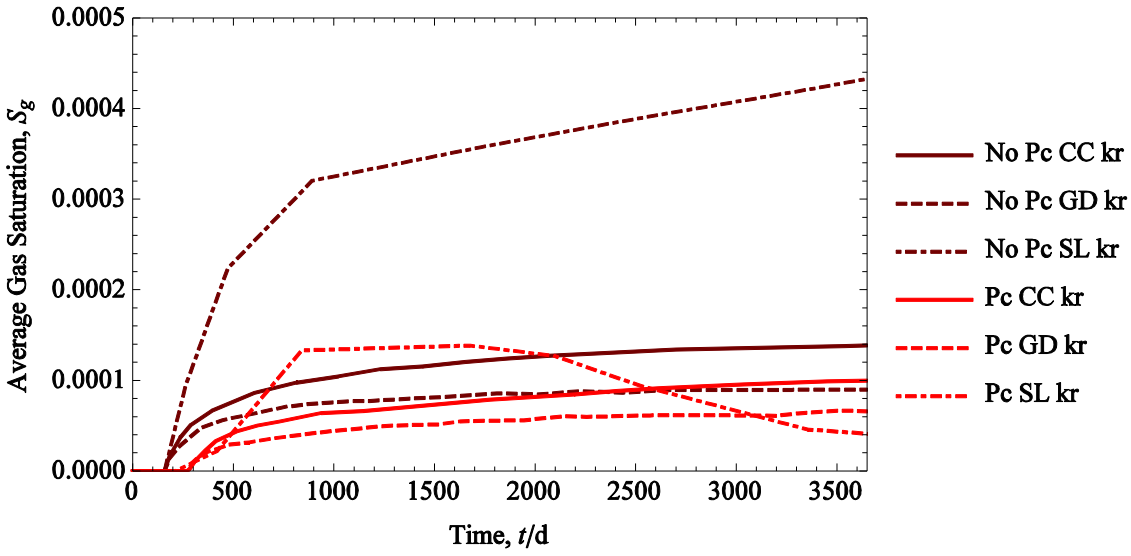

Figure 6-51. Average gas saturation for an Eagle Ford oil reservoir with 5,000 psia initial reservoir pressure.

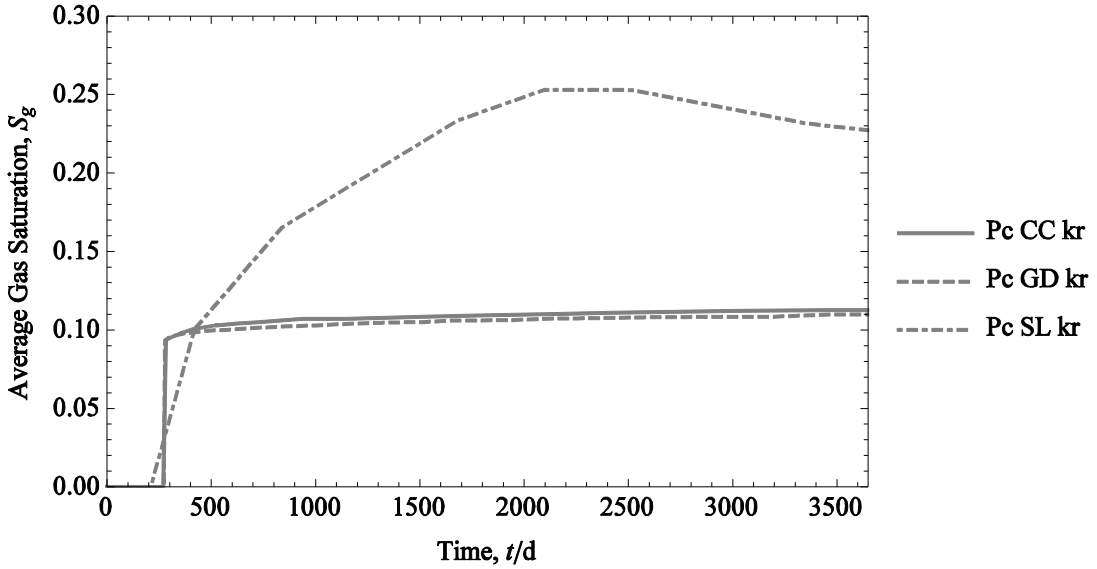

Figure 6-52. Average capillary pressure for an Eagle Ford oil reservoir with 5,000 psia initial reservoir pressure.

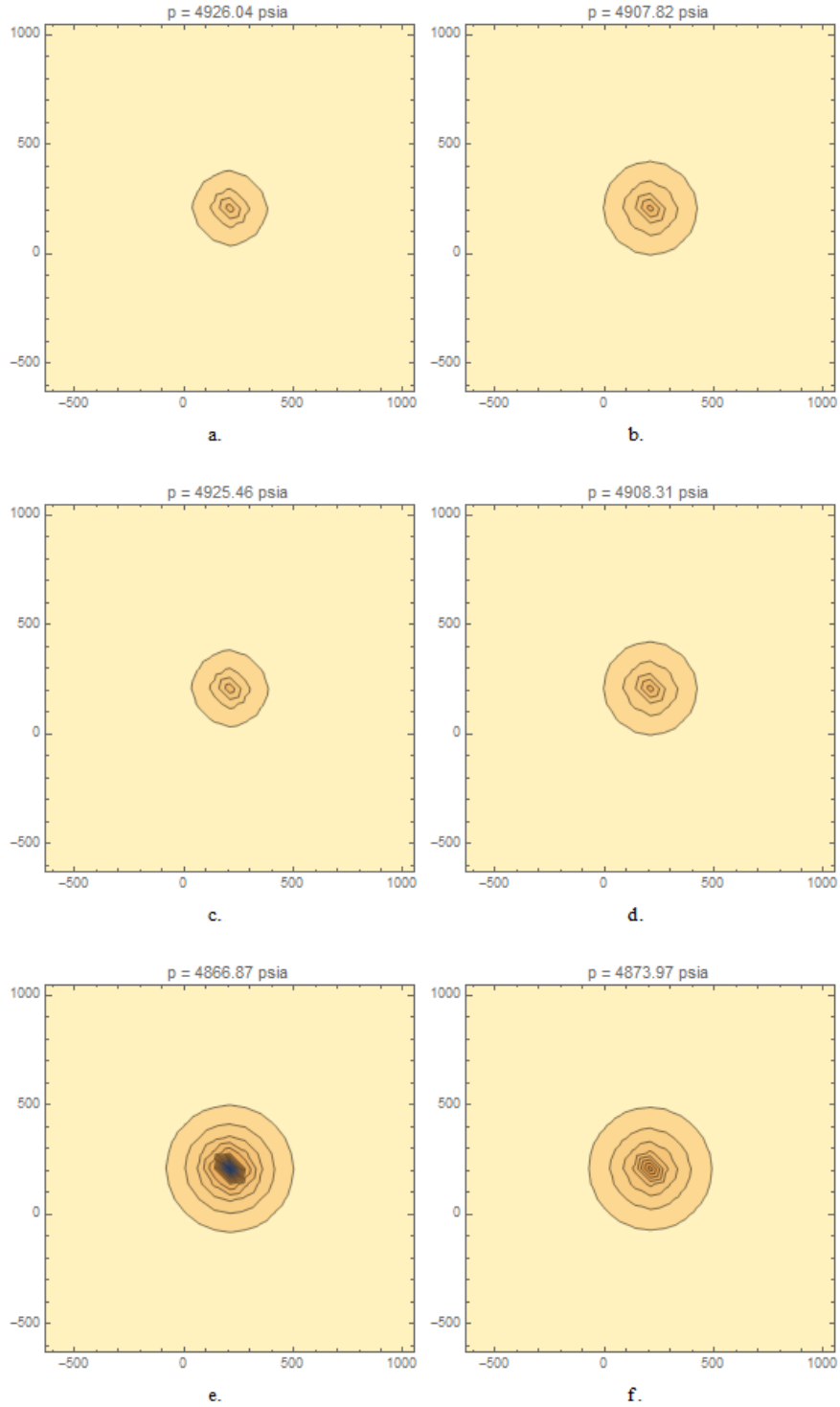

Figure 6-53. Pressure distribution in an Eagle Ford oil reservoir with 5,000 initial reservoir pressure for variations a-f after 30 years of production.

6.7.3 Case 3: Eagle Ford Oil with Low Initial Pressure

We ran this final case to show how production behaves when more of the reservoir is in two-phase. Initially, we see a significant difference in the cases with CC and GD relative permeabilities. CC relative have higher oil rates as seen in Figure 6-54. For the cases with capillary pressure, the gas rates are very similar, seen in Figure 6-55. However without capillary pressure, the gas rate increases significantly for the case with gas depletion. Cumulative oil and gas production shown in Figure 6-56 and Figure 6-57 reflect these differences in production rates.

Reservoir pressure in Figure 6-58 generally decreases faster for the cases with capillary pressure, except the case with gas depletion relative permeabilities without capillary pressure. Due to the lower initial pressure, the average gas saturation in the reservoir is higher than the other cases, shown in Figure 6-59. For all cases, capillary pressure keeps the gas saturation lower than the case without capillary pressure. Figure 6-60 shows that the straight-line relative permeabilities increase the capillary pressure significantly.

Figure 6-61 shows the pressure distribution throughout the reservoir and average pressure for all cases. Figure 6-62 shows the gas saturation distribution. Figure 6-63 shows the difference in capillary pressure distribution throughout the reservoir for the cases with capillary pressure.

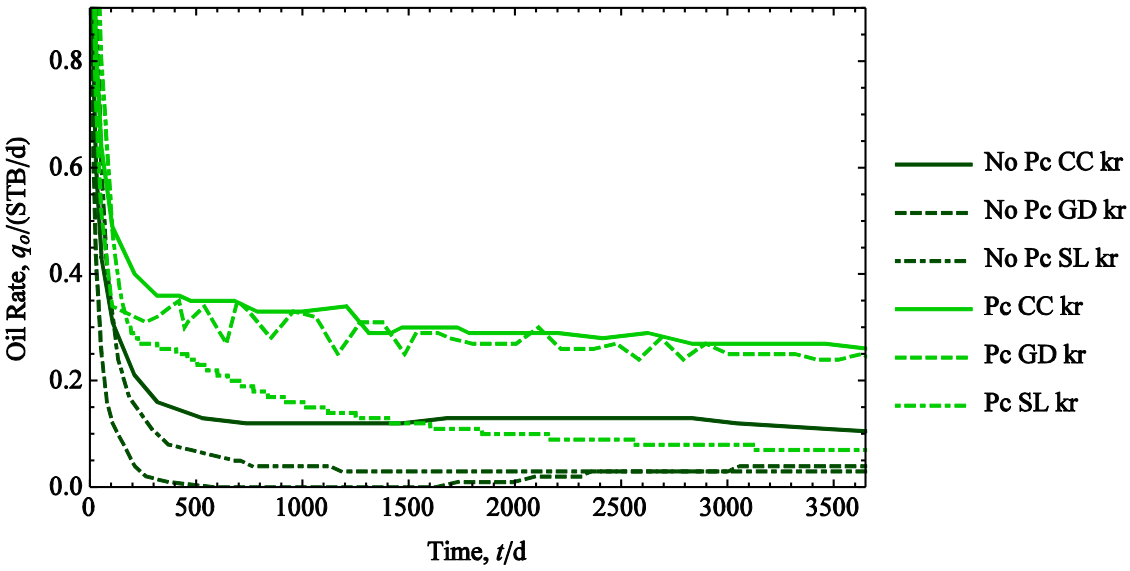

Figure 6-54. Oil production rate from an Eagle Ford oil reservoir with initial pressure of 4,150 psia.

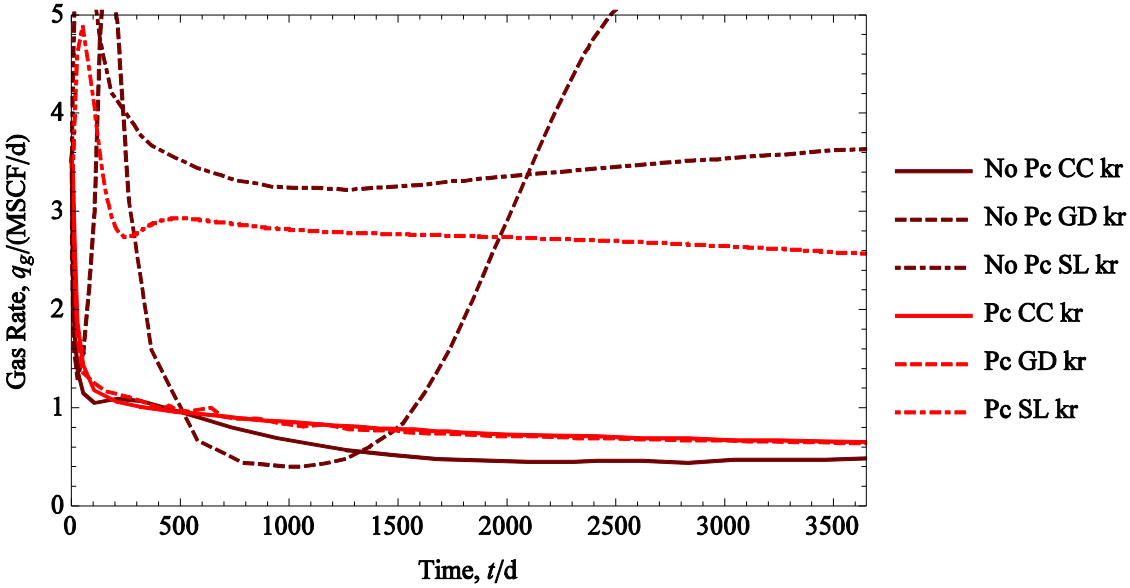

Figure 6-55. Gas production rate from an Eagle Ford oil reservoir with initial pressure of 4,150 psia.

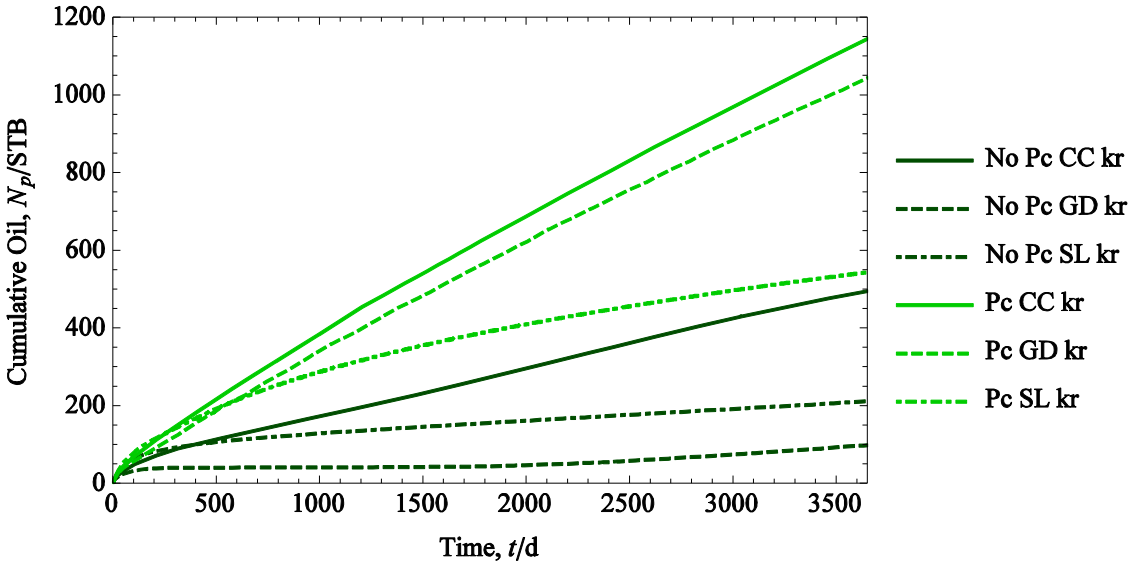

Figure 6-56. Cumulative oil production from an Eagle Ford oil reservoir with initial pressure of 4,150 psia.

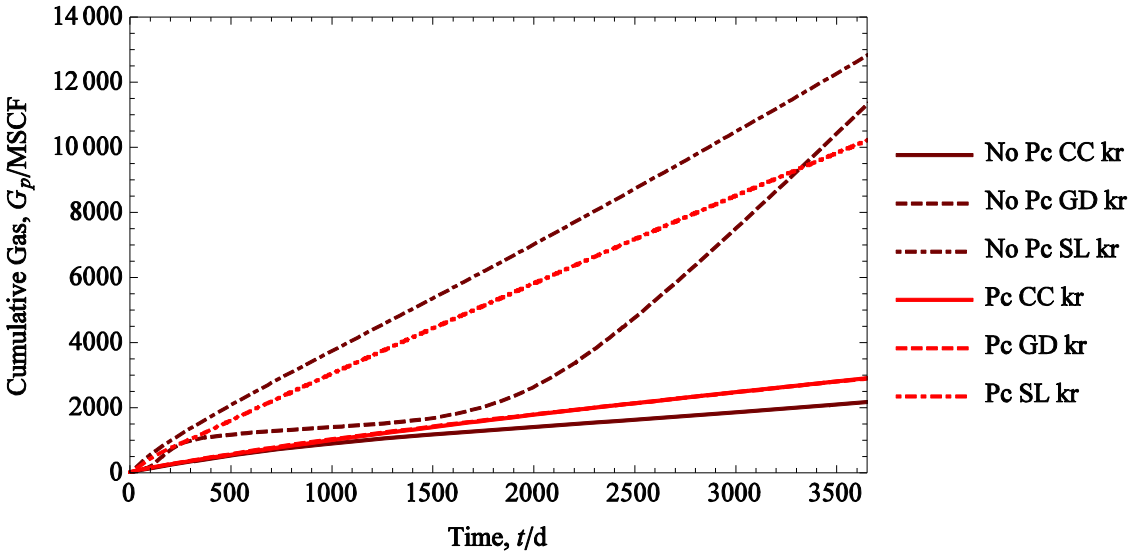

Figure 6-57. Cumulative gas production from an Eagle Ford oil reservoir with initial pressure of 4,150 psia.

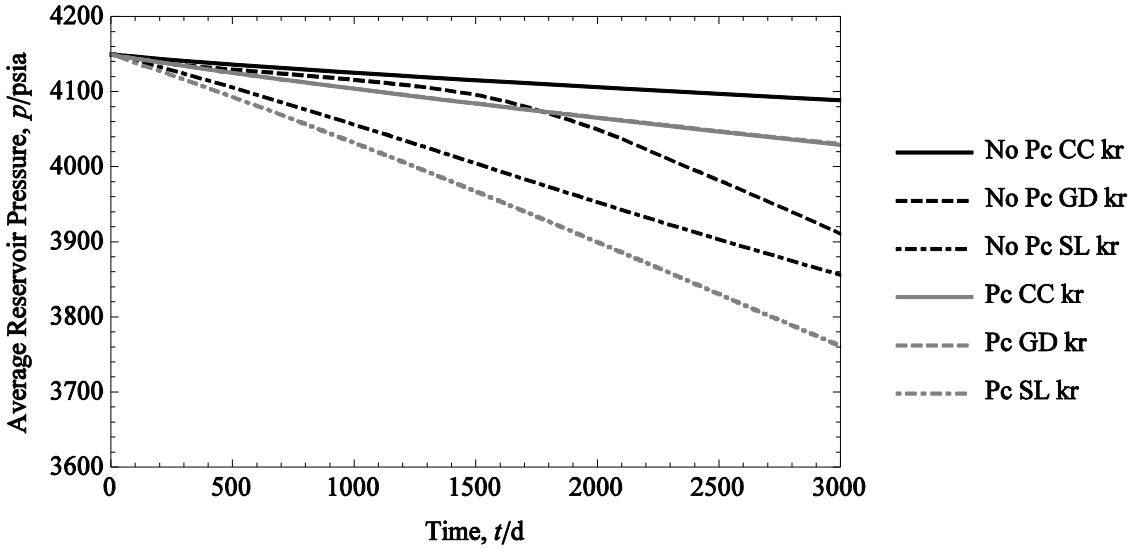

Figure 6-58. Average reservoir pressure of an Eagle Ford oil reservoir with initial pressure of 4,150 psia.

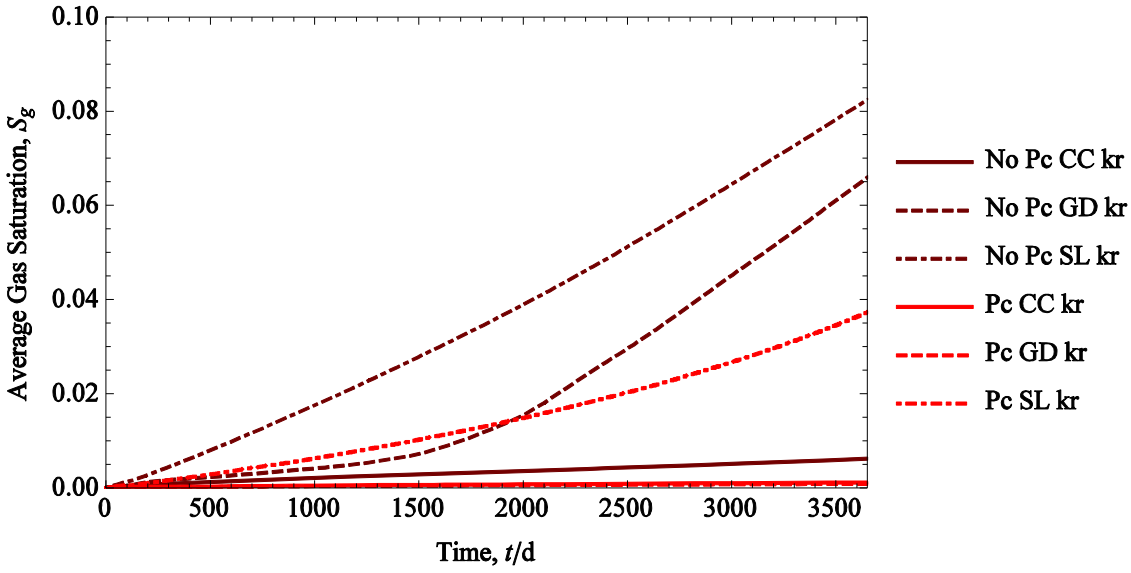

Figure 6-59. Average gas saturation in an Eagle Ford oil reservoir with initial pressure of 4,150 psia.

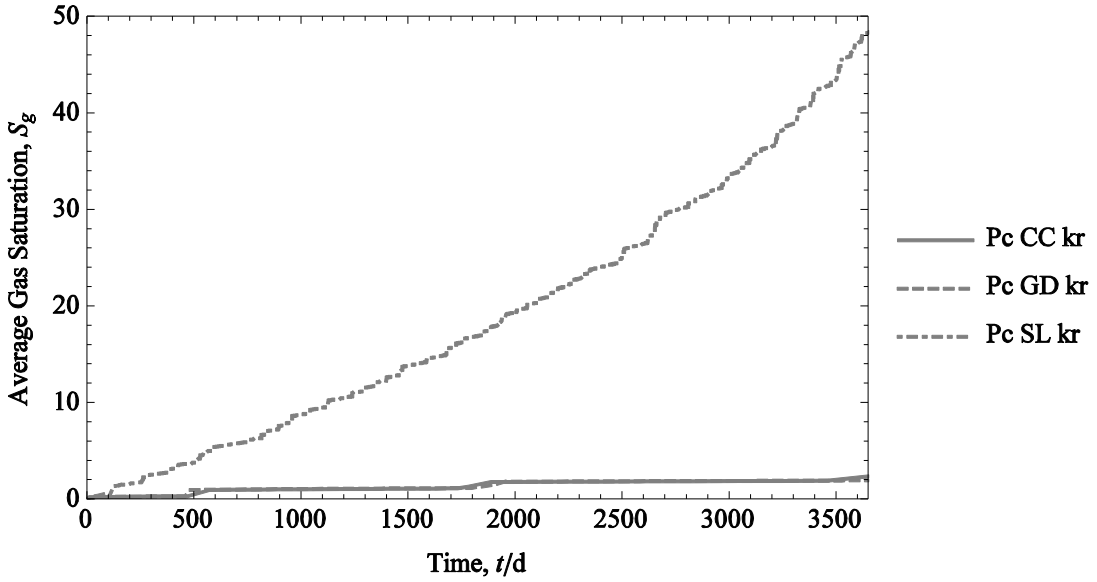

Figure 6-60. Average capillary pressure in an Eagle Ford oil reservoir with initial pressure of 4,150 psia.

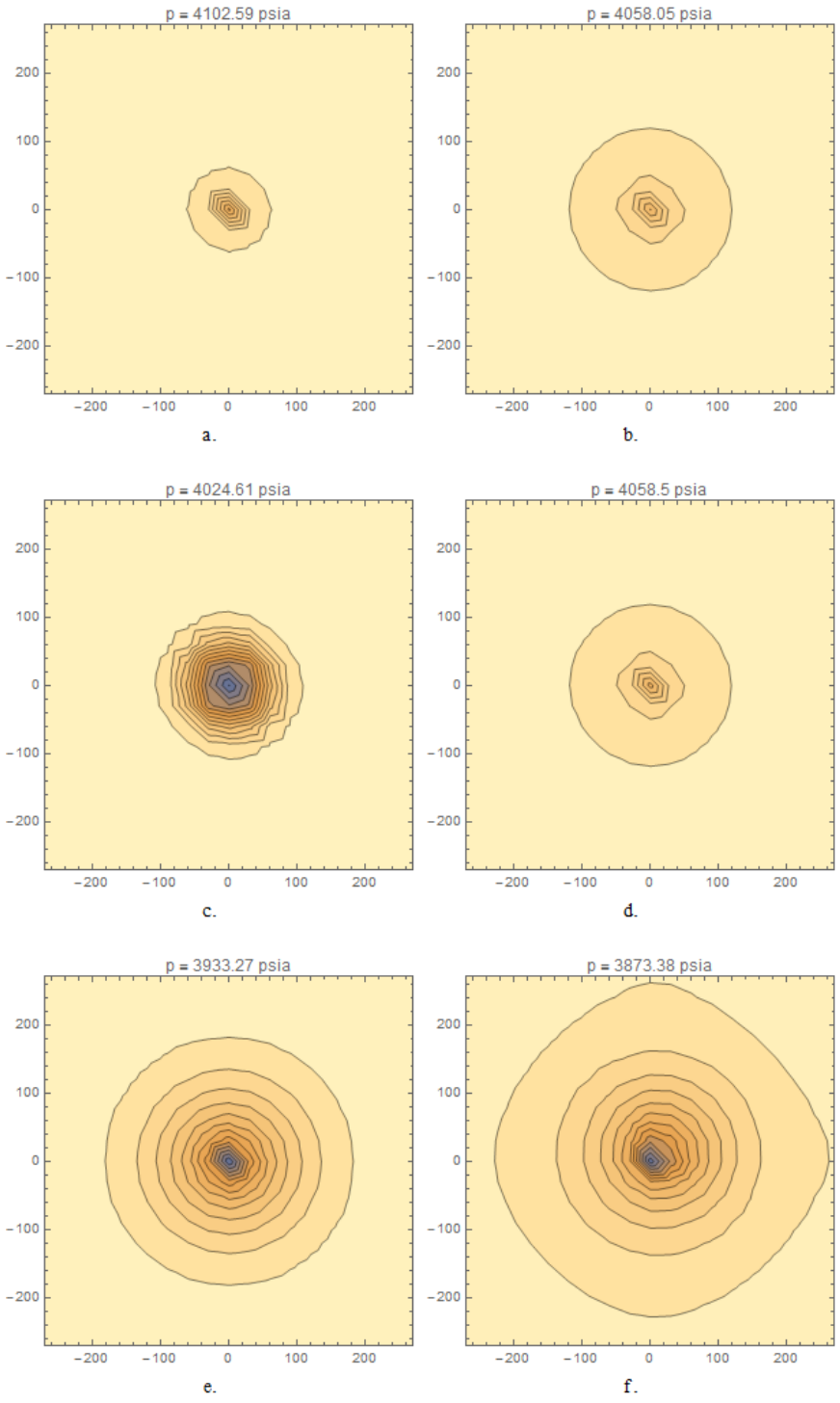

Figure 6-61. Pressure distribution in an Eagle Ford oil reservoir with 4,150 initial reservoir pressure for case 3 with variations a-f after 6 years of production.

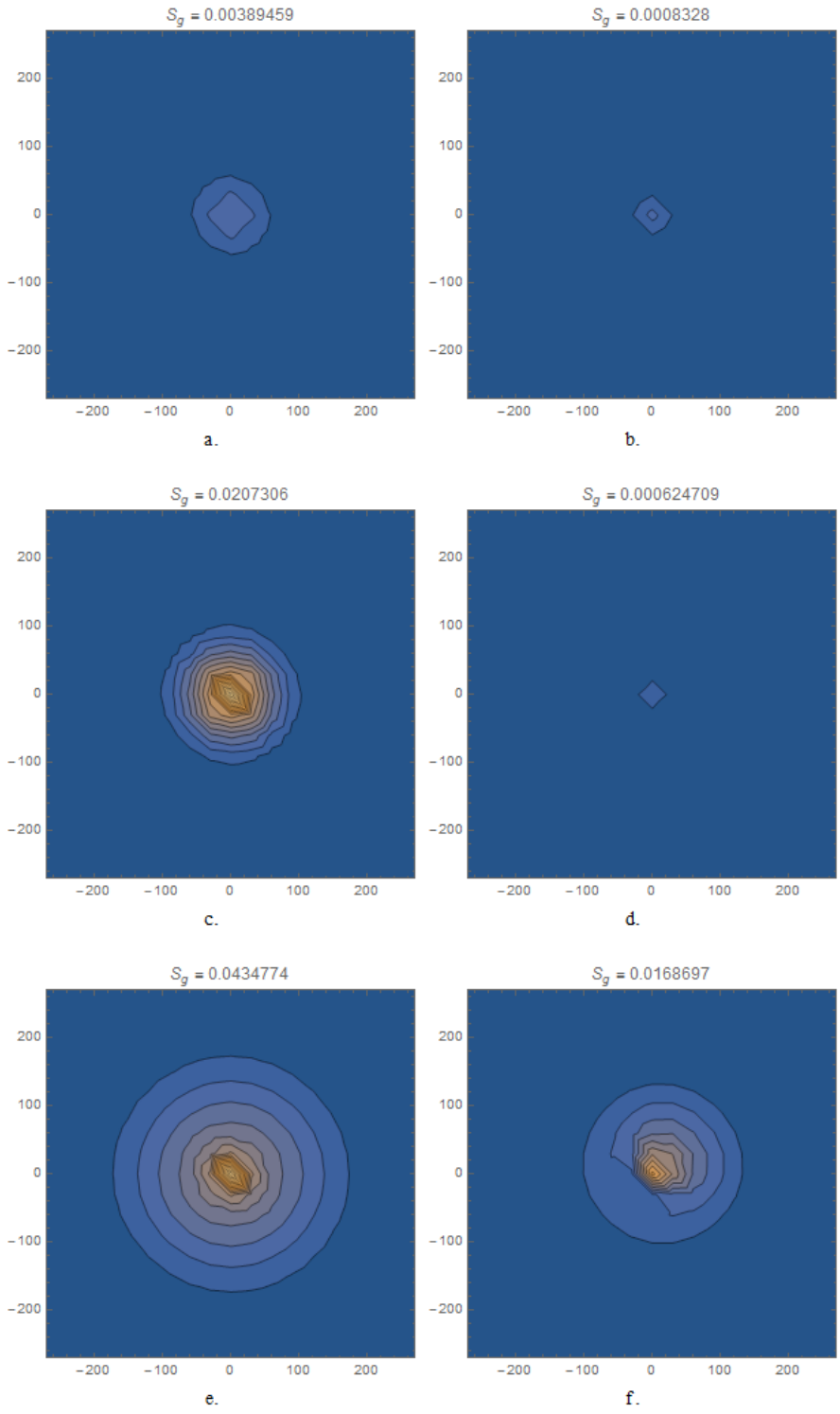

Figure 6-62. Gas saturation distribution in an Eagle Ford oil reservoir with 4,150 initial reservoir pressure for case 3 with variations a-f after 6 years of production.

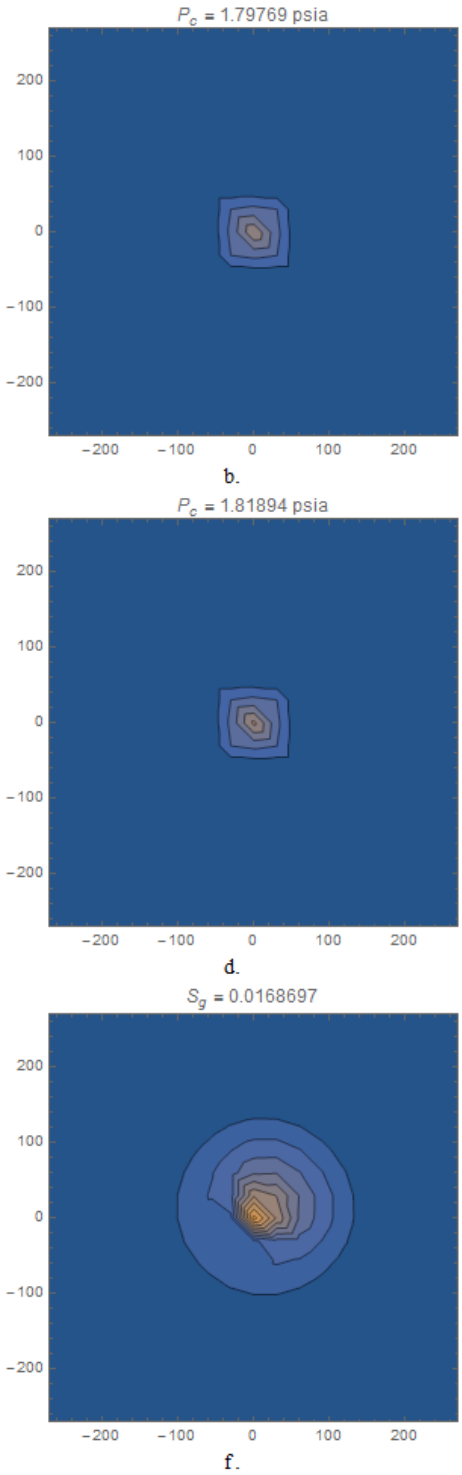

Figure 6-63. Capillary pressure distribution in an Eagle Ford oil reservoir with 4,150 initial reservoir pressure for case 3 with variations a-f after 6 years of production.

CHAPTER VII
FLUIDS

7.1 Synthetic Fluids

Synthetic fluids were created to represent different fluid types. A small number of components was selected to minimize computation time. Table 7-1 shows the component properties of the chosen species and Table 7-2 shows the compositions of the various fluids. Synthetic fluid 1 represents the heaviest oil and the oils transition to volatile oils in synthetic fluids 4-6. Synthetic fluid 7 represents a gas condensate fluid. Phase diagrams of these fluids are shown in Figure 7-1.

Table 7-1. Synthetic fluid component properties

Species	M_i	$p_{c,i}$ (psia)	$T_{c,i}$ (°F)	ω_i	s_i	$Z_{c,i}$	P_i
C_1	16.043	667.4	-116.9	0.008	-0.154	0.288	77
C_2	30	708.5	89.7	0.098	-0.1002	0.284	108
nC_4	58.1	551.3	305.4	0.193	-0.0641	0.2743	189.9
nC_{10}	134	367	659.8	0.444	0.0803	0.249	505.88

$\delta_{ik} = 0$ for all components

Table 7-2. Synthetic fluid compositions.

	1	2	3	4	5	6	7
C_1	0.45	0.5	0.55	0.6	0.65	0.7	0.75
C_2	0.12	0.11	0.11	0.1	0.1	0.1	0.1
nC_4	0.1	0.08	0.06	0.05	0.05	0.05	0.09
C_{10}	0.33	0.31	0.28	0.25	0.2	0.15	0.06

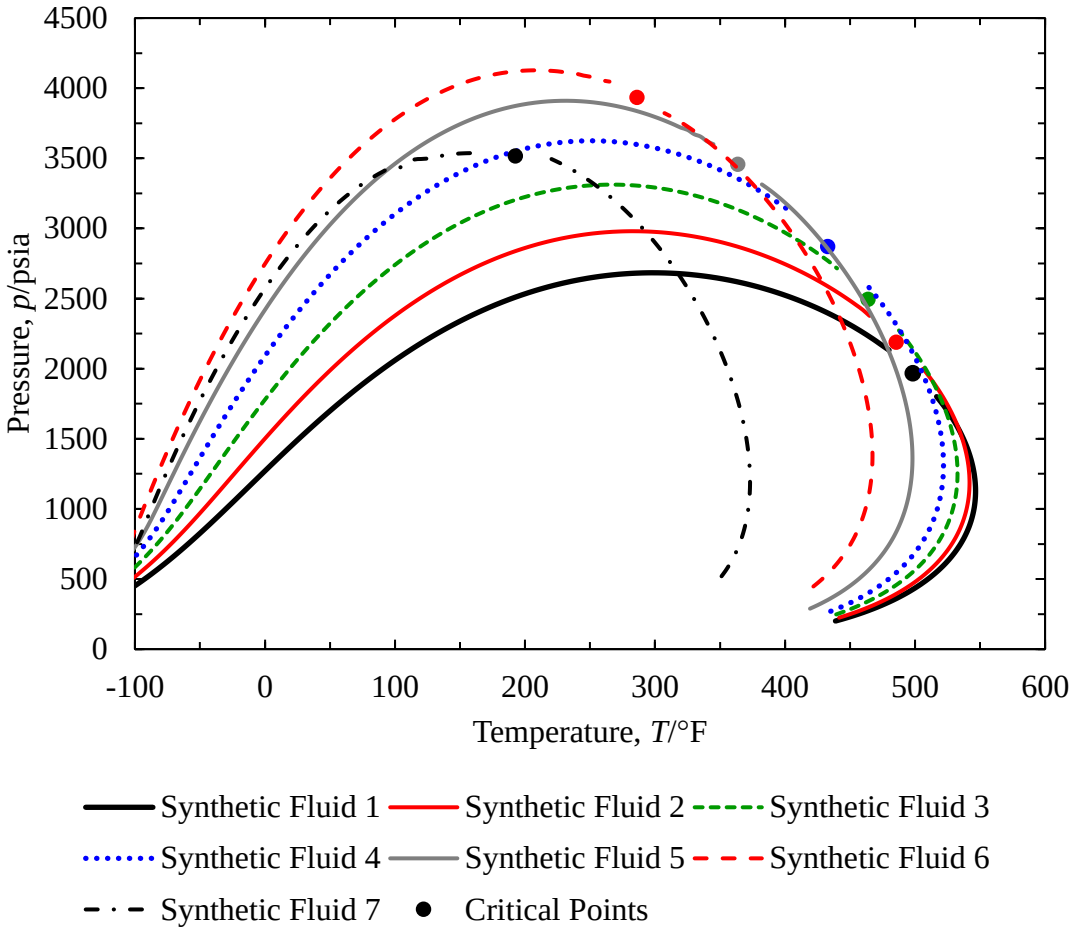

Figure 7-1. Phase diagrams for all synthetic fluids.

7.2 Real Fluids

Yu et al. (2015) presented a fluid characterization for the Bakken formation. The components and properties are listed in Table 7-3 with binary interaction parameters shown in Table 7-4. Gong et al. (2013) presented a fluid characterization for different production regions in the Eagle Ford formation. We selected the fluid from production region 2, listed as a volatile oil and gas condensate bearing region. This fluid is shown in Table 7-5. We also production region 7, listed as a gas condensate region. The compositions and component properties for this fluid are listen in Table 7-6. Ramirez and Aguilera (2014) present an Eagle Ford oil with higher fractions of heavier components,

shown in Table 7-7. Whitson and Sunjerga (2012) present a detailed compositional analysis for several fluids found in the Eagle Ford formation. One oil is selected and is shown in Table 7-8. For use in simulation, this fluid is simplified and shown in Table 7-10.

Table 7-3. Bakken fluid composition and component properties from Yu et al. (2015).

Species	z_i	M_i	$p_{c,i}$ (psia)	$T_{c,i}$ (°F)	ω_i	s_i	P_i
C_1	0.2506	16.04	667.17	-116.59	0.008	-0.154	77
C_2-C_4	0.22	42.82	625.11	194.27	0.1432	-0.0921	145.2
C_5-C_7	0.2	83.74	496.17	461.138	0.2474	-0.0482	250
C_8-C_9	0.13	105.91	454.26	583.142	0.2861	-0.032	306
C_{10+}	0.1994	200	317.2	960.062	0.6869	0.1368	686.3

Table 7-4. Bakken fluid binary interaction coefficients δ_{ik} from Yu et al. (2015).

	C_1	C_2-C_4	C_5-C_7	C_8-C_9	C_{10+}
C_1	0	0.0078	0.0242	0.0324	0.0779
C_2-C_4	0.0078	0	0.0046	0.0087	0.0384
C_5-C_7	0.0242	0.0046	0	0.0006	0.0169
C_8-C_9	0.0324	0.0087	0.0006	0	0.0111
C_{10+}	0.0779	0.0384	0.0169	0.0111	0

Table 7-5. Eagle Ford volatile oil fluid composition and component properties from Gong et al. (2013).

Species	z_i	M_i	$p_{c,i}$ (psia)	$T_{c,i}$ (°F)	ω_i	s_i	P_i
N_2	0.0007	28	492.5	-232.8	0.04	-0.13556	41
CO_2	0.0081	44.01	1070.2	87.6	0.225	-0.05768	78
C_1	0.6554	16.043	667.4	-116.9	0.008	-0.154	77
C_2	0.1297	30	708.5	89.7	0.098	-0.1002	108
C_3	0.0617	44.1	615.9	205.6	0.152	-0.08501	150.3
nC_4	0.0242	58.1	551.3	305.4	0.193	-0.06413	189.9
iC_4	0.015	58.1	529.2	274.6	0.176	-0.07935	181.5
nC_5	0.0102	72.2	489.5	385.3	0.251	-0.04183	268.01
iC_5	0.0108	72.2	491	368.7	0.227	-0.0435	225
C_6	0.0138	86	477.2	453.5	0.275	-0.01478	314.21
C_{7+}	0.0704	177.11	274.3	782.9	0.536	0.12873	666.8

$\delta_{ik} = 0$ for all components

Table 7-6. Eagle Ford gas condensate fluid composition and component properties from Gong et al. (2013).

Species	z_i	M_i	$p_{c,i}$ (psia)	$T_{c,i}$ (°F)	ω_i	s_i	P_i
N_2	0.0011	28	492.5	-232.8	0.04	-0.13556	41
CO_2	0.0127	44.01	1070.2	87.6	0.225	-0.05768	78
C_1	0.6959	16.043	667.4	-116.9	0.008	-0.154	77
C_2	0.1137	30	708.5	89.7	0.098	-0.1002	108
C_3	0.0486	44.1	615.9	205.6	0.152	-0.08501	150.3
nC_4	0.0195	58.1	551.3	305.4	0.193	-0.06413	189.9
iC_4	0.0142	58.1	529.2	274.6	0.176	-0.07935	181.5
nC_5	0.0084	72.2	489.5	385.3	0.251	-0.04183	268.01
iC_5	0.0105	72.2	491	368.7	0.227	-0.0435	225
C_6	0.0117	86	477.2	453.5	0.275	-0.01478	314.21
C_{7+}	0.0637	156.69	295.1	735.6	0.483	0.10851	591.1

$\delta_{ik} = 0$ for all components

Table 7-7. Eagle Ford oil fluid composition and component properties from Ramirez and Aguilera (2014)

Species	z_i	M_i	$p_{c,i}$ (psia)	$T_{c,i}$ (°F)	ω_i	s_i	P_i
CO_2	0.0091	44.01	1069.9	87.89	0.225	-0.0577	78
N_2	0.0016	28.013	492.3	-232.51	0.04	-0.1356	41
C_1	0.3647	16.043	667.2	-116.59	0.008	-0.1540	77
C_2	0.0967	30.07	708.3	90.05	0.098	-0.1002	108
C_3	0.0695	44.097	615.8	205.97	0.152	-0.0850	150.3
C_4-C_6	0.1255	66.869	532	346.19	0.200	-0.0682	206.92
$C_{7+,1}$	0.2000	107.76	430.6	561.11	0.345	-0.0072	337
$C_{7+,2}$	0.1000	198.52	263.1	824.81	0.645	0.1191	613.1
$C_{7+,3}$	0.0329	335.11	147	1072.31	1.067	0.2968	1075.16

$\delta_{ik} = 0$ for all components

Table 7-8. Eagle Ford oil fluid composition and component properties from Whitson and Sunjerga (2012). Parachors are estimated using Eq. (3.34).

Species	z_i	M_i	$p_{c,i}$ (psia)	$T_{c,i}$ (°F)	ω_i	s_i	P_i
H_2S	0.0000	34.08	1300	212.43	0.09	0.1015	85.50
N_2	0.0015	28.01	492.8	-232.47	0.037	-0.0009	61.12
CO_2	0.0232	44.01	1069.5	87.73	0.225	0.2175	82.00
C_1	0.5807	16.04	667	-116.67	0.011	-0.0025	74.05
C_2	0.0743	30.07	706.6	89.93	0.099	0.0589	112.91
C_3	0.0416	44.10	616.1	206.03	0.152	0.0908	154.03
iC_4	0.0096	58.12	527.9	274.43	0.186	0.1095	181.50
nC_4	0.0163	58.12	550.6	305.53	0.200	0.1103	193.90
iC_5	0.0075	72.15	490.4	369.03	0.229	0.0977	225.00
nC_5	0.0080	72.15	488.8	385.83	0.252	0.1195	236.00
C_6	0.0114	82.42	490	464.33	0.2383	0.1342	270.55
C_7	0.0297	96.05	454.2	530.93	0.2741	0.1436	314.69
C_8	0.0276	108.89	421.4	583.73	0.3105	0.1526	354.75
C_9	0.0231	122.04	399.5	633.83	0.3513	0.1701	397.47
C_{10}	0.0198	134.96	360.3	678.33	0.3913	0.1866	439.71
C_{11}	0.0170	147.80	335.6	727.53	0.4309	0.2023	491.65
C_{12}	0.0146	160.55	314	755.23	0.4700	0.217	523.55
C_{13}	0.0126	173.19	294.9	789.03	0.5084	0.2308	565.29
C_{14}	0.0108	185.74	278.1	820.13	0.5462	0.2436	606.63
C_{15}	0.0093	198.18	263.2	849.03	0.5833	0.2555	647.75
C_{16}	0.0080	210.51	249.9	875.83	0.6197	0.2665	688.37
C_{17}	0.0069	222.73	238	900.93	0.6555	0.2766	728.72
C_{18}	0.0060	234.83	227.2	924.43	0.6905	0.2859	768.64
C_{19}	0.0051	246.83	217.6	946.53	0.7249	0.2944	808.17
C_{20}	0.0045	258.71	208.8	967.33	0.7587	0.3022	847.23
C_{21}	0.0039	270.48	200.9	987.03	0.7917	0.3094	885.97
C_{22}	0.0034	282.14	193.6	1005.63	0.8241	0.3159	924.17
C_{23}	0.0029	293.69	187	1023.33	0.8559	0.3219	962.05
C_{24}	0.0025	305.13	180.9	1040.13	0.8870	0.3274	999.44
C_{25}	0.0022	316.47	175.3	1056.13	0.9176	0.3323	1036.40
C_{26+}	0.0161	412.23	140.8	1171.73	1.1619	0.3605	1347.29

Table 7-9. Binary interaction parameters of the Eagle Ford oil in Table 7-8 from Whitson and Sunjerga (2012).

Species	$\delta_{i\mathrm{N}_2}$	$\delta_{i\mathrm{CO}_2}$
H_2S	0.00	0.00
N_2	0.00	0.00
CO_2	0.00	0.00
C_1	0.02	0.12
C_2	0.06	0.12
C_3	0.08	0.12
iC_4	0.08	0.12
nC_4	0.08	0.12
iC_5	0.08	0.12
nC_5	0.08	0.12
C_6	0.08	0.12
C_7	0.08	0.10
C_8	0.08	0.10
C_9	0.08	0.10
C_{10}	0.08	0.10
C_{11}	0.08	0.10
C_{12}	0.08	0.10
C_{13}	0.08	0.10
C_{14}	0.08	0.10
C_{15}	0.08	0.10
C_{16}	0.08	0.10
C_{17}	0.08	0.10
C_{18}	0.08	0.10
C_{19}	0.08	0.10
C_{20}	0.08	0.10
C_{21}	0.08	0.10
C_{22}	0.08	0.10
C_{23}	0.08	0.10
C_{24}	0.08	0.10
C_{25}	0.08	0.10
C_{26+}	0.08	0.10

Table 7-10. Simplified Eagle Ford oil from full characterization in Table 7-8.

Species	z_i	M_i	$p_{c,i}$ (psia)	$T_{c,i}$ (°F)	ω_i	s_i	P_i
CO_2	0.0232	44.01	1069.5	87.73	0.225	0.2175	82.00
C_1	0.5816	16.04	667.0	-116.67	0.011	-0.0025	74.05
C_2	0.0744	30.07	706.6	89.93	0.099	0.0589	112.91
C_3	0.0417	44.1	616.1	206.03	0.152	0.0908	154.03
C_4	0.0259	58.12	542.19	294.00	0.1948	0.1100	189.30
$C_{5\text{-}6}$	0.0269	76.502	489.75	414.41	0.2398	0.1197	247.57
C_{7+}	0.1321	122.96	392.81	632.37	0.3548	0.1723	402.33
C_{13+}	0.0942	255.28	226.23	941.29	0.7408	0.2877	834.82

Table 7-11. Binary interaction parameters for the simplified Eagle Ford fluid in Table 7-10.

Species	CO_2	C_1	C_2	C_3	C_4	$C_{5\text{-}6}$	C_{7+}	C_{13+}
CO_2	0.00	0.12	0.12	0.12	0.12	0.12	0.10	0.10
C_1	0.12	0.00	0.00	0.00	0.00	0.00	0.00	0.00
C_2	0.12	0.00	0.00	0.00	0.00	0.00	0.00	0.00
C_3	0.12	0.00	0.00	0.00	0.00	0.00	0.00	0.00
C_4	0.12	0.00	0.00	0.00	0.00	0.00	0.00	0.00
$C_{5\text{-}6}$	0.12	0.00	0.00	0.00	0.00	0.00	0.00	0.00
C_{7+}	0.10	0.00	0.00	0.00	0.00	0.00	0.00	0.00
C_{13+}	0.10	0.00	0.00	0.00	0.00	0.00	0.00	0.00

CHAPTER VIII
CONCLUSIONS AND RECOMMENDATIONS

8.1 Conclusions

During this research, we arrived at the following conclusions:

1. Incorporating capillary pressure into vapor-liquid equilibrium using the Young-Laplace equation with the PR EOS is an effective method for describing phase behavior in porous media with small pores.
2. When two confined phases are in equilibrium, their densities, viscosities, and phase distributions are different than when those phases are in bulk space. Specifically, when confined, liquid density and viscosity decrease, gas density and viscosity increase, and liquid saturation increases.
3. When modeling confined fluids, the contact angle may change as a function of temperature. This relationship is generally linear and reasonable values aid in more accurately describing experimental data.
4. Our model is validated by closely replicating experimental data of single and multiple component systems with a variety of species types.
5. Capillary pressure significantly impacts simulated oil and gas production from tight reservoirs. For most cases, oil and gas production increase in oil reservoirs, and decrease in gas condensate reservoirs when compared to simulations without including capillary pressure.
6. By simulating CCE and CVD methods for a given fluid and pore size or distribution of pore sizes, capillary pressure curves can be generated. These curves can be integrated to predict oil/gas relative permeability.
7. For reservoirs at high pressures, the oil/gas relative permeability is less significant, but capillary pressure still makes a significant impact on overall production.

8.2 Recommendations for Future Work

While this work attempted to give a comprehensive application of capillary pressure in tight media, we recommend some future work to help this method become more useful.

1. This model only accounts for changes in fluid properties below the bubble point and does not alter fluid properties above the bubble point. We suggest incorporating a model for including confinement when the fluid is single-phase. One useful method would be to incorporate adsorption, as described by Ambrose et al. (2011). A useful check with this would be to ensure continuity of phase properties across the saturation pressure when switching models.
2. Oil/gas relative permeability curves plotted against normalized oil saturation become almost independent of depletion method, making residual oil saturation the determining factor in predicting these curves. We recommend determining a method for predicting residual oil saturation to create better-defined relative permeability curves.
3. The oil/gas relative permeability derivation assumes immiscible flow. A more detailed derivation of the relative permeability equation may include IFT inside the integral. For a given fluid, IFT follows a similar trend when plotted against oil saturation, regardless of pore diameter. A regression of this trend could be included in the integration of capillary pressure.
4. All depletion methods show very similar capillary pressure curves plotted against reservoir pressure, when determined from a simple cell depletion and when determined from reservoir simulation. When using a lookup function, this trend could improve prediction or provide a good guess value.
5. All cases in this work were homogeneous. Heterogeneity in the reservoir would be significant to study. One method would be to assign each cell a particular pore diameter, and calculate permeability from a pore size-permeability relationship.

6. Simulations done in this work assume flow only through the matrix. However, real shale reservoirs use fractures to improve fluid conductivity. Incorporating fractures in simulation and attempting to match production data from the field may aid in validating our method or discovering aspects that require further study.
7. Further simulation studies may show reservoir signatures when including capillary pressure. We suggest simulating various reservoirs to better characterize the behavior of capillary pressure and production in tight media.

REFERENCES

Abu Al-Rub, F.A. and Datta, R. 1998. Theoretical Study of Vapor Pressure of Pure Liquids in Porous Media. *Fluid Phase Equilibria* **147** (1–2): 65-83. DOI: http://dx.doi.org/10.1016/S0378-3812(98)00223-4.

Alkan, H. and Luan, G. 1993. Estimation of Parachors from Critical Properties. Paper submitted to Society of Petroleum Engineers for distribution and possible publication. Society of Petroleum Engineers.

Ambrose, R.J., Hartman, R.C., and Akkutlu, I.Y. 2011. Multi-Component Sorbed Phase Considerations for Shale Gas-in-Place Calculations. Paper presented at the SPE Production and Operations Symposium, Oklahoma City. Society of Petroleum Engineers. DOI: http://dx.doi.org/10.2118/141416-MS.

Amyx, J.W., Bass, D.M., and Whiting, R.L. 1960. *Petroleum Reservoir Engineering*, 306-308. New York: McGraw-Hill.

Ashour, I., Al-Rawahi, N., Fatemi, A. et al. 2011. Applications of Equations of State in the Oil and Gas Industry. In *Thermodynamics - Kinetics of Dynamic Systems*, 167, Rijeka: InTech.

Bentsen, R.G. and Anli, J. 1976. A New Displacement Capillary Pressure Model. *Journal of Canadian Petroleum Technology* **15** (3): 75-79. DOI: http://dx.doi.org/10.2118/76-03-10.

Brooks, R.H. and Corey, A.T. 1964. Hydraulic Properties of Porous Media. *Hydrology Papers*, Colorado State University, (3).

Broseta, D. and Ragil, K. 1995. Parachors in Terms of Critical Temperature, Critical Pressure and Acentric Factor. Paper presented at the SPE Annual Technical Conference and Exhibition, Dallas. Society of Petroleum Engineers. DOI: http://dx.doi.org/10.2118/30784-MS.

Brusilovsky, A.I. 1992. Mathematical Simulation of Phase Behavior of Natural Multicomponent Systems at High Pressures with an Equation of State. *Soc. Pet. Eng. J.* DOI: http://dx.doi.org/10.2118/20180-PA.

Clarke, M.A., Pooladi-Darvish, M., and Bishnoi, P.R. 1999. A Method to Predict Equilibrium Conditions of Gas Hydrate Formation in Porous Media. *Ind. Eng. Chem. Res.* **38** (6): 2485-2490. DOI: http://dx.doi.org/10.1021/ie980625u.

Coats, K.H. 1980. An Equation of State Compositional Model. *SPE Journal* **20** (5):363-376. DOI: http://dx.doi.org/10.2118/8284-PA.

Danesh, A.S., Dandekar, A.Y., Todd, A.C. et al. 1991. A Modified Scaling Law and Parachor Method Approach for Improved Prediction of Interfacial Tension of Gas-Condensate Systems. Paper presented at the SPE Annual Technical Conference and Exhibition, Dallas. Society of Petroleum Engineers. DOI: http://dx.doi.org/10.2118/22710-MS.

Duffy, J.A., Wilkinson, N.J., Fretwell, H.M. et al. 1995. Phase Transitions of Co 2 Confined in Nanometer Pores as Revealed by Positronium Annihilation. *J. Phys.: Condens. Matter* **7** (50): L713.

Dujardin, E., Ebbesen, T.W., Hiura, H. et al. 1994. Capillarity and Wetting of Carbon Nanotubes. *Science* **265** (5180): 1850-1852.

EIA. Shale in the United States. https://www.eia.gov/energy_in_brief/article/shale_in_the_united_states.cfm. Accessed 11/30/2016.

Fanchi, J.R. 1985. Calculation of Parachors for Compositional Simulation. *J. Pet. Technol.* **37** (11): 2049-2050. DOI: http://dx.doi.org/10.2118/13402-PA.

Feng, F. and Akkutlu, I.Y. 2015. Flow of Hydrocarbons in Nanocapillary: A Non-Equilibrium Molecular Dynamics Study. Paper presented at the SPE Asia Pacific Unconventional Resources Conference and Exhibition, Brisbane. Society of Petroleum Engineers. DOI: http://dx.doi.org/10.2118/177005-MS.

Firincioglu, T., Ozkan, E., and Ozgen, C. 2012. Thermodynamics of Multiphase Flow in Unconventional Liquids-Rich Reservoirs. Paper presented at the SPE Annual Technical Conference and Exhibition, San Antonio. Society of Petroleum Engineers. DOI: http://dx.doi.org/10.2118/159869-MS.

Firoozabadi, A. 1999. *Thermodynamics of Hydrocarbon Reservoirs*, 68-74. New York: McGraw-Hill Education.

Freyss, H., Guieze, P., Varotsis, N. et al. 1989. PVT Analysis for Oil Reservoirs. *Technical Review* **37** (1): 4-15.

Gates, J.I. and Lietz, W.T. 1950. Relative Permeabilities of California Cores by the Capillary - Pressure Method. Paper presented at the Pacific Coast District, Division of Production Spring Meeting, Los Angeles. American Petroleum Institute.

Gong, X., Tian, Y., McVay, D.A. et al. 2013. Assessment of Eagle Ford Shale Oil and Gas Resources. Paper presented at the SPE Unconventional Resources Conference Canada, Calgary. Society of Petroleum Engineers. DOI: http://dx.doi.org/10.2118/167241-MS.

Gonzalez Abad, K.G. 2013. Development of a Compositional Reservoir Simulator for Asphaltene Precipitation Based on a Thermodynamically Consistent Model. MS, Texas A&M University.

Gonzalez Abad, K.G. 2016. Adaptive Mesh Refinement and Coarsening for Compositional Reservoir Simulation. PhD, Texas A&M University.

Gubbins, K.E., Long, Y., and Śliwinska-Bartkowiak, M. 2014. Thermodynamics of Confined Nano-Phases. *J. Chem. Thermodyn.* **74**: 169-183. DOI: http://dx.doi.org/10.1016/j.jct.2014.01.024.

Gupta, V. 2010. Graphene as Intermediate Phase in Fullerene and Carbon Nanotube Growth: A Young–Laplace Surface-Tension Model. *Appl. Phys. Lett.* **97** (18): 181910. DOI: doi:http://dx.doi.org/10.1063/1.3509403.

Helland, J.O. and Skjæveland, S.M. 2004. Three-Phase Capillary Pressure Correlation for Mixed-Wet Reservoirs. Paper presented at the SPE International Petroleum Conference in Mexico, Puebla Pue. Society of Petroleum Engineers. DOI: http://dx.doi.org/10.2118/92057-MS.

Holditch, S.A. 2006. Tight Gas Sands. *Journal of Petroleum Technology* **58** (06): 86-93. DOI: http://dx.doi.org/10.2118/103356-JPT.

Islam, A.W., Patzek, T.W., and Sun, A.Y. 2015. Thermodynamics Phase Changes of Nanopore Fluids. *J. Nat. Gas Sci. Eng.* **25**: 134-139. DOI: http://dx.doi.org/10.1016/j.jngse.2015.04.035.

Jayaraman, K., Okamoto, K., Son, S.J. et al. 2005. Observing Capillarity in Hydrophobic Silica Nanotubes. *J. Am. Chem. Soc.* **127** (49): 17385-17392. DOI: http://dx.doi.org/10.1021/ja055535c.

Jhaveri, B.S. and Youngren, G.K. 1988. Three-Parameter Modification of the Peng-Robinson Equation of State to Improve Volumetric Predictions. *SPE Reservoir Eng.* **3** (3): 1033-1040. DOI: http://dx.doi.org/10.2118/13118-PA.

Jin, L., Pu, H., Wang, Y. et al. 2015. The Consideration of Pore Size Distribution in Organic-Rich Unconventional Formations May Increase Oil Production and Reserve by 25%, Eagle Ford Case Study. Paper presented at the Unconventional Resources Technology Conference, San Antonio. Society of Petroleum Engineers. DOI: http://dx.doi.org/10.2118/178507-MS.

Johnson, H.M. 1961. A History of Well Logging. Paper presented at the SPWLA 2nd Annual Logging Symposium, Dallas. Society of Petrophysicists and Well-Log Analysts.

Kruk, M. and Jaroniec, M. 2000. Accurate Method for Calculating Mesopore Size Distributions from Argon Adsorption Data at 87 K Developed Using Model Mcm-41 Materials. *Chemistry of Materials* **12** (1): 222-230. DOI: http://dx.doi.org/10.1021/cm9905601.

Laplace, P.S. 1805. *Traité De Mécanique Céleste*, Vol. 4. Paris: de l'Imprimerie de Crapelet.

León, F., Beakou, A., and Amaya, M.G. 2008. Metal–Electrolyte Interface Interaction on a Negative Electrochemical Device. *J. Mol. Catal. A: Chem.* **281** (1–2): 226-229. DOI: http://dx.doi.org/10.1016/j.molcata.2007.10.007.

Lewis, W.C. 1923. *Vol I: Kinetic Theory*. A System of Physical Chemistry, 9. New York: Longmans, Green and Co.

Li, Y. and Johns, R.T. 2006. Rapid Flash Calculations for Compositional Simulation. *SPE Reservoir Evaluation & Engineering* **9** (05): 521-529. DOI: http://dx.doi.org/10.2118/95732-PA.

Liu, H. and Cao, G. 2016. Effectiveness of the Young-Laplace Equation at Nanoscale. *Scientific Reports* **6**: 23936. DOI: http://dx.doi.org/10.1038/srep23936 http://www.nature.com/articles/srep23936#supplementary-information

Liu, Y., Li, H.A., and Okuno, R. 2016. Phase Behavior of Fluid Mixtures in a Partially Confined Space. Paper presented at the SPE Annual Technical Conference and Exhibition, Dubai. Society of Petroleum Engineers. DOI: http://dx.doi.org/10.2118/181716-MS.

Lohrenz, J., Bray, B.G., and Clark, C.R. 1964. Calculating Viscosities of Reservoir Fluids from Their Compositions. Paper presented at the SPE Annual Fall Meeting, Houston. Society of Petroleum Engineers. DOI: http://dx.doi.org/10.2118/915-PA.

Luo, S., Lutkenhaus, J.L., and Nasrabadi, H. 2015. Experimental Study of Confinement Effect on Hydrocarbon Phase Behavior in Nano-Scale Porous Media Using Differential Scanning Calorimetry. Paper presented at the SPE Annual Technical Conference and Exhibition, Houston. Society of Petroleum Engineers. DOI: http://dx.doi.org/10.2118/175095-MS.

Macleod, D.B. 1923. On a Relation between Surface Tension and Density. *Trans. Faraday Soc.* **19** (July): 38-41. DOI: http://dx.doi.org/10.1039/TF9231900038.

Masters, J.A. 1979. Deep Basin Gas Trap, Western Canada. *AAPG Bulletin* **63** (2): 152-181.

Mathias, P.M., Naheiri, T., and Oh, E.M. 1989. A Density Correction for the Peng—Robinson Equation of State. *Fluid Phase Equilibria* **47** (1): 77-87. DOI: http://dx.doi.org/10.1016/0378-3812(89)80051-2.

Matthews, C.S. and Russell, D.G. 1967. *Pressure Buildup and Flow Tests in Wells*. Spe Monograph: Henry L. Doherty Memorial Fund of AIME.

McCain, W.D. 1990. *The Properties of Petroleum Fluids*, 271-276. Tulsa: PennWell Books.

Melrose, J.C. 1965. On the Thermodynamic Relations between Immersional and Adhesional Wetting. *Journal of Colloid Science* **20** (8): 801-821. DOI: http://dx.doi.org/10.1016/0095-8522(65)90054-1.

Metzger, T., Tsotsas, E., and Prat, M. 2007. Pore-Network Models: A Powerful Tool to Study Drying at the Pore Level and Understand the Influence of Structure on Drying Kinetics. In *Mod. Drying Technol.*: Wiley-VCH Verlag GmbH & Co. KGaA.

Michelsen, M.L. 1982. The Isothermal Flash Problem. Part Ii. Phase-Split Calculation. *Fluid Phase Equilibria* **9** (1): 21-40. DOI: http://dx.doi.org/10.1016/0378-3812(82)85002-4.

Miqueu, C., Mendiboure, B., Graciaa, A. et al. 2003. Modelling of the Surface Tension of Pure Components with the Gradient Theory of Fluid Interfaces: A Simple and Accurate Expression for the Influence Parameters. *Fluid Phase Equilib.* **207** (1–2): 225-246. DOI: http://dx.doi.org/10.1016/S0378-3812(03)00028-1.

Monnery, W.D., Svrcek, W.Y., and Satyro, M.A. 1998. Gaussian-Like Volume Shifts for the Peng−Robinson Equation of State. *Industrial & Engineering Chemistry Research* **37** (5): 1663-1672. DOI: http://dx.doi.org/10.1021/ie970640j.

Morrow, N.R. 1970. Physics and Thermodynamics of Capillary Action in Porous Media. *Ind. Eng. Chem.* **62** (6): 32-56. DOI: http://dx.doi.org/10.1021/ie50726a006.

Nakornthap, K. and Evans, R.D. 1986. Temperature-Dependent Relative Permeability and Its Effect on Oil Displacement by Thermal Methods. *SPE Reservoir Engineering* **1** (3): 230-242. DOI: http://dx.doi.org/10.2118/11217-PA.

Nelson, P.H. 2009. Pore-Throat Sizes in Sandstones, Tight Sandstones, and Shales. *AAPG Bulletin* **93** (3): 329-340. DOI: http://dx.doi.org/10.1306/10240808059.

Nghiem, L.X., Fong, D.K., and Aziz, K. 1981. Compositional Modeling with an Equation of State. *SPE Journal*. DOI: http://dx.doi.org/10.2118/9306-PA.

Nichita, D.V. and Leibovici, C.F. 2013. A Rapid and Robust Method for Solving the Rachford–Rice Equation Using Convex Transformations. *Fluid Phase Equilibria* **353**: 38-49. DOI: http://dx.doi.org/10.1016/j.fluid.2013.05.030.

Nojabaei, B., Johns, R.T., and Chu, L. 2013. Effect of Capillary Pressure on Phase Behavior in Tight Rocks and Shales. *SPE Reservoir Eval. Eng.* **16** (3): 281-289. DOI: http://dx.doi.org/10.2118/159258-PA.

Pang, J., Zuo, J.Y., Zhang, D. et al. 2012. Impact of Porous Media on Saturation Pressures of Gas and Oil in Tight Reservoirs. Paper presented at the SPE Canadian Unconventional Resources Conference, Calgary. Society of Petroleum Engineers. DOI: http://dx.doi.org/10.2118/161143-MS.

Passey, Q.R., Bohacs, K., Esch, W.L. et al. 2010. From Oil-Prone Source Rock to Gas-Producing Shale Reservoir - Geologic and Petrophysical Characterization of Unconventional Shale Gas Reservoirs. Paper presented at the International Oil and Gas Conference and Exhibition in China, Beijing. Society of Petroleum Engineers. DOI: http://dx.doi.org/10.2118/131350-MS.

Péneloux, A., Rauzy, E., and Fréze, R. 1982. A Consistent Correction for Redlich-Kwong-Soave Volumes. *Fluid Phase Equilib.* **8** (1): 7-23. DOI: http://dx.doi.org/10.1016/0378-3812(82)80002-2.

Peng, D.-Y. and Robinson, D.B. 1976. A New Two-Constant Equation of State. *Ind. Eng. Chem. Fundam.* **15** (1): 59-64. DOI: http://dx.doi.org/10.1021/i160057a011.

Peng, Y., Liou, W.W., and Parker, P.P. 2011. Analytical Investigation of Free Surface Flow in Multi-Layer Porous Media. *Colloids Surf., A* **380** (1–3): 213-221. DOI: http://dx.doi.org/10.1016/j.colsurfa.2011.02.031.

Pesaran, A. and Shariati, A. 2013. Effect of Capillary Term Parameters on the Thermodynamic Modeling of Methane Hydrate Formation in Porous Media. *J. Nat. Gas Sci. Eng.* **14**: 192-203. DOI: http://dx.doi.org/10.1016/j.jngse.2013.06.003.

Petke, F.D. and Ray, B.R. 1969. Temperature Dependence of Contact Angles of Liquids on Polymeric Surfaces. *J. Colloid Interface Sci.* **31** (2): 216-227.

Pommer, M.E. 2014. Quantitative Assessment of Pore Types and Pore Size Distribution across Thermal Maturity, Eagle Ford Formation, South Texas. Master of Science, University of Texas.

Pyle, H.C. and Sherborne, J.E. 1939. Core Analysis. *Transactions of the AIME* **132** (01). DOI: http://dx.doi.org/10.2118/939033-G.

Qiao, S.Z., Bhatia, S.K., and Nicholson, D. 2004. Study of Hexane Adsorption in Nanoporous Mcm-41 Silica. *Langmuir* **20** (2): 389-395. DOI: http://dx.doi.org/10.1021/la0353430.

Rachford, H.H., Jr. and Rice, J.D. 1952. Procedure for Use of Electronic Digital Computers in Calculating Flash Vaporization Hydrocarbon Equilibrium. *Journal of Petroleum Technology* **4** (10): 327-328. DOI: http://dx.doi.org/10.2118/952327-G.

Ramirez, J. and Aguilera, R. 2014. Factors Controlling Fluid Migration and Distribution in the Eagle Ford Shale. Paper presented at the SPE/CSUR Unconventional Resources Conference, Calgary. Society of Petroleum Engineers. DOI: http://dx.doi.org/10.2118/171626-MS.

Redlich, O. and Kwong, J.N.S. 1949. On the Thermodynamics of Solutions. V. An Equation of State. Fugacities of Gaseous Solutions. *Chemical Reviews* **44** (1): 233-244. DOI: http://dx.doi.org/10.1021/cr60137a013.

Riewchotisakul, S. and Akkutlu, I.Y. 2016. Adsorption-Enhanced Transport of Hydrocarbons in Organic Nanopores. *SPE Journal* **21** (6): 1960-1969. DOI: http://dx.doi.org/10.2118/175107-PA.

Robinson, D.B. and Peng, D.Y. 1978. *The Characterization of the Heptanes and Heavier Fractions for the Gpa Peng-Robinson Programs*. Tulsa: Gas Processors Association.

Roebuck, I.F., Jr., Henderson, G.E., Douglas, J., Jr. et al. 1969. The Compositional Reservoir Simulator: Case I - the Linear Model. *SPE Journal* **9** (1): 115-130. DOI: http://dx.doi.org/10.2118/2033-PA.

Rossi, M.P., Gogotsi, Y., and Kornev, K.G. 2009. Deformation of Carbon Nanotubes by Exposure to Water Vapor. *Langmuir* **25** (5): 2804-2810. DOI: http://dx.doi.org/10.1021/la802684q.

Rwechungura, R.W., Dadashpour, M., and Kleppe, J. 2011. Advanced History Matching Techniques Reviewed. Paper presented at the SPE Middle East Oil and Gas Show and Conference, Manama. Society of Petroleum Engineers. DOI: http://dx.doi.org/10.2118/142497-MS.

Sandoval, D., Yan, W., Michelsen, M.L. et al. 2015. Phase Envelope Calculations for Reservoir Fluids in the Presence of Capillary Pressure. Paper presented at the SPE Annual Technical Conference and Exhibition, Houston. Society of Petroleum Engineers. DOI: http://dx.doi.org/10.2118/175110-MS.

Schechter, D.S. and Guo, B. 1998. Parachors Based on Modern Physics and Their Uses in Ift Prediction of Reservoir Fluids. *SPE Reservoir Evaluation & Engineering* **1** (03): 207-217. DOI: http://dx.doi.org/10.2118/30785-PA.

Scherer, G.W. 1990. Theory of Drying. *J. Am. Ceram. Soc.* **73** (1): 3-14. DOI: http://dx.doi.org/10.1111/j.1151-2916.1990.tb05082.x.

Schilthuis, R.J. 1935. Technique of Securing and Examining Sub-Surface Samples of Oil and Gas. Paper presented at the Drilling and Production Practice, New York. American Petroleum Institute.

Shereshefsky, J.L. 1928. A Study of Vapor Pressure in Small Capillaries. Part I. Water Vapor. (a). Soft Glass Capillaries 1,2. *Journal of the American Chemical Society* **50** (11): 2966-2980. DOI: http://dx.doi.org/10.1021/ja01398a016.

Shi, X.J. and Yuan, H.p. 2012. Fractal Modeling for Capillary Flow through Fiber Bundle. *J. Text. Inst.* **103** (1): 34-39. DOI: http://dx.doi.org/10.1080/00405000.2010.542009.

Si, C., Wang, X.-D., Yan, W.-M. et al. 2015. A Comprehensive Review on Measurement and Correlation Development of Capillary Pressure for Two-Phase Modeling of Proton Exchange Membrane Fuel Cells. *J. Chem.* **2015**: 17. DOI: http://dx.doi.org/10.1155/2015/876821.

Sing, K.S.W. and Williams, R.T. 2012. Historical Aspects of Capillarity and Capillary Condensation. *Microporous Mesoporous Mater.* **154**: 16-18. DOI: http://dx.doi.org/10.1016/j.micromeso.2011.09.022.

Smith, J., Van Ness, H., and Abbott, M. 2005. *Introduction to Chemical Engineering Thermodynamics*, 396. New York: McGraw Hill.

Soave, G. 1984. Improvement of the Van Der Waals Equation of State. *Chemical Engineering Science* **39** (2): 357-369. DOI: http://dx.doi.org/10.1016/0009-2509(84)80034-2.

Son, S., Chen, L., Kang, Q. et al. 2016. Contact Angle Effects on Pore and Corner Arc Menisci in Polygonal Capillary Tubes Studied with the Pseudopotential Multiphase Lattice Boltzmann Model. *Computation* **4** (1). DOI: http://dx.doi.org/10.3390/computation4010012.

Soreide, I. 1989. Improved Phase Behavior Predictions of Petroleum Reservoir Fluids from a Cubic Equation of State. Doktor Ingenior, Norwegian Institute of Technology.

Standing, M.B. 1977. *Volumetric and Phase Behavior of Oil Field Hydrocarbon Systems*: SPE-AIME.

Stimpson, B.C. and Barrufet, M.A. 2016a. Effects of Confined Space on Production from Tight Reservoirs. Paper presented at the SPE Annual Technical Conference and Exhibition, Dubai. Society of Petroleum Engineers. DOI: http://dx.doi.org/10.2118/181686-MS.

Stimpson, B.C. and Barrufet, M.A. 2016b. Thermodynamic Modeling of Pure Components Including the Effects of Capillarity. *Journal of Chemical & Engineering Data* **61** (8): 2844-2850. DOI: http://dx.doi.org/10.1021/acs.jced.6b00188.

Sugden, S. 1924. The Variation of Surface Tension with Temperature and Some Related Functions. *Journal of the Chemical Society, Transactions* **125** (0): 32-41. DOI: http://dx.doi.org/10.1039/CT9242500032.

Sugden, S. 1930. *The Parachor and Valency*. London: G. Routledge.

Tan, S.P. and Piri, M. 2015. Equation-of-State Modeling of Confined-Fluid Phase Equilibria in Nanopores. *Fluid Phase Equilib.* **393**: 48-63. DOI: http://dx.doi.org/10.1016/j.fluid.2015.02.028.

Teklu, T.W., Alharthy, N., Kazemi, H. et al. 2014. Phase Behavior and Minimum Miscibility Pressure in Nanopores. *SPE Reservoir Eval. Eng.* **17** (3): 396-403. DOI: http://dx.doi.org/10.2118/168865-PA.

Thomeer, J.H.M. 1960. Introduction of a Pore Geometrical Factor Defined by the Capillary Pressure Curve. *Journal of Petroleum Technology* **12** (03): 73-77. DOI: http://dx.doi.org/10.2118/1324-G.

Thomson, W. 1871. On the Equilibrium of Vapour at a Curved Surface of Liquid. *Philosophical Magazine and Journal of Science* **42** (277): 448-452.

Tran, T., Sinurat, P.D., and Wattenbarger, B.A. 2011. Production Characteristics of the Bakken Shale Oil. Paper presented at the SPE Annual Technical Conference and Exhibition, Denver. Society of Petroleum Engineers. DOI: http://dx.doi.org/10.2118/145684-MS.

Tsakiroglou, C.D. 2011. A Method to Calculate the Multiphase Flow Properties of Heterogeneous Porous Media by Using Network Simulations. *AIChE J.* **57** (10): 2618-2628. DOI: http://dx.doi.org/10.1002/aic.12493.

Udell, K.S. 1982. The Thermodynamics of Evaporation and Condensation in Porous Media. Paper presented at the SPE California Regional Meeting, San Francisco. Society of Petroleum Engineers. DOI: http://dx.doi.org/10.2118/10779-MS.

Valbuena Olivares, E. 2015. Production Performance Modeling through Integration of Reservoir and Production Network with Asphaltene Deposition. Doctor of Philosophy, Texas A&M.

Varotsis, N. 1989. A Robust Prediction Method for Rapid Phase-Behavior Calculations. *SPE Reservoir Engineering* **4** (02): 237-243. DOI: http://dx.doi.org/10.2118/16943-PA.

Vorhauer, N., Wang, Y.J., Kharaghani, A. et al. 2015. Drying with Formation of Capillary Rings in a Model Porous Medium. *Transp. Porous Media* **110** (2): 197-223. DOI: http://dx.doi.org/10.1007/s11242-015-0538-1.

Wang, L., Parsa, E., Gao, Y. et al. 2014. Experimental Study and Modeling of the Effect of Nanoconfinement on Hydrocarbon Phase Behavior in Unconventional Reservoirs. Paper presented at the SPE Western North American and Rocky Mountain Joint Meeting, Denver. Society of Petroleum Engineers. DOI: http://dx.doi.org/10.2118/169581-MS.

Watanabe, S., Sugiyama, H., and Miyahara, M. 2008. Molecular Simulation of Condensation Process of Lennard-Jones Fluids Confined in Nanospace with Jungle-Gym Structure. *Adsorption* **14** (2): 165-170. DOI: http://dx.doi.org/10.1007/s10450-007-9087-4.

Watson, P., Cascella, M., May, D. et al. 1986. Prediction of Vapor Pressures and Saturated Molar Volumes with a Simple Cubic Equation of State: Part Ii: The Van Der Waals - 711 Eos. *Fluid Phase Equilibria* **27**: 35-52. DOI: http://dx.doi.org/10.1016/0378-3812(86)87039-X.

Weinaug, C.F. and Katz, D.L. 1943. Surface Tensions of Methane-Propane Mixtures. *Ind. Eng. Chem.* **35** (2): 239-246. DOI: http://dx.doi.org/10.1021/ie50398a028.

Whitson, C.H. and Sunjerga, S. 2012. Pvt in Liquid-Rich Shale Reservoirs. Paper presented at the SPE Annual Technical Conference and Exhibition, San Antonio. Society of Petroleum Engineers. DOI: http://dx.doi.org/10.2118/155499-MS.

Wilkinson, N.J., Alam, M.A., Clayton, J.M. et al. 1992. Positron Annihilation Study of Capillary Condensation of Nitrogen Gas in a Mesoporous Solid. *Physical Review Letters* **69** (24): 3535-3538.

Wilsdon, B., Bonnell, D., and Nottage, M. 1935. Properties of Liquid Films in Fine-Pored Systems. *Nature* **135**: 186-187.

Wilson, G.M. 1969. A Modified Redlich-Kwong Equation of State, Application to General Physical Data Calculations. In *65th National AIChE Meeting*. Cleveland, OH.

Wyllie, M. and Gardner, G. 1958. The Generalized Kozeny-Carman Equation. *World oil* **146** (4): 121-128.

Yarborough, L. 1979. Application of a Generalized Equation of State to Petroleum Reservoir Fluids. In *Equations of State in Engineering and Research*, Advances in Chemistry: American Chemical Society. 182.

Young, A.F., Pessoa, F.L.P., and Ahón, V.R.R. 2016. Comparison of 20 Alpha Functions Applied in the Peng–Robinson Equation of State for Vapor Pressure Estimation. *Industrial & Engineering Chemistry Research* **55** (22): 6506-6516. DOI: http://dx.doi.org/10.1021/acs.iecr.6b00721.

Young, T. 1805. An Essay on the Cohesion of Fluids. *Philos. Trans. R. Soc. London* **95**: 65-87. DOI: http://dx.doi.org/10.1098/rstl.1805.0005.

Yu, W., Lashgari, H.R., Wu, K. et al. 2015. Co2 Injection for Enhanced Oil Recovery in Bakken Tight Oil Reservoirs. *Fuel* **159**: 354-363. DOI: http://dx.doi.org/10.1016/j.fuel.2015.06.092.

Yuan, Y. and Lee, T.R. 2013. Contact Angle and Wetting Properties. In *Surface Science Techniques*, ed. Bracco, G. and Holst, B., Berlin, Heidelberg: Springer Berlin Heidelberg.

Zarragoicoechea, G.J. and Kuz, V.A. 2002. Van Der Waals Equation of State for a Fluid in a Nanopore. *Physical Review E* **65** (2): 021110.

Zarragoicoechea, G.J. and Kuz, V.A. 2004. Critical Shift of a Confined Fluid in a Nanopore. *Fluid Phase Equilib.* **220** (1): 7-9. DOI: http://dx.doi.org/10.1016/j.fluid.2004.02.014.

Zettlemoyer, A.C. 1968. Hydrophobic Surfaces. *Journal of Colloid and Interface Science* **28** (3): 343-369. DOI: http://dx.doi.org/10.1016/0021-9797(68)90066-0.

Zhang, M. and Ayala, L.F. 2016. Analytical Study of Flowing and in-Situ Compositions in Unconventional Liquid-Rich Gas Plays. Paper presented at the SPE Annual Technical Conference and Exhibition, Dubai. Society of Petroleum Engineers. DOI: http://dx.doi.org/10.2118/181567-MS.

Zhang, Y., Lashgari, H.R., Di, Y. et al. 2016. Capillary Pressure Effect on Hydrocarbon Phase Behavior in Unconventional Reservoirs. Paper presented at the SPE Low Perm Symposium, Denver. Society of Petroleum Engineers. DOI: http://dx.doi.org/10.2118/180235-MS.

APPENDIX A

DERIVATIONS

A.1 Derivation of a and b for PR EOS

The Peng-Robinson EOS in factored form is:

$$p = \frac{RT}{V_m - b} - \frac{a}{\left(V_m + b + \sqrt{2}b\right)\left(V_m + b - \sqrt{2}b\right)} \tag{A.1}$$

Applying partial fraction decomposition, the PR EOS is split into:

$$p = \frac{RT}{V_m - b} + \frac{a}{2\sqrt{2}b\left(V_m + b + \sqrt{2}b\right)} - \frac{a}{2\sqrt{2}b\left(V_m + b - \sqrt{2}b\right)} \tag{A.2}$$

The first criterion states that at the critical point, the first derivative of the EOS is zero. This also means there is only one real root, which is the critical point.

$$\left.\frac{dp}{dV_m}\right|_{T_c, V_c} = 0 \tag{A.3}$$

Taking the first derivative of the PR EOS yields:

$$\frac{dp}{dV_m} = -\frac{RT}{(V_m - b)^2} - \frac{a}{2\sqrt{2}b\left(V_m + b + \sqrt{2}b\right)^2} + \frac{a}{2\sqrt{2}b\left(V_m + b - \sqrt{2}b\right)^2} \tag{A.4}$$

The second criterion states that at the critical point, the second derivative equals zero.

$$\left.\frac{d^2p}{dV_m^2}\right|_{T_c, V_{m,c}} = 0 \tag{A.5}$$

Taking the second derivative of the PR EOS yields:

$$\frac{d^2p}{dV_m^2} = \frac{2RT}{(V_m - b)^3} + \frac{a}{\sqrt{2}b\left(V_m + b + \sqrt{2}b\right)^3} - \frac{a}{\sqrt{2}b\left(V_m + b - \sqrt{2}b\right)^3} \tag{A.6}$$

Using the PR EOS at the critical point, applying the first and second derivative criteria, and defining the critical compressibility factor yields the following system of equations. There are four equations with the four unknowns being: Z_c, $V_{m,c}$, a, and b.

$$p_c = \frac{RT_c}{V_{m,c} - b} + \frac{a}{2\sqrt{2}b\left(V_{m,c} + b + \sqrt{2}b\right)} - \frac{a}{2\sqrt{2}b\left(V_{m,c} + b - \sqrt{2}b\right)} \tag{A.7}$$

$$0 = -\frac{RT_c}{\left(V_{m,c} - b\right)^2} - \frac{a}{2\sqrt{2}b\left(V_{m,c} + b + \sqrt{2}b\right)^2} + \frac{a}{2\sqrt{2}b\left(V_{m,c} + b - \sqrt{2}b\right)^2} \tag{A.8}$$

$$0 = \frac{2RT_c}{\left(V_{m,c} - b\right)^3} + \frac{a}{\sqrt{2}b\left(V_{m,c} + b + \sqrt{2}b\right)^3} - \frac{a}{\sqrt{2}b\left(V_{m,c} + b - \sqrt{2}b\right)^3} \tag{A.9}$$

$$Z_c = \frac{p_c V_{m,c}}{RT_c} \tag{A.10}$$

Solving for the unknowns is best done with a mathematical software. Using Mathematica yields the following solutions for the unknowns:

$$Z_c = \frac{1}{32}\left(11 - \frac{7}{\left(-13 + 16\sqrt{2}\right)^{1/3}} + \left(-13 + 16\sqrt{2}\right)^{1/3}\right) \tag{A.11}$$

$$V_{m,c} = Z_c \frac{RT_c}{p_c} \tag{A.12}$$

$$a = a_1(Z_c)\frac{R^2T_c^2}{p_c} \tag{A.13}$$

$$b = b_1(Z_c)\frac{RT_c}{p_c} \tag{A.14}$$

Where the constants are given by:

$$a_1 = \frac{95\left(2^{1/3}\right) + 60\left(2^{5/6}\right) + 5\left(2^{1/6}\right)\left(9 + 2\sqrt{2}\right)\left(4 + 3\sqrt{2}\right)^{1/3} \ldots}{\ldots - 17\left(4 + 3\sqrt{2}\right)^{2/3}} \over 48\left(4 + 3\sqrt{2}\right)^{2/3}} \tag{A.15}$$

$$b_1 = \frac{1}{3}\left(-1 - \frac{2^{2/3}}{\left(4 + 3\sqrt{2}\right)^{1/3}} + \left(8 + 6\sqrt{2}\right)^{1/3}\right) \tag{A.16}$$

Numerically, these constants match the constants presented with the PR EOS.

$$Z_c = 0.3074013 \tag{A.17}$$

$$a = 0.4572355\frac{R^2 T_c^2}{p_c} \tag{A.18}$$

$$b = 0.07779607\frac{RT_c}{p_c} \tag{A.19}$$

A.2 Peng-Robinson Fugacity Equation Derivation

The fugacity equation for the PR EOS equation is solved using the following definition of the fugacity coefficient:

$$\ln \phi_i^j = \int_0^{p^j} \left(Z^j - \frac{1}{p}\right) dp \tag{A.20}$$

A.2.1 Quadratic Mixing Rule for a

For multicomponent mixtures, mixing rules must be applied. The quadratic mixing rule is best applied to the attraction parameter. The quadratic mixing rule for a is defined as:

$$a = \sum_{i=1}^{N_c}\sum_{j=1}^{N_c} x_i x_j \left(a_i a_j \alpha_i \alpha_j\right)^{1/2}\left(1 - \delta_{ij}\right) \tag{A.21}$$

For convenience, the following version of a is defined:

$$a_{ij} = \left(a_i a_j \alpha_i \alpha_j\right)^{1/2}\left(1 - \delta_{ij}\right) \tag{A.22}$$

Making this substitution yields:

$$a = \sum_{i=1}^{N_c}\sum_{j=1}^{N_c} x_i x_j a_{ij} \tag{A.23}$$

The attraction parameter is then written in terms of number of moles as follows:

$$a = \sum_{i=1}^{N_c}\sum_{j=1}^{N_c} \frac{n_i n_j}{n^2} a_{ij} \tag{A.24}$$

The total number of moles n is constant, so it can be factored out:

$$a = \frac{1}{n^2}\sum_{i=1}^{N_c}\sum_{j=1}^{N_c} n_i n_j a_{ij} \tag{A.25}$$

Writing the total number of moles as a sum of individual number of moles gives:

$$a = \frac{1}{\left(\sum_{k=1}^{N_c} n_k\right)^2}\sum_{i=1}^{N_c}\sum_{j=1}^{N_c} n_i n_j a_{ij} \tag{A.26}$$

This can be simplified further by writing a as a product of two functions:

$$a = fg \tag{A.27}$$

The functions f and g are functions of $n_1, n_2, n_3, \ldots, n_{N_c}$:

$$f = \frac{1}{\left(\sum_{k=1}^{N_c} n_k\right)^2} \tag{A.28}$$

$$g = \sum_{i=1}^{N_c}\sum_{j=1}^{N_c} n_i n_j a_{ij} \tag{A.29}$$

A.2.1.1 Derivative of the Quadratic Mixing Rule

When solving for the fugacity coefficient, the derivative of the attraction parameter with respect to number of moles is required.

The derivative of a with respect to the number of moles of a certain component x (where $1 \leq x \leq N_c$) is determined by application of the product rule for derivatives:

$$\frac{da}{dn_x} = \frac{df}{dn_x} g + f \frac{dg}{dn_x} \tag{A.30}$$

The derivative of f can be evaluated fairly straightforwardly:

$$\frac{df}{dn_x} = -\frac{2}{\left(\sum_{k=1}^{N_c} n_k\right)^3} \tag{A.31}$$

The derivative of g is somewhat more complicated. It will be easier to evaluate it by first expanding the terms:

$$\begin{aligned} g = {} & n_1^2 a_{11} + n_1 n_2 a_{12} + n_1 n_3 a_{13} + \cdots + n_1 n_{N_c} a_{1N_c} + n_2 n_1 a_{21} + n_2^2 a_{22} \\ & + n_2 n_3 a_{23} + \cdots + n_2 n_{N_c} a_{2N_c} + n_3 n_1 a_{31} + n_3 n_2 a_{32} + n_3^2 a_{33} \\ & + \cdots + n_3 n_{N_c} a_{3N_c} + \cdots + n_{N_c} n_1 a_{N_c 1} + n_{N_c} n_2 a_{N_c 2} + n_{N_c} n_3 a_{N_c 3} \\ & + \cdots + n_{N_c}^2 a_{N_c N_c} \end{aligned} \tag{A.32}$$

Taking the derivative with respect to component 1 yields:

$$\begin{aligned} \frac{dg}{dn_1} = {} & 2n_1 a_{11} + n_2 a_{12} + n_3 a_{13} + \cdots + n_{N_c} a_{1N_c} + n_2 a_{21} + n_3 a_{31} + \cdots \\ & + n_{N_c} a_{N_c 1} \end{aligned} \tag{A.33}$$

The interaction parameter δ_{ij} is symmetric, so:

$$\delta_{ji} = \delta_{ij} \tag{A.34}$$

Inserting this into the definition of a_{ji}:

$$a_{ji} = \left(a_j a_i \alpha_j \alpha_i\right)^{1/2}\left(1 - \delta_{ij}\right) \tag{A.35}$$

Applying the commutative law of multiplication ($ab = ba$):

$$a_{ji} = \left(a_i a_j \alpha_i \alpha_j\right)^{1/2}\left(1 - \delta_{ij}\right) \tag{A.36}$$

This is the same equation as above, therefore:

$$a_{ji} = a_{ij} \tag{A.37}$$

Inserting this relationship derived from symmetry of the interaction parameter into the derivative:

$$\frac{dg}{dn_1} = 2n_1 a_{11} + n_2 a_{12} + n_3 a_{13} + \cdots + n_{N_c} a_{1N_c} + n_2 a_{12} + n_3 a_{13} + \cdots + n_{N_c} a_{1N_c} \tag{A.38}$$

Combining like terms yields:

$$\frac{dg}{dn_1} = 2n_1 a_{11} + 2n_2 a_{12} + 2n_3 a_{13} + \cdots + 2n_{N_c} a_{1N_c} \tag{A.39}$$

The terms can then be written in summation form:

$$\frac{dg}{dn_1} = 2\sum_{i=1}^{N_c} n_i a_{1i} \tag{A.40}$$

This can then be generalized for any component x:

$$\frac{dg}{dn_x} = 2\sum_{i=1}^{N_c} n_i a_{xi} \tag{A.41}$$

Inserting the derivatives and definitions of the functions of f and g give the derivative of a with respect to any component x:

$$\frac{da}{dn_x} = -\frac{2}{\left(\sum_{k=1}^{N_c} n_k\right)^3}\sum_{i=1}^{N_c}\sum_{j=1}^{N_c} n_i n_j a_{ij} + \frac{2}{\left(\sum_{k=1}^{N_c} n_k\right)^2}\sum_{i=1}^{N_c} n_i a_{xi} \tag{A.42}$$

Factoring out one summation term in the first term:

$$\frac{da}{dn_x} = -\frac{2}{\sum_{k=1}^{N_c} n_k}\left(\frac{1}{\left(\sum_{k=1}^{N_c} n_k\right)^2}\sum_{i=1}^{N_c}\sum_{j=1}^{N_c} n_i n_j a_{ij}\right) + \frac{2}{\left(\sum_{k=1}^{N_c} n_k\right)^2}\sum_{i=1}^{N_c} n_i a_{xi} \tag{A.43}$$

Recognizing that the term in parenthesis is the definition of a, this can be simplified:

$$\frac{da}{dn_x} = -\frac{2a}{\sum_{k=1}^{N_c} n_k} + \frac{2}{\left(\sum_{k=1}^{N_c} n_k\right)^2}\sum_{i=1}^{N_c} n_i a_{xi} \tag{A.44}$$

Inserting the definition of the total number of moles n back into the equation gives the derivative:

$$\frac{da}{dn_x} = -\frac{2a}{n} + \frac{2}{n^2}\sum_{i=1}^{N_c} n_i a_{xi} \tag{A.45}$$

A.2.2 Linear Mixing Rule for b

The linear mixing rule is sufficient for the covolume parameter b.

The linear mixing rule is defined as:

$$b^j = \sum_{i=1}^{N_c} x_i^j b_i \tag{A.46}$$

Writing this in terms of number of moles:

$$b^j = \sum_{i=1}^{N_c} \frac{n_i^j}{n^j} b_i \tag{A.47}$$

The total number of moles n is constant, so it can be factored out:

$$b^j = \frac{1}{n^j} \sum_{i=1}^{N_c} n_i^j b_i \tag{A.48}$$

Writing the total number of moles as a sum of individual number of moles:

$$b^j = \frac{1}{\sum_{i=1}^{N_c} n_i^j} \sum_{i=1}^{N_c} n_i^j b_i \tag{A.49}$$

This can be simplified further by writing b as a product of two functions:

$$b^j = fg \tag{A.50}$$

The functions f and g are functions of $n_1, n_2, n_3, \dots, n_{N_c}$:

$$f = \frac{1}{\sum_{i=1}^{N_c} n_i^j} \tag{A.51}$$

$$g = \sum_{i=1}^{N_c} n_i^j b_i \tag{A.52}$$

A.2.2.1 Derivative of the Linear Mixing Rule

The derivative of b with respect to the number of moles of a certain component x (where $1 \leq x \leq N_c$) is determined by application of the product rule for derivatives:

$$\frac{db^j}{dn_x} = \frac{df}{dn_x} g + f \frac{dg}{dn_x} \tag{A.53}$$

The derivative of f can be evaluates fairly straightforwardly:

$$\frac{df}{dn_x} = -\frac{1}{\left(\sum_{i=1}^{N_c} n_i^j\right)^2} \tag{A.54}$$

The derivative of g is also fairly simple, since it will only have one term that contains the component x:

$$\frac{dg}{dn_x} = b_x \tag{A.55}$$

Inserting the derivatives and definitions of the functions of f and g give the derivative of b with respect to any component x:

$$\frac{db^j}{dn_x} = -\frac{1}{\left(\sum_{i=1}^{N_c} n_i^j\right)^2}\sum_{i=1}^{N_c} n_i^j b_i + \frac{1}{\sum_{i=1}^{N_c} n_i^j} b_x \tag{A.56}$$

Factoring out the summation term in the denominator:

$$\frac{db^j}{dn_x} = \frac{1}{\sum_{i=1}^{N_c} n_i^j}\left(b_x - \frac{1}{\sum_{i=1}^{N_c} n_i^j}\sum_{i=1}^{N_c} n_i^j b_i\right) \tag{A.57}$$

Recognizing that the second term in the parentheses is the definition of b, this can be simplified:

$$\frac{db^j}{dn_x} = \frac{1}{\sum_{i=1}^{N_c} n_i^j}(b_x - b) \tag{A.58}$$

Inserting the definition of the total number of moles of n back into the equation gives the derivative:

$$\frac{db^j}{dn_x} = \frac{b_x - b^j}{n^j} \tag{A.59}$$

A.2.3 Fugacity Coefficient Equation

The equation for the fugacity coefficient is:

$$RT \ln \phi_x^j = -\int_{\infty}^{V_t^j}\left[\left(\frac{\partial P}{\partial n_x^j}\right)_{T,n_j \neq x} - \frac{RT}{V_t^j}\right] dV_t^j - RT \ln Z^j \tag{A.60}$$

The Peng Robinson Equation of State can be written in the following form including total volume and number of moles:

$$P = \frac{RT}{\frac{V_t}{n} - b} + \frac{1}{2\sqrt{2}b}\frac{(a\alpha)}{\left(\frac{V_t}{n} + b + \sqrt{2}b\right)} - \frac{1}{2\sqrt{2}b}\frac{(a\alpha)}{\left(\frac{V_t}{n} + b - \sqrt{2}b\right)} \tag{A.61}$$

Taking the derivative of P with respect to n_x for the fugacity equation is:

$$\begin{aligned}\frac{\partial P}{\partial n_x} = {} & \frac{RT\left(\frac{V_t}{n^2} + \frac{\partial b}{\partial n_x}\right)}{\left(\frac{V_t}{n} - b\right)^2} - \frac{1}{2\sqrt{2}b^2}\frac{(a\alpha)}{\left(\frac{V_t}{n} + b + \sqrt{2}b\right)}\left(\frac{\partial b}{\partial n_x}\right) \\ & + \frac{1}{2\sqrt{2}b}\frac{1}{\left(\frac{V_t}{n} + b + \sqrt{2}b\right)}\left(\frac{\partial (a\alpha)}{\partial n_x}\right) \\ & + \frac{1}{2\sqrt{2}b}\frac{(a\alpha)\left(\frac{V_t}{n^2} - \frac{\partial b}{\partial n_x} - \sqrt{2}\frac{\partial b}{\partial n_x}\right)}{\left(\frac{V_t}{n} + b + \sqrt{2}b\right)^2} \\ & + \frac{1}{2\sqrt{2}b^2}\frac{(a\alpha)}{\left(\frac{V_t}{n} + b - \sqrt{2}b\right)}\left(\frac{\partial b}{\partial n_x}\right) \\ & - \frac{1}{2\sqrt{2}b}\frac{1}{\left(\frac{V_t}{n} + b - \sqrt{2}b\right)}\left(\frac{\partial (a\alpha)}{\partial n_x}\right) \\ & + \frac{1}{2\sqrt{2}b}\frac{(a\alpha)\left(-\frac{V_t}{n^2} - \frac{\partial b}{\partial n_x} + \sqrt{2}\frac{\partial b}{\partial n_x}\right)}{\left(\frac{V_t}{n} + b - \sqrt{2}b\right)^2}\end{aligned} \tag{A.62}$$

Inserting the derivatives, applying partial fraction decomposition, and simplifying:

$$\begin{aligned}\frac{\partial P}{\partial n_x} = {} & \frac{RT}{(V_t - bn)} + \frac{C_1}{\left(\frac{V_t}{n} - b\right)^2} + \frac{C_2}{\left(\frac{V_t}{n} + b_1\right)} - \frac{C_2}{\left(\frac{V_t}{n} + b_2\right)} + \frac{C_4}{\left(\frac{V_t}{n} + b_1\right)^2} \\ & + \frac{C_5}{\left(\frac{V_t}{n} + b_2\right)^2}\end{aligned} \tag{A.63}$$

where the coefficients are:

$$C_1 = RT\left(\frac{b_x}{n}\right) \tag{A.64}$$

$$C_2 = \frac{1}{2\sqrt{2}b}\left(\frac{(a\alpha)b_x}{bn} + \frac{2}{n}\sum_{i=1}^{N_c} y_i(a\alpha)_{xi}\right) \tag{A.65}$$

$$C_4 = -\frac{(a\alpha)}{2\sqrt{2}b}\left(\frac{b_x}{n}\left(\sqrt{2}+1\right)\right) \tag{A.66}$$

$$C_5 = -\frac{(a\alpha)}{2\sqrt{2}b}\left(\frac{b_x}{n}\left(\sqrt{2}-1\right)\right) \tag{A.67}$$

Inserting this into the fugacity equation:

$$\begin{aligned} RT\ln\phi_x = -\int_{\infty}^{V_t}\Bigg[&\frac{RT}{(V_t-bn)} + \frac{C_1}{\left(\frac{V_t}{n}-b\right)^2} + \frac{C_2}{\left(\frac{V_t}{n}+b_1\right)} - \frac{C_2}{\left(\frac{V_t}{n}+b_2\right)} \\ &+ \frac{C_4}{\left(\frac{V_t}{n}+b_1\right)^2} + \frac{C_5}{\left(\frac{V_t}{n}+b_2\right)^2} - \frac{RT}{V_t}\Bigg]dV_t - RT\ln Z \end{aligned} \tag{A.68}$$

Evaluating this integral:

$$\begin{aligned} RT\ln\phi_x = \Bigg[&RT\ln(V_t-bn) - \frac{C_1 nRT}{\left(\frac{V_t}{n}-b\right)} + C_2 n\ln\left(\frac{V_t}{n}+b_1\right) \\ &- C_2 n\ln\left(\frac{V_t}{n}+b_2\right) - \frac{C_4 n}{\left(\frac{V_t}{n}+b_1\right)} - \frac{C_5 n}{\left(\frac{V_t}{n}+b_2\right)} - RT\ln V_t\Bigg]_{\infty}^{V_t} \\ &- RT\ln Z \end{aligned} \tag{A.69}$$

Inserting the bounds of integration and simplifying:

$$RT\ln\phi_x = RT\ln\left(\frac{V_t - bn}{V_t Z}\right) - \frac{C_1 nRT}{\left(\frac{V_t}{n} - b\right)} + C_2 n\ln\left(\frac{\frac{V_t}{n} + b_1}{\frac{V_t}{n} + b_2}\right) - \frac{C_4 n}{\left(\frac{V_t}{n} + b_1\right)} - \frac{C_5 n}{\left(\frac{V_t}{n} + b_2\right)} \tag{A.70}$$

The following form of the real gas equation is useful for simplifying:

$$\frac{V_t}{n} = \frac{ZRT}{P} \tag{A.71}$$

Substituting in Z, b_1, and b_2:

$$RT\ln\phi_x = RT\ln\left(\frac{\frac{ZRT}{P}n - bn}{\frac{ZRT}{P}nZ}\right) - \frac{C_1 nRT}{\left(\frac{ZRT}{P} - b\right)} + C_2 n\ln\left(\frac{\frac{ZRT}{P} + \left(\sqrt{2}+1\right)b}{\frac{ZRT}{P} - \left(\sqrt{2}-1\right)b}\right) - \frac{C_4 n}{\left(\frac{ZRT}{P} + b\left(1+\sqrt{2}\right)\right)} - \frac{C_5 n}{\left(\frac{ZRT}{P} + b\left(1-\sqrt{2}\right)\right)} \tag{A.72}$$

Inserting in the coefficients and simplifying yields:

$$\ln\phi_x = \ln\left(\frac{Z-\frac{bP}{RT}}{Z^2}\right) + \frac{(a\alpha)}{2\sqrt{2}bRT}\left(\frac{b_x}{b}+\frac{2}{(a\alpha)}\sum_{i=1}^{N_c} y_i(a\alpha)_{xi}\right)\ln\left(\frac{Z+\left(\sqrt{2}+1\right)\frac{bP}{RT}}{Z-\left(\sqrt{2}-1\right)\frac{bP}{RT}}\right) + \frac{b_x}{bRT}\left(\frac{(a\alpha)b\left(\sqrt{2}+1\right)}{2\sqrt{2}b\left(\frac{ZRT}{P}+b\left(1+\sqrt{2}\right)\right)} + \frac{(a\alpha)b\left(\sqrt{2}-1\right)}{2\sqrt{2}b\left(\frac{ZRT}{P}+b\left(1-\sqrt{2}\right)\right)} - \frac{RTb}{\left(\frac{Z}{P}-\frac{b}{RT}\right)}\right) \quad \text{(A.73)}$$

The last term in parentheses is a form of the PR EOS and the overall equation simplifies to:

$$\ln\phi_x = -\ln(Z-B) + \frac{(a\alpha)}{2\sqrt{2}b}\left(\frac{b_x}{b}+\frac{2}{(a\alpha)}\sum_{i=1}^{N_c} y_i(a\alpha)_{xi}\right)\ln\left(\frac{Z+\left(\sqrt{2}+1\right)B}{Z-\left(\sqrt{2}-1\right)B}\right) + \frac{b_x}{b}(Z-1) \quad \text{(A.74)}$$

Applying the definitions of A and B and defining ψ_i, the fugacity equation becomes:

$$\ln\phi_x = \frac{b_x}{b}(Z-1) - \ln(Z-B) - \frac{A}{2\sqrt{2}B}\left(\frac{\psi_i}{(a\alpha)}-\frac{b_x}{b}\right)\ln\left(\frac{Z+\left(\sqrt{2}+1\right)B}{Z-\left(\sqrt{2}-1\right)B}\right) \quad \text{(A.75)}$$

$$\psi_i = 2\sum_{i=1}^{N_c} y_i(a\alpha)_{xi} \quad \text{(A.76)}$$

A.3 Helmholtz Energy

A.3.1 First Law of Thermodynamics

Beginning with the differential form of the first law of thermodynamics:

$$dU_t = dQ + dW \tag{A.77}$$

The definitions of differential heat (dQ) and differential work (dW) are:

$$dQ = TdS_t \tag{A.78}$$

$$dW = -PdV_t + \sigma dA \tag{A.79}$$

Substituting these into the first law of thermodynamics:

$$dU_t = TdS_t - PdV_t + \sigma dA \tag{A.80}$$

A.3.2 Helmholtz Energy

The Helmholtz energy is defined as:

$$F_t = U_t - TS_t \tag{A.81}$$

Taking the total differential:

$$dF_t = dU_t - S_t dT - TdS_t \tag{A.82}$$

Substituting the first law of thermodynamics in for the dU_t term:

$$dF_t = TdS_t - PdV_t + \sigma dA - S_t dT - TdS_t \tag{A.83}$$

Cancelling terms:

$$dF_t = -PdV_t - S_t dT + \sigma dA \tag{A.84}$$

A.3.3 Closed System Relationships

Taking the derivative with respect to dV_t:

$$\frac{d}{dV_t}(dF_t) = \frac{d}{dV_t}(-PdV_t - S_t dT + \sigma dA) \tag{A.85}$$

Applying the differential to the difference:

$$\frac{d}{dV_t}(dF_t) = -\frac{d}{dV_t}(PdV_t) - \frac{d}{dV_t}(S_t dT) + \frac{d}{dV_t}(\sigma dA) \tag{A.86}$$

Recognizing the last two terms do not change with volume and simplifying:

$$\frac{d}{dV_t}(dF_t) = -P \tag{A.87}$$

This relationship is true for constant temperature, surface area, and number of moles of each species. The relationship can be written:

$$\left[\frac{dF_t}{dV_t}\right]_{T,A,n} = -P \tag{A.88}$$

Following the similar method but taking the derivative with respect to temperature yields:

$$\left[\frac{dF_t}{dT}\right]_{V_t,A,n} = -S_t \tag{A.89}$$

The same method achieves a result for the derivative with respect to surface area:

$$\left[\frac{dF_t}{dA}\right]_{T,V_t,n} = \sigma \tag{A.90}$$

A.3.4 Open System

Allowing for flow of mass into and out of the system, the Helmholtz energy becomes a function of temperature, volume, and number of moles of each species, n_i:

$$F_t = f(V_t, T, A, n_1, n_2, \ldots, n_i) \tag{A.91}$$

Taking the total derivative of this equation:

$$\begin{aligned} dF_t = \left[\frac{\partial F_t}{\partial V_t}\right]_{T,A,n} dV_t + \left[\frac{\partial F_t}{\partial T}\right]_{V_t,A,n} dT + \left[\frac{\partial F_t}{\partial A}\right]_{T,V_t,n} dA + \left[\frac{\partial F_t}{\partial n_1}\right]_{T,V_t,A,n_{j\neq 1}} dn_1 \\ + \left[\frac{\partial F_t}{\partial n_2}\right]_{T,V_t,A,n_{j\neq 2}} dn_2 + \cdots + \left[\frac{\partial F_t}{\partial n_i}\right]_{T,V_t,A,n_{j\neq i}} dn_i \end{aligned} \tag{A.92}$$

Simplifying the mole terms:

$$dF_t = \left[\frac{\partial F_t}{\partial V_t}\right]_{T,n} dV_t + \left[\frac{\partial F_t}{\partial T}\right]_{V_t,n} dT + + \left[\frac{\partial F_t}{\partial A}\right]_{T,V_t,n} dA \sum_i \left[\frac{\partial F_t}{\partial n_i}\right]_{T,V_t,n_{j\neq i}} dn_i \quad \text{(A.93)}$$

Substituting the derived relationships for the first two terms:

$$dF_t = -PdV_t - S_t dT + \sigma dA + \sum_i \left[\frac{\partial F_t}{\partial n_i}\right]_{T,V_t,n_{j\neq i}} dn_i \quad \text{(A.94)}$$

A.3.5 Chemical Potential

In this case, the last term can be defined as chemical potential:

$$\mu_i = \left[\frac{\partial F_t}{\partial n_i}\right]_{T,V_t,n_{j\neq i}} \quad \text{(A.95)}$$

Substituting this into the Helmholtz equation:

$$dF_t = -PdV_t - S_t dT + \sigma dA + \sum_i \mu_i dn_i \quad \text{(A.96)}$$

A.3.6 Helmholtz Energy

Assuming one mole, this can be reduced to the general form of Helmholtz energy:

$$dF = -PdV - SdT + \sigma dA + \sum_i \mu_i dx_i \quad \text{(A.97)}$$

A.4 Young Laplace from Thermodynamics

A.4.1 Two-Phase System

The two-phase system is described as a bubble surrounded by a fluid. The bubble fluid and the surrounding fluid have different pressures and compositions as shown below:

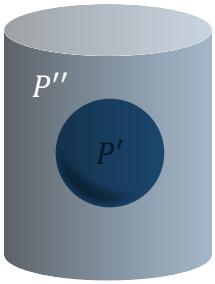

A.4.2 Helmholtz Energy for Phases

Referring to the derivations of the Helmholtz energy for the case with and without interfacial work, the interfacial work can be assumed to be part of one phase, so the Helmholtz energy equations for each phase become:

$$dF_t' = -P'dV_t' - S_t'dT' + \sum_i \mu_i' dn_i' + \sigma dA \tag{A.98}$$

$$dF_t'' = -P''dV_t'' - S_t''dT'' + \sum_i \mu_i'' dn_i'' \tag{A.99}$$

A.4.3 Total Helmholtz Energy

In order to relate the Helmholtz energy for the two equations, the following relationship is required, which states that the Helmholtz energy for the total system is the sum of the two energies for each phase:

$$dF_t = dF_t' + dF_t'' \tag{A.100}$$

Substituting the Helmholtz energy equations for each phase:

$$dF_t = -P'dV_t' - S_t'dT' + \sum_i \mu_i' dn_i' + \sigma dA - P''dV_t'' - S_t''dT'' + \sum_i \mu_i'' dn_i'' \tag{A.101}$$

Since this two-phase system is closed, the following relations are true (where c_1 and c_2 are constants):

$$V_t' + V_t'' = c_1 \tag{A.102}$$

$$n_i' + n_i'' = c_2 \tag{A.103}$$

Solving for the surrounding phase:

$$V_t'' = c_1 - V_t{}' \tag{A.104}$$

$$n_i'' = c_2 - n_i{}' \tag{A.105}$$

Taking the total differential of each phase:

$$dV_t'' = dc_1 - dV_t{}' \tag{A.106}$$

$$dn_i'' = dc_2 - dn_i{}'' \tag{A.107}$$

Since the derivative of a constant is zero, these relations simplify to:

$$dV_t'' = -dV_t{}' \tag{A.108}$$

$$dn_i'' = -dn_i{}' \tag{A.109}$$

Substituting these equations into the total Helmholtz equation above:

$$\begin{aligned} dF_t = -P'dV_t' - S_t'dT' + \sum_i \mu_i' dn_i' + \sigma dA - P''(-dV_t') - S_t''dT'' \\ + \sum_i \mu_i''(-dn_i') \end{aligned} \tag{A.110}$$

Factoring out the negatives:

$$dF_t = -P'dV_t' - S_t'dT' + \sum_i \mu_i' dn_i' + \sigma dA + P''dV_t' - S_t''dT'' - \sum_i \mu_i'' dn_i' \tag{A.111}$$

Recalling that $x_1 dt + x_2 dt = (x_1 + x_2)dt$, this can be simplified:

$$dF_t = (P'' - P')dV_t' - S_t'dT' + \sum_i (\mu_i' - \mu_i'')dn_i' + \sigma dA - S_t''dT'' \quad \text{(A.112)}$$

A.4.4 Assumptions

An assumption that is made is that these two phases are in thermal equilibrium, on other words, their temperatures are equal:

$$T' = T'' = T \quad \text{(A.113)}$$

Therefore, the derivatives are also the same:

$$dT' = dT'' = dT \quad \text{(A.114)}$$

Making this substitution:

$$dF_t = (P'' - P')dV_t' - S_t'dT + \sum_i (\mu_i' - \mu_i'')dn_i' + \sigma dA - S_t''dT \quad \text{(A.115)}$$

Rearranging:

$$dF_t = -(S_t' + S_t'')dT - (P' - P'')dV_t' + \sum_i (\mu_i' - \mu_i'')dn_i' + \sigma dA \quad \text{(A.116)}$$

Assuming any changes in the process are isothermal, $dT = 0$, therefore:

$$dF_t = -(P' - P'')dV_t' + \sum_i (\mu_i' - \mu_i'')dn_i' + \sigma dA \quad \text{(A.117)}$$

At equilibrium, the chemical potentials must be the same, so:

$$\mu_i' = \mu_i'' = c_3 \quad \text{(A.118)}$$

Making this substitution:

$$dF_t = -(P' - P'')dV_t' + \sum_i (c_3 - c_3)dn_i' + \sigma dA \quad \text{(A.119)}$$

Simplifying:

$$dF_t = -(P' - P'')dV_t' + \sigma dA \quad \text{(A.120)}$$

At equilibrium, the energy is in equilibrium and therefore, $dF_t = 0$. Making this replacement:

$$0 = -(P' - P'')dV_t' + \sigma dA \quad \text{(A.121)}$$

Rearranging:

$$(P' - P'') = \sigma \frac{dA}{dV_t'} \quad \text{(A.122)}$$

A.4.5 Bubble Geometry

In the case of a bubble in a fluid, the bubble will take a spherical shape, thus minimizing the surface area. The area and volume equations for a sphere are:

$$A = 4\pi R_c^2 \quad \text{(A.123)}$$

$$V_t' = \frac{4}{3}\pi R_c^3 \quad \text{(A.124)}$$

Taking the total derivative:

$$dA = 8\pi R_c \quad \text{(A.125)}$$

$$dV_t' = 4\pi R_c^2 \quad \text{(A.126)}$$

Making these substitutions:

$$(P' - P'') = \sigma \frac{8\pi R_c}{4\pi R_c^2} \quad \text{(A.127)}$$

Simplifying yields the Young-Laplace equation:

$$(P' - P'') = \frac{2\sigma}{R_c} \quad \text{(A.128)}$$

A.4.6 Capillary Pressure Equation

The definition of capillary pressure is the difference between phase pressures caused by capillary action. This can be expressed:

$$P' - P'' = P_c \tag{A.129}$$

Making this substitution:

$$P_c = \frac{2\sigma}{R_c} \tag{A.130}$$

Inserting a capillary into both phases in the following manner yields the familiar capillary behavior:

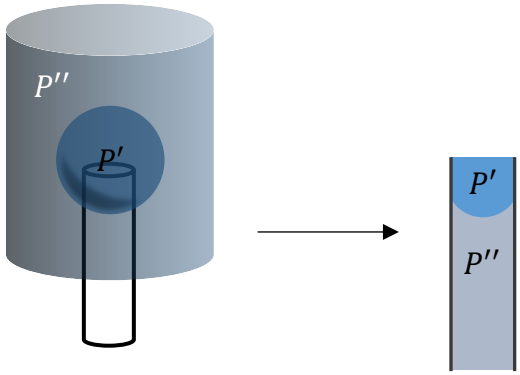

The following equation relates the radius of curvature to the capillary radius:

$$\cos(\theta) = \frac{r}{R_c} \tag{A.131}$$

Solving for the radius:

$$R_c = \frac{r}{\cos(\theta)} \tag{A.132}$$

Substituting this into the capillary pressure equation:

$$P_c = \frac{2\sigma}{\left(\frac{r}{\cos(\theta)}\right)} \tag{A.133}$$

Simplifying yields the commonly known equation for capillary pressure:

$$P_c = \frac{2\sigma \cos(\theta)}{r} \tag{A.134}$$

A.5 Single Component Saturation

For a pore containing liquid and gas:

$$V_l = S_l V_t \tag{A.135}$$

$$V_g = (1 - S_l)V_t \tag{A.136}$$

The number of moles in each phase can be calculated using the molar volumes:

$$n_l = \frac{V_l}{V_m^l} \tag{A.137}$$

$$n_g = \frac{V_g}{V_m^g} \tag{A.138}$$

Writing a mole balance gives:

$$n_t = n_l + n_g \tag{A.139}$$

Writing in terms of volumes:

$$n_t = \frac{V_l}{V_m^l} + \frac{V_g}{V_m^g} \tag{A.140}$$

Writing in terms of saturation and total volume:

$$n_t = \frac{S_l V_t}{V_m^l} + \frac{(1 - S_l)V_t}{V_m^g} \tag{A.141}$$

The total number of moles and total volume can be specified to create a closed system. The only unknown is liquid saturation. To do this, the equation above is divided by V_t and expanded:

$$\frac{n_t}{V_t} = \frac{S_l}{V_m^l} + \frac{1}{V_m^g} - \frac{S_l}{V_m^g} \tag{A.142}$$

Factoring and rearranging yields:

$$\frac{n_t}{V_t} - \frac{1}{V_m^g} = S_l\left(\frac{1}{V_m^l} - \frac{1}{V_m^g}\right) \tag{A.143}$$

Then, while showing saturation at various pressures, the system (total volume and number of moles) can remain the same to provide an accurate comparison, as if the system were closed and undergoing temperature and pressure changes.

A.6 Thomeer Model Linearization with Known Endpoint

Unknowns are P_{ct}, G, and S_∞

$$P_c = P_{ct} \exp\left[\frac{-G}{\ln(S_o^*/S_\infty)}\right] \tag{A.144}$$

Given $P_c(S_o^* = 1) = P_{c1}$ is known,

$$P_{c1} = P_{ct} \exp\left[\frac{-G}{\ln(1/S_\infty)}\right] \tag{A.145}$$

Solving for G:

$$G = -\ln\left(\frac{P_{c1}}{P_{ct}}\right)\ln\left(\frac{1}{S_\infty}\right) \tag{A.146}$$

Substituting into the model (unknowns are P_{ct} and S_∞):

$$P_c = P_{ct} \exp\left[\frac{\ln\left(\frac{P_{c1}}{P_{ct}}\right)\ln\left(\frac{1}{S_\infty}\right)}{\ln(S_o^*/S_\infty)}\right] \tag{A.147}$$

Replacing variables:

$$y = a \exp\left[\frac{\ln\left(\frac{c}{a}\right)\ln\left(\frac{1}{b}\right)}{\ln\left(\frac{x}{b}\right)}\right] \tag{A.148}$$

Where (unknowns are a and b)

$$y = P_c \tag{A.149}$$

$$x = S_o^* \tag{A.150}$$

$$a = P_{ct} \tag{A.151}$$

$$b = S_\infty \tag{A.152}$$

$$c = P_{c1} \tag{A.153}$$

Simplifying:

$$y = a\left(\frac{c}{a}\right)^{\ln\left(\frac{1}{b}\right)/\ln\left(\frac{x}{b}\right)} \tag{A.154}$$

Taking the natural logarithm of both sides:

$$\ln(y) = \ln\left[a\left(\frac{c}{a}\right)^{\ln\left(\frac{1}{b}\right)/\ln\left(\frac{x}{b}\right)}\right] \tag{A.155}$$

Simplifying:

$$\ln(y) = \ln(a) + \frac{\ln\left(\frac{c}{a}\right)\ln\left(\frac{1}{b}\right)}{\ln\left(\frac{x}{b}\right)} \tag{A.156}$$

Expanding logarithms:

$$\ln(y) = \ln(a) + \frac{-\ln(b)\left[\ln(c) - \ln(a)\right]}{\ln(x) - \ln(b)} \tag{A.157}$$

Simplifying by common denominator, expanding, and combining:

$$\ln(y) = \frac{\ln(a)\ln(x) - \ln(b)\ln(c)}{\ln(x) - \ln(b)} \tag{A.158}$$

Replacing variables:

$$u = \frac{dv - fg}{v - f} \tag{A.159}$$

Where (unknowns are d and f)

$$u = \ln(y) \tag{A.160}$$

$$v = \ln(x) \tag{A.161}$$

$$d = \ln(a) \tag{A.162}$$

$$f = \ln(b) \tag{A.163}$$

$$g = \ln(c) \tag{A.164}$$

Simplifying:

$$uv = dv + f(u - g) \tag{A.165}$$

Placing in linear form:

$$\frac{uv}{u - g} = \frac{dv}{u - g} + f \tag{A.166}$$

Replacing variables:

$$Y = MX + B \tag{A.167}$$

Where (unknowns are M and B):

$$Y = \frac{uv}{u - g} = \frac{\ln(y)\ln(x)}{\ln(y) - \ln(c)} = \frac{\ln(P_c)\ln(S_o^*)}{\ln(P_c) - \ln(P_{c1})} \tag{A.168}$$

$$X = \frac{v}{u-g} = \frac{\ln(x)}{\ln(y)-\ln(c)} = \frac{\ln(S_o^*)}{\ln(P_c)-\ln(P_{c1})} \tag{A.169}$$

$$M = \ln(a) = \ln(P_{ct}) \tag{A.170}$$

$$B = \ln(b) = \ln(S_\infty) \tag{A.171}$$

The linear form can be solved using a linear regression to find M and B with the known X's and Y's. The unknowns are then calculated:

$$P_{ct} = \exp(M) \tag{A.172}$$

$$S_\infty = \exp(B) \tag{A.173}$$